

Supporting Information for

Two-photon, visible light water splitting at a molecular ruthenium complex

Jacob Schneidewind*, Miguel A. Argüello Cordero, Henrik Junge, Stefan Lochbrunner, Matthias Beller

*Corresponding author, e-mail: Jacob.Schneidewind@catalysis.de

Other supplementary materials for this manuscript:

Original data and analysis code are publicly available at:

<https://github.com/jschneidewind/Water-Splitting>

1 Table of Contents	
1.1 Table of Figures	4
1.2 Table of Tables	6
2 Methods and Materials.....	8
3 Synthesis Procedures and Characterization	9
3.1 Synthesis of Complex 1.....	9
3.1.1 Synthesis using N ₂ O	9
3.1.2 Photographs Showing Synthesis and Product.....	11
3.1.3 Synthesis using Ag ₂ O.....	12
3.1.4 Synthesis via Reflux of 2-trans.....	12
3.2 Synthesis of Complex 2-trans.....	13
3.2.1 Synthesis in H ₂ O	13
3.2.2 Crystallization of 2-trans.....	13
3.3 Synthesis of (p-cymene)RuCl ₂ (CO)	13
3.4 Synthesis of (PNN)RuCl ₂ (CO)	13
4 Procedures for Irradiation and Subsequent Data Analysis.....	14
4.1 NMR Scale Irradiation	14
4.1.1 Irradiation Procedure.....	14
4.1.2 Interpretation of NMR Results	14
4.1.3 Data Analysis for Concentration-Time Profile	15
4.1.4 Data Analysis for Dual Irradiation.....	16
4.2 Liquid Phase O ₂ Measurement.....	17
4.2.1 Irradiation Procedure.....	17
4.2.2 General Remarks on Data Analysis	18
4.2.3 Data Analysis for Intensity Experiments.....	19
4.2.4 Data Analysis for Kinetic Isotope Effect and Temperature Dependence	20
4.2.5 Data Analysis for Dual Irradiation Experiments.....	21
4.2.6 Note on Reaction Order/Concentration Dependence	22
4.3 Gas Phase O ₂ Measurement.....	23
4.3.1 Irradiation Procedure.....	23
4.3.2 Data Analysis and O ₂ Consumption Reaction.....	23
4.4 Comparison of 2-cis and O ₂ Formation Rates.....	24
4.5 Photographs of Irradiation Set-Ups	26
5 H₂O₂ Disproportionation	28
5.1 Experimental Procedure	28
5.2 Data Analysis	28
6 Chemical Actinometry	30
6.1 Light Source Spectra	30
6.2 Experimental Procedure	31
6.3 Chemical Actinometry Data and Analysis	31
7 NMR Data	33
7.1 Characterization of 1.....	33
7.2 Characterization of 2-trans.....	42
7.3 Characterization of (p-cymene)RuCl ₂ (CO)	44
7.4 Characterization of (PNN)RuCl ₂ (CO)	45
7.5 Data for Irradiated Samples	47
7.6 Isomerization Reactions in the Dark	62
7.7 Data for $\partial(^{31}\text{P}) = 86$ ppm Product	65
8 Other Analytical Data	67
8.1 IR Spectrum of Complex 1	67
8.2 EPR Spectrum of Complex 1 Synthesis Raw Product.....	68
8.3 Time-Resolved UV/Vis Spectroscopy	69
8.3.1 Experimental Procedure.....	69

8.3.2	Results and Analysis	69
9	Ultrafast Pump-Probe Spectroscopy.....	73
9.1	Experimental Procedure and Analysis.....	73
9.2	Results and Interpretation.....	73
10	Photochemical Kinetic Model	76
10.1	Description of Kinetic Model.....	76
10.2	Relationship between Initial Rate and Photon Flux	76
10.3	Interpretation of Results.....	77
10.4	Comparison of Experimental Dual Irradiation Rates with Kinetic Model	78
10.5	Modelling of Other Photochemical Mechanisms	79
10.5.1	Bimolecular reaction pathways	79
10.5.2	Three-photon pathway with one stable intermediate	83
10.5.3	Three-photon pathway with two transient intermediates.....	85
11	Computational Section	87
11.1	Computational Methods	87
11.1.1	DFT Methods	87
11.1.2	CASSCF Methods.....	88
11.2	DFT Results	89
11.2.1	Relative Energies of [A] and [B] Isomers, Oxo Dimer, $[F]S_0 \rightarrow [A\text{-Mono}]S_0$	89
11.2.2	TD-DFT Computed UV-Vis Spectra	91
11.2.3	Natural Transition Orbitals for $[A]S_0$	92
11.2.4	Natural Transition Orbitals for $[B]T_0$	98
11.2.5	Natural Transition Orbitals for $[B\text{-Mono}]D_0$ (Me Model).....	100
11.2.6	Spin Density Plots	101
11.2.7	Scan-[DE] T_0	104
11.2.8	O-O Bond Formation Scans.....	105
11.2.9	Theoretical NMR Data for $[F]S_0$ Isomers.....	106
11.2.10	Theoretical UV-Vis Spectrum for $[F\text{-Trans-Up}]S_0$	107
11.3	CASSCF Results	108
11.3.1	Comparison of DFT and CASSCF Energies and Absorption Wavelengths	108
11.3.2	Energy Profile including PCM Solvation.....	109
11.3.3	Active Space Orbitals.....	110
11.3.4	Surfaces for $[B\text{-Mono}]D_n$	112
11.3.5	Difference Orbitals for Conical Intersections	113
11.3.6	Surfaces for $[C\text{-Mono}]D_0$	114
11.4	Integration of Computational and Experimental Results	115
11.4.1	Dual Irradiation Experiments	115
11.4.2	Decay Associated Spectra	118
11.5	Modelling Solar-to-Hydrogen Efficiency	119
11.5.1	Model Description	119
11.5.2	Results	121
11.6	Structures and Coordinates for Computed Species.....	126
12	References.....	157

1.1 Table of Figures

Figure 3.1-1 Photographs of synthesis stages during preparation of complex 1	11
Figure 3.1-2 Reaction set-up for reaction of 2-trans with N ₂ O	11
Figure 3.1-3 Complex 1 as a solid (left) and in aqueous solution (right)	12
Figure 4.1-1 Concentration-time profile for irradiation of complex 1 with QTH light source	16
Figure 4.2-1 Exemplary liquid phase O ₂ raw data (320 – 500 nm, 1 W intensity setting)	18
Figure 4.2-2 Exemplary liquid phase O ₂ data analyzed as described in 4.2.2 (320 – 500 nm, 1 W intensity setting)	19
Figure 4.2-3 Comparison of square (left) and linear (right) fit of intensity/rate dataset	20
Figure 4.3-1 Gas phase O ₂ detection data for irradiation of complex 1 with Hg light source (320 – 500 nm)	23
Figure 4.5-1 Set-up for irradiation on NMR scale	26
Figure 4.5-2 Set-up for irradiation with liquid phase O ₂ detection	26
Figure 4.5-3 Irradiation set-up (liquid phase O ₂ detection) in use (left) and close-up of assembled reactor	27
Figure 5.2-1 Liquid phase O ₂ measurement for H ₂ O ₂ disproportionation catalyzed by complex 1	29
Figure 6.1-1 Spectral power distribution of Hg light source with used filter settings	30
Figure 6.1-2 Measured power of QTH light source with different longpass filters	30
Figure 6.3-1 Chemical actinometry data for different power setting of Hg light source (320 – 500 nm)	31
Figure 7.1-1 ¹ H NMR spectrum of 1 in H ₂ O (298 K)	33
Figure 7.1-2 ³¹ P{ ¹ H} NMR spectrum of 1 in H ₂ O (298 K)	34
Figure 7.1-3 ¹ H NMR spectrum of 1 in DMSO-d ₆ (298 K)	35
Figure 7.1-4 ¹³ C{ ¹ H} NMR spectrum of 1 in DMSO-d ₆ (298 K)	36
Figure 7.1-5 ³¹ P{ ¹ H} NMR spectrum of 1 in DMSO-d ₆ (298 K)	37
Figure 7.1-6 ¹ H NMR spectrum of 1 in H ₂ O (298 K) synthesized using Ag ₂ O	38
Figure 7.1-7 ³¹ P{ ¹ H} NMR spectrum of 1 in H ₂ O (298 K) synthesized using Ag ₂ O	39
Figure 7.1-8 ¹ H NMR of 2-trans in H ₂ O (298 K) after three days of reflux, displaying formation of 1	40
Figure 7.1-9 ³¹ P{ ¹ H} NMR of 2-trans in H ₂ O (298 K) after three days of reflux, displaying formation of 1	41
Figure 7.2-1 ¹ H NMR spectrum of 2-trans in H ₂ O (298 K)	42
Figure 7.2-2 ³¹ P{ ¹ H} NMR spectrum of 2-trans in H ₂ O (298 K)	43
Figure 7.3-1 ¹ H NMR spectrum of (p-cymene)RuCl ₂ (CO) in CD ₂ Cl ₂ (298 K)	44
Figure 7.4-1 ¹ H NMR spectrum of (PNN)RuCl ₂ (CO) in CD ₂ Cl ₂ (298 K)	45
Figure 7.4-2 ³¹ P{ ¹ H} NMR spectrum of (PNN)RuCl ₂ (CO) in CD ₂ Cl ₂ (298 K)	46
Figure 7.5-1 ¹ H NMR spectrum of 1 (in H ₂ O, 298 K) after irradiation with QTH light source for 46h	47
Figure 7.5-2 ³¹ P{ ¹ H} NMR spectrum of 1 (in H ₂ O, 298 K) after irradiation with QTH light source for 46h	48
Figure 7.5-3 ¹ H- ³¹ P HMBC (hydride region) NMR spectrum of 1 (in H ₂ O, 298 K) after irradiation	50
Figure 7.5-4 ¹ H- ³¹ P HMBC (aliphatic region) NMR spectrum of 1 (in H ₂ O, 298 K) after irradiation	51
Figure 7.5-5 ¹ H NMR spectrum of 2-trans (in H ₂ O, 298 K) after irradiation (320 – 500 nm, 4h) in presence of O ₂	52
Figure 7.5-6 ³¹ P{ ¹ H} NMR spectrum of 2-trans (in H ₂ O, 298 K) after irradiation (320 – 500 nm, 4h) in presence of O ₂	53
Figure 7.5-7 ¹ H NMR spectrum of 1 (in 52 mM KOH aq., 298 K, Ag ₂ O synthesis route) in air before irradiation.	54
Figure 7.5-8 ³¹ P{ ¹ H} NMR spectrum of 1 (in 52 mM KOH aq., 298 K, Ag ₂ O synthesis route) in air before irradiation.	55
Figure 7.5-9 ¹ H NMR spectrum of 1 (in 52 mM KOH aq., 298 K, Ag ₂ O synthesis route) in air after irradiation (QTH, 16h)	56
Figure 7.5-10 ³¹ P{ ¹ H} NMR spectrum of 1 (in 52 mM KOH aq., 298 K, Ag ₂ O synthesis route) in air after irradiation (QTH, 16h)	57
Figure 7.5-11 ¹ H NMR spectrum of 2-trans (in H ₂ O, 298 K) before irradiation, under argon	58
Figure 7.5-12 ³¹ P{ ¹ H} NMR spectrum of 2-trans (in H ₂ O, 298 K) before irradiation, under argon	59
Figure 7.5-13 ¹ H NMR spectrum of 2-trans (in H ₂ O, 298 K) after irradiation (Hg light source, 320 – 500 nm, 21 h), under argon	60
Figure 7.5-14 ³¹ P{ ¹ H} NMR spectrum of 2-trans (in H ₂ O, 298 K) after irradiation (Hg light source, 320 – 500 nm, 21 h), under argon	61
Figure 7.6-1 Stacked ¹ H NMR spectra of 1 (in H ₂ O, 298 K) immediately after irradiation (top, green) and same sample after two more days in the dark (bottom, red)	62
Figure 7.6-2 Superimposed ³¹ P{ ¹ H} NMR spectra of 1 (in H ₂ O, 298 K) immediately after irradiation (green) and same sample after two more days in the dark (red)	63
Figure 7.6-3 ³¹ P{ ¹ H} NMR spectrum of 1 (in 52 mM KOH aq., 298 K, Ag ₂ O synthesis route) immediately after irradiation (top) and the same sample after twelve more days in the dark (bottom)	64
Figure 7.7-1 ¹ H NMR spectrum of raw product (in D ₂ O, 298 K) after reaction of 2-trans with N ₂ O for 20h in presence of 83 equivalents of H ₂ O	65

Figure 7.7-2 $^{31}\text{P}\{\text{H}\}$ NMR spectrum of raw product (in D_2O , 298 K) after reaction of 2-trans with N_2O for 20h in presence of 83 equivalents of H_2O	66
Figure 8.1-1 IR Spectrum (ATR) of complex 1 along with theoretical spectrum for $[\text{A}]\text{S}_0$	67
Figure 8.2-1 EPR spectrum of green raw product obtained via reaction of 2-trans with N_2O	68
Figure 8.3-1 Time-resolved UV/Vis spectra recorded during irradiation of complex 1 in H_2O	69
Figure 8.3-2 Hyperspectral images showing time-dependent UV/Vis data and MCR results	70
Figure 8.3-3 Pure component spectra and concentration-time profile obtained using MCR	71
Figure 8.3-4 Fitting of kinetic model to MCR concentration-time profile	72
Figure 9.2-1 Decay associated spectra (magic angle polarization) and predicted DAS for [B-Trans]T_0	74
Figure 9.2-2 Decay associated spectra (magic angle polarization) and predicted DAS for $[\text{A}]\text{T}_0$	74
Figure 9.2-3 Decay associated spectra (magic angle polarization) and predicted DAS for [B]T_0	75
Figure 10.3-1 Photochemical kinetic model used to describe the two-photon water splitting reaction	77
Figure 10.5-1 Photochemical kinetic model for bimolecular reaction pathway	79
Figure 10.5-2 Photochemical kinetic model for bimolecular pathway with two-photon generation of intermediate	80
Figure 10.5-3 Photochemical kinetic model for bimolecular pathway with two-photon generation of short-lived intermediate	81
Figure 10.5-4 Photochemical kinetic model for bimolecular pathway with two-photon generation of stable intermediate	82
Figure 10.5-5 Photochemical kinetic model for three-photon pathway with one stable intermediate	83
Figure 10.5-6 Photochemical kinetic model for three-photon pathway with one stable intermediate, optimized using Differential Evolution	84
Figure 10.5-7 Photochemical kinetic model for three-photon pathway with two transient intermediates	85
Figure 10.5-8 Photochemical kinetic model for three-photon pathway with two transient intermediates, fitted to experimental data	86
Figure 11.2-1 UV-Vis spectra computed for $[\text{A}]\text{S}_0$ and $[\text{B}]\text{T}_0$ along with isomers/monomers	91
Figure 11.2-2 Transition 1 (405 nm, $f = 0.033$) for $[\text{A}]\text{S}_0$, particle (top) and hole (bottom), isovalue = 0.02	92
Figure 11.2-3 Transition 2 (391 nm, $f = 0.0141$) for $[\text{A}]\text{S}_0$, particle (top) and hole (bottom), isovalue = 0.02	93
Figure 11.2-4 Transition 3 (383 nm, $f = 0.014$) for $[\text{A}]\text{S}_0$, particle (top) and hole (bottom), isovalue = 0.02	94
Figure 11.2-5 Transition 4 (371 nm, $f = 0.0065$) for $[\text{A}]\text{S}_0$, particle (top) and hole (bottom), isovalue = 0.02	95
Figure 11.2-6 Transition 5 (353 nm, $f = 0.0596$) for $[\text{A}]\text{S}_0$, particle (top) and hole (bottom), isovalue = 0.02	96
Figure 11.2-7 Transition 6 (352 nm, $f = 0.0287$) for $[\text{A}]\text{S}_0$, particle (top) and hole (bottom), isovalue = 0.02	97
Figure 11.2-8 Transition 2 (933 nm, $f = 0.0029$) for $[\text{B}]\text{T}_0$, particle (top) and hole (bottom), isovalue = 0.1	98
Figure 11.2-9 Transition 8 (539 nm, $f = 0.0066$) for $[\text{B}]\text{T}_0$, particle (top) and hole (bottom), isovalue = 0.1	99
Figure 11.2-10 Transition 2 (804 nm, $f = 0.0004$) for $[\text{B-Mono}]\text{D}_0$ (Me model), hole (left) and particle (right), isovalue = 0.1	100
Figure 11.2-11 Transition 4 (495 nm, $f = 0.0027$) for $[\text{B-Mono}]\text{D}_0$ (Me model), hole (left) and particle (right), isovalue = 0.1	100
Figure 11.2-12 Spin density (isovalue = 0.004) for $[\text{B}]\text{T}_0$	101
Figure 11.2-13 Spin density (isovalue = 0.004) for $[\text{C}]\text{T}_0$	102
Figure 11.2-14 Spin density (isovalue = 0.004) for $[\text{D}]\text{T}_0$ [$\text{F}]\text{S}_0$ (Dimer Model)	103
Figure 11.2-15 Energy profile for relaxed PES Scan-[DE] T_0 (gas phase and SMD energies)	104
Figure 11.2-16 Energy profiles for relaxed PES scans of O-O bond formation	105
Figure 11.2-17 Comparison of computed UV-Vis spectrum for [F-Trans-Up]S_0 and experimental spectrum for 2-trans reported by Milstein and co-workers	107
Figure 11.3-1 CASSCF energy profile including PCM solvation	109
Figure 11.3-2 Active space orbitals of $[\text{B-Mono}]\text{D}_0$ used for CASSCF(13,11) calculations (isovalue = 0.05)	111
Figure 11.3-3 Singly occupied MO (left, isovalue = 0.05) and spin density (right, isovalue = 0.006) for $[\text{B-Mono}]\text{D}_0$	112
Figure 11.3-4 Unrelaxed transition difference density for $[\text{B-Mono}]\text{D}_0 \rightarrow [\text{B-Mono}]\text{D}_2$	112
Figure 11.3-5 Difference orbitals for [BC] D_2/D_1 MECI with largest population changes (isovalue = 0.05)	113
Figure 11.3-6 Difference orbitals for [BC] D_1/D_0 MECI with largest population changes (isovalue = 0.05)	113
Figure 11.3-7 Singly occupied MO (left, isovalue = 0.05) and spin density (right, isovalue = 0.006) for $[\text{C-Mono}]\text{D}_0$	114
Figure 11.4-1 Dual irradiation data and predicted behavior of $[\text{A}]\text{S}_0$ (scaled)	115
Figure 11.4-2 Dual irradiation data and predicted behavior of $[\text{A}]\text{T}_0$ (scaled)	116
Figure 11.4-3 Dual irradiation data and predicted behavior of $[\text{B-Mono}]\text{D}_0$ (scaled)	117
Figure 11.4-4 Dual irradiation data and predicted behavior of $[\text{B-Mono-Trans}]\text{D}_0$ (A, scaled) and $[\text{B-Mono-Trans-Up}]\text{D}_0$ (B, scaled)	117
Figure 11.5-1 STH efficiency heat map for two-photon water splitting	121
Figure 11.5-2 Solar AM 1.5 G spectrum with highlighted wavelength ranges for optimal T-1-1-2 water splitting	125
Figure 11.6-1 $[\text{A}]\text{S}_0$ Structure and Coordinates	126

Figure 11.6-2 [A-RR]S ₀ Structure and Coordinates	127
Figure 11.6-3 [A-RS-1]S ₀ Structure and Coordinates	128
Figure 11.6-4 [A-RS-2]S ₀ Structure and Coordinates	129
Figure 11.6-5 [A]T ₀ Structure and Coordinates	130
Figure 11.6-6 [A-Mono]S ₀ Structure and Coordinates	131
Figure 11.6-7 [B]T ₀ Structure and Coordinates	132
Figure 11.6-8 [B-Mono]D ₀ (Me Model) Structure and Coordinates	133
Figure 11.6-9 [B-Mono]D ₀ Structure and Coordinates	134
Figure 11.6-10 [B-Mono-Up]D ₀ Structure and Coordinates	135
Figure 11.6-11 [B-Trans]T ₀ Structure and Coordinates	136
Figure 11.6-12 [B-Mono-Trans]D ₀ Structure and Coordinates	137
Figure 11.6-13 [B-Mono-Trans-Up]D ₀ Structure and Coordinates	138
Figure 11.6-14 [B-Alt]T ₀ Structure and Coordinates	139
Figure 11.6-15 [BC] D ₁ /D ₀ MECI Structure and Coordinates	140
Figure 11.6-16 [BC] D ₂ /D ₁ MECI Structure and Coordinates	141
Figure 11.6-17 [C]T ₀ Structure and Coordinates	142
Figure 11.6-18 [C-Mono]D ₀ Structure and Coordinates	143
Figure 11.6-19 [C-Mono]D ₀ (Me Model) Structure and Coordinates	144
Figure 11.6-20 TS-[CD]T ₀ Structure and Coordinates	145
Figure 11.6-21 [D]T ₀ [F]S ₀ (Dimer Model) Structure and Coordinates	146
Figure 11.6-22 [D]T ₀ Structure and Coordinates	147
Figure 11.6-23 Scan-[DE]T ₀ Geometry 5 Structure and Coordinates	148
Figure 11.6-24 [E]S ₀ Structure and Coordinates	149
Figure 11.6-25 ³ O ₂ Coordinates	149
Figure 11.6-26 [F]S ₀ Structure and Coordinates	150
Figure 11.6-27 [F-Up]S ₀	151
Figure 11.6-28 [F-Trans]S ₀ Structure and Coordinates	152
Figure 11.6-29 [F-Trans-Up]S ₀ Structure and Coordinates	153
Figure 11.6-30 [F-Cis]S ₀ Structure and Coordinates	154
Figure 11.6-31 [F-Cis-Up]S ₀	155
Figure 11.6-32 [Oxo Dimer]S ₀ Structure and Coordinates	156

1.2 Table of Tables

Table 4.1-1 Optimized parameters for kinetic model	16
Table 4.2-1 Overall quantum yield (320 – 500 nm) calculated based on intensity experiments	20
Table 4.2-2 H/D kinetic isotope effect and temperature dependence of O ₂ formation	21
Table 4.4-1 Comparison of 2-cis and O ₂ initial rates of formation	25
Table 10.3-1 Optimized parameters for photochemical kinetic model ^[a]	77
Table 10.4-1 Comparison of experimental and predicted reaction probabilities	78
Table 10.5-1 Optimized parameters for bimolecular reaction pathway	79
Table 10.5-2 Optimized parameters for bimolecular two-photon reaction pathway	80
Table 10.5-3 Plotting parameters for bimolecular two-photon pathway with short-lived intermediate	81
Table 10.5-4 Optimized parameters for bimolecular two-photon pathway with stable intermediate	82
Table 10.5-5 Optimized parameters for three-photon pathway (with one stable intermediate)	83
Table 10.5-6 Optimized parameters for three-photon pathway (with one stable intermediate), optimized using differential evolution	84
Table 10.5-7 Plotting parameters for three-photon pathway (with two transient intermediates)	85
Table 10.5-8 Optimized parameters for three-photon model (with two transient intermediates)	86
Table 11.2-1 Relative energies of [A]S ₀ and [A-Mono]S ₀	89
Table 11.2-2 Relative energies of [A] isomers	89
Table 11.2-3 Relative energies of [B]T ₀ isomers	89
Table 11.2-4 Relative energies of [B-Mono]D ₀ isomers	90
Table 11.2-5 Relative energy of [B-Alt]T ₀	90
Table 11.2-6 Relative energy of Oxo Dimer	90
Table 11.2-7 Reaction Energy for [F]S ₀ + H ₂ O → [A-Mono]S ₀ + H ₂	90
Table 11.2-8 Relative energies and theoretical NMR data for [F]S ₀ isomers	106
Table 11.3-1 Comparison of DFT and CASSCF reaction energies for [B] → [C] and absorption wavelengths for [B-Mono]D ₀	108
Table 11.5-1 Maximum theoretical solar-to-hydrogen efficiencies for single absorber mechanisms	123
Table 11.5-2 Maximum theoretical solar-to-hydrogen efficiencies for dual absorber mechanisms	123
Table 11.5-3 Maximum theoretical solar-to-hydrogen efficiencies for triple absorber mechanisms	124

2 Methods and Materials

All experiments involving ruthenium complexes (unless stated otherwise) were carried out under argon using either standard Schlenk technique or in an argon filled glovebox (MBRAUN). Organic solvents were purified using a solvent purification system (Innovative Technology) and stored under argon. Water was purified using a Merck Milli-Q system, followed by degassing using argon sparging and storage under argon. Organic deuterated solvents were degassed using three freeze-pump-thaw cycles and stored over 3 Å molecular sieves. D₂O was distilled under argon.

Carbonylchlorohydridotris(triphenylphosphine)ruthenium(II) ((PPh₃)₃RuCl(CO)H) was purchased from Strem Chemicals, 2-((Di-tert-butylphosphinomethyl)-6-diethylaminomethyl)pyridine (in the following abbreviated as PNN) was purchased from Sigma Aldrich. Potassium *tert*-butoxide was purchased from TCI, nitrous oxide was purchased from Linde and all other chemicals were purchased from Sigma Aldrich. Chemicals were used as received.

(PNN)RuCl(CO)H was prepared as previously described.¹

Nuclear magnetic resonance (NMR) spectra were recorded on a Bruker AV-300 (300 MHz), AV-400 (400 MHz) or f300 (300 MHz) spectrometer and analyzed using MestreNova. ¹H and ¹³C chemical shifts are reported relative to the respective solvent peak as parts per million. ³¹P chemical shifts are reported relative to 0.3M H₃PO₄ in D₂O (set to δ (³¹P) = -0.425 ppm) as parts per million. ³¹P NMR spectra were recorded as quantitative spectra typically containing the H₃PO₄ standard in a flame sealed capillary. Integrals are reported relative to the H₃PO₄ standard (e.g. allowing for comparable integrals before and after irradiation). Multiplicities are indicated using the following abbreviations: s (singlet), d (doublet), t (triplet), q (quartet), m (multiplet), b (broad).

Infrared spectroscopy was performed using a Bruker-ALPHA FT-IR spectrometer in attenuated total reflectance measurement mode. The following abbreviations are used: br (broad), s (singlet), vs (very strong singlet), m (multiplet).

Electron paramagnetic resonance (EPR) spectroscopy was performed using a X-band Bruker EMX CW-micro EPR spectrometer equipped with an ER4119HS high-sensitivity resonator using a microwave power of ca. 6.9 mW, modulation frequency of 100 kHz and modulation amplitude up to 5 G.

UV/Vis spectroscopy was performed using an Analytik Jena SPECORD S 600 diode array UV/Vis spectrometer (1 cm quartz cuvette, 40 ms integration time, 100 accumulations, pure water used as reference). Fluorescence spectroscopy was performed using a Cary Eclipse fluorescence spectrometer (Agilent), with 20 nm slit widths for excitation and emission (excitation wavelength: 370 nm).

Elemental analysis was performed using a Leco TruSpec Micro CHNS analyzer.

Oxygen measurements were performed using a FireStingO2 optical oxygen meter (PyroScience GmbH) along with trace range robust probes (PyroScience GmbH, for liquid phase measurements) or trace range oxygen sensor spots (PyroScience GmbH, for gas phase measurements). Temperature compensation was done using a Pt100 temperature sensor (Therma Thermofühler GmbH).

Irradiation was performed using two different light sources:

(a) A Lumatec SUPERLITE S 04 with a liquid light guide (Lumatec, light guide diameter: 1 cm). This is a mercury vapor light source with an integrated filter wheel to select different wavelength regions (for the spectral power distribution of the selected filter configurations, see Figure 6.1-1). This light source is referred to as the “Hg light source” in the following.

(b) A 250 W quartz tungsten halogen (abbreviated as QTH) Research Light Source with a F/1, 1.5 inch, two element, plano convex condenser (Newport). The light source was equipped with a 6 cm quartz distilled water filter (Quantum Design), which filters out all wavelengths below 280 nm and above 1000 nm, and a manual light source shutter (Newport). Furthermore, the light source was combined with different colored class alternative longpass filters (Newport) to further control the irradiation wavelengths. This light source is referred to as the “QTH light source” in the following.

3 Synthesis Procedures and Characterization

3.1 Synthesis of Complex 1

3.1.1 Synthesis using N₂O

Complex **1** was synthesized following a modified version of the previously reported procedure.²

(PNN)RuCl(CO)H (302.5 mg, 0.62 mmol) and KOtBu (69.5 mg, 0.62 mmol) were placed in a Schlenk flask, followed by addition of 30 ml Et₂O, yielding a dark red suspension. The suspension was stirred at room temperature for one hour, yielding a dark red solution with a small amount of solid (KCl). The solution was filtered into a separate Schlenk flask to remove the formed KCl and then the solvent was removed under vacuum, yielding a black-red solid of (PNN*)Ru(CO)H (PNN* indicates dearomatization of the PNN ligand). (PNN*)Ru(CO)H was directly used for the next reaction step without further purification and assuming quantitative conversion.

To the Schlenk flask containing (PNN*)Ru(CO)H, 16 ml THF were added, yielding a dark red solution (see Figure 3.1-1). To this solution, 9 equivalents of H₂O (100 µl, 5.6 mmol) were added, resulting in an immediate color change from dark red to dark yellow/orange (see Figure 3.1-1) due to formation of complex **2-trans**. It is important at this stage to add no more than 9 equivalents of H₂O, as the presence of more water leads to a different reaction product (see Figure 7.7-1) when **2-trans** is exposed to N₂O.

The THF solution of **2-trans** containing 9 equivalents of H₂O was transferred to a separate reaction assembly (see Figure 3.1-2), where it was sparged with N₂O for 10 – 20 min. Afterwards, the Schlenk flask containing the solution of **2-trans** was closed under a N₂O atmosphere and was stirred at room temperature in the dark for 22 h. After the reaction time, a dark green solution was formed (see Figure 3.1-1). If more than 9 equivalents of water were present in the reaction solution, a dark red solution was formed instead, containing the different reaction product shown in Figure 7.7-1.

The dark green solution was concentrated in volume by roughly half, followed by addition of 100 ml Et₂O, leading to precipitation of a solid. The solid was filtered off, washed three times with 1 ml Et₂O each and dried under vacuum, yielding **1** as a yellow solid (70 mg, 23% yield with respect to (PNN)Ru(CO)ClH, see Figure 3.1-3). The final product typically contains up to 3% of unreacted **2-trans**, which could not be removed. Unfortunately, repeated attempts to crystallize **1** were unsuccessful.

We would like to note at this point that complex **1** is in fact a yellow solid, yielding a yellow solution in H₂O (see Figure 3.1-3), and not a green solid yielding a green aqueous solution as described before.² The green color of the solution after reaction with N₂O can be attributed to Ru(III) species, which are formed as side products during the reaction (see Figure 8.2-1 for an EPR spectrum of the green raw product after reaction with N₂O). Complex **1**, however is an EPR inactive Ru(II) species. The green color of the final product, which was previously described, might therefore be attributed to some residual Ru(III) species. These residual Ru(III) species might also explain the additional absorption features in the originally reported UV/Vis spectrum² compared to our UV/Vis spectrum. Furthermore, we found that in chlorinated solvents (such as dichloromethane, DCM), **1** can be converted to chloride complexes (possibly due to reaction with trace amounts of HCl present in the solvent). We therefore avoided the use of chlorinated solvents with **1**.

Spectroscopic data for **1**:

¹H NMR (400 MHz, H₂O, r.t.) δ 7.37 (t, J = 7.9 Hz, 1H, py-H⁴), 7.10 (d, J = 7.9 Hz, 1H, py-H³), 7.00 (d, J = 7.8 Hz, 1H, py-H⁵), 3.87 (dd, J = 15.3, 3.2 Hz, 1H, py-NCH₂), 3.75 (d, J = 15.2 Hz, 1H, py-NCH₂), 3.48 (dd, J = 17.5, 10.9 Hz, 1H, py-PCH₂), 3.04 (dd, J = 17.4, 7.4 Hz, 1H, py-PCH₂), 2.79 (dq, J = 13.9, 6.9 Hz, 1H, CH₂CH₃), 2.50 (dq, J = 14.4, 7.2 Hz, 1H, CH₂CH₃), 2.45 – 2.29 (m, 2H,

CH_2CH_3), 1.02 (d, $J = 14.5$ Hz, 9H, $P(C(CH_3)_3)_2$), 0.76 (t, $J = 7.0$ Hz, 3H, CH_2CH_3), 0.71 (t, $J = 7.1$ Hz, 3H, CH_2CH_3), 0.68 (d, $J = 13.0$ Hz, 9H, $P(C(CH_3)_3)_2$) ppm. (see Figure 7.1-1)

1H NMR data is provided in H_2O since it avoids disappearance of methylene protons (which occurs for D_2O). In the 1H NMR spectrum of **1** in $DMSO-d_6$, a broadened singlet can be observed at $\delta(^1H) = 4.22$ ppm, integrating to 2H (see Figure 7.1-3). This signal might be attributed to the two hydroxo protons,³ being shifted significantly downfield compared to the previously described value of $\delta(^1H) = -7.4$ ppm due to interaction with $DMSO-d_6$.

^{13}C NMR (101 MHz, $DMSO-d_6$, r.t.) δ 207.92 (d, $J = 15.1$ Hz, CO), 164.41 (s, py-C³), 160.55 (s, py-C⁵), 138.51 (s, py-C⁴), 122.22 (d, $J = 8.1$ Hz, py-C⁶), 120.97 (s, py-C²), 62.10 (s, py-NCH₂), 51.00 (s, CH_2CH_3), 44.17 (s, CH_2CH_3), 37.78 (d, $J = 12.9$ Hz, $P(C(CH_3)_3)_2$), 37.60 (d, $J = 24.8$ Hz, py-PCH₂), 36.51 (d, $J = 15.0$ Hz, $P(C(CH_3)_3)_2$), 30.48 (d, $J = 3.6$ Hz, $P(C(CH_3)_3)_2$), 28.97 (d, $J = 2.6$ Hz, $P(C(CH_3)_3)_2$), 9.28 (s, CH_2CH_3), 8.87 (s, CH_2CH_3) ppm. (see Figure 7.1-4)

$^{31}P\{^1H\}$ NMR (162 MHz, $DMSO-d_6$, r.t.) δ 92.56 (s, P^tBu_2) ppm. (see Figure 7.1-5)

$^{31}P\{^1H\}$ NMR (162 MHz, H_2O , r.t.) δ 88.24 (s, P^tBu_2) ppm. (see Figure 7.1-2)

IR (ATR): $\tilde{\nu} = 3393$ br (OH), 2948m, 1917vs (CO), 1568s cm^{-1} . (see Figure 8.1-1)

UV/Vis (H_2O): λ_{abs} ($\epsilon / cm^{-1} M^{-1}$) = 370 (1630), 305 (3510).

Elemental analysis: anal. calc. for $C_{20}H_{37}N_2O_3PRu \cdot 3 H_2O$: C, 44.52; H, 8.03; N, 5.19. Found: C, 44.25; H, 8.078; N, 5.002.

3.1.2 Photographs Showing Synthesis and Product



Figure 3.1-1 Photographs of synthesis stages during preparation of complex 1

Left: Solution of $[\text{Ru}(\text{PNN}^*)(\text{CO})\text{H}]$ in THF (dark red solution).

Middle: Solution on the left after addition of 9 equivalents of H_2O , forming complex **2-trans** (dark yellow/orange solution).

Right: Solution in the middle after reaction with N_2O for 22h (dark green solution).

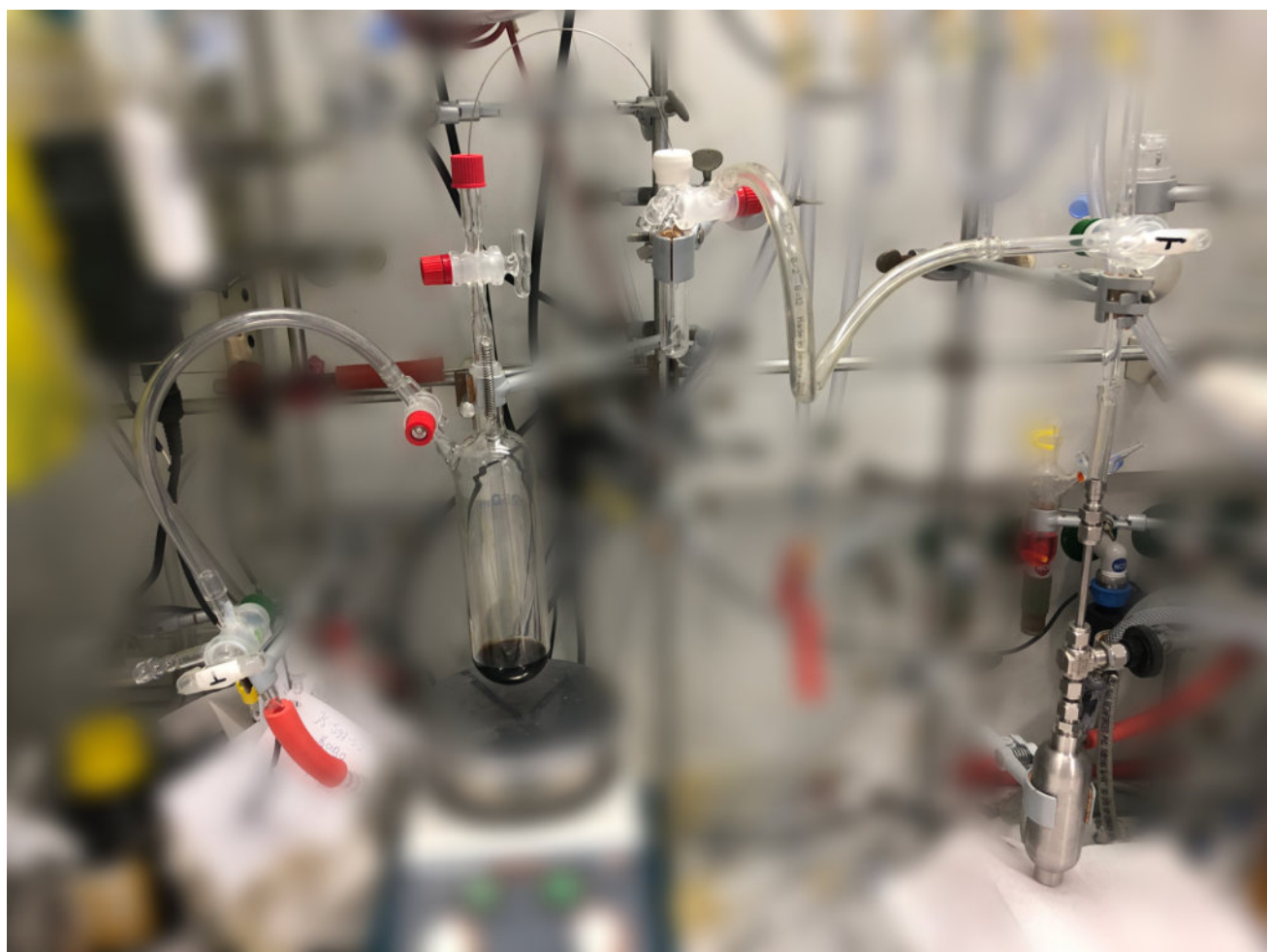


Figure 3.1-2 Reaction set-up for reaction of 2-trans with N_2O

From right to left: N_2O gas tank (right bottom) is connected to a T-piece (right), which leads to the Schlenk line (top connection) and to a Schlenk flask (top middle). This Schlenk flask is topped with a rubber septum containing a cannula (top), which leads into the main reaction flask (containing **2-trans**) through a septum (red cap) and a valve. The main reaction flask is connected to a second T-piece valve (left), which leads to the Schlenk line (bottom) and to a separate bubble counter (left). Background is blurred to highlight the reaction assembly.



Figure 3.1-3 Complex 1 as a solid (left) and in aqueous solution (right)

3.1.3 Synthesis using Ag_2O

(PNN)RuCl₂(CO) (66 mg, 0.126 mmol, mixture of cis and trans isomers) and Ag₂O (179 mg, 0.772 mmol) were placed in a Schlenk flask along with 4.5 ml of acetone and 0.6 ml of H₂O, yielding a dark yellow suspension. The suspension was stirred for 2 h in the dark, after which it was filtered into a separate Schlenk flask, yielding a dark yellow solution. Subsequently, all volatiles were removed under vacuum and the dark yellow residue was redissolved in 2.1 ml THF, yielding a dark yellow solution with some insoluble material. The insoluble materials were removed via filtration, and 18 ml Et₂O were added to the dark yellow THF solution to precipitate the product. The solid was filtered off, washed three times with 1 ml Et₂O each and dried under vacuum, yielding a yellow solid.

While this synthesis procedure does yield complex **1** (see Figure 7.1-6 and Figure 7.1-7 for NMR spectra of the product), the obtained product is less pure than the one obtained via the N₂O synthesis route. The main impurity can be observed at $\delta(^3\text{P}) = 55.12$ ppm, which might be attributed to an alkyl phosphinic acid resulting from ligand oxidation by Ag₂O. Due to the less pure nature of the product, the N₂O synthesis route was the preferred one. However, further improvements to this silver based synthesis route might offer a more simple and general access to ruthenium dihydroxo complexes.

3.1.4 Synthesis via Reflux of **2-trans**

This is a modified version of the previously described procedure for the synthesis of **1** via reflux of **2-trans**.²

(PNN*)Ru(CO)H was synthesized as described in 3.1.1, using 53 mg (0.109 mmol) of (PNN)RuCl(CO)H. To the Schlenk flask containing solid (PNN*)Ru(CO)H, 2.5 ml of H₂O were added, yielding a clear, light yellow solution of **2-trans**.

The solution was then refluxed for three days, during which time the color of the solution changed to dark red/orange and a small amount of black, insoluble material formed.

At the end of the reaction time, the solution was cooled to room temperature and analyzed using NMR spectroscopy (see Figure 7.1-8 and Figure 7.1-9), showing formation of **1** along with unreacted **2-trans** and other, unidentified reaction products. The obtained product was not isolated.

3.2 Synthesis of Complex **2-trans**

3.2.1 Synthesis in H₂O

Complex **2-trans** was synthesized in H₂O as described in 3.1.4, yielding a clear, light yellow solution. The obtained product was analyzed using NMR spectroscopy (see Figure 7.2-1 and Figure 7.2-2) and was not isolated. Obtained NMR data was consistent with the previously described.²

3.2.2 Crystallization of **2-trans**

(PNN*)Ru(CO)H (31 mg, 0.069 mmol, synthesized as described in 3.1.1) was dissolved in 1.1 ml toluene, yielding a dark red solution. To this solution, 9 equivalents of H₂O (11 µl, 0.61 mmol) were added, leading to a rapid color change to form a clear orange solution with a small aqueous phase at the bottom. The organic phase was transferred to a separate Schlenk flask and stored at -32 °C overnight, yielding colorless/light yellow crystals. In an ice bath, the liquid phase was removed using a syringe and the crystals were washed twice with 0.4 ml ice-cold heptane.

The thus obtained crystals were used in both the N₂O and reflux synthesis route for complex **1**, yielding the same results as in situ prepared **2-trans** (as described above).

When the aqueous phase of this synthesis (still containing some of the toluene phase as well) was stored at room temperature for one day, colorless, plate-shaped crystals of **2-trans** suitable for X-ray crystallography were formed.

3.3 Synthesis of (p-cymene)RuCl₂(CO)

(p-cymene)RuCl₂(CO) was prepared using a previously described procedure.⁴

In a 50 ml Schlenk flask (internal volume ca. 65 ml), a orange/red solution of [(p-cymene)RuCl₂]₂ (200 mg, 0.33 mmol) in 4 ml DCM was placed under vacuum using freeze-pump-thaw and warmed back to room temperature. Subsequently, 16 ml of CO gas (ca. 0.66 mmol, 2 equivalents) were injected into the Schlenk flask through a septum using a gas-tight syringe. The solution was then stirred at room temperature for 45 min, during which the color changed to deep red. Subsequently, the solvent was removed, yielding a salmon pink solid (187 mg, 85% yield). Characterization by NMR spectroscopy (see Figure 7.3-1) was consistent with the previously reported data.⁴

3.4 Synthesis of (PNN)RuCl₂(CO)

(p-cymene)RuCl₂(CO) (375 mg, 1.12 mmol) was suspended in THF (10 ml) and a solution of PNN (376 mg, 1.17 mmol in 15 ml THF) was added, yielding a red suspension. It was then refluxed for 15 h, yielding an orange solution with a yellow solid. The reaction solution was cooled to room temperature and stored at -32 °C overnight, leading to precipitation of more yellow solid. After warming back to room temperature, the volume of the reaction solution was reduced by ca. 70% under vacuum, followed by addition of 80 ml of heptane. The solid was filtered off from the yellow suspension and washed three times with 4 ml of heptane, followed by drying under vacuum. This yielded a yellow solid (457 mg, 78% yield with respect to (p-cymene)RuCl₂(CO)). Characterization by NMR spectroscopy showed the presence of a mixture of the cis and trans isomers (see Figure 7.4-1 and Figure 7.4-2, ca. 3% of impurity are visible at $\delta(^{31}P) = 74.57$ ppm) and the obtained data was consistent with the previously reported.⁵

4 Procedures for Irradiation and Subsequent Data Analysis

4.1 NMR Scale Irradiation

4.1.1 Irradiation Procedure

550 μl of a 0.01M solution of **1** (prepared via the N_2O synthesis route) in H_2O was placed inside a J. Young NMR tube along with a flame sealed capillary containing a 0.3M H_3PO_4 solution in D_2O . ^1H and quantitative $^{31}\text{P}\{^1\text{H}\}$ NMR spectra were then recorded before irradiation. Subsequently, the NMR tube was irradiated with either the QTH or Hg light source (or both) while being cooled with a 20 W fan (for the irradiation set-up see Figure 4.5-1).

For the concentration-time profile experiments, only the QTH light source was used for irradiation, being equipped with the distilled water filter. The total irradiation time was 46.5 h. For dual irradiation experiments, either or both light sources were used, the Hg light source being filtered to 320 – 400 nm (see Figure 6.1-1, fixed intensity setting) and the QTH light source being equipped with a > 495 nm longpass filter in addition to the distilled water filter. For each dual irradiation experiment, the irradiation time was 17 h. In all cases care was taken not to alter the positioning of either the NMR tube or light sources between experiments, so as not to change the photon flux received by the NMR tube. QTH and Hg light sources were arranged at a 90° angle.

After irradiation with the QTH light source (no longpass filter) or Hg light source, the color of the solution changed to yellow/orange. In case of irradiation with the QTH light source equipped with a > 495 nm longpass filter, no color change occurred. Immediately after irradiation, ^1H and quantitative $^{31}\text{P}\{^1\text{H}\}$ NMR spectra were recorded.

Irradiation experiments could also be performed in the same way using complex **1** prepared via the Ag_2O synthesis route. In this case, however, **1** had to be dissolved in a 52 mM aqueous KOH solution instead of pure H_2O . This was likely necessary to compensate for the weakly acidic nature of **1** obtained via the Ag_2O route (likely due to the phosphinic acid impurity). When irradiation of **1** (Ag_2O route) was performed in 52 mM KOH aq., the results were effectively identical to those obtained using the above-described procedure. For simplicity, however, all reported experiments (except noted otherwise) were performed using **1** obtained via the N_2O synthesis route in pure H_2O .

4.1.2 Interpretation of NMR Results

Irradiation with either the QTH light source (no longpass filter) or Hg light source resulted in the same qualitative changes as observed by NMR spectroscopy. Figure 7.5-1 and Figure 7.5-2 show representative examples of ^1H and $^{31}\text{P}\{^1\text{H}\}$ spectra recorded after irradiation, respectively. In the ^1H spectrum, appearance of a new hydride signal at $\delta(^1\text{H}) = -5.24$ ppm can be observed. In the $^{31}\text{P}\{^1\text{H}\}$ spectrum, the major changes are a significant reduction in signal intensity for $\delta(^{31}\text{P}) = 88.22$ ppm (complex **1**), and the appearance of two new signals at $\delta(^{31}\text{P}) = 104.36$ ppm and $\delta(^{31}\text{P}) = 95.12$ ppm (along with some smaller signals).

Through ^1H - ^{31}P HMBC (see Figure 7.5-3) it could be established that the hydride at $\delta(^1\text{H}) = -5.24$ ppm and the $\delta(^{31}\text{P}) = 104.36$ ppm signal are coupled, showing that this is a species distinct from **2-trans** ($\delta(^1\text{H}) = -18.9$ ppm, $\delta(^{31}\text{P}) = 104.2$ ppm, see Figure 7.5-3). However, it can be observed that in the dark (over the course of hours and days), the $\delta(^{31}\text{P}) = 104.36$ ppm species converts to **2-trans** (see Figure 7.6-1 and Figure 7.6-2). Furthermore, when **2-trans** is irradiated (Hg light source, 320 – 500 nm) in the presence of O_2 , it converts to the $\delta(^{31}\text{P}) = 104.36$ ppm species (see Figure 7.5-5 and Figure 7.5-6). The interconversion of these two species indicates that they are isomers. When comparing their NMR characteristics, the biggest difference is the significantly downfield shifted hydride signal at $\delta(^1\text{H}) = -5.24$ ppm for the $\delta(^{31}\text{P}) = 104.36$ ppm species. Such a chemical shift is consistent with the hydride being trans to a CO ligand.^{6,7} This is corroborated by DFT calculations for different isomers of **2**, which predict a change of ca. 10 ppm for the hydride signal when the hydride ligand is trans to the CO ligand (see Table 11.2-8), as compared to being trans to

the OH ligand (as is the case for **2-trans**). Furthermore, DFT calculations predict **2-cis** (where the hydride ligand is trans to CO and the OH ligand is in the equatorial position) to be less stable than **2-trans** by more than 40 kJ/mol. This difference in stability would explain the spontaneous conversion of the $\delta(^{31}\text{P}) = 104.36$ ppm species to **2-trans**. Based on the characteristic hydride shift and these DFT results, we therefore assign the $\delta(^{31}\text{P}) = 104.36$ ppm species to **2-cis**.

In the absence of O₂, **2-trans** was found to only react slowly under irradiation, with ca. 10% conversion after 21 h of irradiation. It appears to decompose to unidentified products at $\delta(^{31}\text{P}) = 86$ ppm and $\delta(^{31}\text{P}) = 92$ ppm (see Figure 7.5-14)

The second major product of irradiation can be observed at $\delta(^{31}\text{P}) = 95.12$ ppm. For this species, the phosphorous signal couples to two different tert-butyl groups (see ¹H-³¹P HMBC of aliphatic region in Figure 7.5-4). This indicates that, just like complex **1**, this complex has no symmetry, resulting in two chemically distinct tert-butyl groups. This observation rules out that this species is the trans isomer of **1**. In the dark, the species slowly converts back to **1** (see Figure 7.6-3, in this case the experiment was performed using **1** prepared via the Ag₂O route in 52 mM KOH aq., but the same is observed using the standard reaction conditions). We tentatively assign this species to **Oxo Dimer**, an oxo-bridged dimer formed via formal dehydration of **1** (see Figure 11.6-32 for the computed structure). DFT calculations predict **Oxo Dimer** to be slightly less stable than **1**, explaining why slow hydrolysis back to **1** might occur in the dark. Furthermore, a reasonable pathway for photochemical **Oxo Dimer** formation can proposed based on Ru-O bond formation in intermediate [B-Trans]T₀ (see 9.2).

Due to these isomerization reactions, NMR spectra for quantitative analysis were recorded immediately after irradiation.

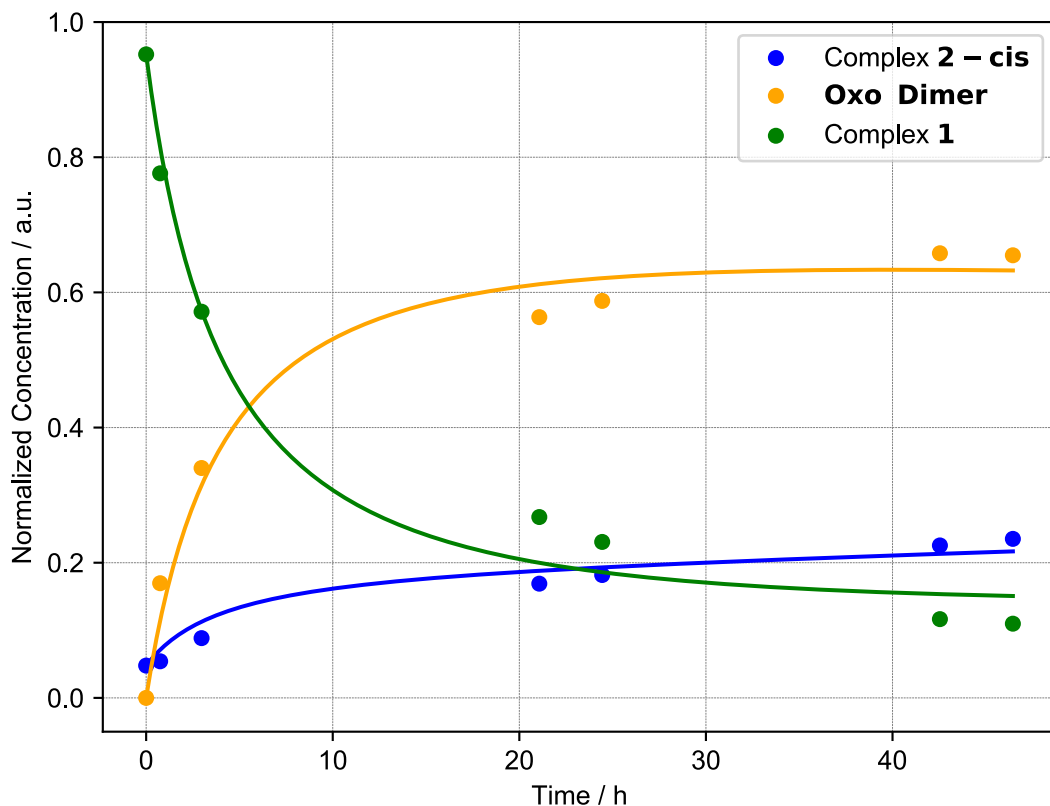
4.1.3 Data Analysis for Concentration-Time Profile

For the concentration-time profile, quantitative ³¹P{¹H} NMR spectra were recorded before (t = 0 h) and after 0.75, 2.97, 21.07, 24.44, 42.54 and 46.45 h of irradiation (irradiation of the sample was stopped after the indicated time, NMR spectra were recorded and irradiation was then resumed). For each time point, the relative concentrations of **1**, **2-cis** and **Oxo Dimer** were determined via integration of the corresponding ³¹P{¹H} NMR signals. For t = 0 h, a small amount of **2-trans** could be observed, which was treated as **2-cis** in the following (since **2-trans** can photochemically convert to **2-cis**, see above). Therefore, the amount of **2-cis** at t = 0 h is not equal to zero. For all subsequent time points, no **2-trans** was observed.

For data analysis, the concentrations of **1**, **2-cis** and **Oxo Dimer** were normalized, so that for each time point the sum of the concentrations for these three compounds would be equal to one. This normalization ignores the formation of other products. However, since the amount of side products observable by ³¹P{¹H} spectroscopy amounts to only around 7% after 46.45 h of irradiation this was deemed acceptable.

The resulting, normalized concentrations of **1**, **2-cis** and **Oxo Dimer** are shown in Figure 4.1-1 as dots. These datapoints were then fitted with a kinetic model based on the reaction network shown in Table 4.1-1, with k_1 , k_2 and k_3 being the optimization parameters. Fitting was performed via the following steps:

1. Converting the reaction network to the corresponding rate laws describing the time-dependent concentration changes of **1**, **2-cis** and **Oxo Dimer**;
2. At each optimization step, numerically solving the resulting system of differential equations with an updated guess for k_1 , k_2 and k_3 (generated using the L-BFGS-B algorithm), until convergence was reached. The optimized parameters for k_1 , k_2 and k_3 are shown in Table 4.1-1.



From the data shown in Figure 4.1-1 it can be seen that **Oxo Dimer** is not an intermediate formed en route to **2-cis**, as the rate of **2-cis** formation does not increase with increasing **Oxo Dimer** concentration.

Figure 4.1-1 Concentration-time profile for irradiation of complex 1 with QTH light source

Dots show normalized concentrations obtained via integration of NMR spectra measured after indicated irradiation times. Lines are kinetic fit obtained using the kinetic model: $\mathbf{1} + \mathbf{1} \rightleftharpoons \text{Oxo Dimer}$ (k_1), $\mathbf{1} + \mathbf{1} \rightarrow 2 \text{ 2-cis}$ (k_2), and $\text{Oxo Dimer} \rightarrow \mathbf{1} + \mathbf{1}$ (k_3).

Table 4.1-1 Optimized parameters for kinetic model

$\text{Oxo Dimer} \xrightleftharpoons[k_3]{k_1} \mathbf{1} \xrightarrow{k_2} 2 \text{ 2-cis} (+ \text{O}_2)$		
k_1 / h^{-1}	k_2 / h^{-1}	k_3 / h^{-1}
0.197	0.04	0.0076

4.1.4 Data Analysis for Dual Irradiation

For the dual irradiation data set, two irradiation experiments using only the Hg light source (320 – 400 nm), two experiments using both the Hg light source (320 – 400 nm) and the QTH light source (> 495 nm) as well as one experiment using only the QTH light source (> 495 nm) were performed.

For each experiment, quantitative $^{31}\text{P}\{^1\text{H}\}$ NMR spectra were recorded before and after irradiation. Relative concentrations of **1**, **2-trans** (before irradiation), **2-cis** (after irradiation), **Oxo Dimer** and an unidentified byproduct at $\delta(^{31}\text{P}) = \sim 97$ ppm were determined via integration. For each experiment, concentrations were normalized so that the sum of the concentrations of all components would be

the same before and after irradiation. When comparing the different experiments, the sum of all normalized concentrations differed at most 4% between them.

For each experiment, the yield of **2-cis** was determined by subtracting the normalized concentration of **2-trans** before irradiation from the normalized concentration of **2-cis** after irradiation. This was done to correct for any **2-cis** that was formed via photochemical isomerization of **2-trans**. The thus obtained corrected concentration of **2-cis** was divided by the sum of all concentrations for the experiment to give the yield of **2-cis**. Reported yields for irradiation with either the Hg light source (320 – 400 nm) or both light sources are the averages of two separate irradiation experiments.

4.2 Liquid Phase O₂ Measurement

4.2.1 Irradiation Procedure

A 5 ml Schlenk flask with a GL14-threaded neck was equipped with a 5 mm PTFE stirring bar and a trace range robust O₂ probe, positioned so that it would later be immersed in the liquid phase (see Figure 4.5-3). The O₂ probe was connected to the Schlenk flask in a gas tight manner via the GL14-threaded neck with a 3 mm BOLA laboratory screw joint.

The Schlenk flask was then connected to the Schlenk line using a T-piece adapter, with one connection to the Schlenk line, one to the Schlenk flask and one connection being closed with a septum. Subsequently, ca. 500 - 550 µl of an aqueous solution of **1** (prepared via the N₂O synthesis route, 0.01 or 0.005 M concentration, it was confirmed that both concentrations gave the same results, see 4.2.6) was transferred into the Schlenk flask. The transfer was done via cannula transfer through the septum inlet of the T-piece adapter and through the valve of the Schlenk flask, taking care not to introduce any external O₂ into the flask.

Once the transfer was complete, the Schlenk flask was closed and placed into a double-walled beaker filled with water (see Figure 4.5-2 and Figure 4.5-3), which was thermostatted to 16.5 °C (unless stated otherwise). A PT100 temperature sensor (for temperature compensation of the O₂ measurement) was placed next to the Schlenk flask into the same water bath and the whole assembly was allowed to equilibrate for 15 – 20 min while being stirred at 1400 rpm.

After equilibration, the baseline O₂ concentration was typically measured for 15 – 30 min. Afterwards the flask was irradiated for 240 – 400 s. In case of the intensity dataset, irradiation was performed using the Hg light source (320 – 500 nm) with variable intensity settings. The same light source was used to measure the kinetic isotope effect and temperature dependence of the reaction. For the dual irradiation dataset, irradiation was performed using the Hg light source (320 – 400 nm), the QTH light source (different longpass filters), or both. When both light sources were used, the shutters of both were opened simultaneously. See Figure 4.5-2 and Figure 4.5-3 for the irradiation set-ups. In all cases, care was taken not to alter the position of the light sources or the reactor between experiments, so as not to change the photon flux received by the reactor. Hg and QTH light source were arranged at a 90° angle.

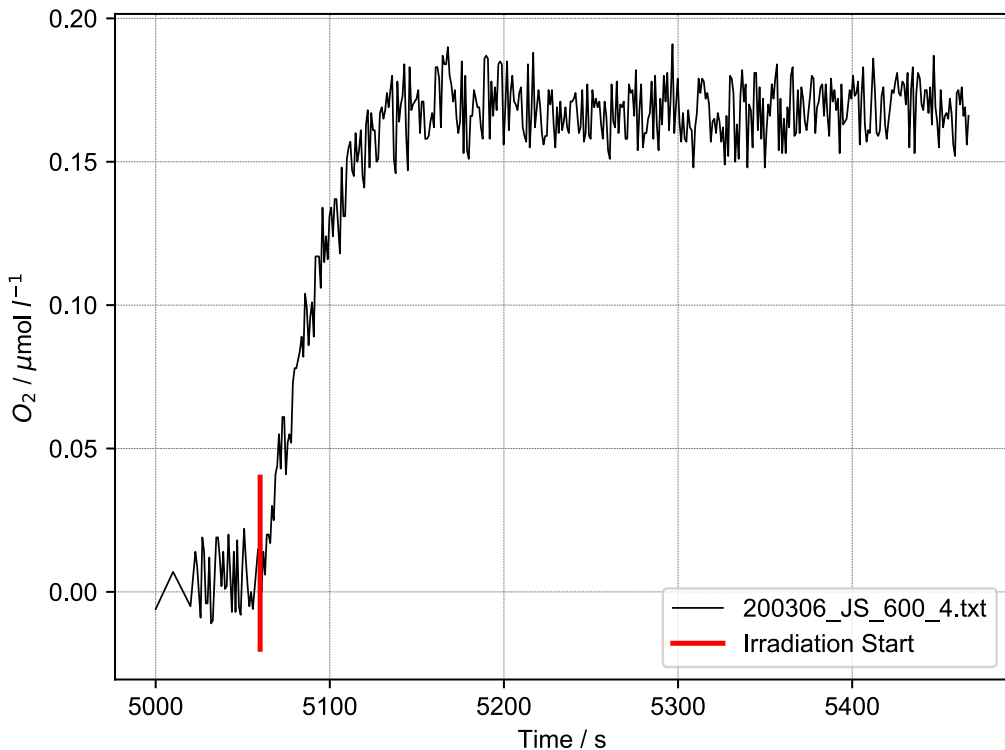


Figure 4.2-1 Exemplary liquid phase O₂ raw data (320 – 500 nm, 1 W intensity setting)

4.2.2 General Remarks on Data Analysis

For data analysis, the irradiation start point was set to $t = 0$ s. Furthermore, the baseline O₂ concentration was calculated using the average of all datapoints recorded before irradiation start and subtracted from the datapoints, so that $[O_2](t = 0\text{ s}) = 0\text{ }\mu\text{mol/l}$.

To determine reaction rates, the following rate law was used:

$$\frac{d[O_2]}{dt} = k_0 - k_1 [O_2] \quad \text{Equation (1)}$$

For this rate law, O₂ is assumed to be formed in a zero-order reaction with rate constant k_0 and to be consumed in a first-order reaction with rate constant k_1 . The assumption that O₂ is formed in a zero-order reaction stems from the fact that O₂ concentrations are only measured in the initial reaction phase, where the concentration change of 1 is negligible. The first order reaction consuming O₂ can be seen as an overall description of O₂ loss in the liquid phase due to diffusion into the gas phase and due to consumption by side reactions (see 4.3.2), both of which can be assumed to be first order in O₂ in the initial reaction phase.

When integrated, Equation (1) gives the following function:

$$[O_2](t) = [O_2]_0 e^{-k_1 t} - k_0 e^{-k_1 t} \frac{1}{k_1} + \frac{k_0}{k_1} \quad \text{Equation (2)}$$

With $[O_2]_0$ being the O₂ concentration at $t = 0$ s (which is equal to zero given our preprocessing). Equation (2) was fitted to all datapoints from $t = 0$ s until the end of irradiation, optimizing the parameters k_0 and k_1 . k_0 is not only the zero-order rate constant for O₂ formation but also the initial rate of O₂ formation (since $[O_2]_0 = 0\text{ }\mu\text{mol/l}$, unit of initial rate is $\mu\text{mol l}^{-1}\text{ s}^{-1}$). k_1 is the overall observed rate constant for the disappearance of O₂ (due to diffusion and side reactions).

To obtain k_0 with higher precision (for kinetic isotope effect, temperature dependence and dual irradiation data sets), a second analysis procedure was also used (“average k_1 procedure”): for this

procedure, Equation (2) was first fitted to the data optimizing both k_0 and k_1 . Within one group of experiments (e.g. all experiments with the same intensity and temperature), the average k_1 value was determined. Afterwards, Equation (2) was fitted to the data of each experiment in the group again, this time fixing k_1 to be the group's average value. Therefore, only k_0 has to be optimized and it is obtained with higher precision.

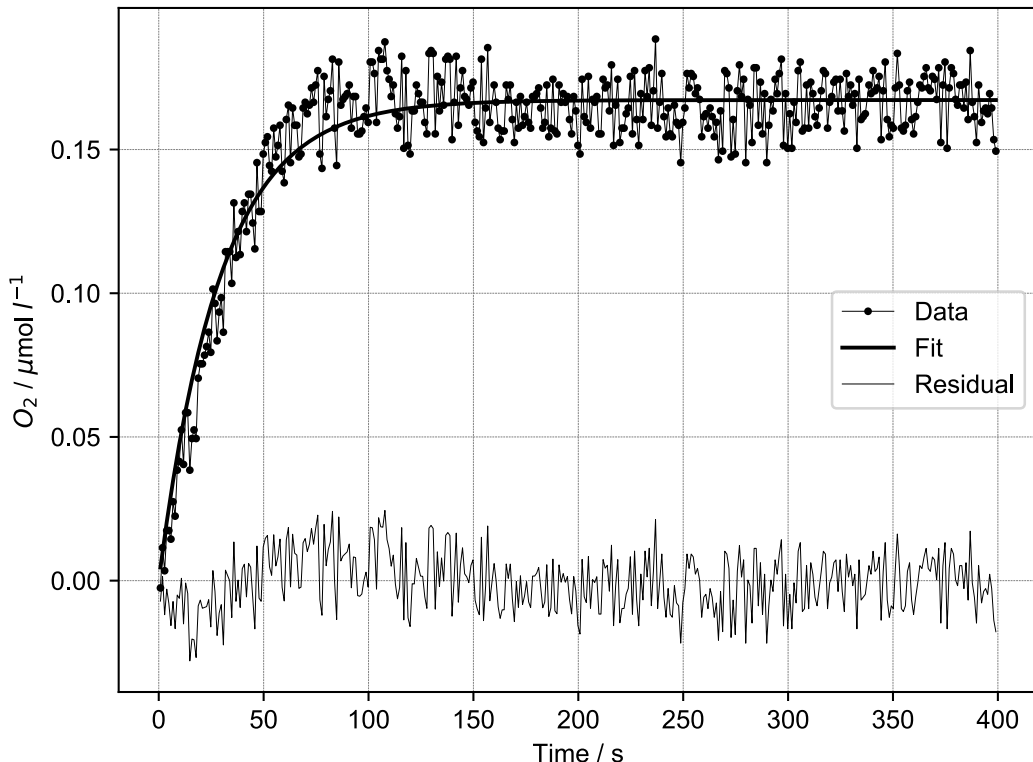


Figure 4.2-2 Exemplary liquid phase O₂ data analyzed as described in 4.2.2 (320 – 500 nm, 1 W intensity setting)

4.2.3 Data Analysis for Intensity Experiments

For the intensity dataset, irradiation was performed with five different intensity settings for the Hg light source (320 – 500 nm): 0.25, 0.375, 0.5, 0.75 and 1 W (the power values are not identical to the power received by the reactor, but they are proportional, see Chemical Actinometry section). For each intensity setting, at least two experiments were performed. Initial rates were calculated as described in 4.2.2 and for each intensity setting, the average of the corresponding experiments is reported (maximum deviation between experiments: 0.0005 $\mu\text{mol l}^{-1} \text{s}^{-1}$). In case of the intensity dataset, no difference was observed whether the average k_1 procedure was used or not. Temperature changes during irradiation were negligible (typically below 0.6 °C on the highest intensity setting).

The obtained initial rates were then fitted with a square function ($f(x) = ax^2$), optimizing only a . This showed that the dependence of initial O₂ formation rate on intensity can be described well using a square relationship.

As can be seen in Figure 4.2-3, comparing a square with a linear function for fitting the intensity/rate dataset shows that a square function yields a superior fit, with a sum of squared residuals that is three times lower than for the linear fit.

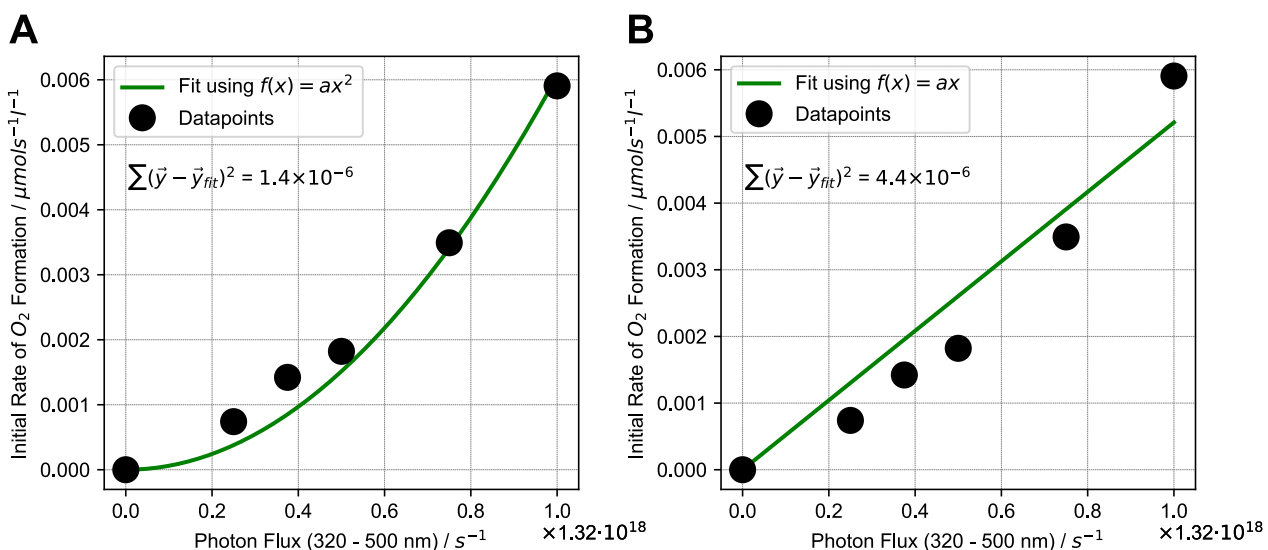


Figure 4.2-3 Comparison of square (left) and linear (right) fit of intensity/rate dataset
Sum of squared residuals is shown for each plot as an inset.

Based on initial rates from the intensity experiments and known photon fluxes (see Chemical Actinometry section), the overall quantum yields ($320 - 500 \text{ nm}$) at different fluxes can be calculated (see Table 4.2-1).

Table 4.2-1 Overall quantum yield ($320 - 500 \text{ nm}$) calculated based on intensity experiments

Photon flux / s^{-1}	Quantum yield / %
$3.3 \cdot 10^{17}$	$6.8 \cdot 10^{-5}$
$4.9 \cdot 10^{17}$	$8.7 \cdot 10^{-5}$
$6.6 \cdot 10^{17}$	$8.3 \cdot 10^{-5}$
$9.9 \cdot 10^{17}$	$1.1 \cdot 10^{-4}$
$1.3 \cdot 10^{18}$	$1.4 \cdot 10^{-4}$

As can be seen in Table 4.2-1, the quantum yield increases with increasing photon flux due to the square initial rate/photon flux relationship. It should be noted that the overall quantum yield is the product of photon flux, quantum efficiency for the first photochemical step, lifetime of the intermediate and quantum efficiency of the second photochemical step (see Photochemical Kinetic Model section). With the available data it is not possible to determine the precise individual values of those quantum efficiencies and intermediate lifetime, since kinetic modelling does not give unique solutions (see 10.3). We consider it likely that the very low overall quantum yield can be explained by a short lifetime of the intermediate, making it less likely that it absorbs a photon before decaying back to the starting material. This would also mean that significant increases in quantum yield can be obtained by increasing the lifetime of the intermediate. For example, if the lifetime of $[\mathbf{B}]T_0$ is indeed around 65 ns, increasing it to 650 μs would increase the overall quantum yield by a factor of 10,000 to 1.4% (for a photon flux of $1.3 \cdot 10^{18} \text{ s}^{-1}$). Such an improvement would be independent from improvements of the actual quantum efficiencies of both steps.

4.2.4 Data Analysis for Kinetic Isotope Effect and Temperature Dependence

To determine a possible H/D kinetic isotope effect (KIE), the standard irradiation procedure was used, but instead of H_2O , **1** was dissolved in D_2O (due to rapid exchange of hydroxo protons, the deuterated derivative of **1** is quickly formed). Irradiation was performed using the Hg light source ($320 - 500 \text{ nm}$) with the 1 W intensity setting. Two separate experiments in D_2O were performed and initial rates were calculated as described in 4.2.2, using the average k_1 procedure, and then averaged. As a reference, 1 W experiments from the intensity dataset were used, which were also analyzed using the average k_1 procedure and averaged. The obtained H/D KIE is 1.18.

To determine a possible temperature dependence of the reaction, the standard irradiation procedure was used, but instead of setting the thermostat temperature to 16.5 °C, it was set to 26.5 °C. Irradiation was performed using the Hg light source (320 – 500 nm) with the 1 W intensity setting. Two separate experiments at 26.5 °C were performed and initial rates were calculated as described in 4.2.2, using the average k_1 procedure, and then averaged. As a reference, 1 W experiments from the intensity dataset were used, which were also analyzed using the average k_1 procedure and averaged. The obtained ratio of initial rates at 16.5 °C and 26.5 °C is 0.78. The fact that the observed initial rate is in fact slightly slower at higher temperature might be attributed to accelerated, thermal side reactions consuming O₂.

Table 4.2-2 H/D kinetic isotope effect and temperature dependence of O₂ formation

$\frac{k_0(H)}{k_0(D)}$	$\frac{k_0(26.5 \text{ } ^\circ\text{C})}{k_0(16.5 \text{ } ^\circ\text{C})}$
1.18	0.78

4.2.5 Data Analysis for Dual Irradiation Experiments

For the dual irradiation dataset, there are three distinct groups of experiments:

1. Irradiation using the Hg light source (320 – 400 nm, 0.3 W intensity setting)
2. Irradiation using the QTH light source (different longpass filters)
3. Irradiation using both the Hg (320 – 400 nm, 0.3 W intensity setting) and QTH (different longpass filters) light source (dual irradiation)

The QTH light source was used with five different longpass filters: 455 nm, 495 nm, 550 nm, 590 nm and 630 nm cut-on wavelength. For irradiation using the QTH light source or dual irradiation, there are thus five subgroups each, corresponding to each longpass filter.

For the dual irradiation dataset it was found that data analysis could be improved (lower spread of initial rates for reproduction experiments) by correcting the analysis start point: instead of fitting Equation (2) from the start of irradiation, the start point was shifted forward to the point minimizing the residual for the fit of Equation (2) (a correction of typically 0 – 30 s). This correction allows excluding early datapoints, which tend to underreport O₂ concentration due to a time delay caused by diffusion into the sensor matrix.

Furthermore, it should be noted that dual irradiation experiments proved to be very sensitive to the alignment of the two light sources, since the beams had to overlap properly to observe a synergistic effect. Thus, some experiments could not be used for data analysis due to improper light source alignment.

For experiments using only the Hg light source, initial rates were calculated as described in 4.2.2, using the average k_1 procedure. Thus obtained k_0 values were averaged to give the average 320 – 400 nm initial rate.

For both QTH and dual irradiation, the following procedure was used to calculate initial rates: Equation (2) was fitted to all experiments, optimizing both k_0 and k_1 . Subsequently, a linear regression model was fitted to the k_1 values of all QTH or dual irradiation experiments, respectively. For each group, this linear model provides a description of the dependence of k_1 on longpass filter cut-on wavelength. Subsequently, Equation (2) was again fitted to all experiments, this time fixing k_1 to be the linear regression value of the respective linear model (QTH or dual irradiation) and wavelength. For the dual irradiation group, thus obtained k_0 values were averaged for each wavelength. For the QTH irradiation group, another linear regression model was fitted to the k_0 values, this time yielding a linear model to describe the dependence of k_0 on longpass filter cut-on wavelength.

To give the reported excess initial rate of O₂ formation, the following method was used: for each wavelength, the average 320 – 400 nm initial rate as well as the QTH linear regression k_0 value for the respective wavelength were subtracted from the average dual irradiation initial rate.

At this point we would like to note that the small apparent O₂ signals observed when only the longpass filtered QTH light source was used are likely not due to actual O₂ evolution. This is based on the observation that no **2-cis** was formed when only the QTH light source (> 495 nm) was used for irradiation. Rather, the small signals might be caused by the temperature change of ca. 2 °C caused by the QTH light source despite the reactor being submersed in a water bath. Regardless, through the above described analysis method, any contribution of the QTH light source to the observed O₂ signal during dual irradiation is accounted for by subtracting the obtained QTH linear regression k_0 values. Furthermore, subtraction of the average 320 – 400 nm initial rate accounts for the contribution of the Hg light source during dual irradiation. Reported excess initial rates are therefore the result of a synergistic effect of both light sources.

4.2.6 Note on Reaction Order/Concentration Dependence

As noted in 4.2.1, the observed reaction rates are identical for 0.01 and 0.005 M solutions of **1**. This is because in this concentration range, complete photon absorption by the sample solution occurs, leading to an apparent zero order reaction in **1**.⁸ Attempts to perform measurements using solutions of significantly lower concentration, below the complete absorption regime, were unsuccessful. Hence, the actual reaction order in **1** could not be determined.

4.3 Gas Phase O₂ Measurement

4.3.1 Irradiation Procedure

A 5 ml Schlenk flask (internal volume ca. 10 ml) with a NS14 ground glass joint was topped with a hollow, flat top glass stopper, on the inside of which a contactless trace range oxygen sensor spot was glued. This allows measurement of gas phase O₂ concentration inside the reactor via contactless read out through the glass stopper. The Schlenk flask was then connected to the Schlenk line using a T-piece adapter, with one connection to the Schlenk line, one to the Schlenk flask and one connection being closed with a septum. Subsequently, 2 ml of an aqueous solution of **1** (prepared via the N₂O synthesis route, 0.01 M) was transferred into the Schlenk flask. The transfer was done via cannula transfer through the septum inlet of the T-piece adapter and through the valve of the Schlenk flask, taking care not to introduce any external O₂ into the flask.

Once the transfer was complete, the Schlenk flask was closed and stirred overnight in the dark at room temperature to equilibrate. A PT100 temperature sensor (for temperature compensation of the O₂ measurement) was placed next to the Schlenk flask.

After equilibration, an optical fiber was mounted to the outside of the flat top glass stopper to read out the oxygen sensor spot. Then, the baseline O₂ concentration was measured for ca. 4 h. Afterwards the flask was irradiated for 16 h using the Hg light source (320 – 500 nm, 0.15 W intensity setting), resulting in a color change to a yellow/orange solution. During irradiation the flask was cooled using a 20 W fan.

4.3.2 Data Analysis and O₂ Consumption Reaction

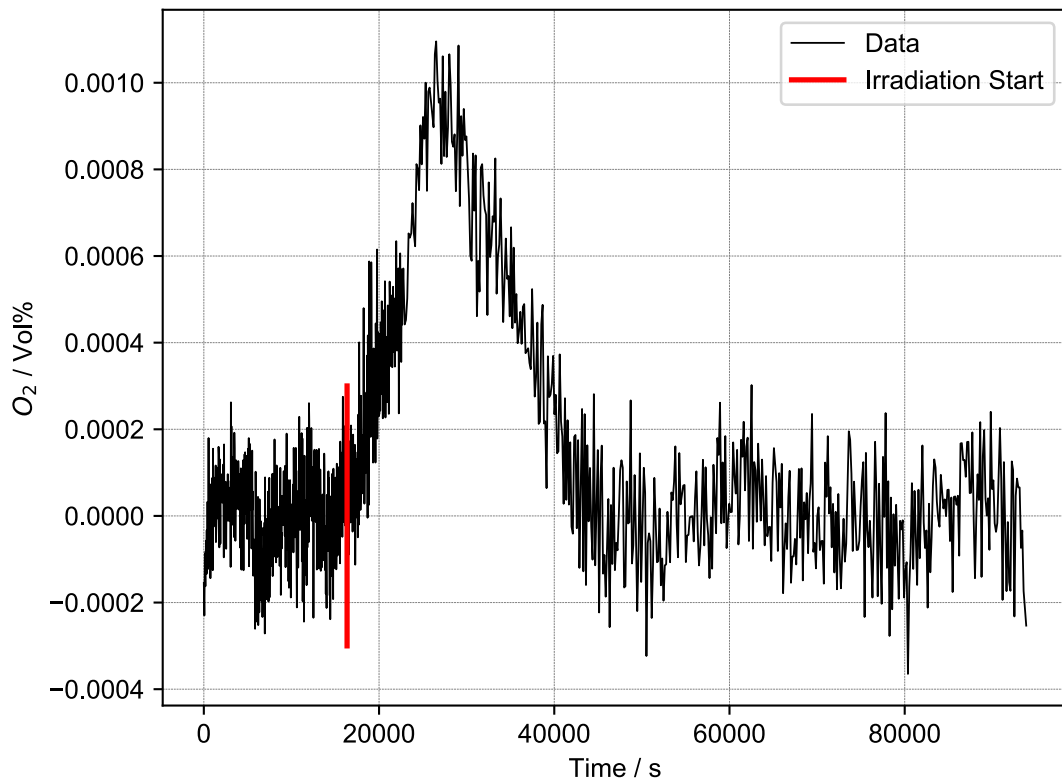


Figure 4.3-1 Gas phase O₂ detection data for irradiation of complex **1** with Hg light source (320 – 500 nm)

Data has been baseline corrected with a sixth-degree polynomial fitted to baseline intervals [0 s, 16350 s] and [46300 s, 94000 s]. Irradiation was turned on at t = 16350 and turned off at t = 76000 s.

The obtained gas phase O₂ concentration data shows a small peak shaped feature resulting from O₂ evolution superimposed on a continuously decreasing background. Therefore, a sixth-degree polynomial was fitted to baseline intervals [0 s, 16350 s] (t = 16350 s is the start time for irradiation) and [46300 s, 94000 s] and subtracted from the entire measurement to obtain a baseline corrected signal, shown in Figure 4.3-1.

As can be seen in Figure 4.3-1, once irradiated is started, an increase in the gas phase O₂ concentration can be detected due to O₂ evolution for ca. 3 h. Afterwards, the O₂ concentration drops back to baseline value again over the course of ca. 6 h. This kind of behavior is consistent with a two-reaction sequence, wherein O₂ is formed in the first reaction (O₂ evolution from **1**, decreasing reaction rate over time due to consumption of **1**) and consumed in the second reaction.

In a separate experiment, complex **1** (synthesized via Ag₂O synthesis route, in 52 mM KOH aq.) was irradiated using the QTH light source (only water filter) in air, resulting in conversion of **1** into mostly NMR inactive species (see Figure 7.5-7 - Figure 7.5-10). We hypothesized that **1**, when irradiated in the presence of O₂, oxidizes to form mostly Ru(III) species as well as phosphorous oxides. This can explain the consumption of O₂ during water splitting and the formation of NMR inactive species when **1** is irradiated in air.

4.4 Comparison of **2-cis** and O₂ Formation Rates

To confirm that **2-cis** and O₂ are indeed both formed in the same reaction, their initial rates of formation were compared. If both are formed in the same reaction, their normalized rates are expected to be identical. With the available experimental data and techniques, however, only an approximate comparison can be made since **2-cis** and O₂ formation had to be studied in different experimental set-ups (NMR scale irradiation and liquid phase O₂ measurement, respectively). Therefore, multiple normalizations had to be applied to enable comparison, which will be explained in the following.

For **2-cis**, the initial rate of formation was calculated from the kinetic model shown in Figure 4.1-1. The thus obtained initial rate is 1E-05 s⁻¹ in normalized units or 0.1 μmol l⁻¹ s⁻¹ (given a concentration of 0.01 M).

For O₂, the initial rate of formation was taken from the intensity data set for the 1 W intensity setting, being 0.0059 μmol l⁻¹ s⁻¹.

The first normalization is based on the stoichiometry of the reaction (see Table 4.4-1), which shows that **2-cis** would be formed at twice the rate of O₂. Hence, stoichiometry adjusted rates are 0.05 μmol l⁻¹ s⁻¹ for **2-cis** and 0.0059 μmol l⁻¹ s⁻¹ for O₂.

The second normalization that has to be applied has to correct for the different areas, which were irradiated in each set-up. For NMR scale irradiation, the irradiated area was 0.424 × 4 cm (1.696 cm²), while the irradiated area was 0.8 × 1 cm (0.8 cm²) for liquid phase O₂ measurements. Since the reaction rate is proportional to irradiated area for a photochemical reaction (the light cone was bigger than the reactor in both cases), initial rates normalized to 1 cm² are 0.0295 μmol l⁻¹ s⁻¹ for **2-cis** and 0.0074 μmol l⁻¹ s⁻¹ for O₂.

The last normalization is based on the different flux densities used in the experiments. The initial rate of O₂ formation is based on irradiation with the Hg light source with the 1 W intensity setting, which corresponds to a photon flux of 1.32E+18 s⁻¹ received by the reactor (see Chemical Actinometry). For NMR scale irradiation, the QTH light source (equipped with only the water filter) was used instead. The photon flux of the QTH light source cannot be easily determined using the applied chemical actinometry method, so it is estimated based on power meter measurements. It

should be noted that these power values are not identical to the power received by the reactor. Instead, they are only proportional.

Based on power meter measurements, ca. 27% of the QTH output power is in the useful wavelength range of 320 – 630 nm. Total power measured in the position of the NMR tube was 645 mW, giving ca. 173 mW of power in the 320 – 630 nm wavelength range, with a mean photon wavelength of 475 nm.

Using the same power meter, a power of 127 mW was measured in the position of the liquid phase O₂ reactor for the Hg light source (320 – 500 nm, 1.32E+18 s⁻¹ flux, mean photon wavelength of 410 nm). Based on the mean photon wavelengths (475 nm for QTH, 410 nm for Hg) and measured power values (173 mW for QTH, 127 mW for Hg), one can estimate a photon flux of ca. 2.09E+18 being received by the NMR tube using the following equation:

$$Flux_{QTH} = \frac{E_{Hg} P_{QTH}}{E_{QTH} P_{Hg}} Flux_{Hg} \quad \text{Equation (3)}$$

With E_{Hg} and E_{QTH} being the mean photon energies in eV for the QTH and Hg light sources, respectively, and P_{QTH} and P_{Hg} being the measured power values. Based on the intensity dataset, it was found that rate of O₂ formation shows a square dependence on photon flux. If we assume that the same holds true for **2-cis** (since **2-cis** has shown the same synergistic effect in dual irradiation experiments as O₂ formation), the square of the ratio between the Hg and QTH light source flux values gives a flux correction factor of 2.5. Applying this factor to the **2-cis** initial rate of formation gives a flux-normalized rate of 0.0118 μmol l⁻¹ s⁻¹. Comparing this to the normalized initial rate of O₂ formation, 0.0074 μmol l⁻¹ s⁻¹, shows that they differ by less than 40%. Considering that these two rates were measured using different methods (NMR and O₂ detection) and in different set-ups, we consider this to be an acceptable agreement.

Table 4.4-1 Comparison of 2-cis and O₂ initial rates of formation



Estimated, normalized initial rate of 2-cis formation / μmol l ⁻¹ s ⁻¹	Estimated, normalized, initial rate of O ₂ formation / μmol l ⁻¹ s ⁻¹
0.0118	0.0074

4.5 Photographs of Irradiation Set-Ups

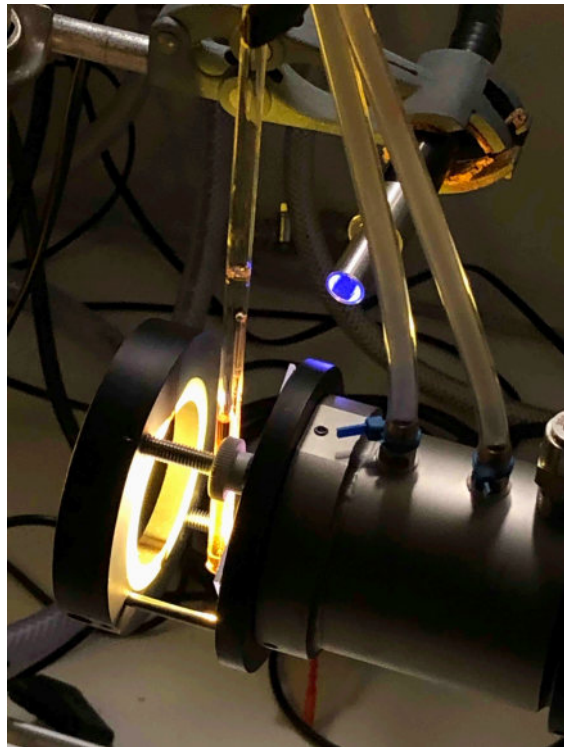


Figure 4.5-1 Set-up for irradiation on NMR scale

Hg light source provides irradiation through the light guide in the back (320 – 400 nm filtered in this picture) and the QTH light source is visible on the right (water cooled IR filter and filter holder are visible, > 495 nm filtered in this picture).

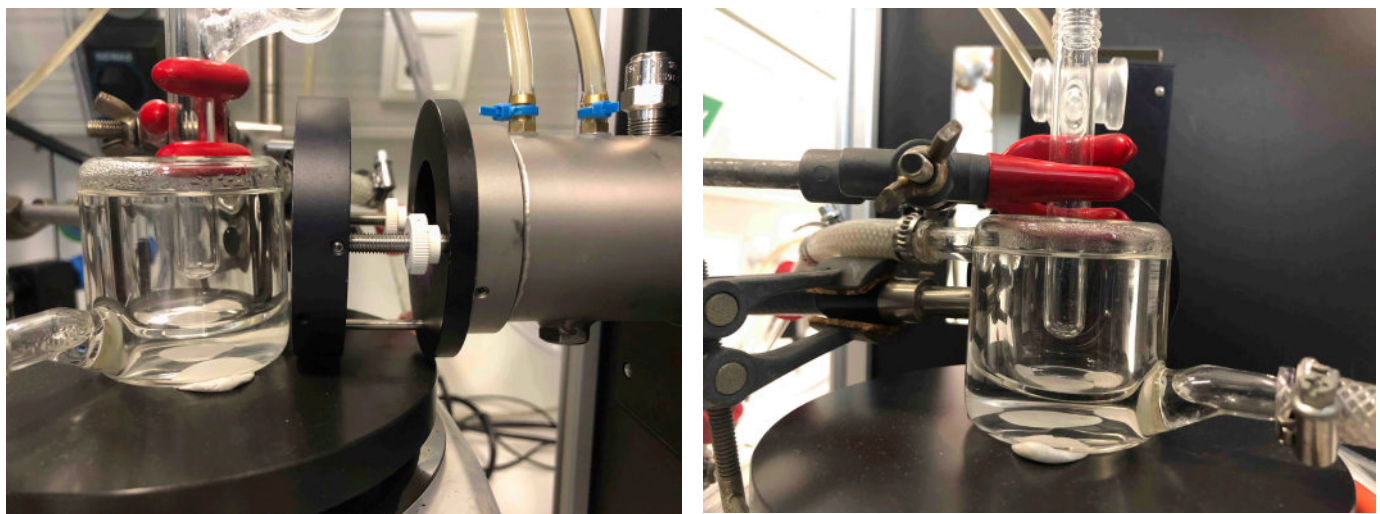


Figure 4.5-2 Set-up for irradiation with liquid phase O₂ detection

Left: Front view of set-up showing QTH light source (right) and water filled, thermostatted beaker with Schlenk flask reactor.

Right: Side view of set-up showing light guide of Hg light source (left) and side view of thermostatted reaction assembly.

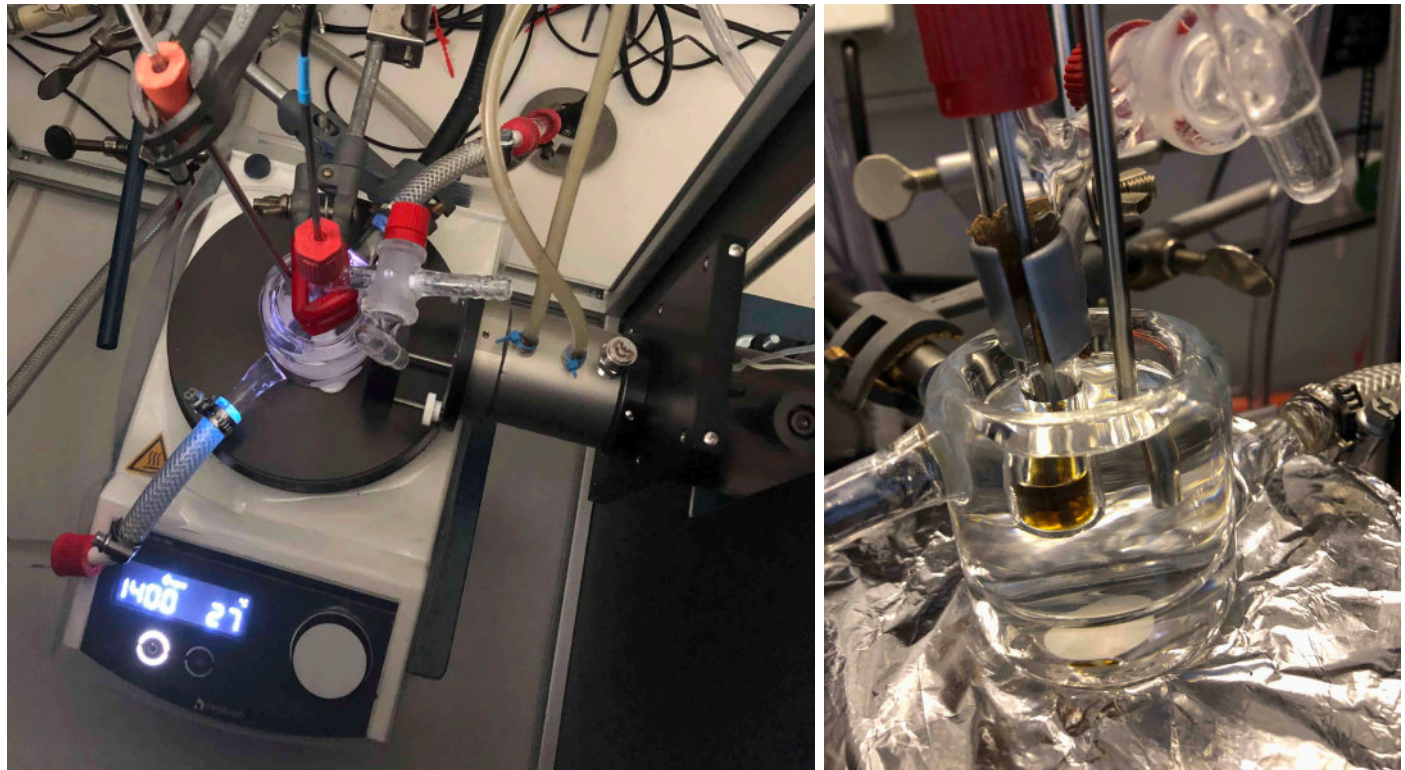


Figure 4.5-3 Irradiation set-up (liquid phase O₂ detection) in use (left) and close-up of assembled reactor

Left: Irradiation set-up in use (only Hg light source, 320 – 400 nm filtered, is turned on). QTH light source (with shutter, water cooled IR filter and filter holder) is visible on the right. Center shows the Schlenk reactor submerged in the thermostatted beaker with an O₂ sensor connected via a BOLA laboratory screw joint (red cap). Next to the reactor, a PT100 temperature sensor is submerged in the thermostatted beaker. Note that the temperature shown on the stir plate is not indicative of the actual reaction temperature.

Right: Close-up of assembled reactor with submerged PT100 temperature sensor on the right. Inside of the reactor, an aqueous solution of complex **1** can be seen, inside of which the O₂ sensor is submerged.

5 H₂O₂ Disproportionation

5.1 Experimental Procedure

Following the procedure described in 4.2.1, ca. 400 µl of degassed 5×10⁻⁵ M aqueous H₂O₂ were transferred into a Schlenk flask equipped for liquid phase O₂ measurement. Throughout the experiment, the flask was connected to the Schlenk line (under argon), allowing for the injection of other reagents. A PT100 temperature sensor was placed next to the flask for temperature compensation of the O₂ measurement. While being stirred and at room temperature, the baseline O₂ concentration was measured, followed by injection of 500 µl of an aqueous solution of **1** (synthesized using N₂O synthesis route, 0.005 M) through the septum of the T-piece adapter. After 50 min, 100 µl of a degassed 3 M potassium iodide (KI) solution were injected, followed by another 40 min of O₂ measurement.

5.2 Data Analysis

This H₂O₂ disproportionation experiment was performed to investigate the feasibility of a stepwise water splitting mechanism, wherein irradiation of **1** first produces H₂O₂, followed by H₂O₂ disproportionation to O₂ and H₂O catalyzed by **1**. In our view, complex **1** would be the only viable candidate for a H₂O₂ disproportionation catalyst in this scenario, since O₂ formation occurs directly at the start of irradiation (see for example Figure 4.2-1). At the start of the reaction, only **1** is present in significant quantities and it would therefore be the only compound that could catalyze H₂O₂ disproportionation at this point.

The used quantity of H₂O₂ (20 nmol) corresponds to roughly 200 times the amount of O₂ formed within the first 90 s of a liquid phase O₂ measurement experiment (Hg light source, 320 – 500 nm, 1 W setting, ~ 0.11 nmol). Furthermore, it is roughly 1% of the amount of **1** used (2.5 µmol). Therefore, this amount it is likely an overestimation of the highest H₂O₂ concentration that might occur for a H₂O₂ mechanism. Thus, the observed rate of H₂O₂ disproportionation catalyzed by **1** will be an upper bound for the H₂O₂ disproportionation rate possible under water splitting reaction conditions. If this rate is slower than the observed initial rate of O₂ formation during liquid phase O₂ measurement, a mechanism involving H₂O₂ disproportionation can be seen as unlikely.

The results of the experiment are shown in Figure 5.2-1. It can be seen that the baseline O₂ concentration of the H₂O₂ solution is elevated (1.9 µmol l⁻¹), since it proved challenging to remove all dissolved O₂ from it. Addition of the solution of **1** (having a lower O₂ concentration) at t = 150 s therefore leads to a drop in O₂ concentration. After equilibration, a linear increase in O₂ concentration with a rate of 1.2×10⁻⁵ µmol l⁻¹ s⁻¹ can be observed (see Figure 5.2-1B). We attribute this to H₂O₂ disproportionation catalyzed by **1**. At t = 3100 s, a 3 M KI solution was added to the reactor. Since KI is a known and fast-acting H₂O₂ disproportionation catalyst, this was done to confirm that H₂O₂ disproportionation can be observed under these reaction conditions. Indeed, addition of KI leads to a rapid increase in O₂ concentration, followed by return to baseline value (likely due to diffusion of O₂ into the gas phase). Importantly, after addition of KI and equilibration, no increase in O₂ concentration can be observed anymore (see Figure 5.2-1B). This suggests that all H₂O₂ has been consumed by KI catalyzed disproportionation. In turn, this supports the hypothesis that the increase in O₂ concentration before KI addition was due to catalytic H₂O₂ disproportionation and not some other process (such as leakage).

Within this interpretation, the rate of H₂O₂ disproportionation catalyzed by **1** (1.2×10⁻⁵ µmol l⁻¹ s⁻¹) is more than an order of magnitude slower than the initial O₂ formation rate during water splitting (5.9×10⁻³ µmol l⁻¹ s⁻¹ for Hg light source, 320 – 500 nm, 1 W setting). Therefore, it is unlikely that a mechanism involving H₂O₂ disproportionation is responsible for O₂ evolution in this system. However, a variable not included in this experiment is irradiation. It is possible that irradiation could accelerate H₂O₂ disproportionation. This possibility could not be investigated in this experiment since irradiation would lead to a combined increase of O₂ concentration due to H₂O₂

disproportionation and O₂ evolution from **1**, which could not be distinguished. Theoretical evidence, however, also suggests that light-induced H₂O₂ formation from **1** is unlikely (see 11.2.8).

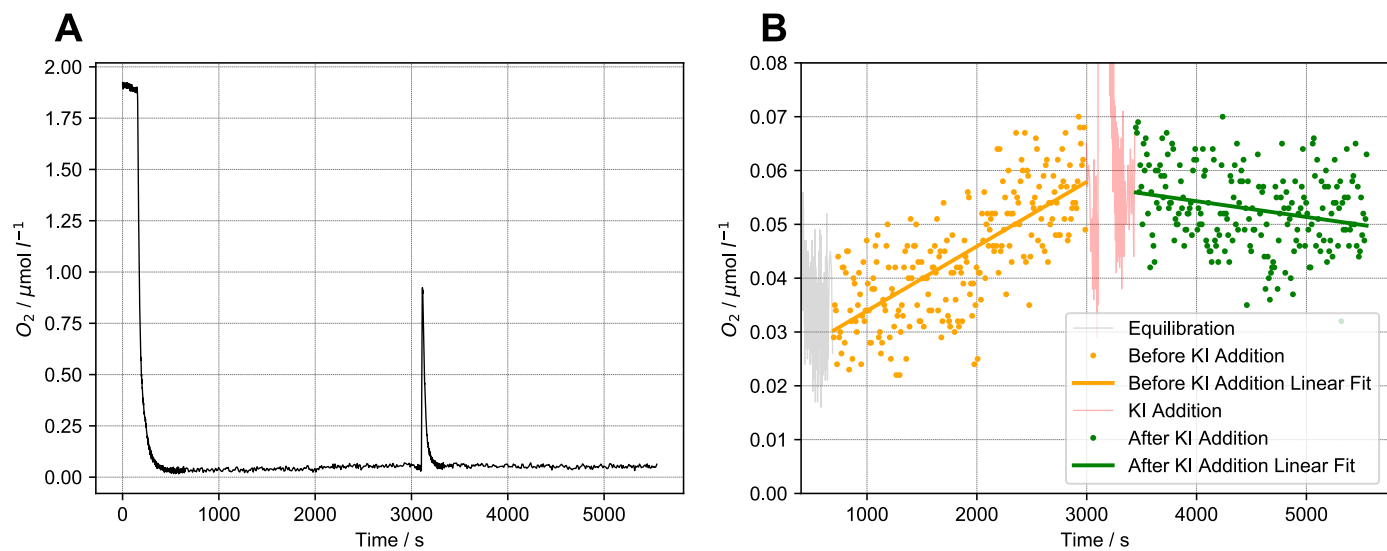


Figure 5.2-1 Liquid phase O₂ measurement for H₂O₂ disproportionation catalyzed by complex 1

A Overview of entire liquid phase O₂ measurement. At t = 0 s, only the aqueous 4×10⁻⁵ M H₂O₂ solution is present in the reactor. At t = 150 s, the ca. 5×10⁻³ M aqueous solution of complex **1** is injected, leading to a drop in the liquid phase O₂ concentration (since the solution of complex **1** had a lower O₂ concentration compared to the H₂O₂ solution). At t = 3100 s, 3 M aqueous KI solution was added, leading to a spike in the O₂ concentration (O₂ concentration drops again due to diffusion into the gas phase).

B Zoom-in of region before (yellow) and after (green) KI addition, with linear fits. The slope before KI addition is 1.2×10⁻⁵ $\mu\text{mol l}^{-1} \text{s}^{-1}$, after KI addition it is -2.9×10⁻⁶ $\mu\text{mol l}^{-1} \text{s}^{-1}$.

6 Chemical Actinometry

6.1 Light Source Spectra

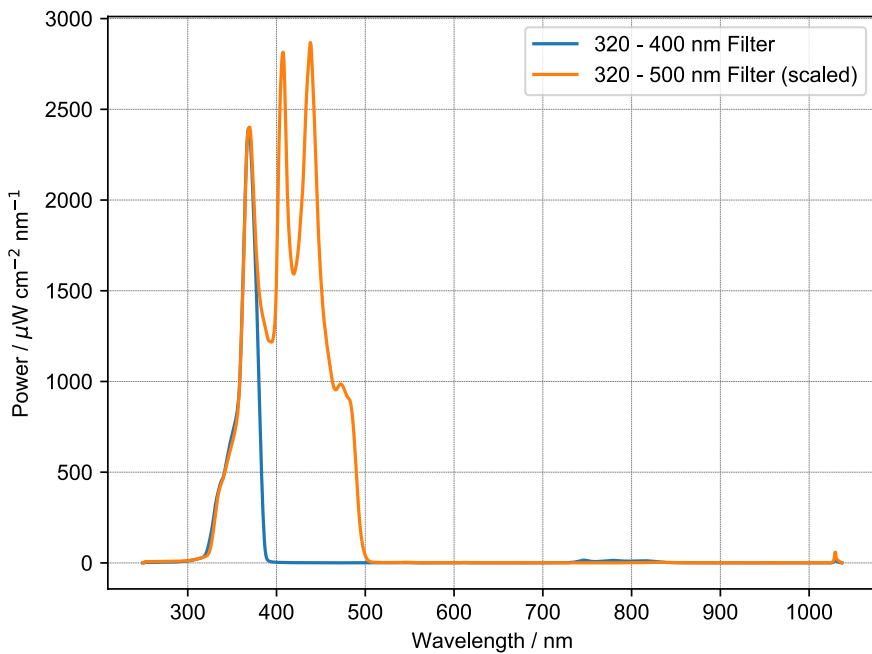


Figure 6.1-1 Spectral power distribution of Hg light source with used filter settings

Note: the actual amount of power reaching the reaction solution depends strongly on the reaction configuration, which is why chemical actinometry was performed (see below).

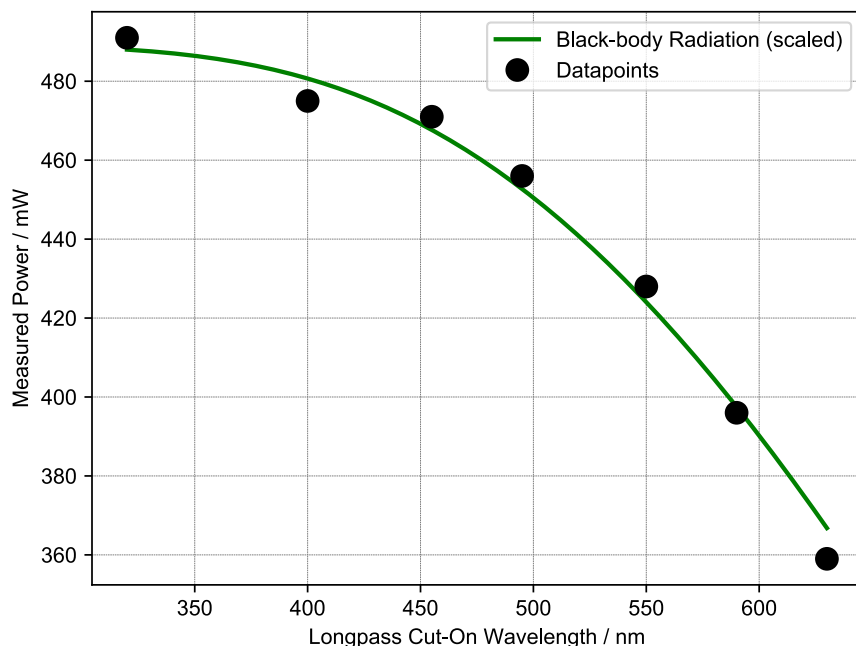


Figure 6.1-2 Measured power of QTH light source with different longpass filters

Graph shows power measured in liquid phase O₂ reactor position with different longpass filters (black dots). The scaled, predicted behavior for an ideal blackbody radiation source (3400 K) is shown in green.

6.2 Experimental Procedure

Potassium ferrioxalate actinometry was performed as described in ref.⁹. All experiments were carried out in air and in the dark. The $K_3[Fe(C_2O_4)_3]$ solution was prepared by combining an aqueous 0.2 M solution of $Fe_2(SO_4)_3$ with an aqueous 1.2 M solution of $K_2C_2O_4$. Blank experiments were performed to confirm that the absorbance of the solution was below 0.06 at 510 nm.

For each actinometry experiment, 550 μ l of $K_3[Fe(C_2O_4)_3]$ solution were transferred into the liquid phase O₂ measurement reactor, which was positioned in the same way as during liquid phase O₂ measurements. It was then irradiated using the Hg light source (320 – 400 nm or 320 – 500 nm filter) for a precise amount of time (between 3 – 10 s, depending on the intensity setting). Afterwards, an aliquot of 100 μ l was removed from the reactor, combined with 2 ml of a 0.2 wt% phenanthroline solution, 50 μ l of buffer solution and diluted up to 10 ml in a volumetric flask. Afterwards, the absorbance of the solution at 510 nm was measured using UV/Vis spectroscopy in a 1 cm cuvette.

6.3 Chemical Actinometry Data and Analysis

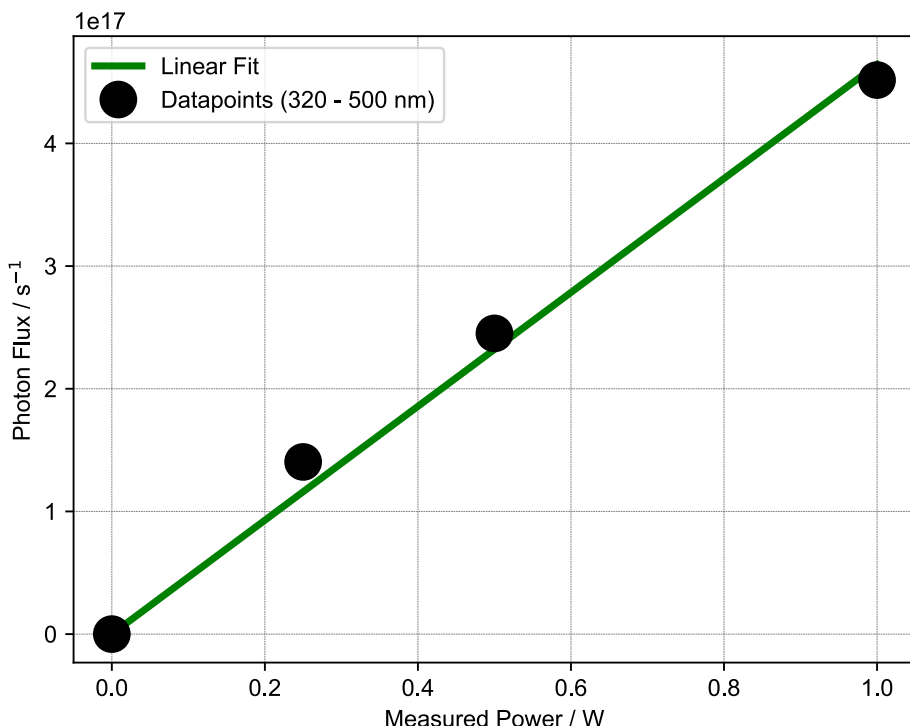


Figure 6.3-1 Chemical actinometry data for different power setting of Hg light source (320 – 500 nm)
Slope of linear fit: 4,64E+17. Note that the used ferrioxalate method does not detect all photons with wavelengths > 400 nm, which is why in the following a correction is applied to the raw photon flux values shown in this figure.

Using the obtained absorbance values, photon flux received by the reactor was calculated using the formula in ref.⁹, using a quantum yield of 1.16 and the previously reported extinction coefficient of 1.11E+04 M⁻¹ cm⁻¹ for the iron(II) phenanthroline complex.

Figure 6.3-1 shows the obtained photon flux values for 0.25, 0.5 and 1 W intensity settings of the Hg light source (320 – 500 nm), establishing a linear correlation between intensity settings and photon flux received by the reactor.

For the 320 – 400 nm filtered Hg light source, a photon flux of 4.15E+17 s⁻¹ was determined (0.3 W intensity setting).

Due to the short path length of the liquid phase O₂ measurement reactor (8 mm) and the low extinction coefficient of K₃[Fe(C₂O₄)₃] for wavelengths longer than 400 nm,⁹ photon flux values for the 320 – 500 nm filtered Hg light source are underestimated. In contrast, for the 320 – 400 nm filtered Hg light source, it can be assumed that quantitative photon absorption occurred. Hence, the determined photon flux value (for 320 – 400 nm) combined with the spectral power distribution of the light source (see Figure 6.1-1) can be used to calculate the correct 320 – 500 nm photon flux values:

1. The 320 – 520 nm spectral power distribution is converted to a spectral photon distribution through division of the power distribution by respective photon energies.
2. The spectral photon distribution is integrated from 320 – 500 nm and 320 – 390 nm (390 nm is the actual cut-off of the 320 – 400 nm filter, see Figure 6.1-1).
3. The 320 – 390 nm integral is used to scale the spectral photon distribution, so that the 320 – 390 nm integral is equal to the experimental photon flux of 4.15E+17 s⁻¹.
4. Integration of the scaled spectral photon distribution from 320 – 500 nm gives the corresponding photon flux for this filter setting, which is 1.56E+18 s⁻¹. It has to be considered, however, that this is the 320 – 500 nm photon flux when the light source is in the 0.3 W 320 – 400 nm intensity setting.
5. Experimentally, it was determined that the 0.3 W intensity setting (320 – 400 nm) corresponds to 1.18 W for 320 – 500 nm. Based on the linear relationship between intensity setting and photon flux (see Figure 6.3-1), it can therefore be determined that for the 1 W intensity setting (320 – 500 nm), the photon flux is 1.32E+18 s⁻¹.
6. Therefore, intensity settings for 320 – 500 nm can be converted to photon flux by multiplication by 1.32E+18 s⁻¹.

7 NMR Data

7.1 Characterization of 1

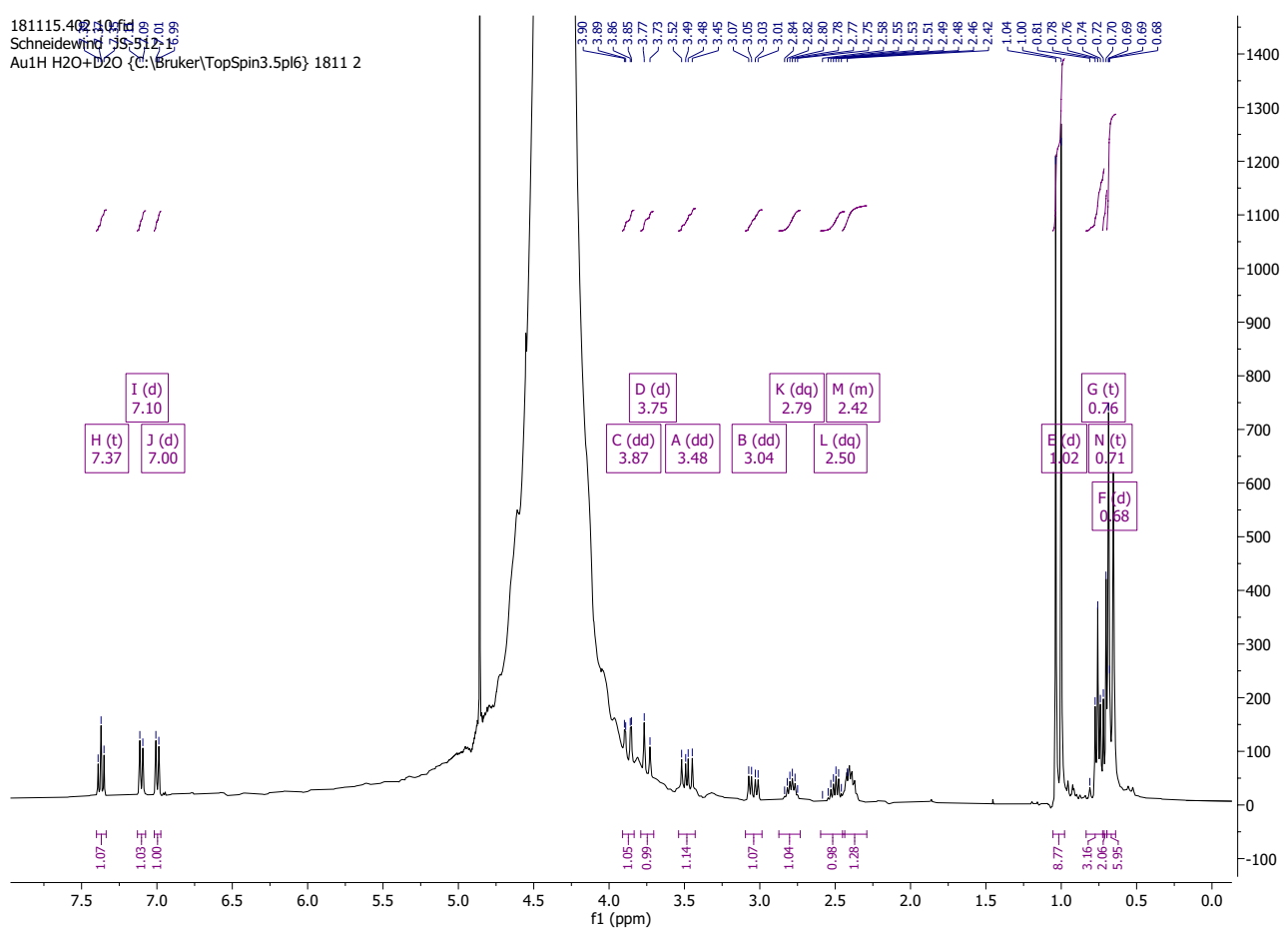
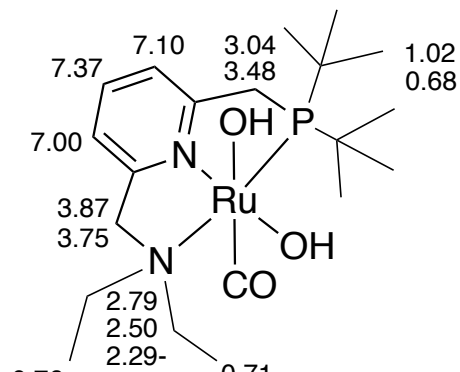


Figure 7.1-1 ^1H NMR spectrum of 1 in H_2O (298 K).

181115.402.11.fid
Schneidewind JS-512-1
Au31P-quant H2O+D2O {C:\Bruker\TopSpin3.5pl6} 1811 2

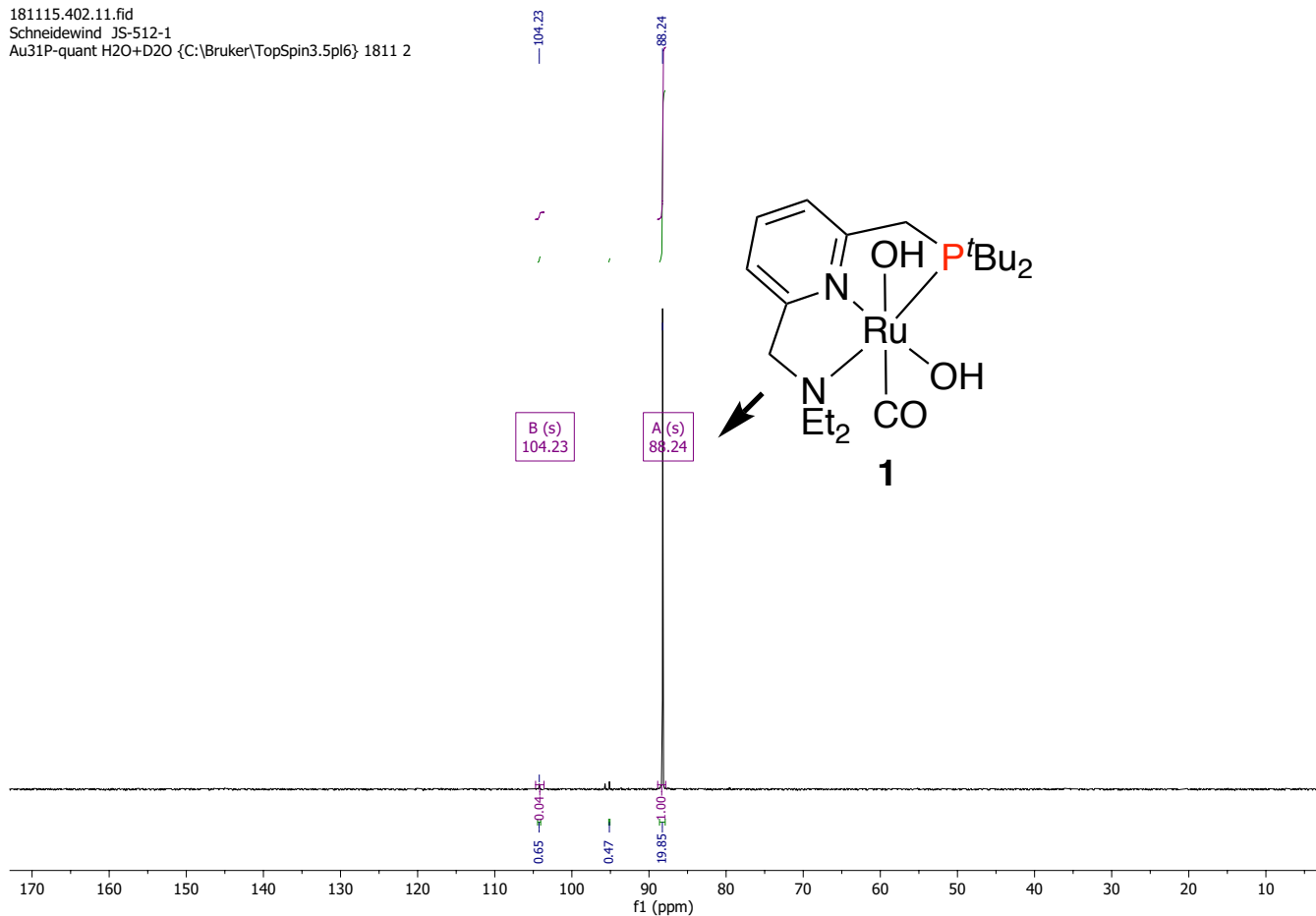
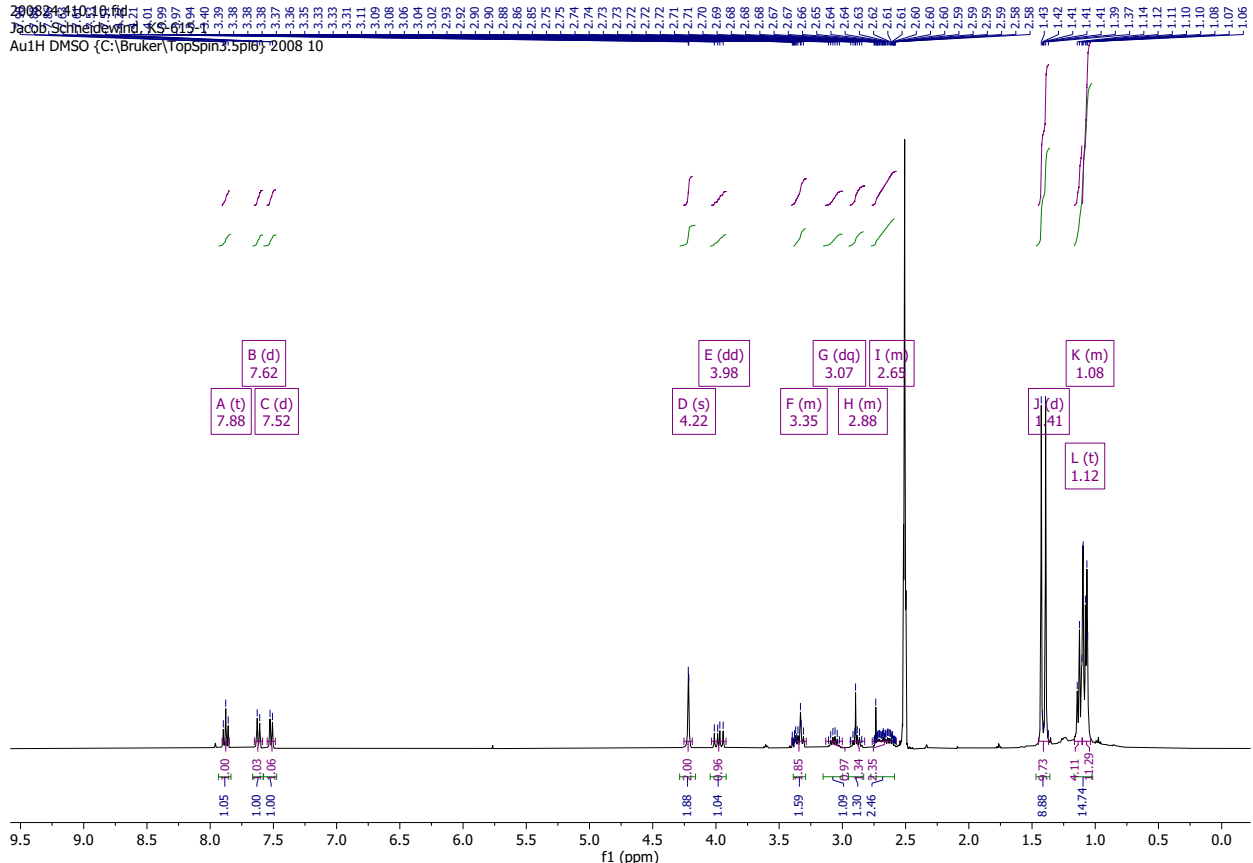
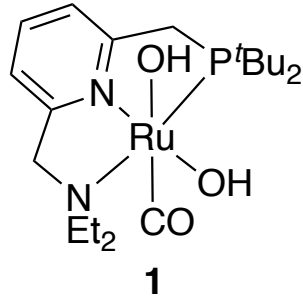


Figure 7.1-2 ${}^{31}\text{P}\{\text{H}\}$ NMR spectrum of **1** in H_2O (298 K)
(small amount of residual **2-trans** is visible at $\delta({}^{31}\text{P}) = 104.23$ ppm)



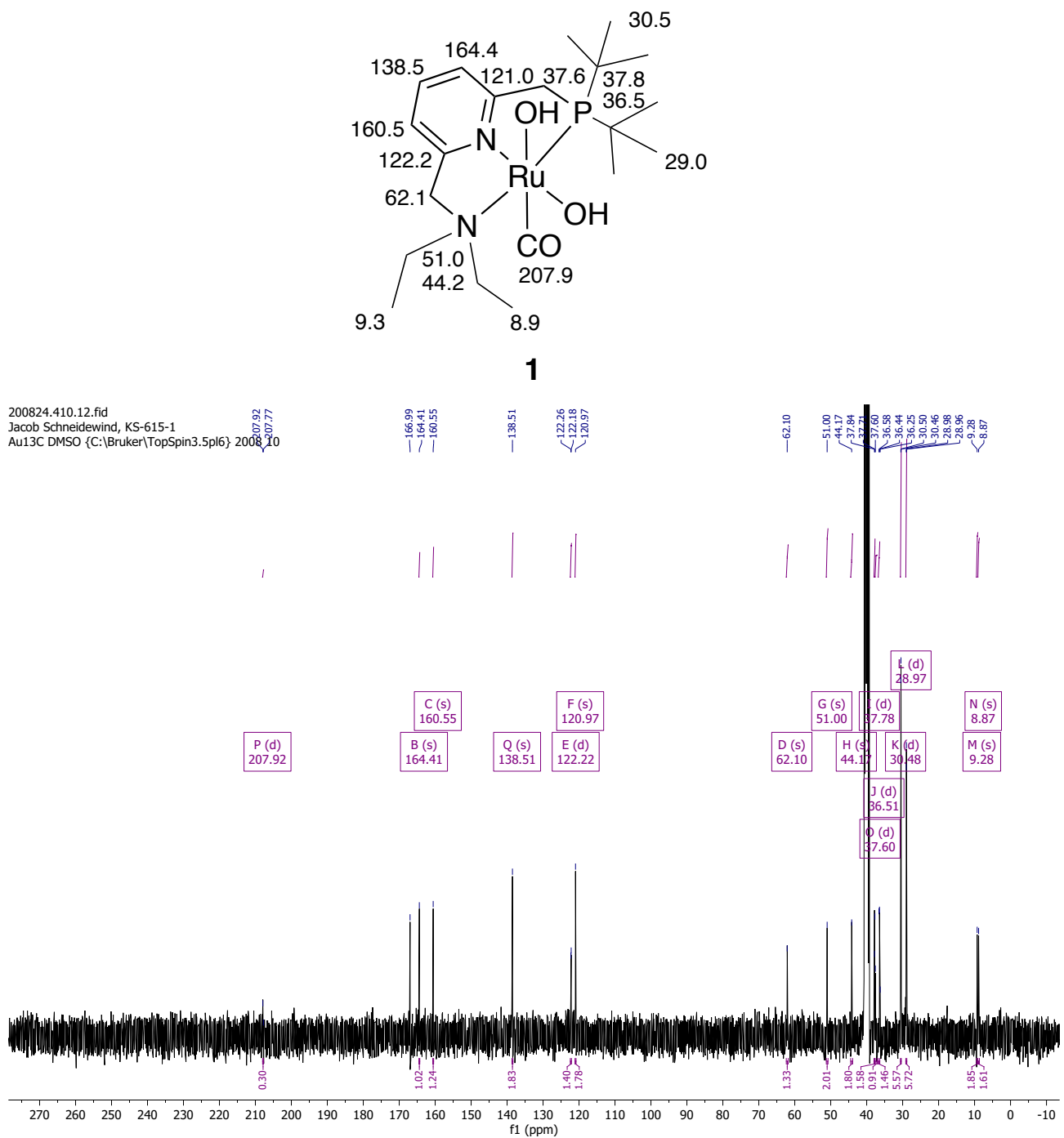


Figure 7.1-4 $^{13}\text{C}\{\text{H}\}$ NMR spectrum of **1** in DMSO-d_6 (298 K)

200824.410.11.fid
Jacob Schneidewind, KS-615-1
Au31P-quant DMSO {C:\Bruker\TopSpin3.5pl6} 2008 10

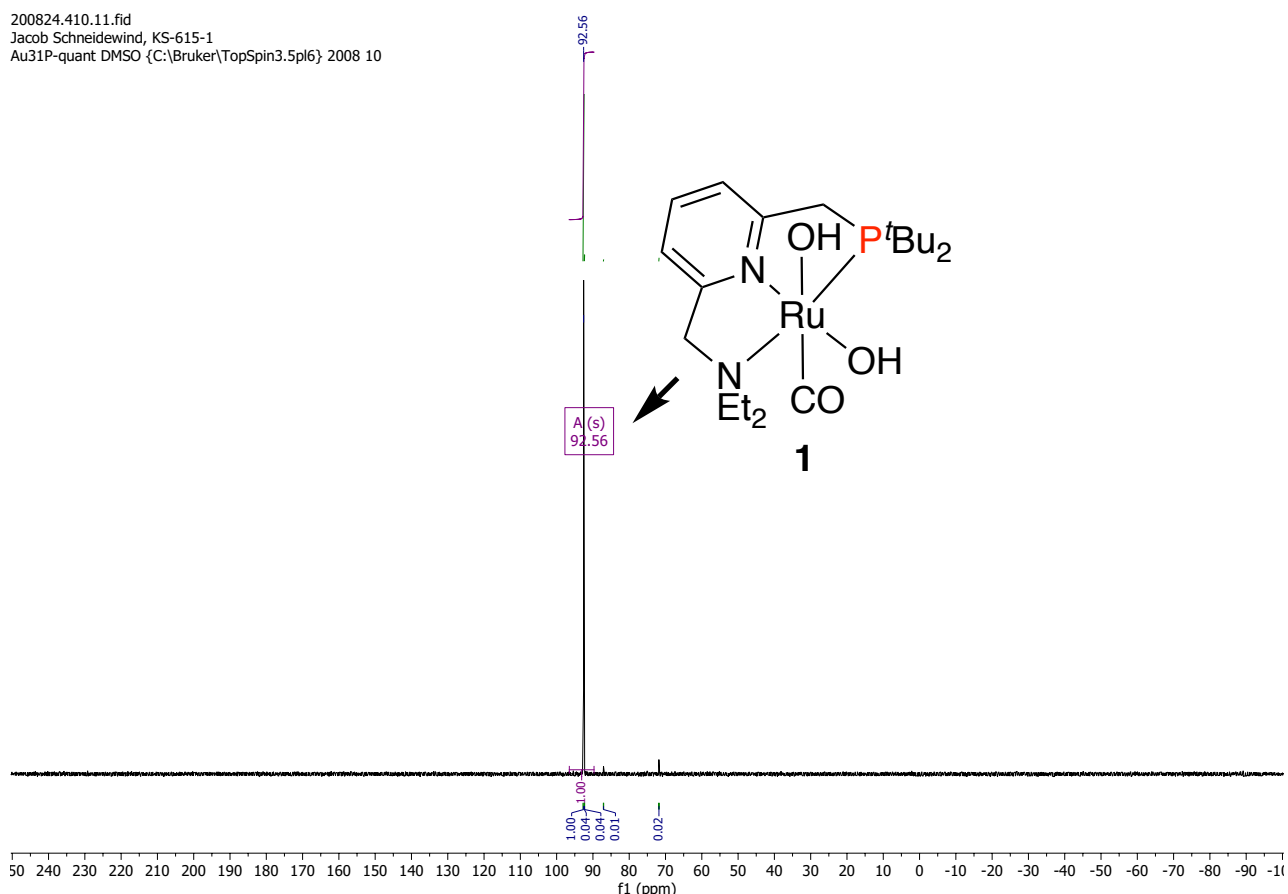
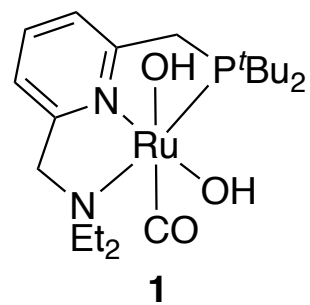


Figure 7.1-5 ${}^{31}\text{P}\{{}^1\text{H}\}$ NMR spectrum of **1** in DMSO-d_6 (298 K)



191024.402.10.fid
 Schneidewind JS-575-1
 Au1H H2O+D2O {C:\Bruker\TopSpin3.5pl6} 1910 2

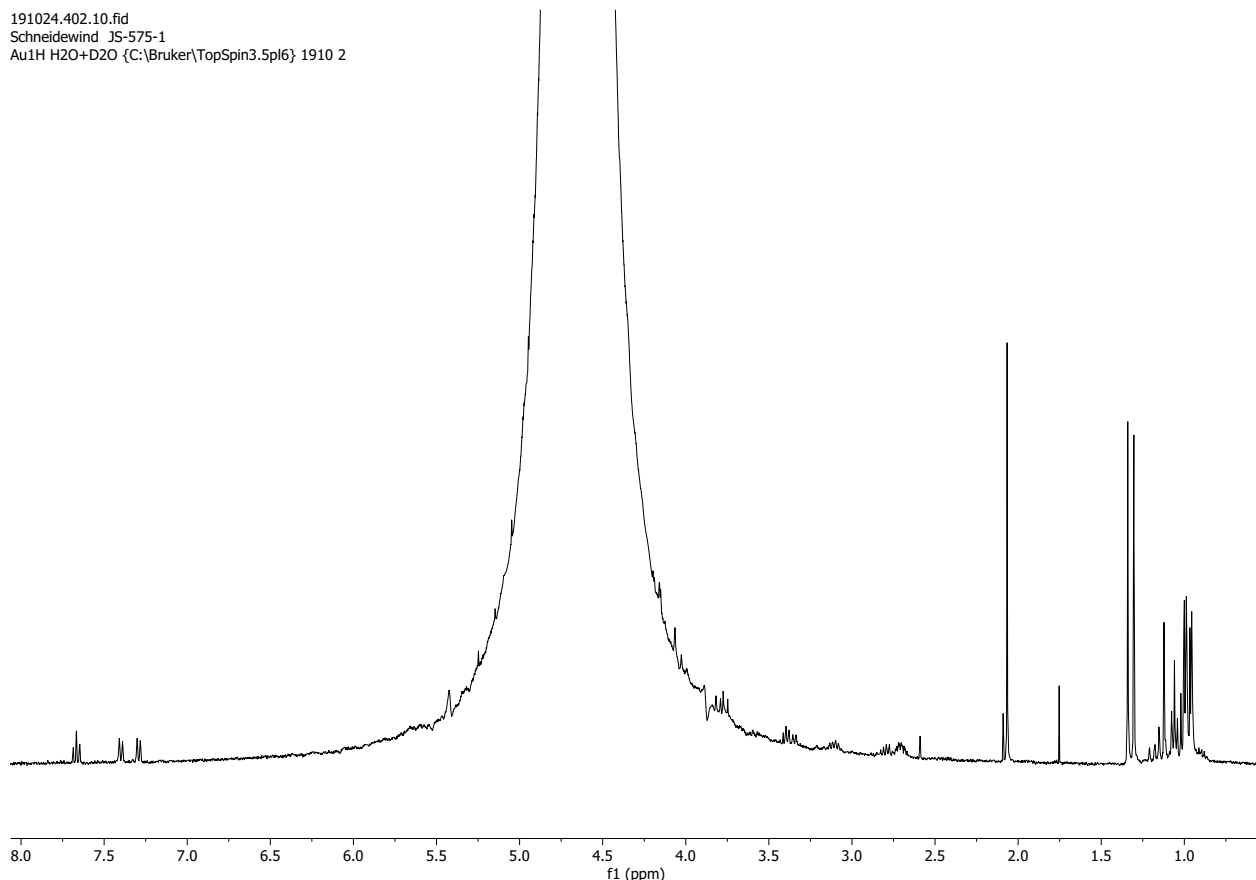


Figure 7.1-6 ¹H NMR spectrum of 1 in H₂O (298 K) synthesized using Ag₂O

191024_402.11.fid
Schnellwind JS-575-1
Au31Pquant H2O+D2O {C:\Bruker\TopSpin3.5pl6} 1910 2

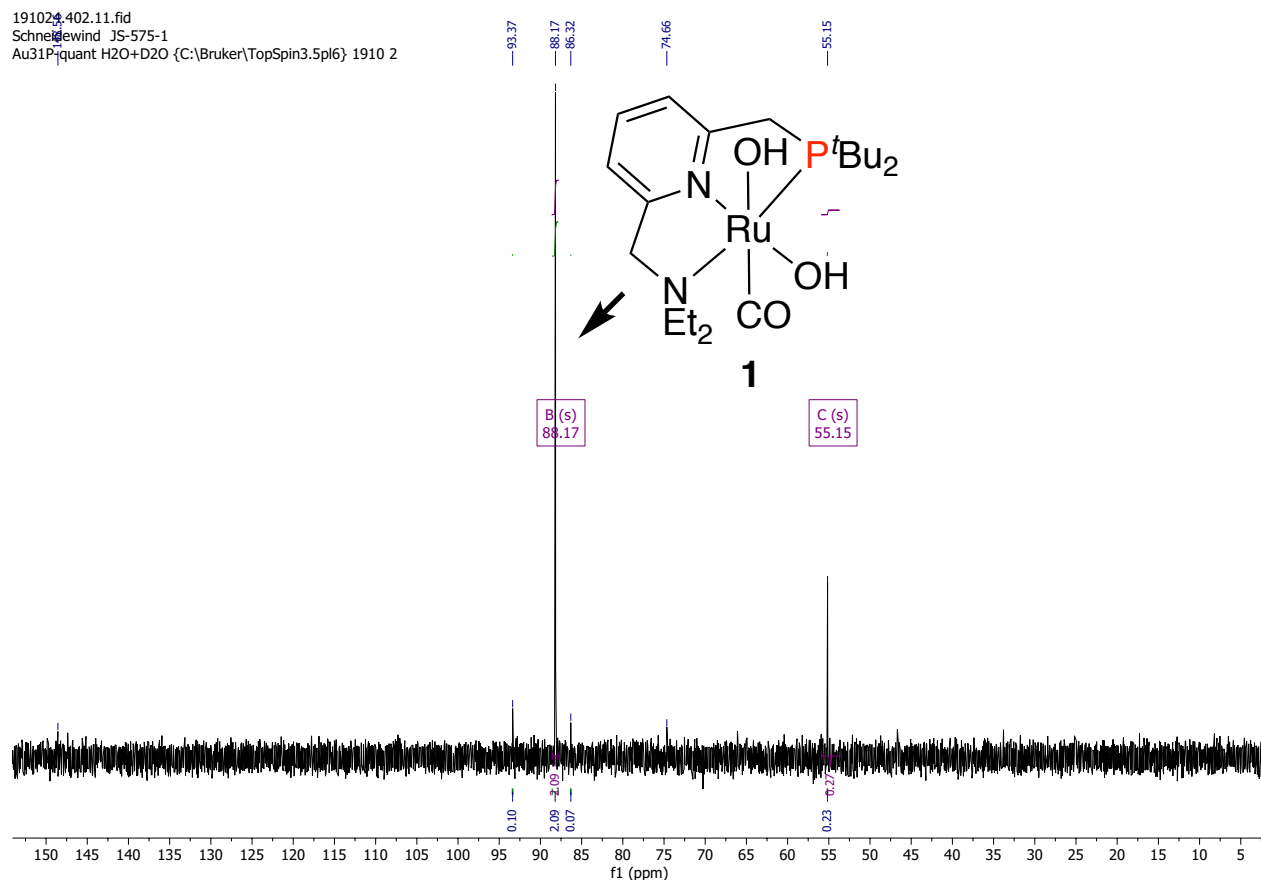


Figure 7.1-7 ${}^{31}\text{P}\{{}^1\text{H}\}$ NMR spectrum of **1** in H_2O (298 K) synthesized using Ag_2O

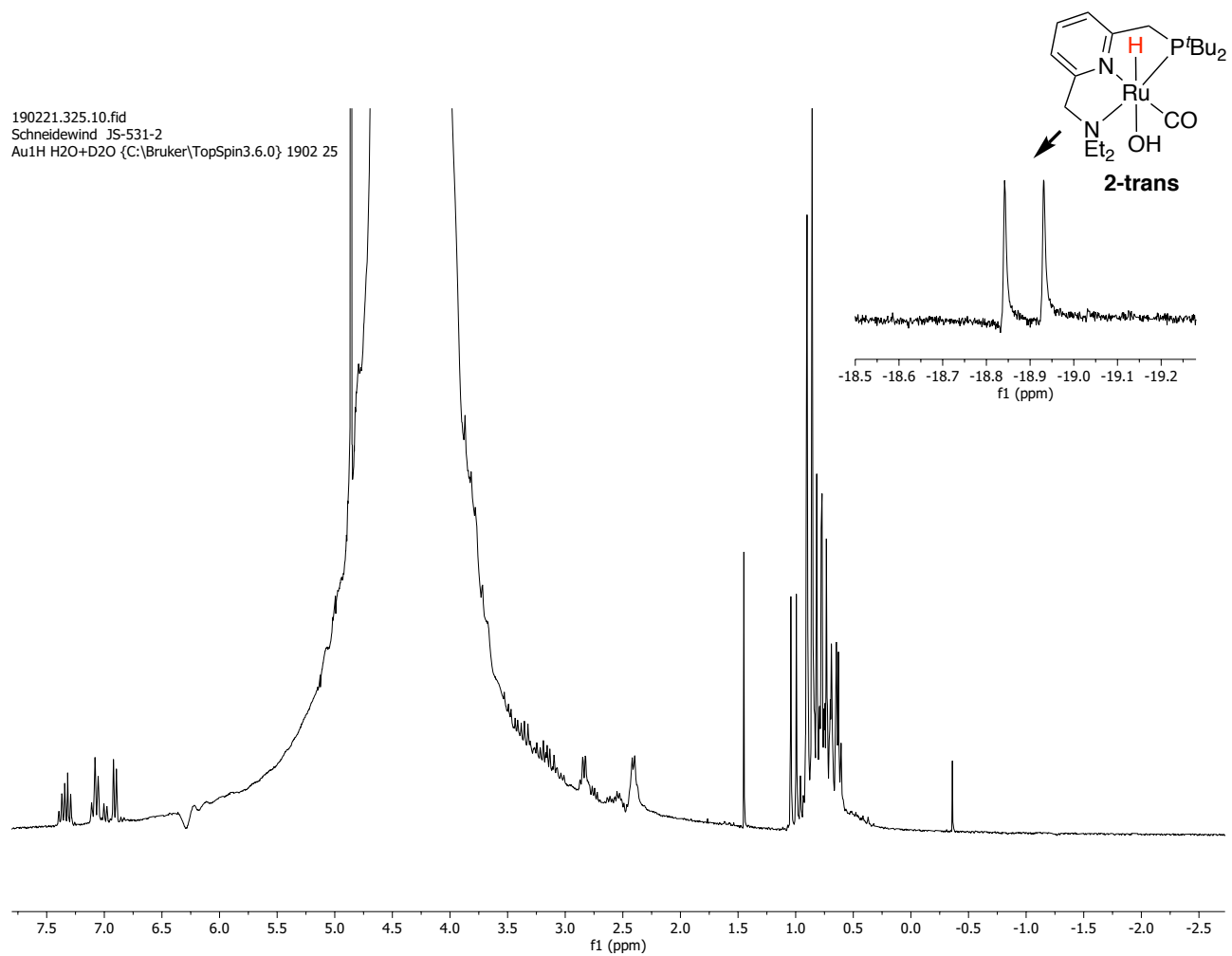


Figure 7.1-8 ^1H NMR of **2-trans** in H_2O (298 K) after three days of reflux, displaying formation of **1** (inlet showing hydride peak of residual **2-trans**)

190221.325.11.fid
Schneidewind JS-53123
Au31P-quant H₂O+D₂O {C:\Bruker\TopSpin3.6.0} 1902 25

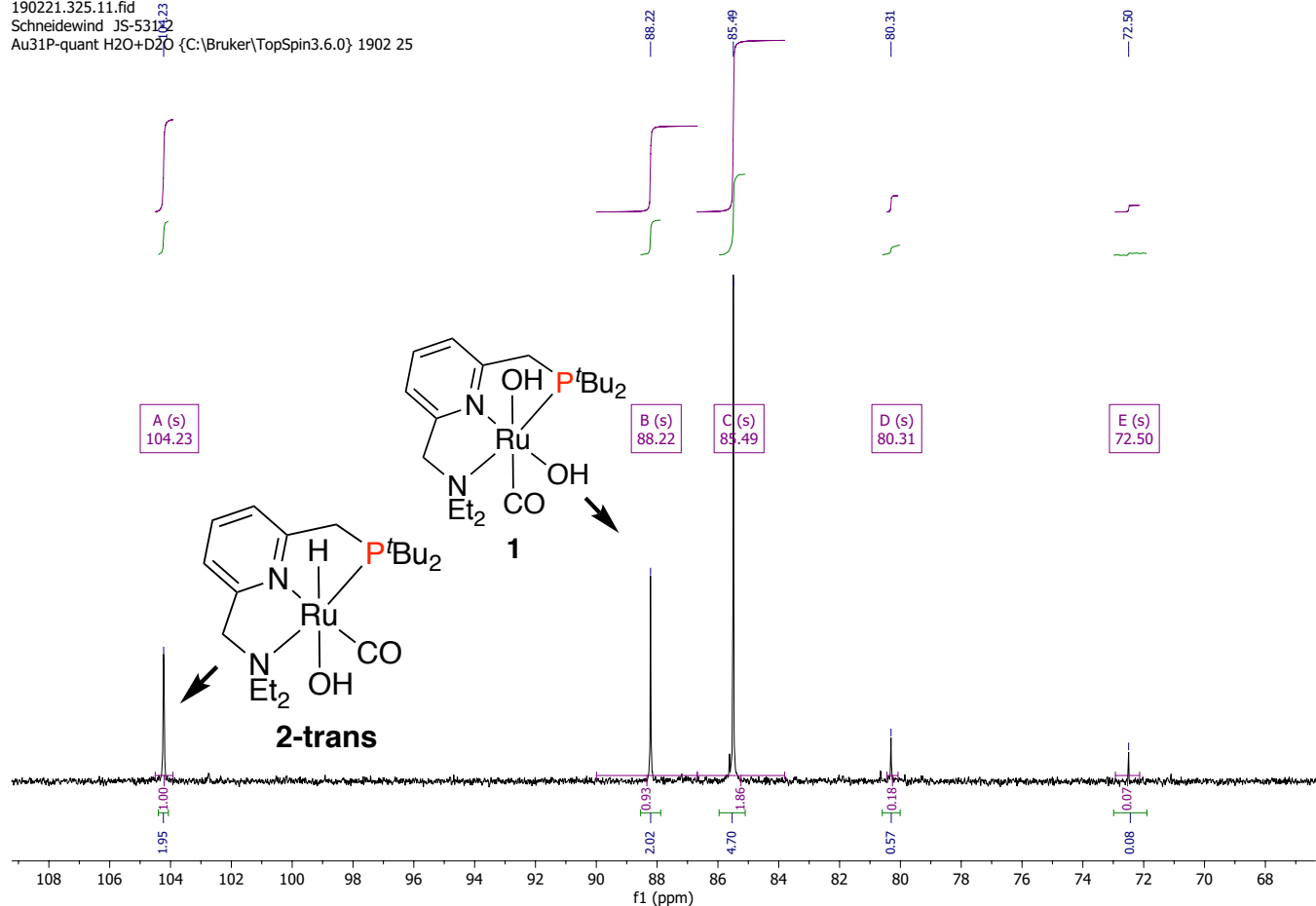


Figure 7.1-9 ³¹P{¹H} NMR of 2-trans in H₂O (298 K) after three days of reflux, displaying formation of 1

7.2 Characterization of 2-trans

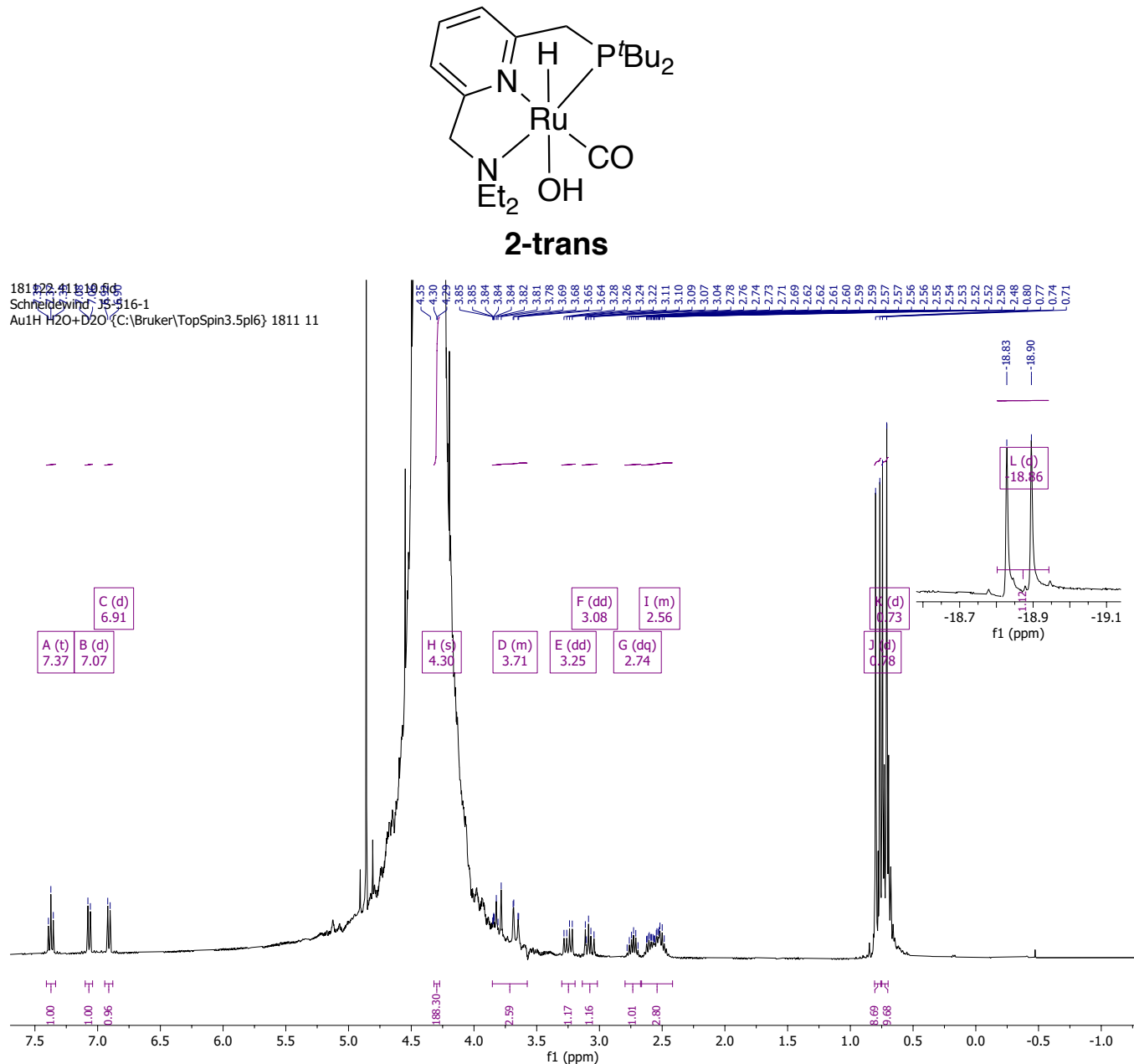


Figure 7.2-1 ^1H NMR spectrum of 2-trans in H_2O (298 K)
(inlet showing hydride peak)

181122.411.11.fid
Schneidewind JS-516-1
Au31P-quant H₂O+D₂O {C:\Bruker\TopSpin3.5pl6} 1811 11

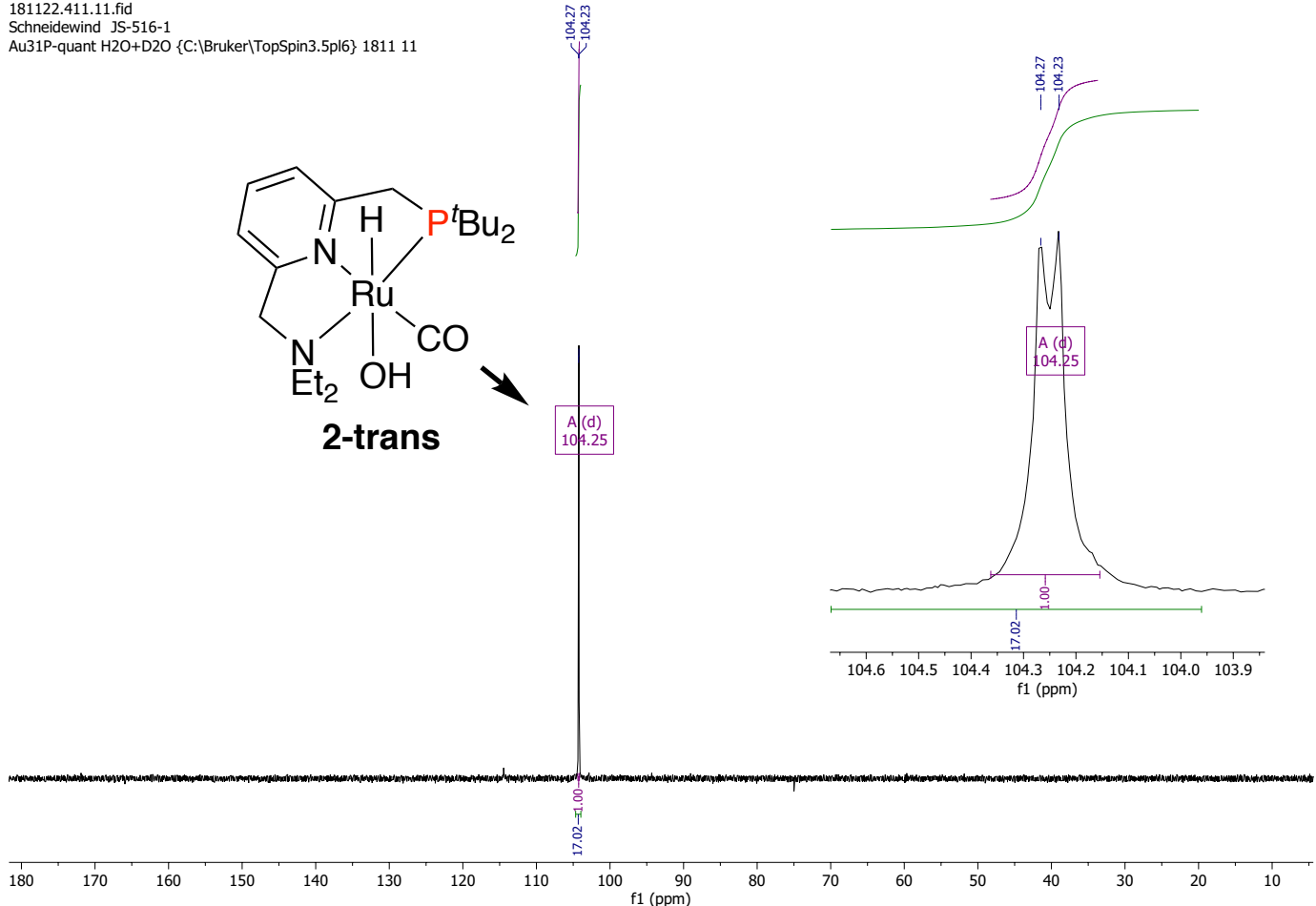


Figure 7.2-2 $^{31}\text{P}\{^1\text{H}\}$ NMR spectrum of 2-trans in H_2O (298 K)
(inlet shows splitting of ^{31}P signal due to coupling to hydride ligand, which is outside of decoupler range)

7.3 Characterization of (p-cymene)RuCl₂(CO)

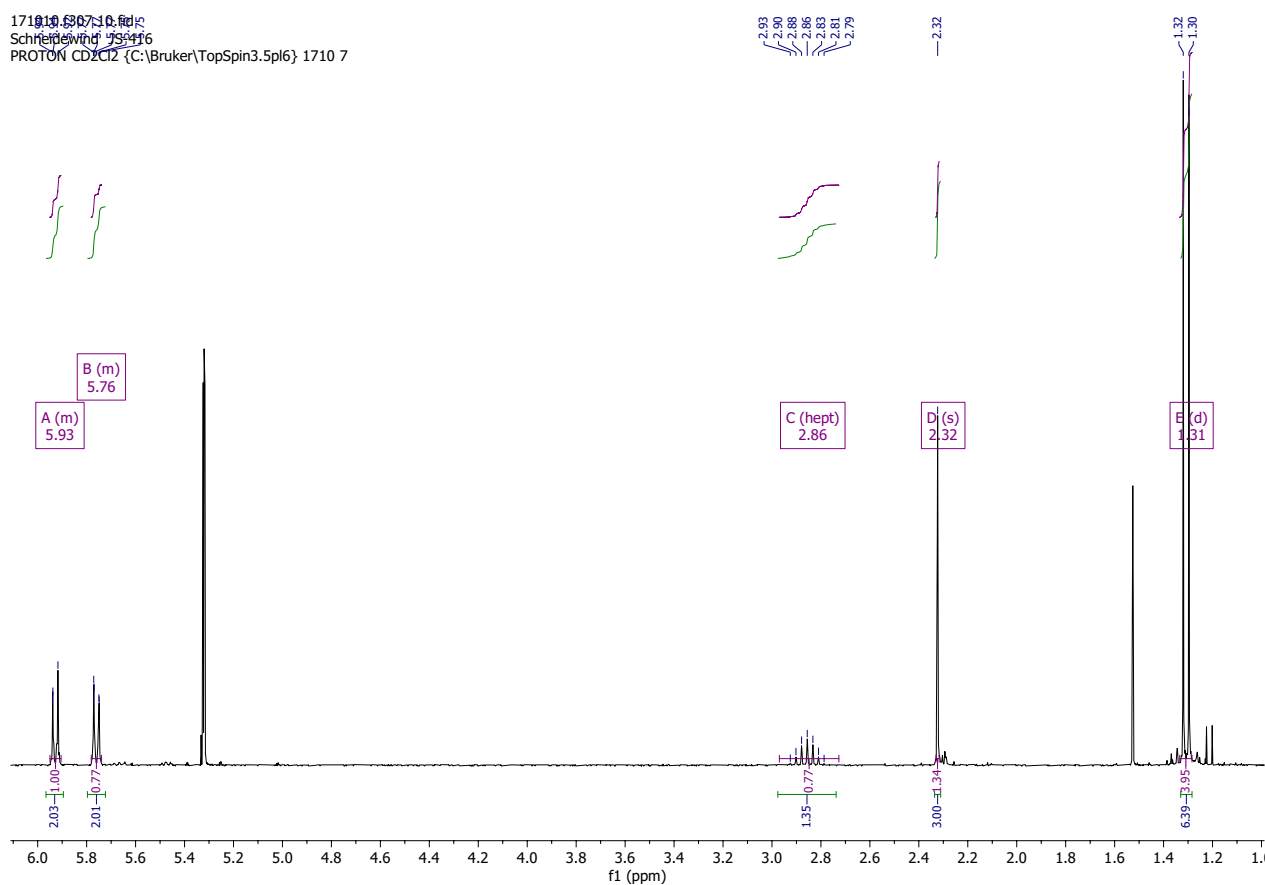
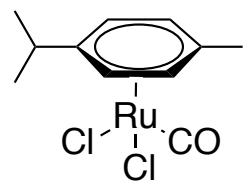


Figure 7.3-1 ^1H NMR spectrum of (p-cymene)RuCl₂(CO) in CD₂Cl₂ (298 K)

7.4 Characterization of (PNN)RuCl₂(CO)

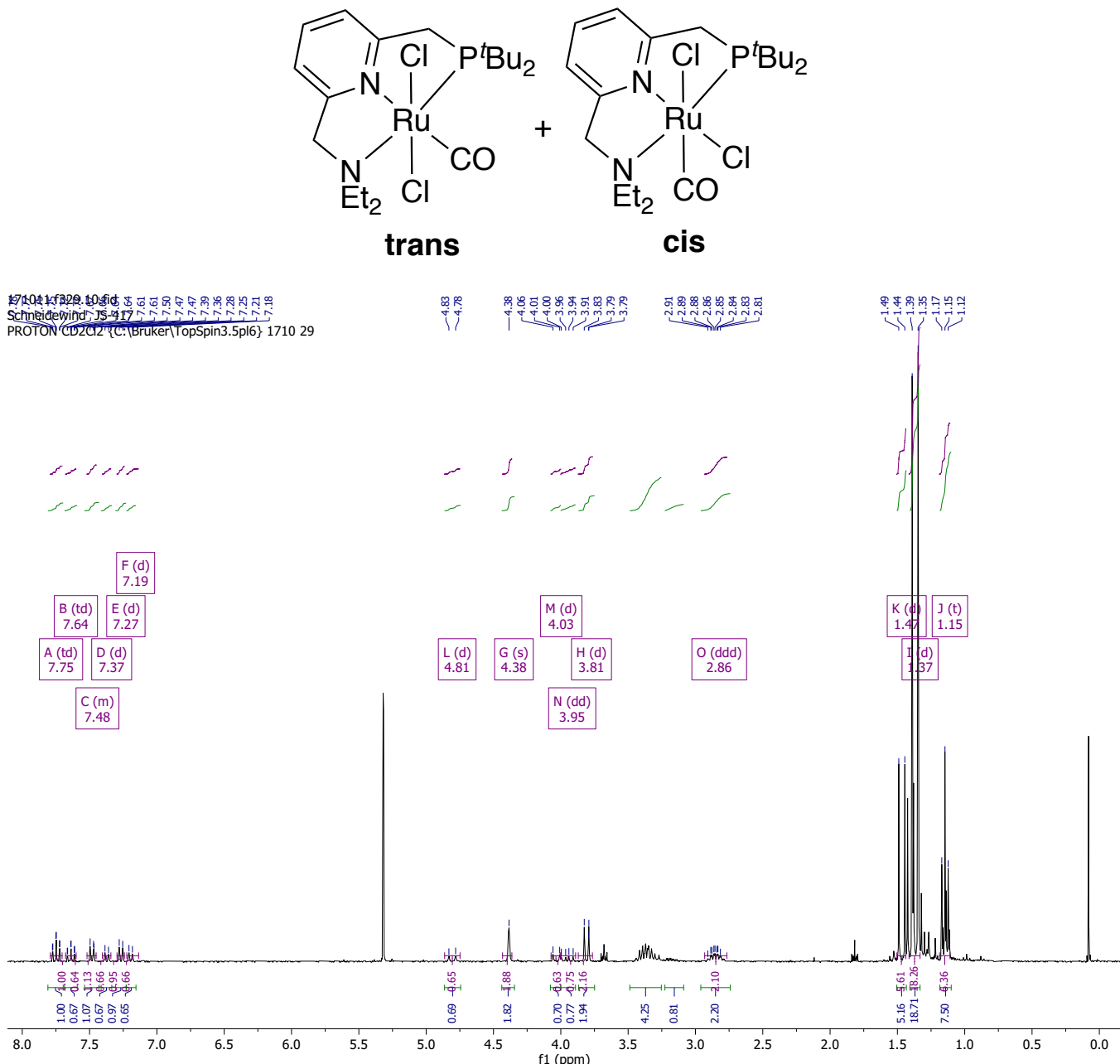


Figure 7.4-1 ¹H NMR spectrum of (PNN)RuCl₂(CO) in CD₂Cl₂ (298 K)
(mixture of cis and trans isomers)

171011.f329.11.fid
Schneidewind JS-417
P31quant CD₂Cl₂ {C:\Bruker\TopSpin3.5pl6} 1710 29

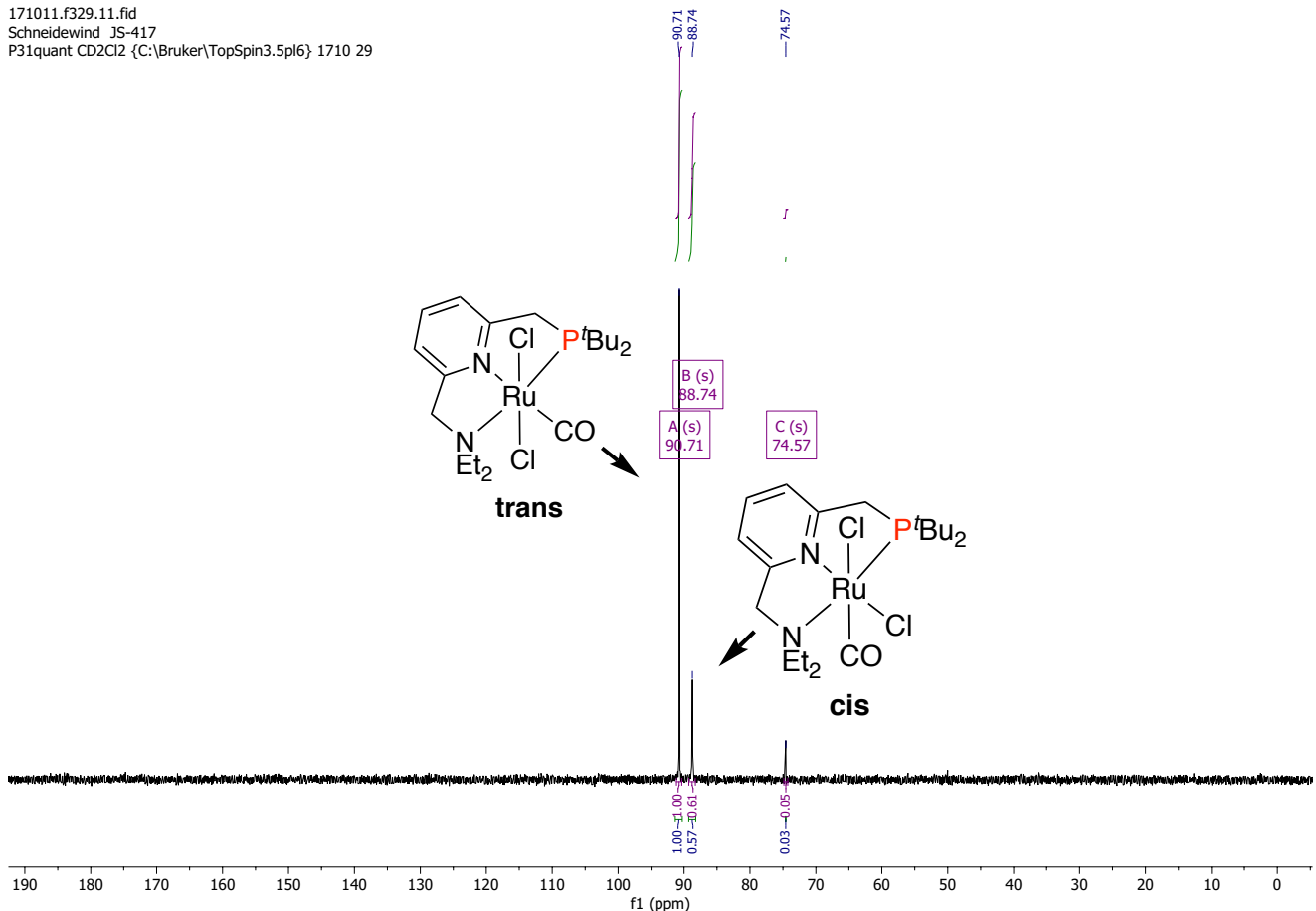


Figure 7.4-2 ³¹P{¹H} NMR spectrum of (PNN)RuCl₂(CO) in CD₂Cl₂ (298 K)
(mixture of cis and trans isomers)

7.5 Data for Irradiated Samples

200207.f331.10.fid
Schneidewind JS-594-1-7
PROTON H2O+D2O {C:\Bruker\TopSpin3.6.0} 2002 31

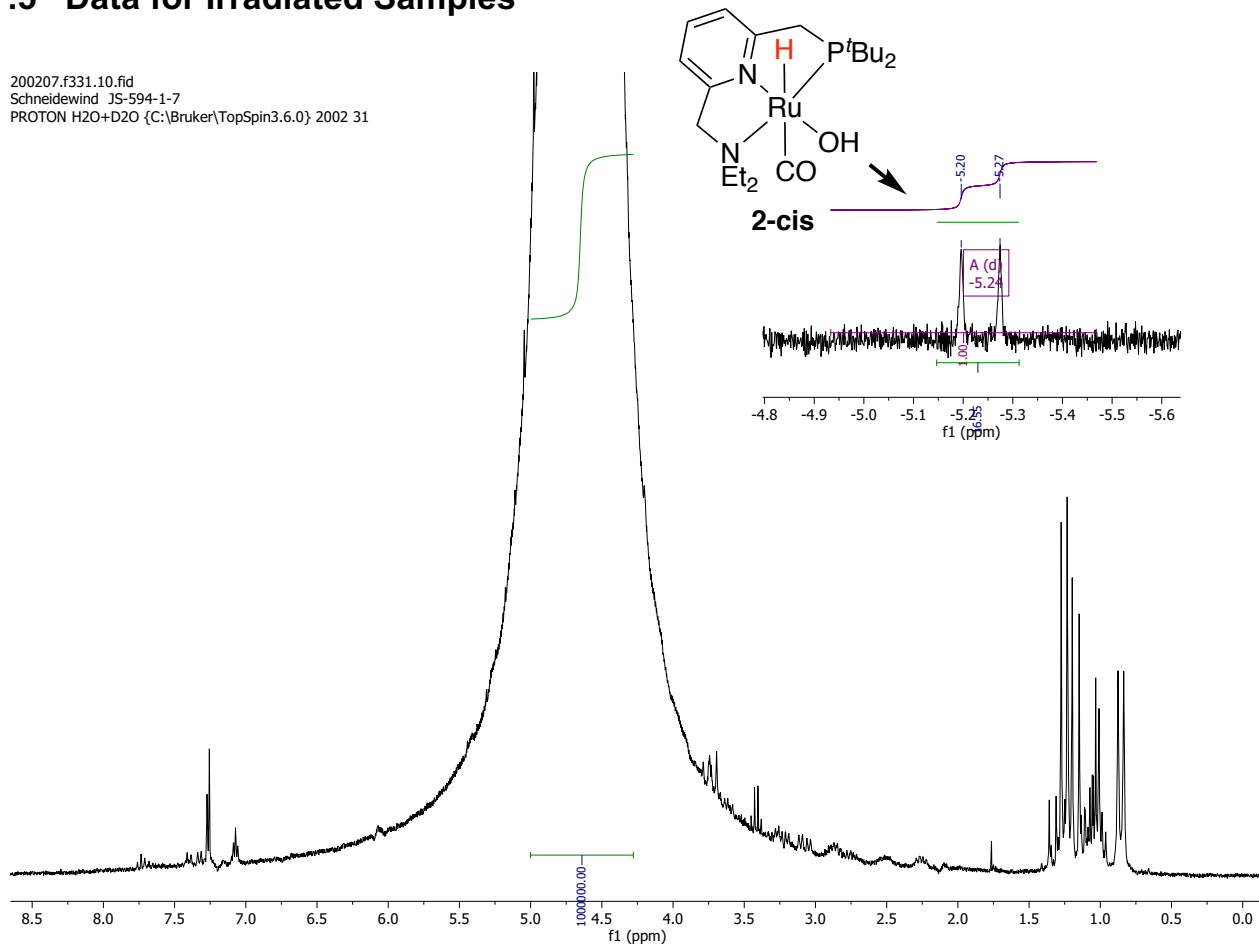


Figure 7.5-1 ${}^1\text{H}$ NMR spectrum of 1 (in H_2O , 298 K) after irradiation with QTH light source for 46h (irradiation without longpass filters, inlet showing hydride peak for 2-cis)

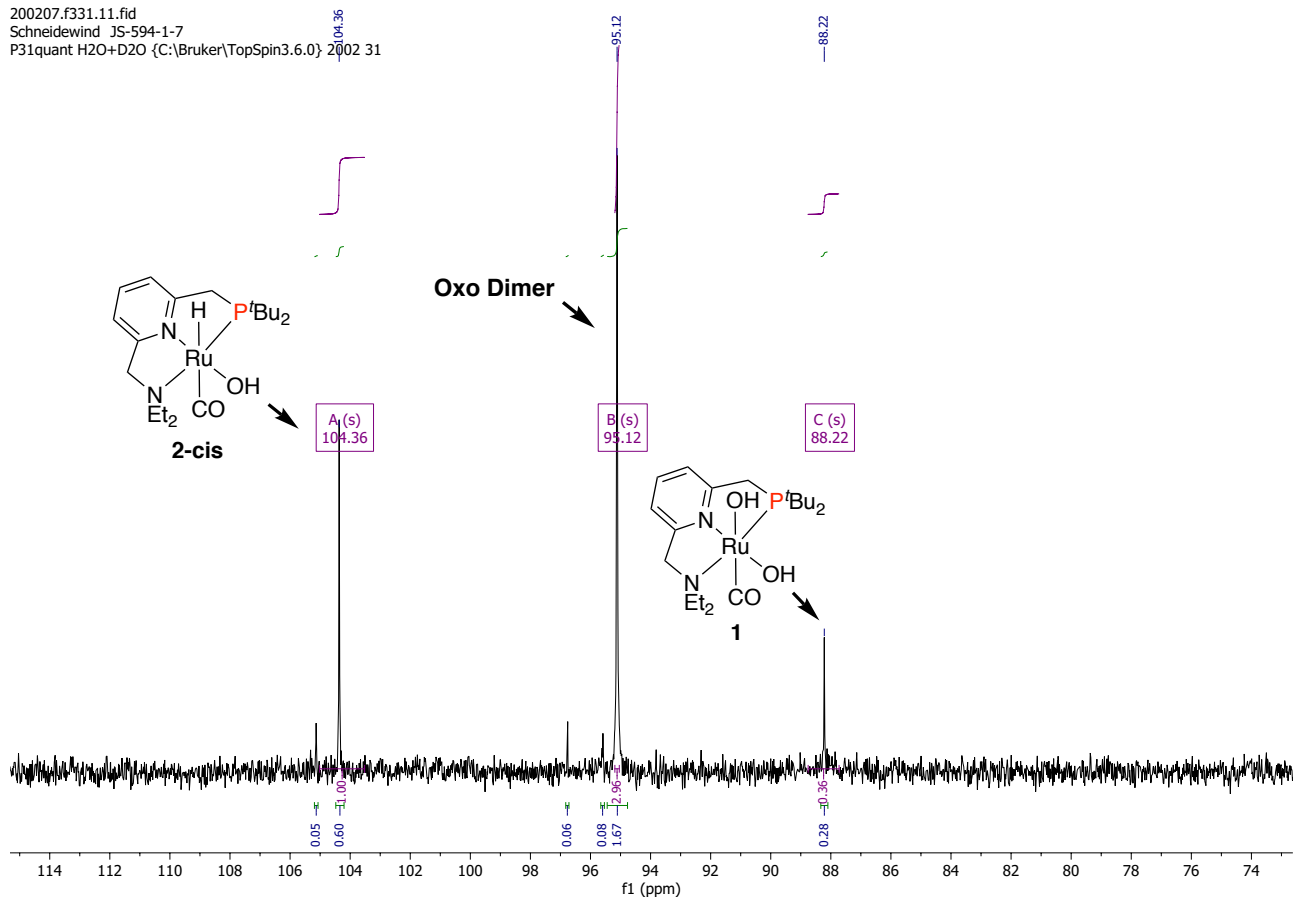
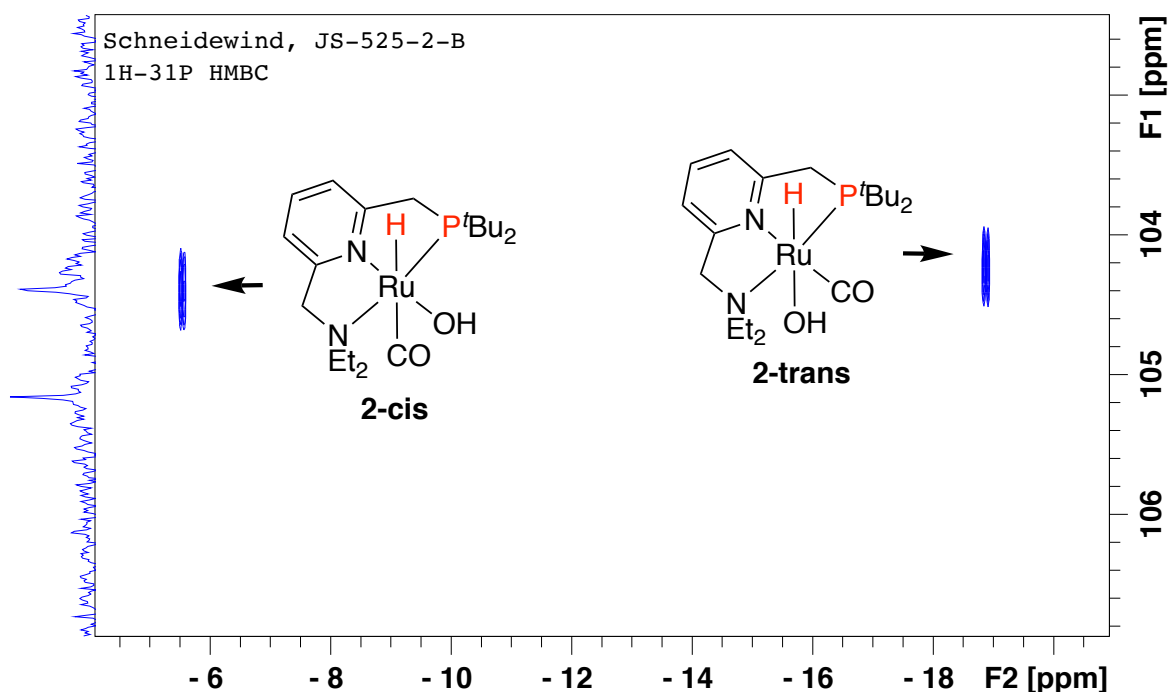
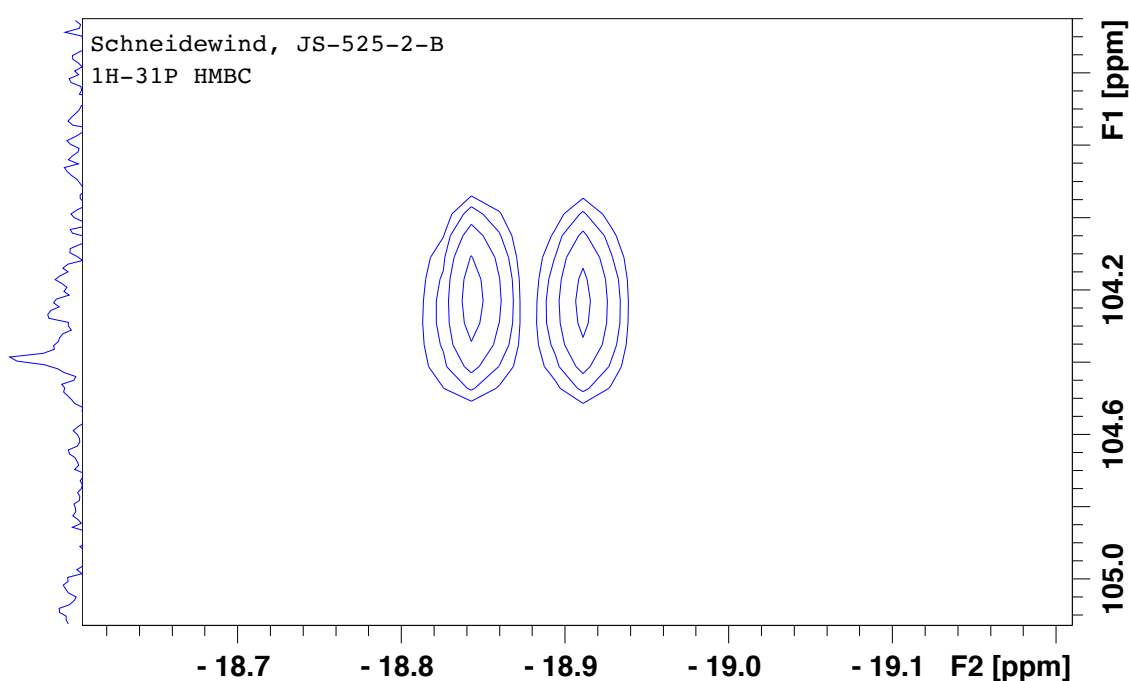


Figure 7.5-2 $^{31}\text{P}\{\text{H}\}$ NMR spectrum of 1 (in H_2O , 298 K) after irradiation with QTH light source for 46h (irradiation without longpass filters)

190130.40a 4 1 K:\nmr\AV400\data\1901\nmr



190130.40a 4 1 K:\nmr\AV400\data\1901\nmr



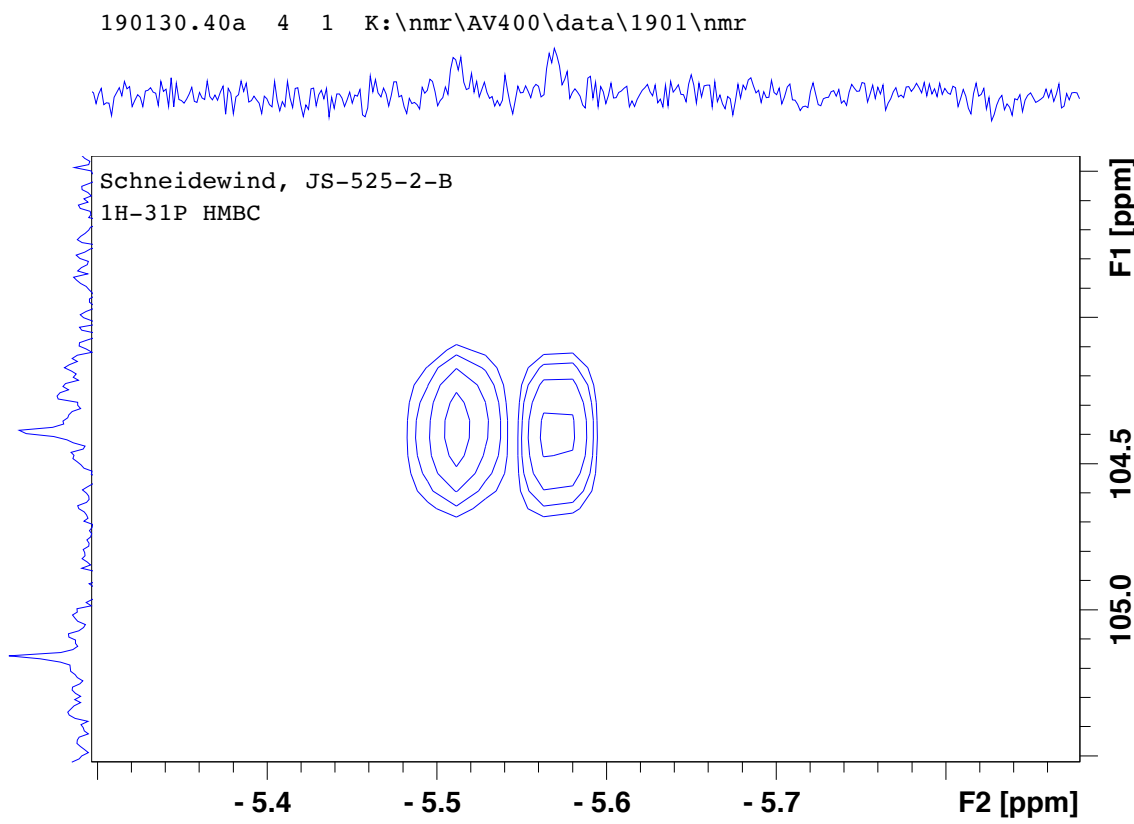


Figure 7.5-3 ^1H - ^{31}P HMBC (hydride region) NMR spectrum of 1 (in H_2O , 298 K) after irradiation
 Top: overview of entire ^1H - ^{31}P spectrum. Middle: Zoom showing coupling of $\delta(^{31}\text{P}) = 104.25 \text{ ppm}$ with $\delta(^1\text{H}) = -18.86 \text{ ppm}$, corresponding to **2-trans**. Bottom: Zoom showing coupling of $\delta(^{31}\text{P}) = 104.36 \text{ ppm}$ with $\delta(^1\text{H}) = -5.24 \text{ ppm}$ corresponding to **2-cis**. Note that **2-trans** is present in this sample since the HMBC measurement was performed five days after irradiation, allowing for partial isomerization of **2-cis** to **2-trans**.

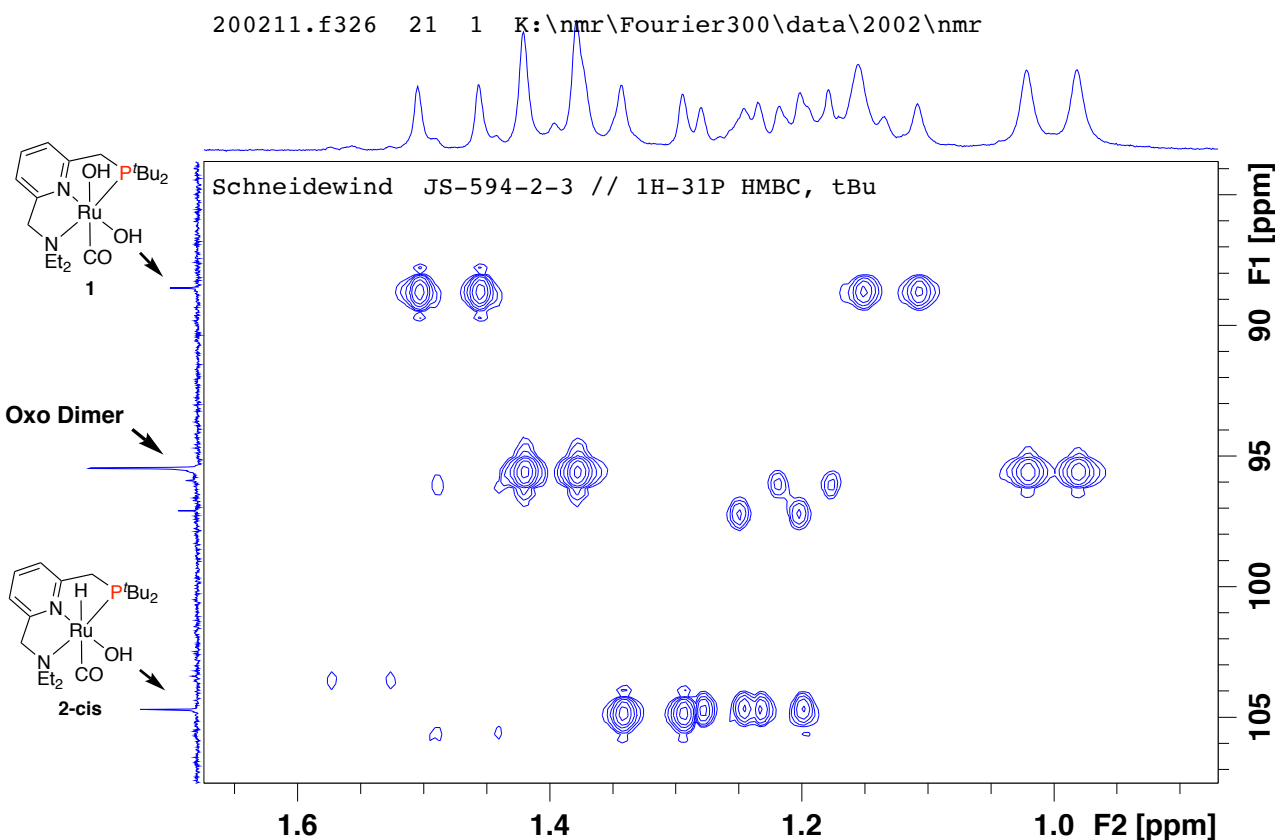


Figure 7.5-4 ^1H - ^{31}P HMBC (aliphatic region) NMR spectrum of **1** (in H_2O , 298 K) after irradiation

Note that this spectrum was measured directly after irradiation hence no **2-trans** is present. The $\delta(^{31}\text{P}) = 95.12$ ppm signal couples with two doublets at $\delta(^1\text{H}) = 1.4$ ppm and $\delta(^1\text{H}) = 1.0$, which correspond to the two tBu groups of the PNN ligand. This shows that the tBu groups in this species are not equivalent and hence this species has no symmetry.

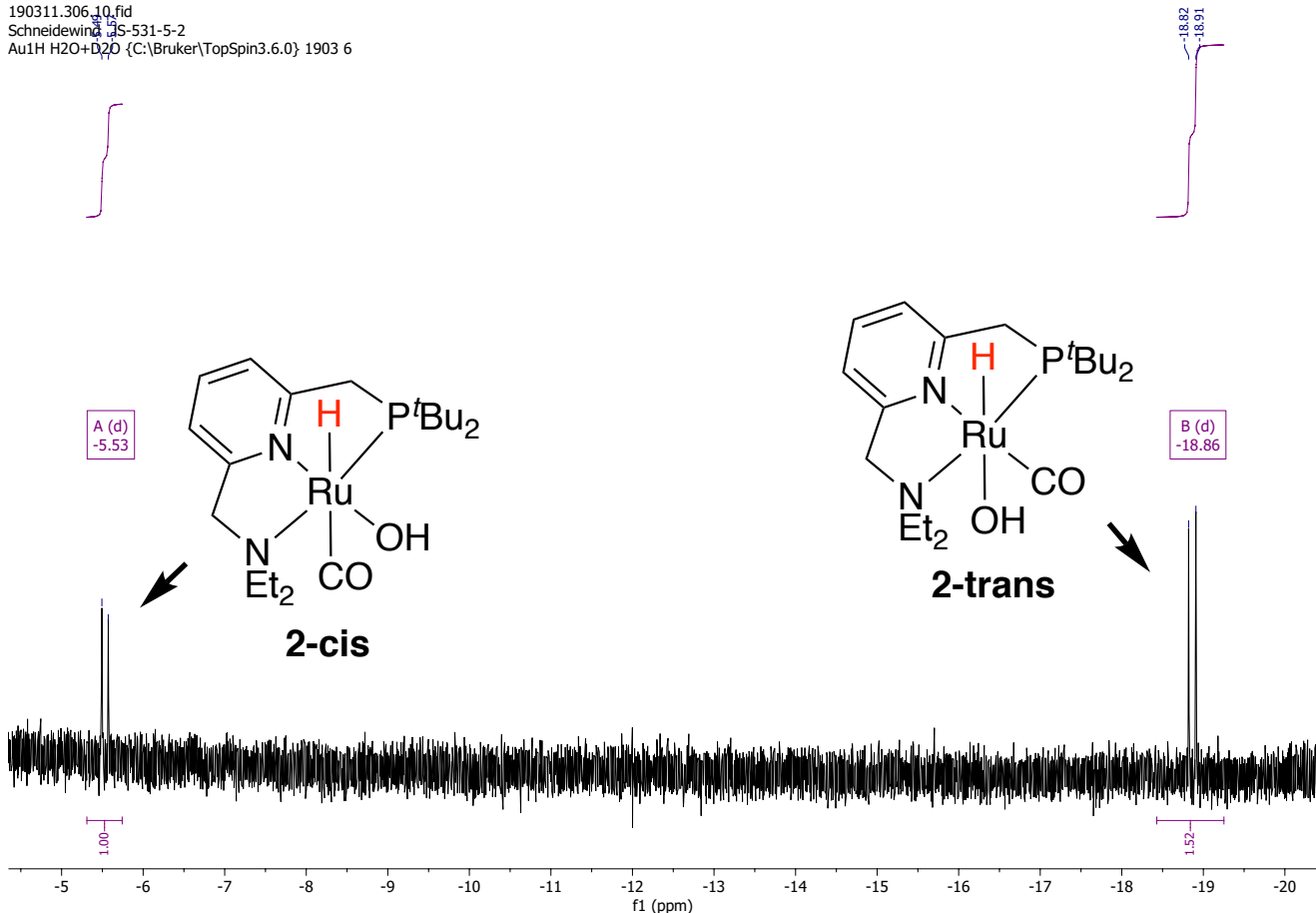


Figure 7.5-5 ${}^1\text{H}$ NMR spectrum of **2-trans** (in H_2O , 298 K) after irradiation (320 – 500 nm, 4h) in presence of O_2

190311.306.11.fid
Schneidewind JS-531-5-2
Au31P-quant H2O+D2O {C:\Bruker\TopSpin3.6.0} 1903 6

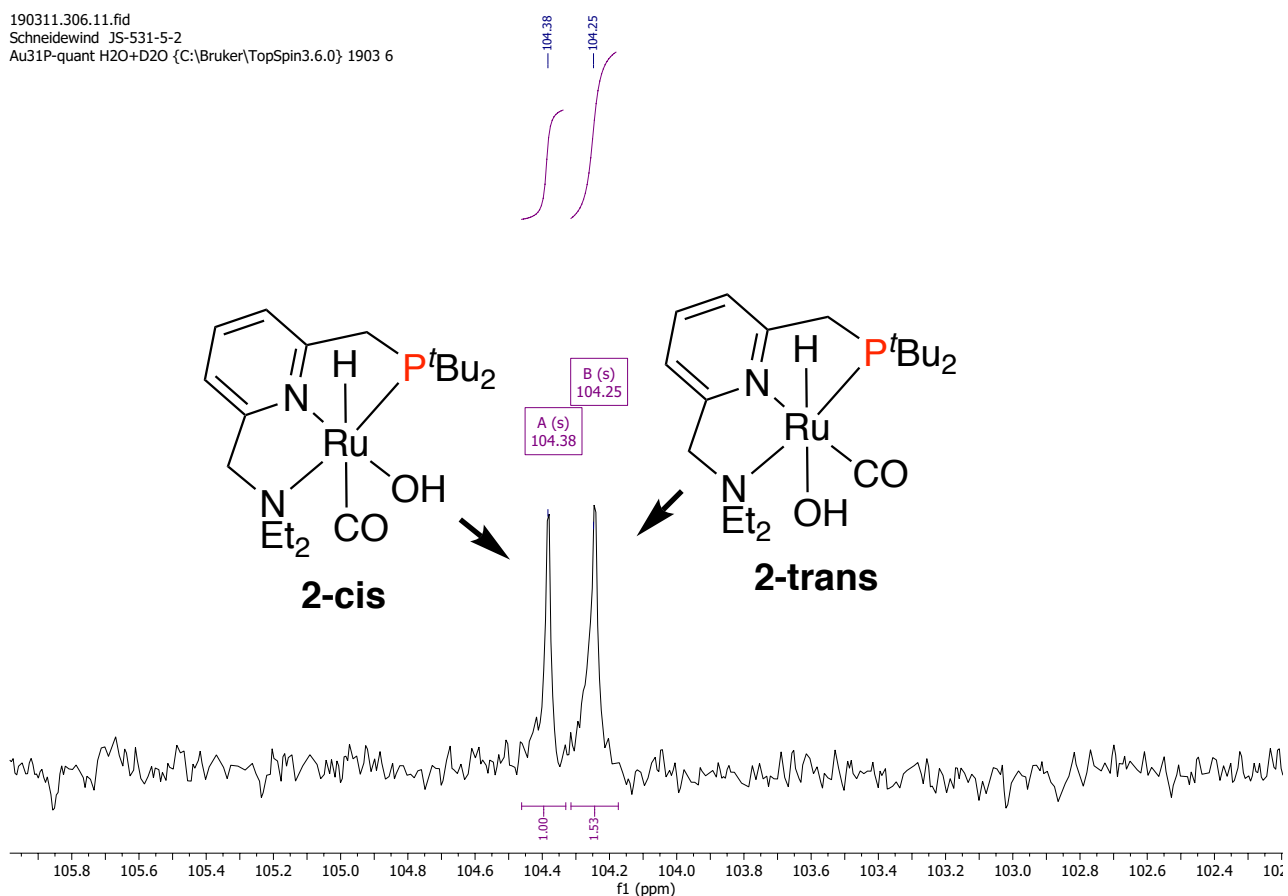


Figure 7.5-6 $^{31}\text{P}\{\text{H}\}$ NMR spectrum of 2-trans (in H_2O , 298 K) after irradiation (320 – 500 nm, 4h) in presence of O_2

200129.326.10.fid
Schneidewind JS-575-2-2
Au1H H2O+D2O {C:\Bruker\TopSpin3.6.0} 2001 26

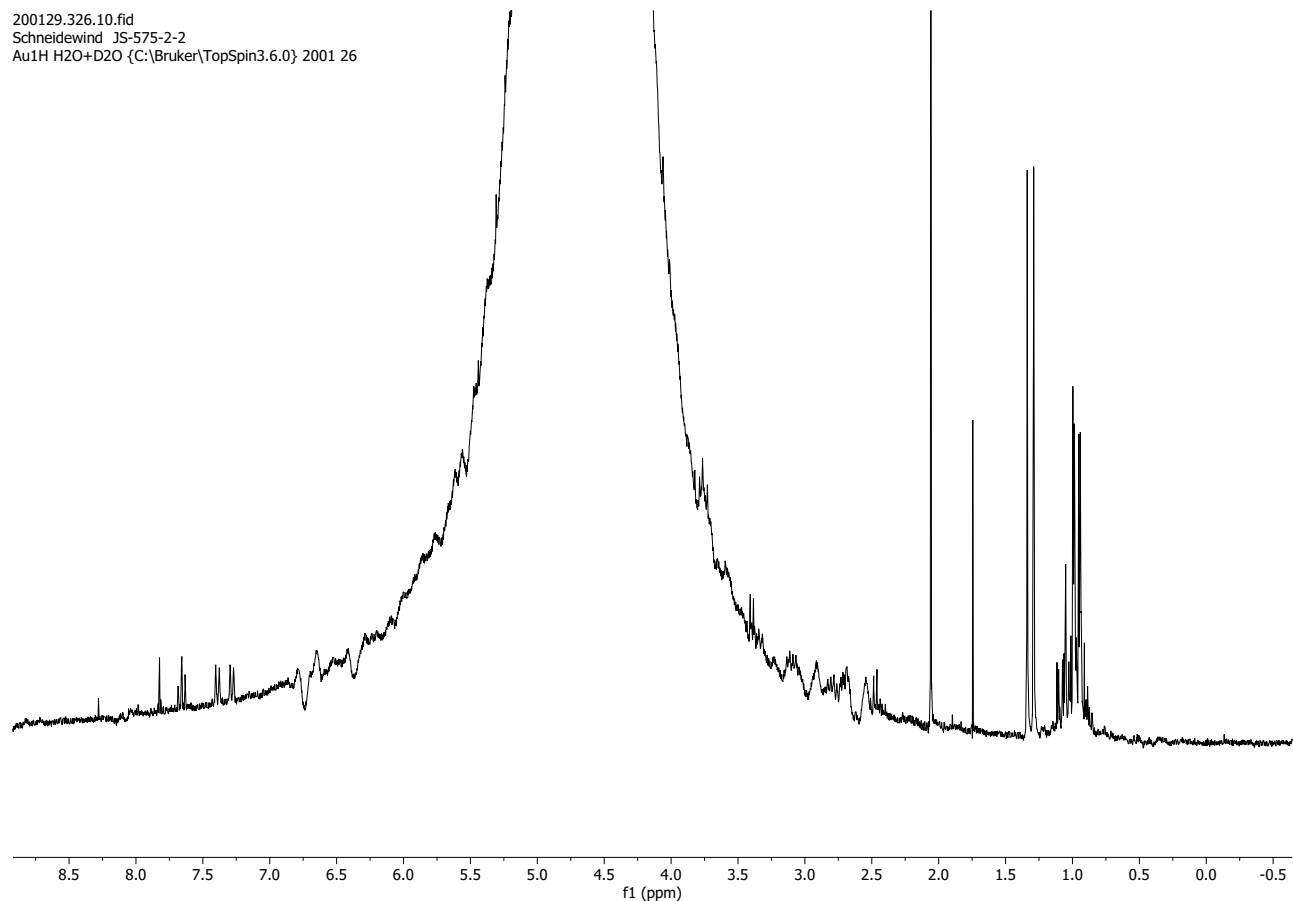


Figure 7.5-7 ¹H NMR spectrum of 1 (in 52 mM KOH aq., 298 K, Ag₂O synthesis route) in air before irradiation.

200129.326.11.fid
Schneidewind JS-575-2-2
Au31P-quant H2O+D2O {C:\Bruker\TopSpin3.6.0} 2001 26

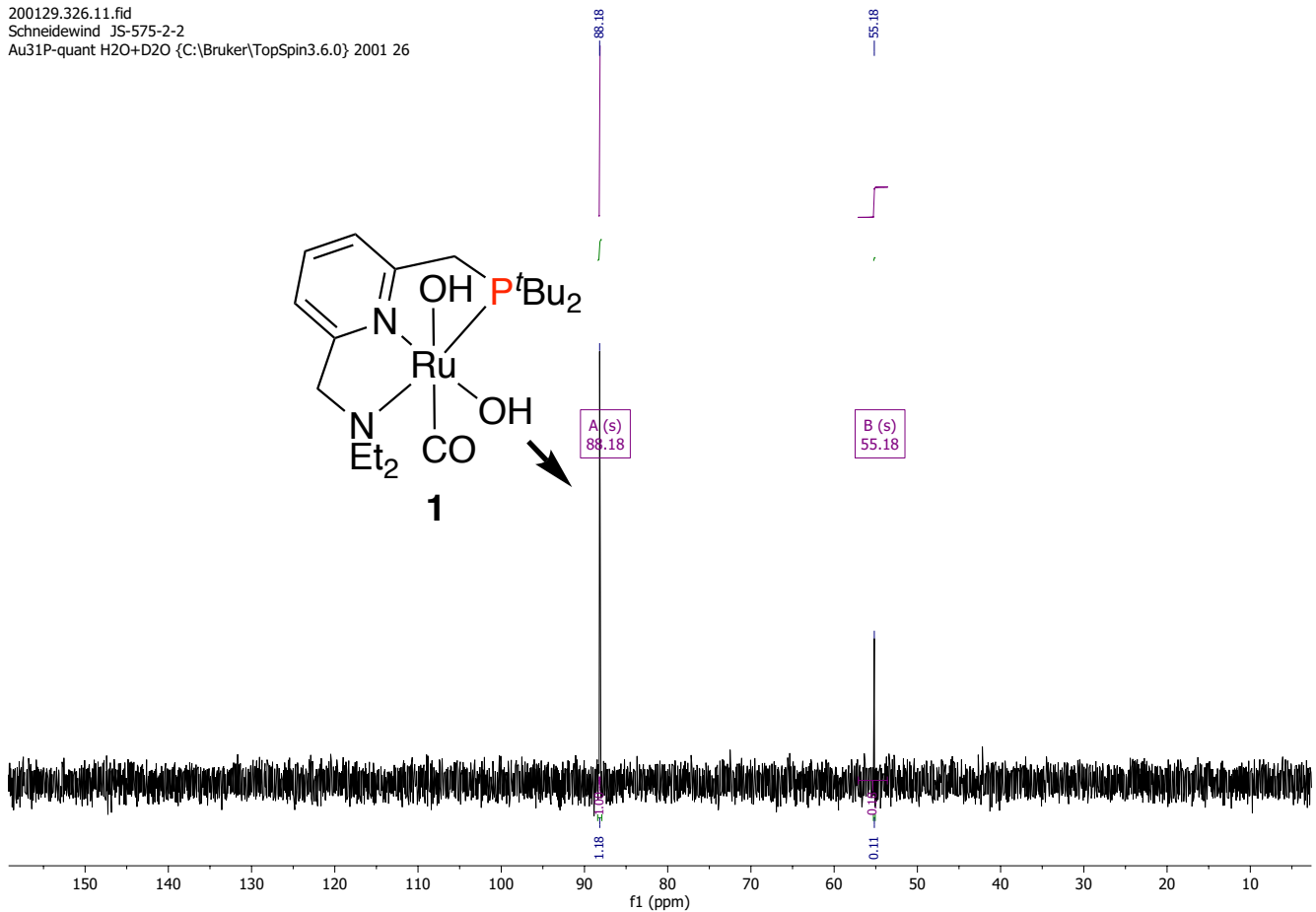


Figure 7.5-8 $^{31}\text{P}\{\text{H}\}$ NMR spectrum of 1 (in 52 mM KOH aq., 298 K, Ag_2O synthesis route) in air before irradiation.

Integrals are relative to H_3PO_4 capillary standard.

200130.301.10.fid
Schneidewind JS-575-2-3
Au1H H2O+D2O {C:\Bruker\TopSpin3.6.0} 2001 1

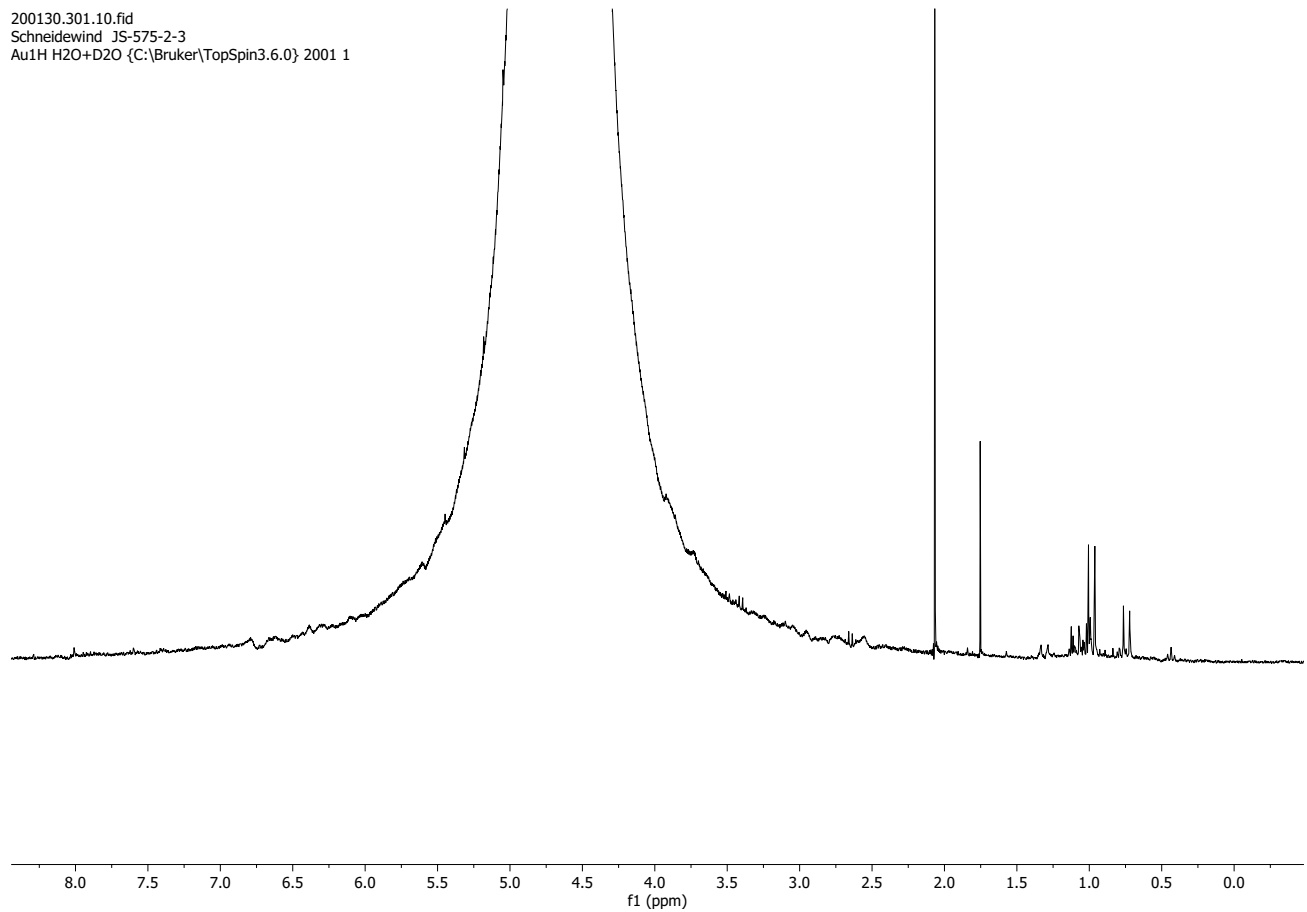


Figure 7.5-9 ¹H NMR spectrum of **1** (in 52 mM KOH aq., 298 K, Ag₂O synthesis route) in air after irradiation (QTH, 16h)

200130.301.11.fid
Schneidewind JS-575-2-3
Au31P-quant H2O+D2O {C:\Bruker\TopSpin3.6.0} 2001 1

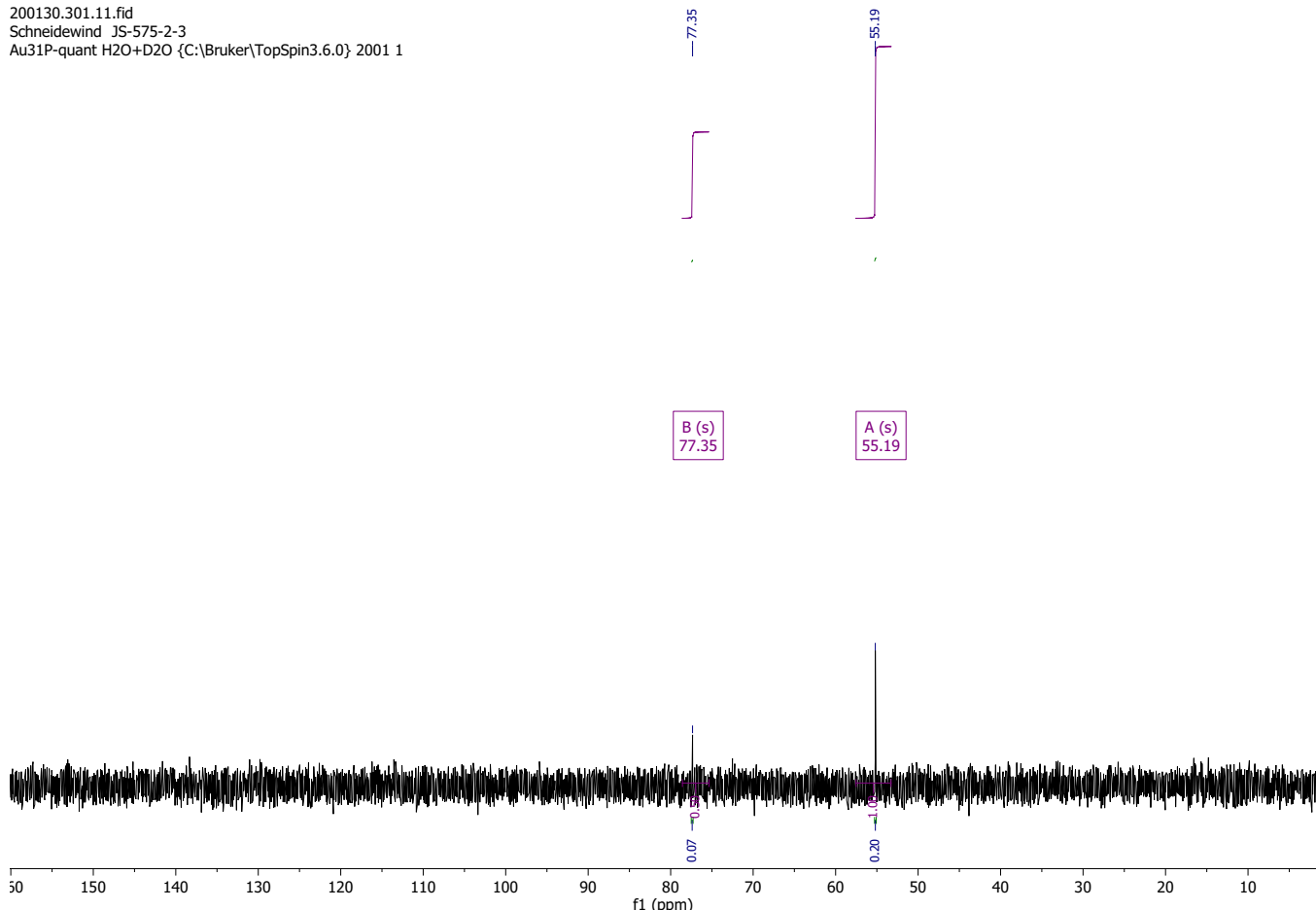


Figure 7.5-10 $^{31}\text{P}\{\text{H}\}$ NMR spectrum of 1 (in 52 mM KOH aq., 298 K, Ag_2O synthesis route) in air after irradiation (QTH, 16h)
Integrals are relative to H_3PO_4 capillary standard.

190219.331.10.fid
Schneidewind JS-531-1
Au1H H2O+D2O {C:\Bruker\TopSpin3.6.0} 1902 31

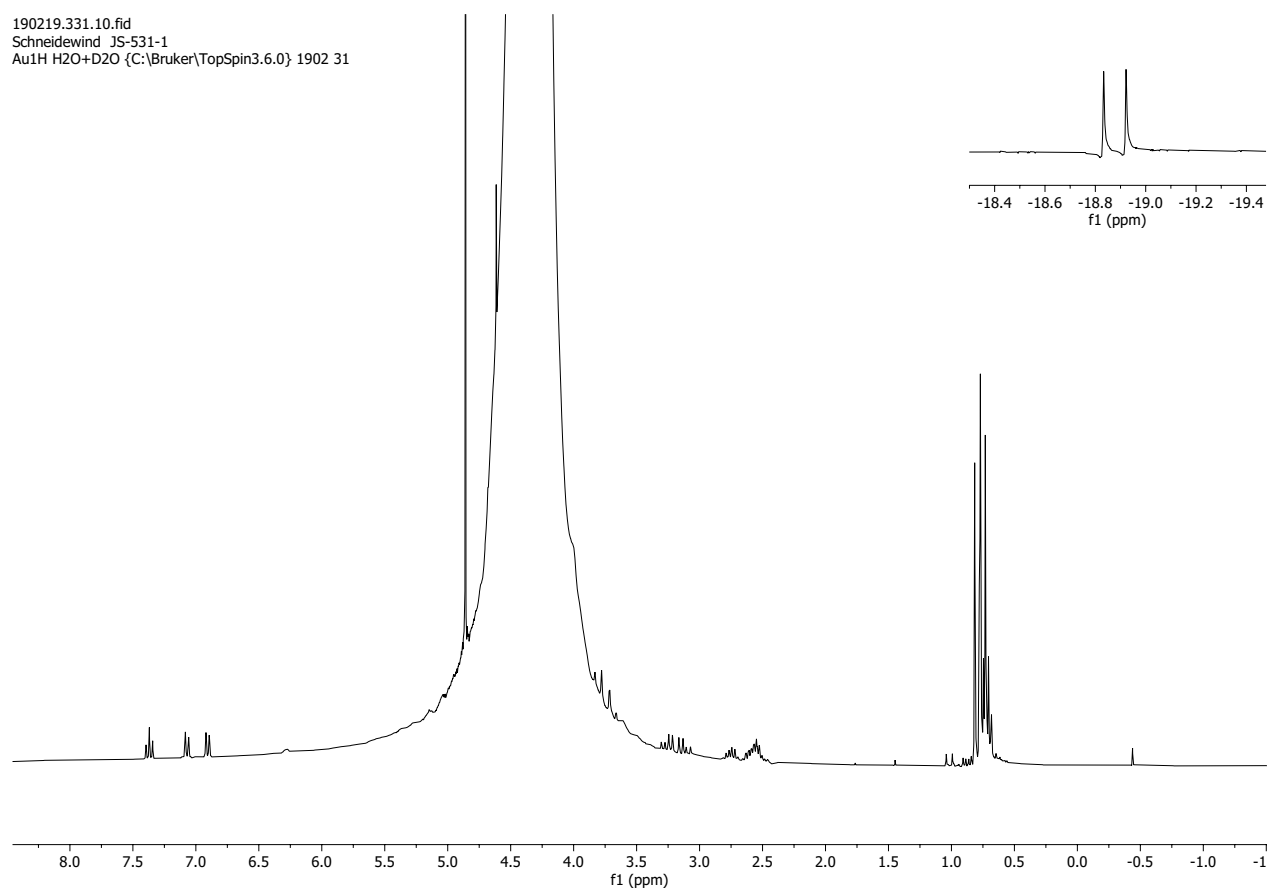
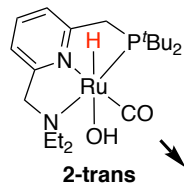


Figure 7.5-11 ^1H NMR spectrum of 2-trans (in H_2O , 298 K) before irradiation, under argon

Sample was previously refluxed for 16 h in H_2O , causing presence of small amounts of 1 and 86 ppm product.
Inset shows hydride peak.

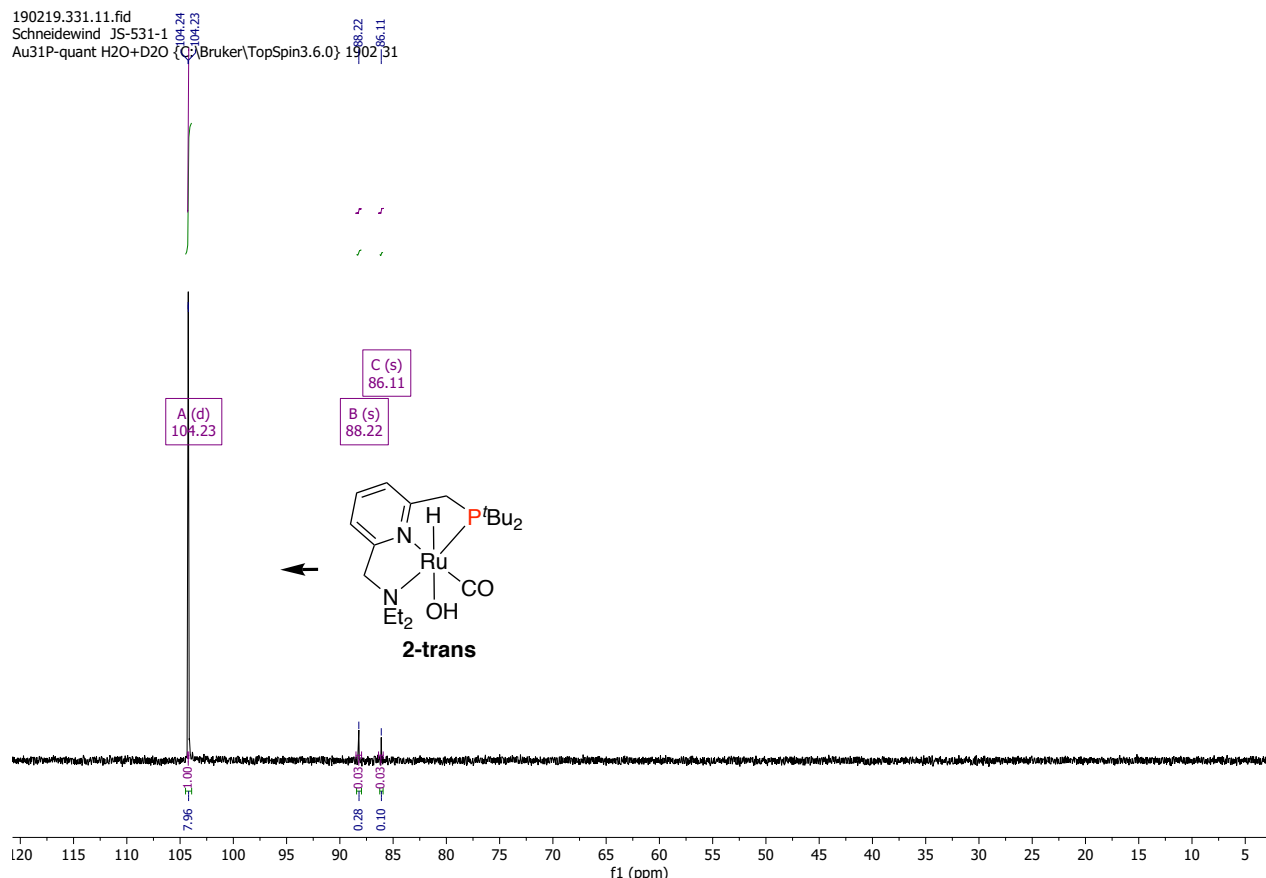


Figure 7.5-12 ^{31}P { ^1H } NMR spectrum of **2-trans** (in H_2O , 298 K) before irradiation, under argon

Sample was previously refluxed for 16 h in H_2O , causing presence of small amounts of **1** and 86 ppm product. Integrals are relative to H_3PO_4 standard.

190221.307.10.fid
Schneidewind JS-531-1-3
Au1H H₂O+D₂O {C:\Bruker\TopSpin3.6.0} 1902 7

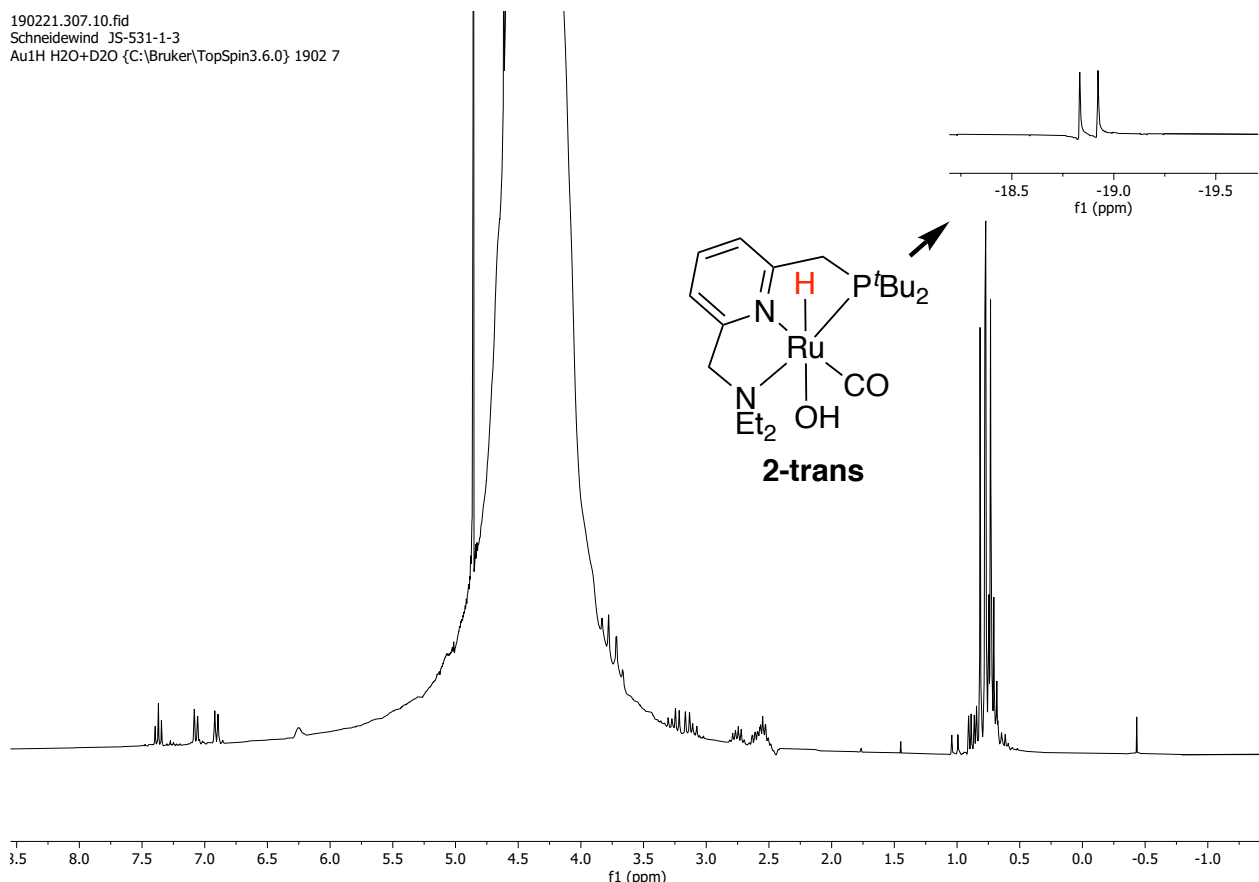


Figure 7.5-13 ¹H NMR spectrum of 2-trans (in H₂O, 298 K) after irradiation (Hg light source, 320 – 500 nm, 21 h), under argon

Sample was previously refluxed for 16 h in H₂O, causing presence of small amounts of 1 and 86 ppm product. Inlet shows hydride peak.

190221.307.11.fid
Schneidewind JS-531-1-30423
Au31P-quant H2O+D2O {C}\Bruker\TopSpin3.6.0} 190221

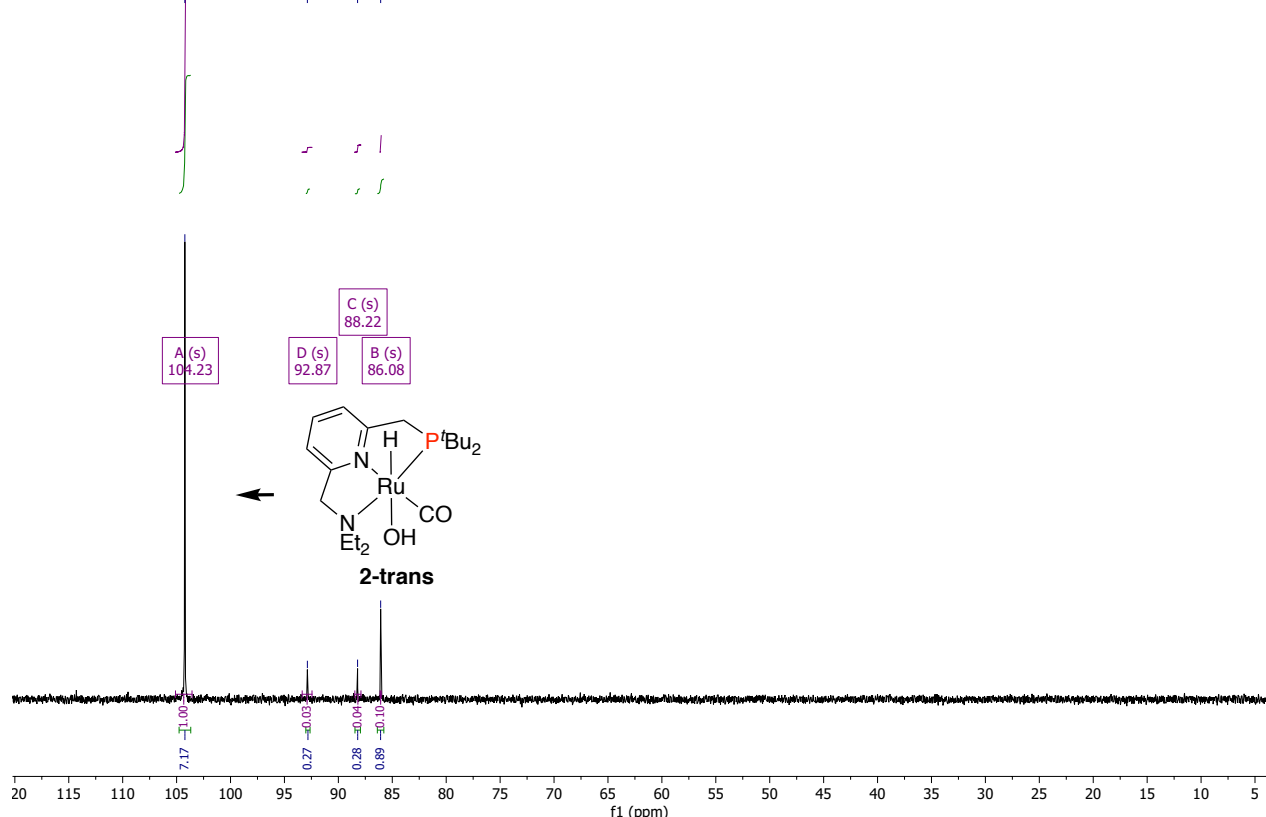


Figure 7.5-14 $^{31}\text{P}\{\text{H}\}$ NMR spectrum of 2-trans (in H_2O , 298 K) after irradiation (Hg light source, 320 – 500 nm, 21 h), under argon

Sample was previously refluxed for 16 h in H_2O , causing presence of small amounts of 1 and 86 ppm product. Integrals are relative to H_3PO_4 standard.

7.6 Isomerization Reactions in the Dark

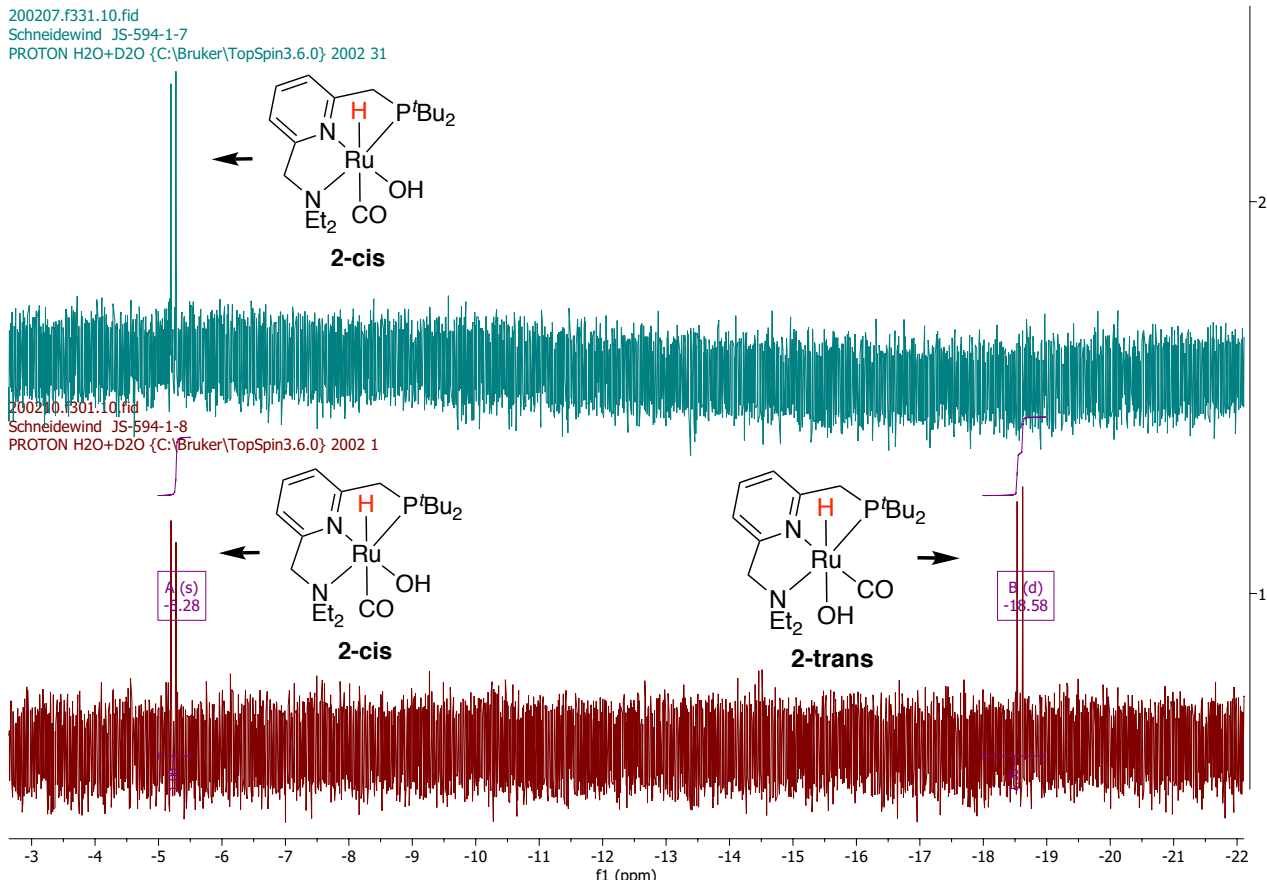


Figure 7.6-1 Stacked ^1H NMR spectra of 1 (in H_2O , 298 K) immediately after irradiation (top, green) and same sample after two more days in the dark (bottom, red)

200210.f301.11.fid
Schneidewind JS-594-1-8
P31quant H2O+D2O {C:\Bruker\TopSpin3.6.0} 2002 1

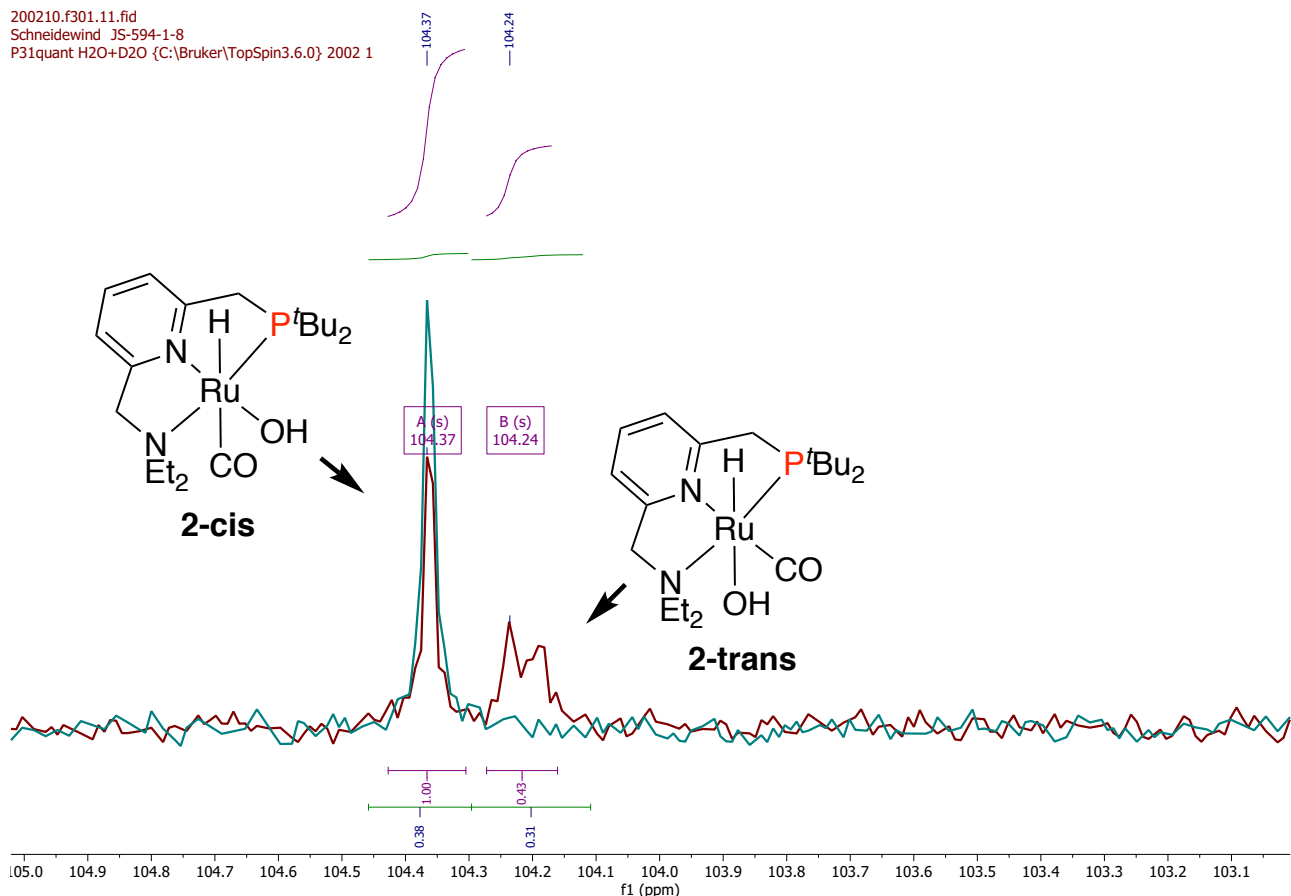
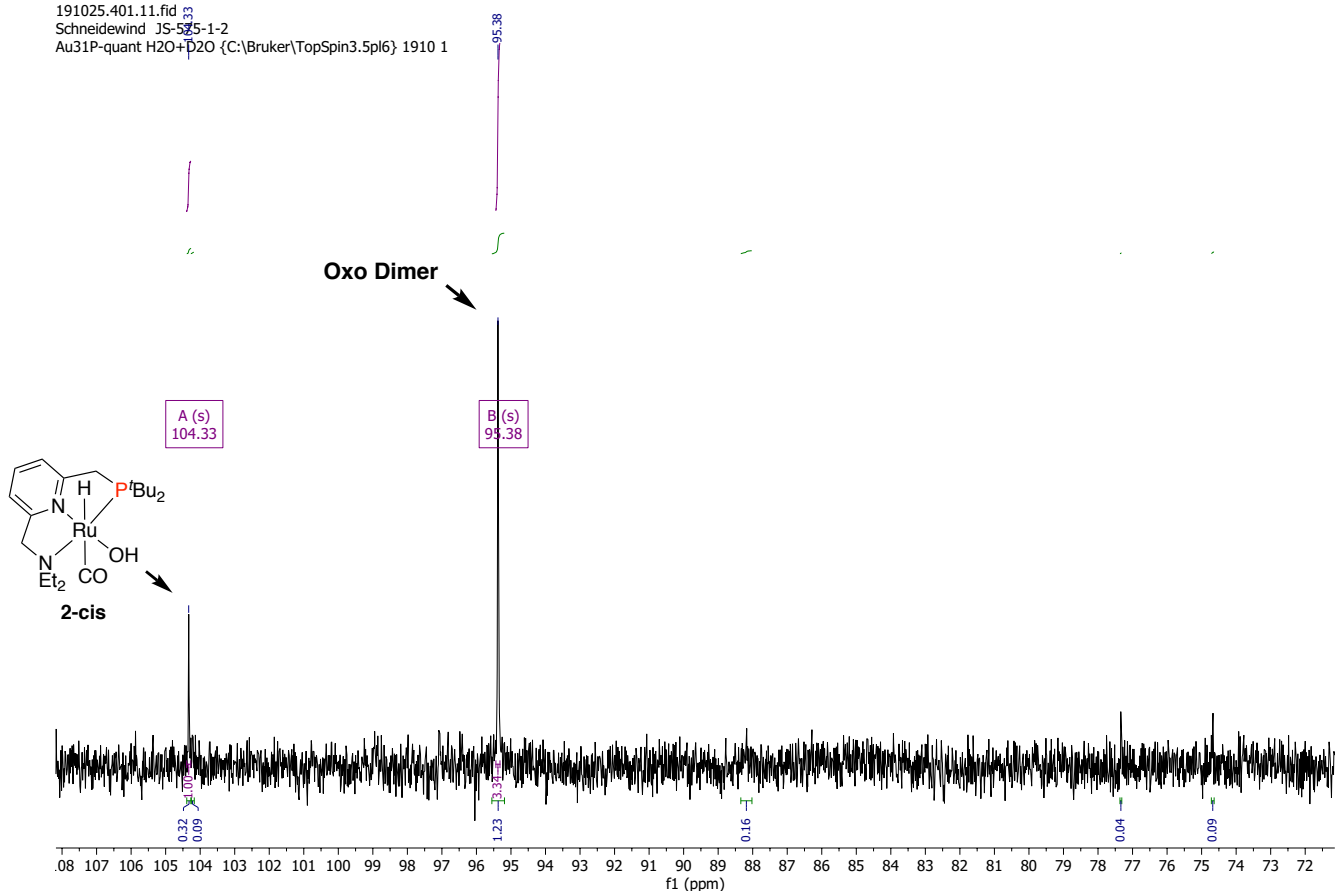


Figure 7.6-2 Superimposed $^{31}\text{P}\{\text{H}\}$ NMR spectra of 1 (in H_2O , 298 K) immediately after irradiation (green) and same sample after two more days in the dark (red)

191025.401.11.fid³³
 Schneidewind JS-575-1-2
 Au31P-quant H2O+D2O {C:\Bruker\TopSpin3.5pl6} 1910 1



191105.406.11.fid³³
 Schneidewind JS-575-1-3
 Au31P-quant H2O+D2O {C:\Bruker\TopSpin3.5pl6} 1911 6

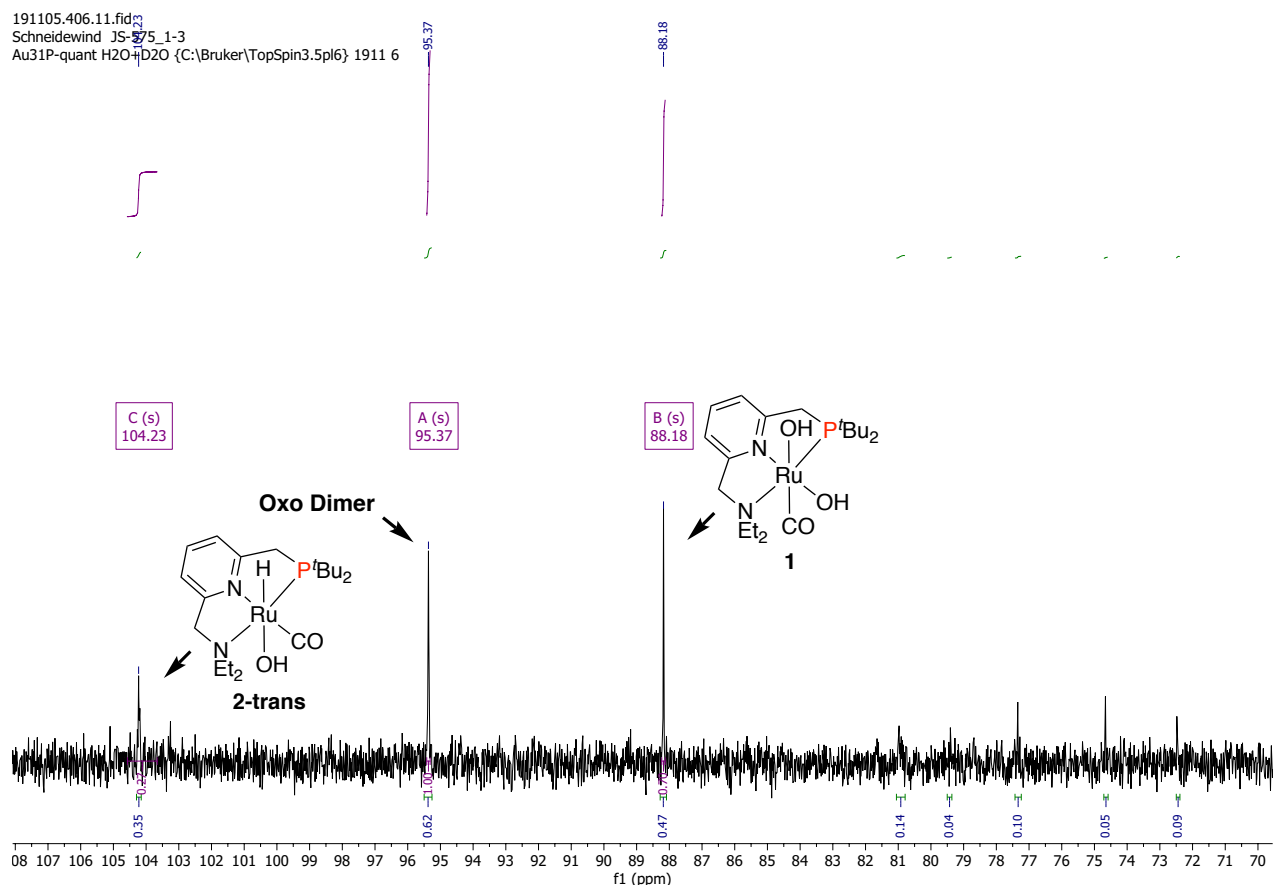


Figure 7.6-3 $^3\text{P}\{^1\text{H}\}$ NMR spectrum of **1** (in 52 mM KOH aq., 298 K, Ag_2O synthesis route) immediately after irradiation (top) and the same sample after twelve more days in the dark (bottom)

7.7 Data for $\partial(^3\text{P}) = 86$ ppm Product

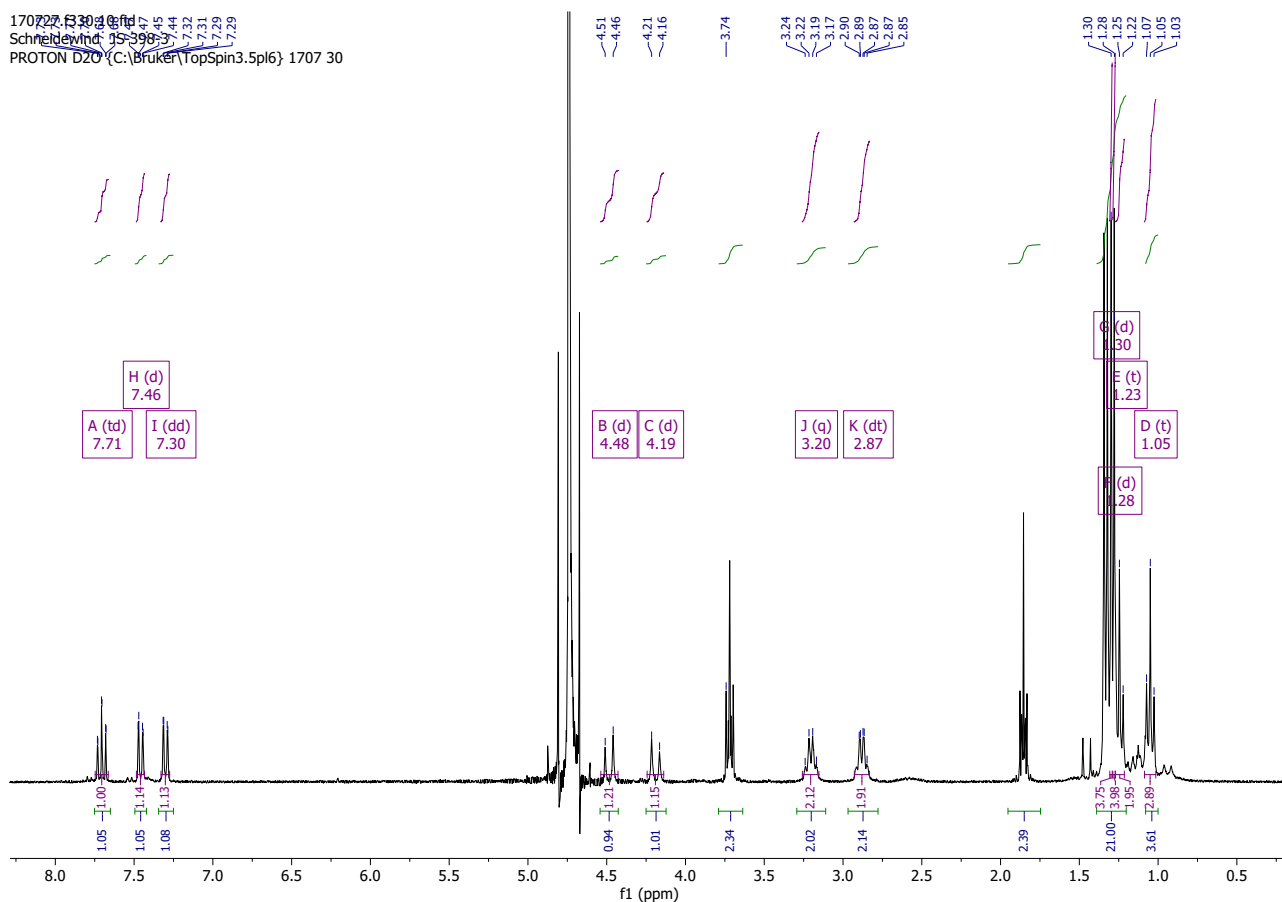


Figure 7.7-1 ^1H NMR spectrum of raw product (in D_2O , 298 K) after reaction of 2-trans with N_2O for 20h in presence of 83 equivalents of H_2O

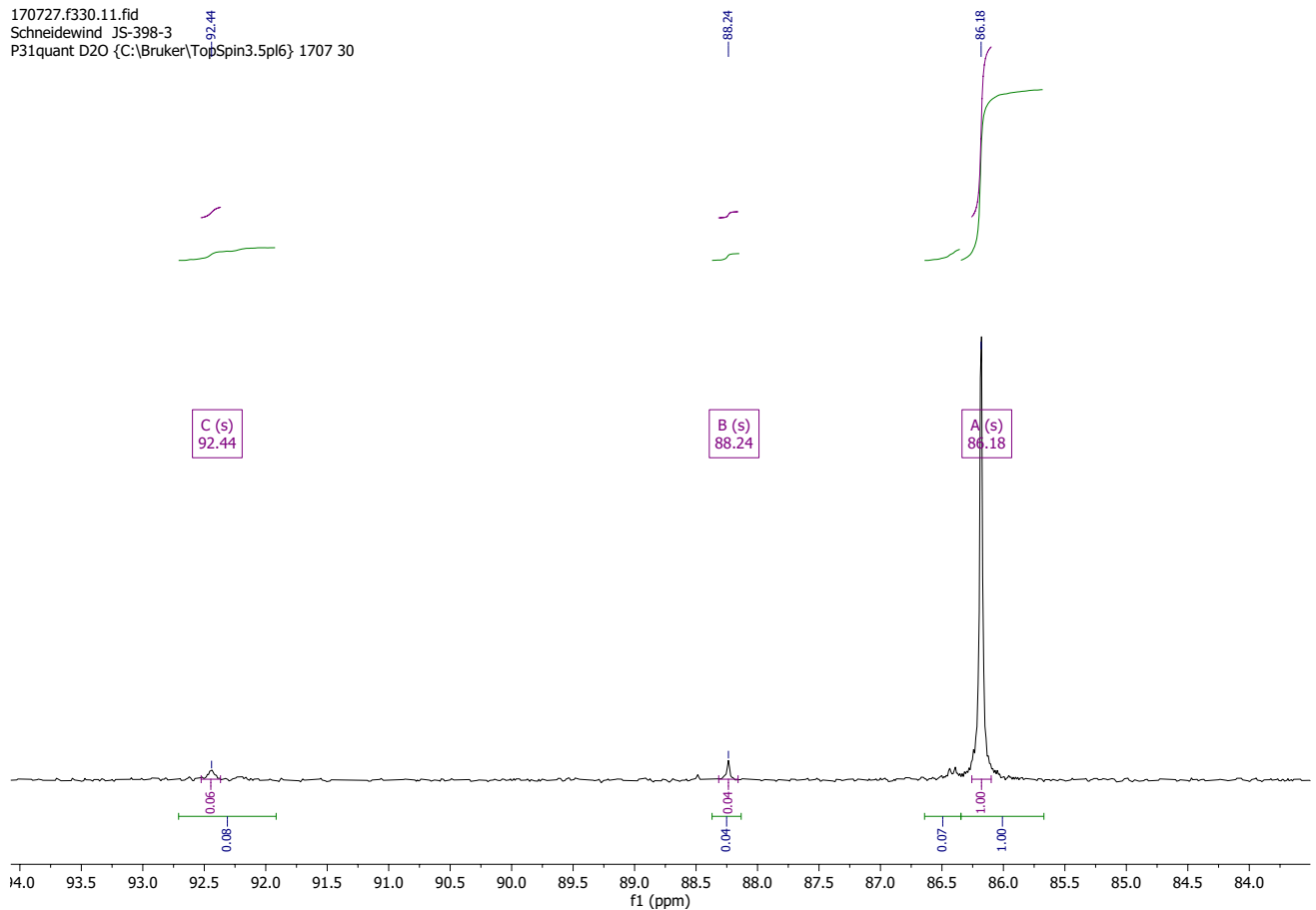


Figure 7.7-2 $^{31}\text{P}\{\text{H}\}$ NMR spectrum of raw product (in D_2O , 298 K) after reaction of 2-trans with N_2O for 20h in presence of 83 equivalents of H_2O

8 Other Analytical Data

8.1 IR Spectrum of Complex 1

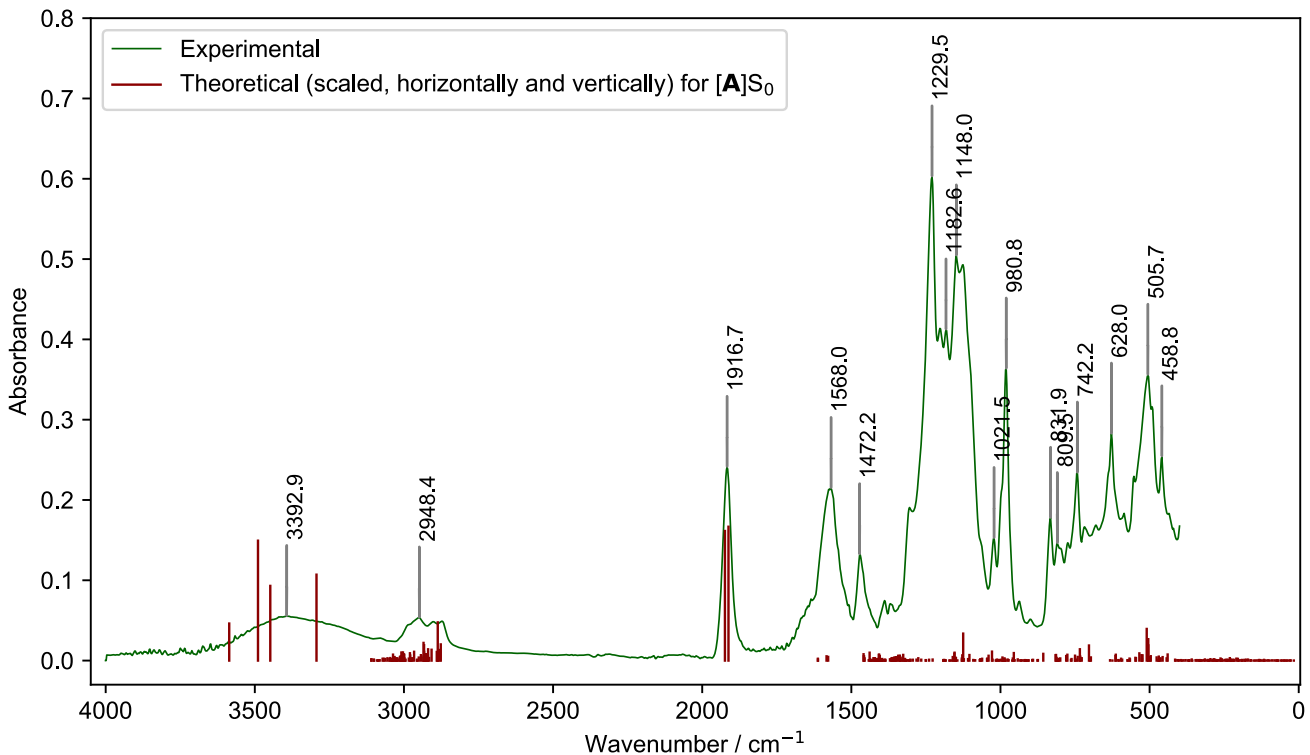


Figure 8.1-1 IR Spectrum (ATR) of complex 1 along with theoretical spectrum for [A]S₀

Note: theoretical spectrum is shown as vertical lines for each transition. The theoretical spectrum has been scaled horizontally by a factor of 0.96 and has been scaled vertically.

8.2 EPR Spectrum of Complex 1 Synthesis Raw Product

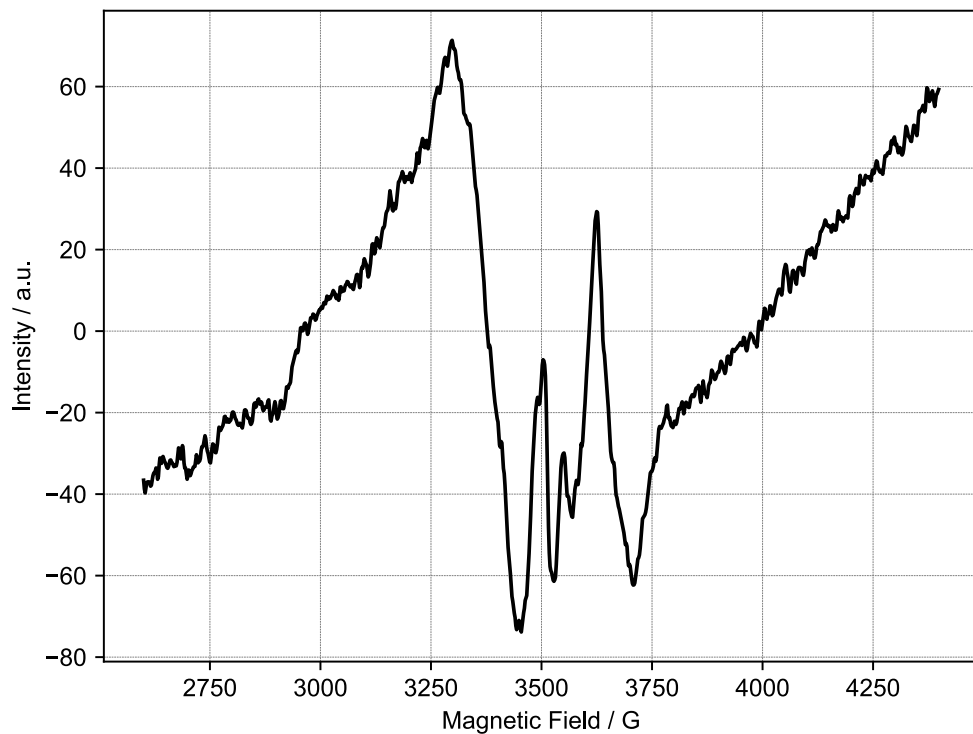


Figure 8.2-1 EPR spectrum of green raw product obtained via reaction of 2-trans with N₂O

N₂O reaction of **2-trans** was carried out as described in 3.1.1, but after the reaction, the solvent was completely removed under vacuum and the dark green solid residue was washed with Et₂O and pentane. The residue was then dissolved in DCM, yielding a green solution, which was transferred to a capillary and measured.

8.3 Time-Resolved UV/Vis Spectroscopy

8.3.1 Experimental Procedure

Under argon, 1.7 ml of a 8×10^{-4} M aqueous solution of **1** (prepared using N₂O synthesis route) were transferred to a screw cap quartz cuvette with a rubber septum (1 cm path length). Subsequently, a UV/Vis spectrum was recorded (timestamp t = 0 min).

Afterwards, the cuvette was placed into a double-walled beaker filled with water, which was thermostatted to 16.5 °C. It was then irradiated using the Hg light source (320 – 500 nm, intensity setting 1 W). After the indicated irradiation times (1, 3, 5, 10, 20, 30, 60, 90, 120, 190, 240 min), the irradiation was stopped and a UV/Vis spectrum was recorded.

The initially light-yellow solution gradually changed color during the first ca. 10 min of irradiation towards bright yellow/orange. For the remainder of the reaction time the color remained relatively constant.

8.3.2 Results and Analysis

8.3.2.1 UV/Vis spectra

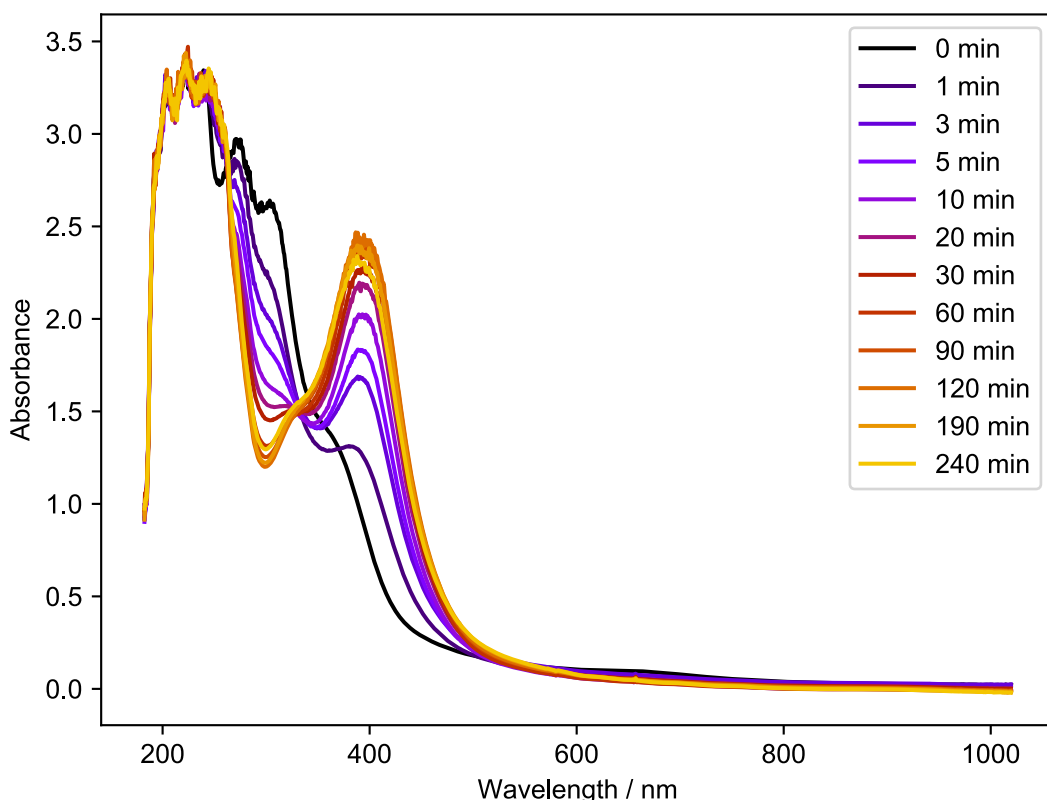


Figure 8.3-1 Time-resolved UV/Vis spectra recorded during irradiation of complex 1 in H₂O

Concentration: 8×10^{-4} M, path length: 1 cm, irradiation using Hg light source (320 – 500 nm, 1 W intensity setting).

Figure 8.3-1 shows the recorded UV/Vis spectra. Clearly apparent are bleaching at $\lambda = 300$ nm and the appearance of a new absorption feature at $\lambda = 395$ nm. However, there is no clear isosbestic point, indicating that more than two species are involved in the observed reaction(s). This is not surprising, since the NMR-based concentration-time profile (see Figure 4.1-1) showed that three species are involved (**1**, **2-cis** and **Oxo Dimer**). Hence, it is not possible to recover concentration data by only monitoring specific absorption wavelengths. Instead, multivariate curve resolution has to be used to solve this mixture analysis problem.

8.3.2.2 Data Analysis using Multivariate Curve Resolution

Multivariate curve resolution (MCR) allows for the estimation of pure component spectra and concentration-time profiles from convoluted spectra through a non-linear optimization process. It was performed using the pyMCR library¹⁰ with non-negative least squares and a concentration normalization constraint (meaning that concentrations have to be constant across all timepoints). As an initial guess for the time-dependent concentrations, a concentration profile was generated using the kinetic model described in 4.1.3. The results are shown in Figure 8.3-2 and Figure 8.3-3.

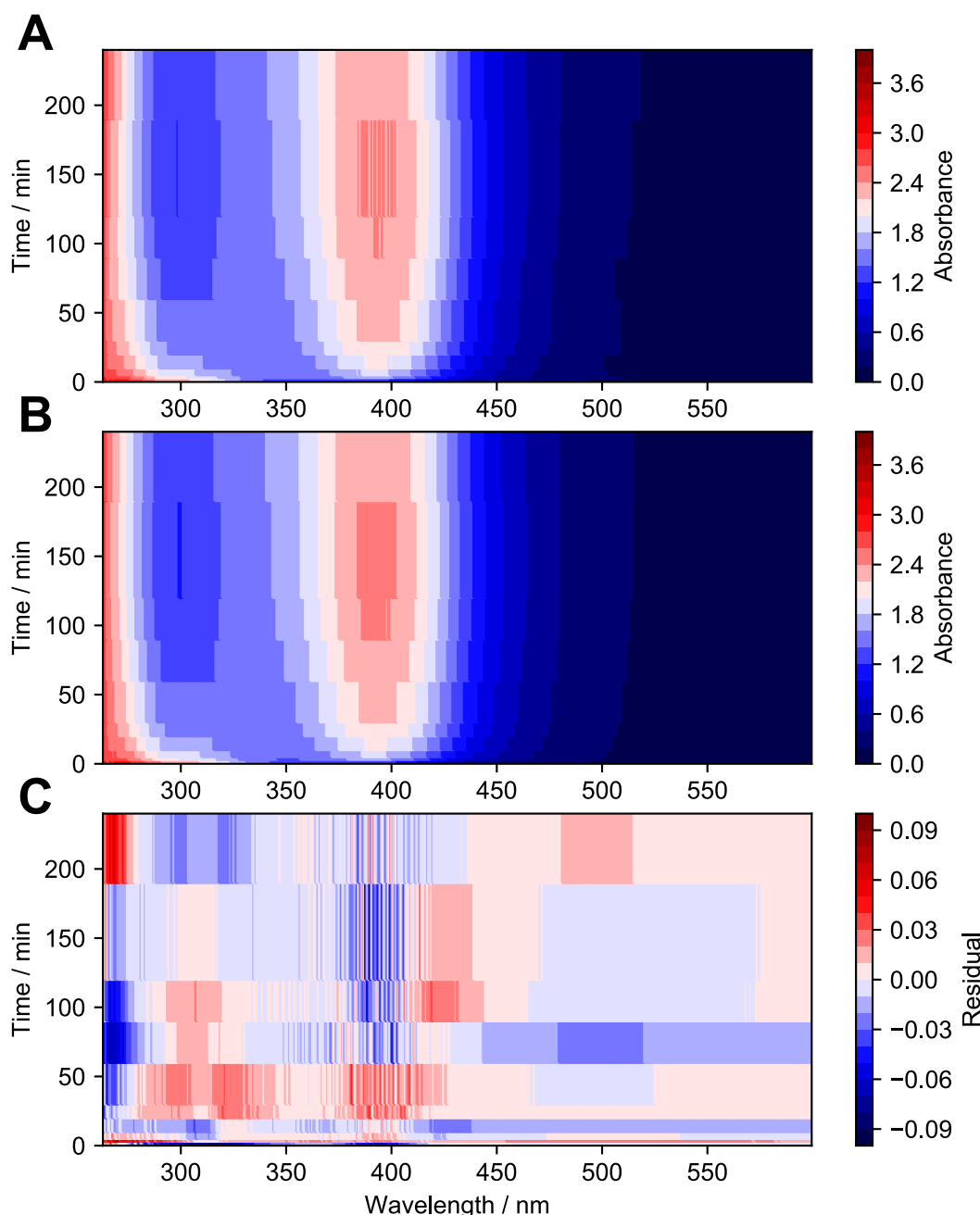


Figure 8.3-2 Hyperspectral images showing time-dependent UV/Vis data and MCR results

A Time-resolved UV/Vis spectra shown as a hyperspectral image

B Hyperspectral image of MCR results (modelling time-resolved data in A)

C Residuals obtained by subtraction of MCR results from time-resolved UV/Vis data

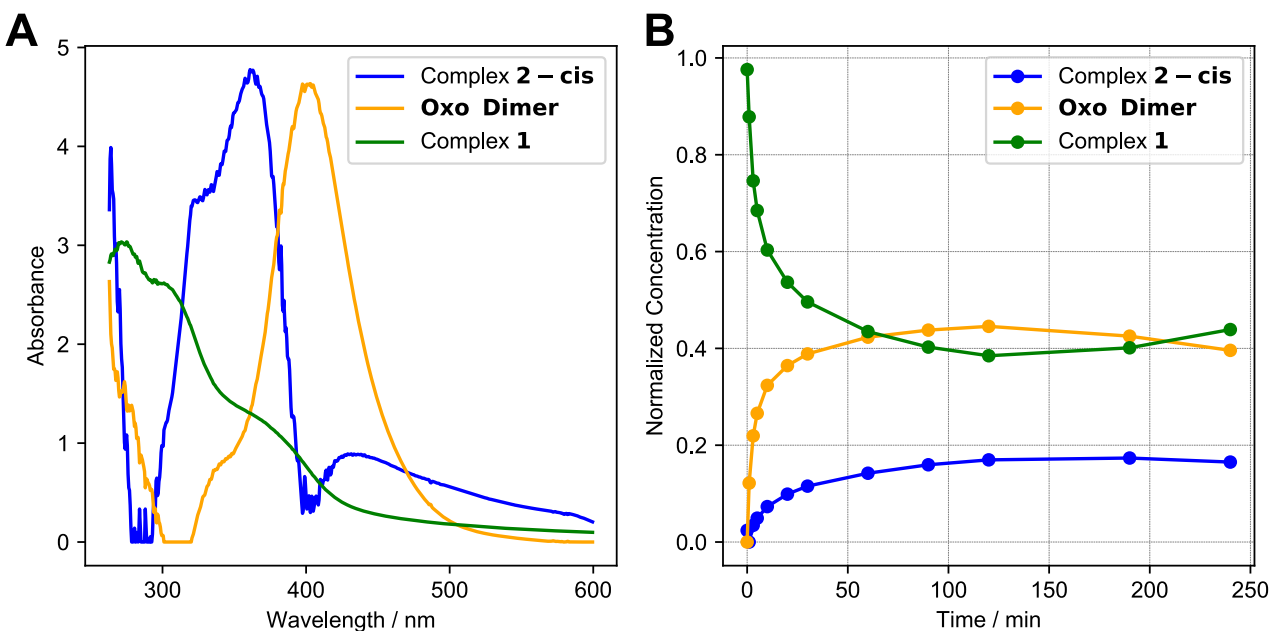


Figure 8.3-3 Pure component spectra and concentration-time profile obtained using MCR

A Pure component spectra for **1**, **2-cis** and **Oxo Dimer** obtained using MCR.

B Concentration-time profile for **1**, **2-cis** and **Oxo Dimer** obtained using MCR.

As can be seen in Figure 8.3-3, there is good agreement between the time-resolved UV/vis data and the MCR results modelling it, with only small residuals between the two. Figure 8.3-3 shows the corresponding pure component spectra and concentration-time profiles for the MCR results. At this point it is not possible to assess the quality of the pure component spectra, since no experimental UV/Vis spectra for **2-cis** or **Oxo Dimer** are available (since both are thermally unstable, with **2-cis** converting to **2-trans** and **Oxo Dimer** converting back to **1** over time, see 4.1.2). We therefore attempted to judge the viability of the MCR results by analyzing the concentration-time profile. Based on the NMR-based concentration-time profile shown in Figure 4.1-1, a kinetic model to describe the temporal evolution of **1**, **2-cis** and **Oxo Dimer** is available. If the MCR results offer a viable description of the reaction system, the corresponding MCR concentration-time profile should be consistent with this kinetic model. We therefore fitted the kinetic model to the MCR concentration-time profile data using the method described in 4.1.3. The results are shown in Figure 8.3-4.

While the fitted kinetic model shows somewhat reasonable agreement with the MCR concentration-time data for **1** and **Oxo Dimer**, the agreement is poor in case of **2-cis**. We attribute this to the fact that **Oxo Dimer** is formed in significantly higher yields than **2-cis** (ca. 60% vs. ca. 20%, see Figure 4.1-1), which complicates the accurate description of **2-cis** by MCR. Since **2-cis** is a comparatively small component of the reaction system, its concentration change over time has a comparatively small effect on the temporal evolution of UV/Vis spectra. This makes it difficult to accurately recover data on the concentration change of **2-cis** from the convoluted spectra. We are therefore not confident that time-resolved UV/Vis spectroscopy in combination with MCR can provide reliable kinetic data for **2-cis**.

As **2-cis** is the product of interest in our case (since its formation contains information about the water splitting reaction, while **Oxo Dimer** is only a side product), time-resolved UV/Vis spectroscopy is not be a suitable method for kinetic studies of the studied reaction system. However, we expect that improved water splitting systems with suppressed side product formation and higher hydride complex yields can be studied using the described UV/Vis and MCR methodology.

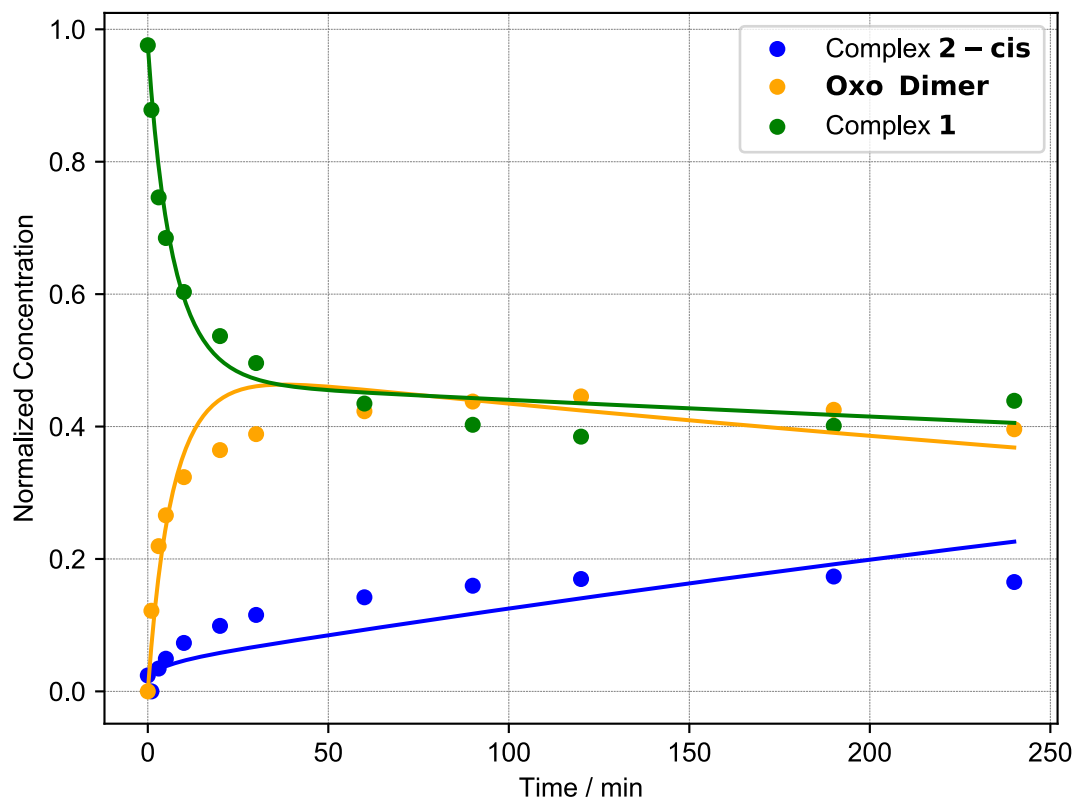


Figure 8.3-4 Fitting of kinetic model to MCR concentration-time profile

Fitting of the kinetic model was performed as described in 4.1.3 using the same reaction network. Dots show MCR concentration-time data and lines show kinetic model fit.

9 Ultrafast Pump-Probe Spectroscopy

9.1 Experimental Procedure and Analysis

Transient absorption spectra were recorded with a time resolution of ca. 200 fs by means of a pump-probe setup based on a Ti:sapphire laser system (Spectra-Physics, Spitfire Pro) operating at a centre wavelength of 800 nm and a repetition rate of 1 kHz. Pump pulses at a centre wavelength of 400 nm were generated by frequency doubling a part of the output of the Ti:sapphire system using a BBO-crystal. The energy of the pump pulses was between 0.8 and 1 μ J. A white light continuum for probing was obtained by focussing a small fraction of the Ti:sapphire output into a CaF₂-crystal. Pump and probe beam were focussed into the sample so that their overlapping spots had an effective diameter of 360 μ m for the pump and 210 μ m for the probe. Measurements were performed with the polarizations of the pump and probe beam set to parallel, perpendicular, and in magic-angle (54.7°). After passing through the sample, the probe beam was dispersed by a prism and transient absorption changes were recorded by an array detector in a spectrally resolved fashion.

Complex **1** was dissolved in oxygen-free water and the sample solution was transferred into a 1 mm fused silica cuvette under inert conditions. The optical density at 400 nm was ca. 0.7 to obtain transient spectra with a good signal to noise ratio (concentration \approx 0.007 M). The cuvette was mounted and measured on a rotation stage. A rotation frequency of about 1 Hz resulted in a sufficiently fast refreshing of the sample in the interaction region to avoid degeneration of the signal during the measurements. Transient absorption data was analyzed by global fitting of a sum of exponential decays revealing time constants and the corresponding decay associated spectra (DAS). To describe the ultrafast dynamics with sufficient accuracy, two exponential decay components are necessary and a long lived one with an “infinite” lifetime (>> 2 ns) much longer than the time range of 2 ns covered by our setup.

9.2 Results and Interpretation

Decay associated spectra for the two detected species ($\tau = 6$ ps and $\tau = 150$ ps) are shown in Figure 9.2-1. The $\tau = 6$ ps species can likely be attributed to an emissive S_n state of **1**, since the positive mΔOD between 450 and 650 nm agrees well with the measured fluorescence of **1**, suggesting that this feature is due to stimulated emission. The short lifetime of only 6 ps can also explain the weak nature of **1**’s fluorescence.

The experimental DAS for the $\tau = 150$ ps species agrees well with the computed DAS for [B-Trans]T₀ (see 11.4.2 for details on computed DAS spectra). The lifetime of this species, however, is too short to explain the observed reaction rates based on the kinetic model (see 10.3), which predicts a minimum lifetime of $\tau \approx 10$ ns for the second-photon absorbing intermediate. We propose that [B-Trans]T₀ might partially isomerize to [B]T₀ or [B]T₀ might be formed directly from [A]S_n, but in amounts which are below the detection limit of the used experimental set-up (TD-DFT calculations predict that [B]T₀ absorbs 400 – 700 nm light more weakly compared to [B-Trans]T₀, see Figure 11.2-1, further complicating direct detection). [B]T₀ and [B-Trans]T₀ might have different relaxation channels, especially because Ru-O bond formation can lead to **Oxo Dimer** formation for [B-Trans]T₀ but not for [B]T₀. The lifetime of [B]T₀ might therefore be longer than the lifetime of [B-Trans]T₀, explaining why [B]T₀ can act as the second-photon absorbing intermediate.

As can be seen in Figure 9.2-2, [A]T₀ yields a theoretical DAS which is inconsistent with experimental data, suggesting that it is not the species corresponding to $\tau = 150$ ps. Furthermore, the predicted DAS for [B]T₀ also shows poor agreement with experimental data (see Figure 9.2-3).

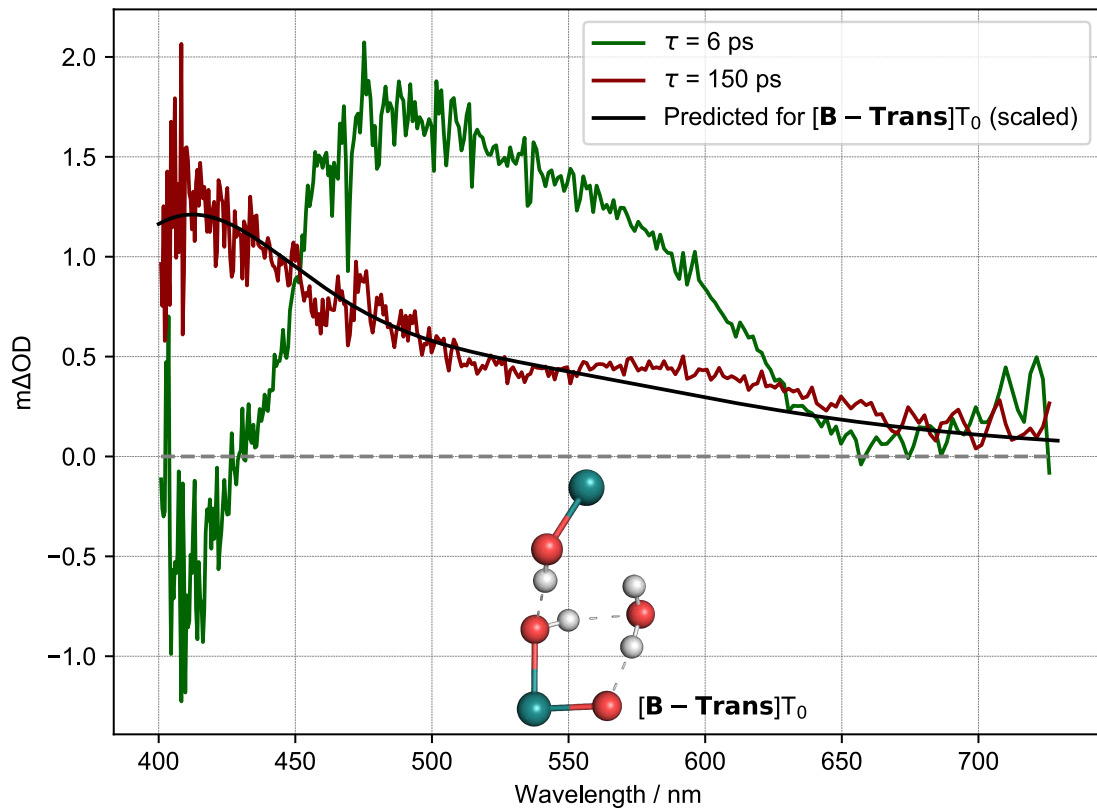


Figure 9.2-1 Decay associated spectra (magic angle polarization) and predicted DAS for $[\text{B-Trans}]T_0$
 Predicted DAS for $[\text{B-Trans}]T_0$ was computed as the difference spectrum between $[\text{A-Mono}]S_0$ and $[\text{B-Trans}]T_0$. For the structure of $[\text{B-Trans}]T_0$ see Figure 11.6-11). Inlet shows structure of $[\text{B-Trans}]T_0$ with other ligands omitted for clarity.

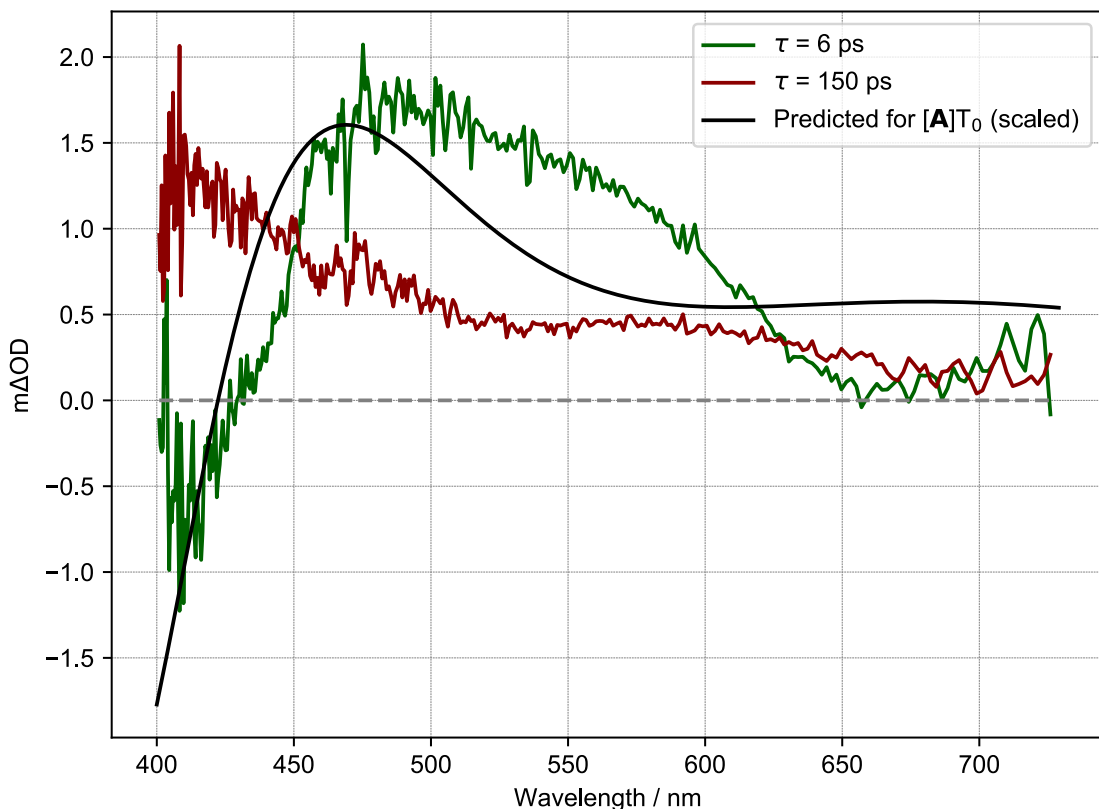


Figure 9.2-2 Decay associated spectra (magic angle polarization) and predicted DAS for $[\text{A}]T_0$
 Predicted DAS for $[\text{A}]T_0$ was computed as the difference spectrum between $[\text{A-Mono}]S_0$ and $[\text{A}]T_0$.

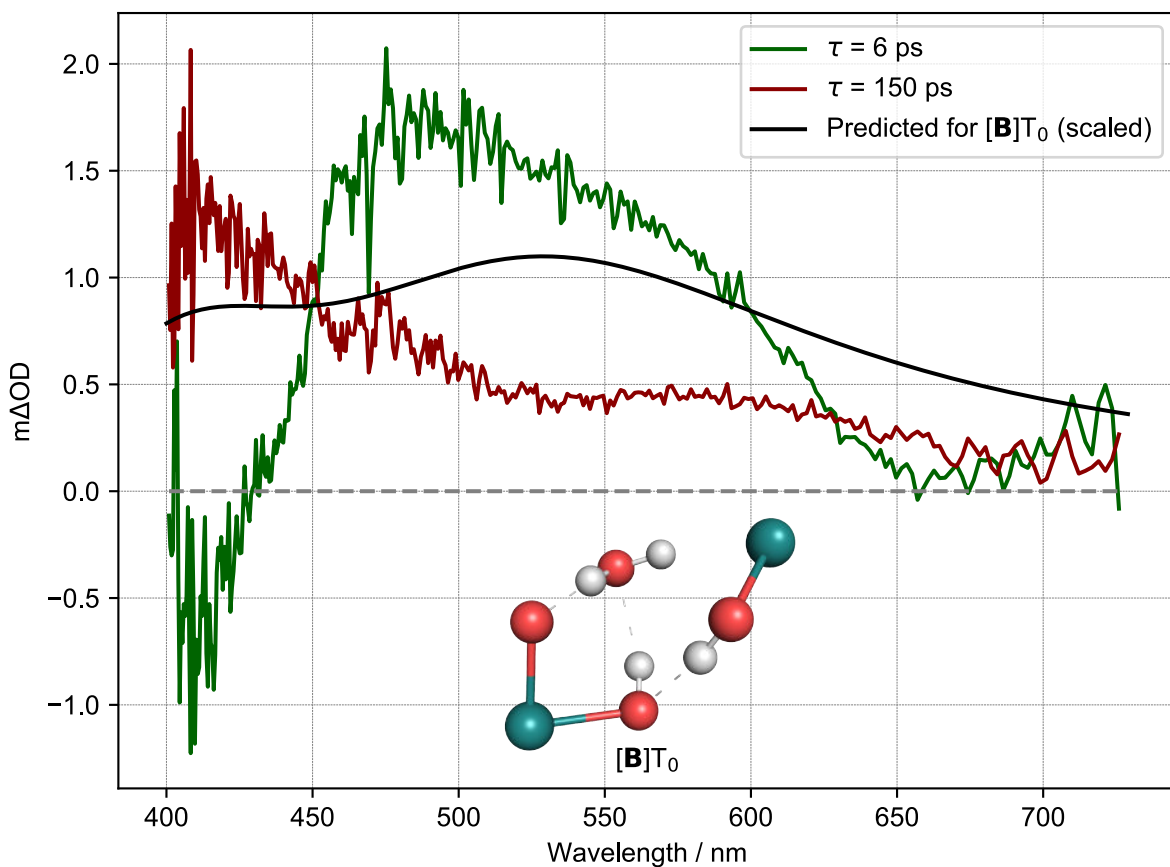


Figure 9.2-3 Decay associated spectra (magic angle polarization) and predicted DAS for $[\mathbf{B}]T_0$
 Predicted DAS for $[\mathbf{B}]T_0$ was computed as the difference spectrum between $[\mathbf{A}\text{-Mono}]S_0$ and $[\mathbf{B}]T_0$. Inlet shows structure of $[\mathbf{B}]T_0$ with other ligands omitted for clarity.

10 Photochemical Kinetic Model

10.1 Description of Kinetic Model

A simple kinetic model to describe the two-photon water splitting reaction was developed using the reaction sequence shown in Table 10.3-1. In this reaction sequence, starting complex **A** absorbs a photon to form transient intermediate **B**. **B** decays back to **A** with a lifetime of τ . Furthermore, **B** can absorb a second photon to form O_2 (+ corresponding complex, which is not part of this kinetic model). O_2 can then be consumed by a third reaction (forming **X**), which also requires photon absorption (see 4.3.2). This reaction sequence is therefore a simplified version of the water splitting mechanism determined using DFT and CASSCF calculations, combined with the experimentally observed, O_2 consuming reaction.

The reaction sequence can be described using the following system of differential equations:

$$\frac{d[A]}{dt} = \frac{1}{\tau}[B] - q_1 c_{abs} Flux [A] \quad \text{Equation (4)}$$

$$\frac{d[B]}{dt} = -\frac{1}{\tau}[B] + q_1 c_{abs} Flux [A] - q_2 c_{abs} Flux [B] \quad \text{Equation (5)}$$

$$\frac{d[C]}{dt} = q_2 c_{abs} Flux [B] - q_3 c_{abs} Flux [C] \quad \text{Equation (6)}$$

$$\frac{d[D]}{dt} = q_3 c_{abs} Flux [C] \quad \text{Equation (7)}$$

Wherein q_n are the respective quantum efficiencies for each reaction step, *Flux* is the photon flux and c_{abs} is the absorption cross-section. For simplicity, it was assumed that absorption cross sections are the same for each step ($1.15E-17 \text{ cm}^2$, which corresponds to an extinction coefficient of $3000 \text{ M}^{-1} \text{ cm}^{-1}$). Furthermore, it was assumed that *Flux* is the same for each reaction step.

The kinetic model was fitted to experimental data from the intensity dataset. For this, all experiments with the same photon flux were averaged. Afterwards, the data was normalized to express the amount of O_2 as a fraction of the initial amount of **1** (based on 0.005 M concentration of **1**). This gave the averaged and normalized experimental data shown in Figure 10.3-1A. For the photon flux = $3.3e+17$ data, Gaussian noise with the same standard deviation as the experimental data was appended from 240 s , since the experimental data was only available up to this time.

Fitting was performed by numerically solving the system of differential equations with an updated guess for τ , q_1 , q_2 and q_3 at each optimization step, with *Flux* being the corresponding photon flux for each data series. Updated guesses were generated using the Nelder-Mead or Differential Evolution algorithm. This was done until convergence was reached. It should be noted that only one set of optimization parameters (τ , q_1 , q_2 and q_3) describes all experiments with different photon flux values. The resulting fit is shown in Figure 10.3-1A. Optimized parameters are shown in Table 10.3-1.

10.2 Relationship between Initial Rate and Photon Flux

The described kinetic model was also used to explore the relationship between initial rate of O_2 formation and photon flux. For this, the optimized parameters shown in Table 10.3-1 were used, unless noted otherwise. With these parameters and within the photon flux range of the intensity dataset, a square relationship between initial rate of O_2 formation and photon flux is obtained (just like it was observed experimentally). In other words, fitting a function of the form $f(x) = ax^b$ (optimizing a and b) to the initial rate/photon flux data gives a value of 2 for power b .

We were interested to see how the relationship between initial rate and photon flux would change for increasing lifetimes τ of **B**. Thus, keeping q_1 , q_2 and q_3 constant, τ was changed over several orders of magnitude, and for each τ value, power b was determined within the intensity dataset photon flux range. Corresponding results are shown in Figure 10.3-1. It can be seen that starting at

$\tau = 10^{-2}$ s, the relationship of initial and photon flux starts to transition to linear one, meaning that power b changes gradually from 2 to 1.

10.3 Interpretation of Results

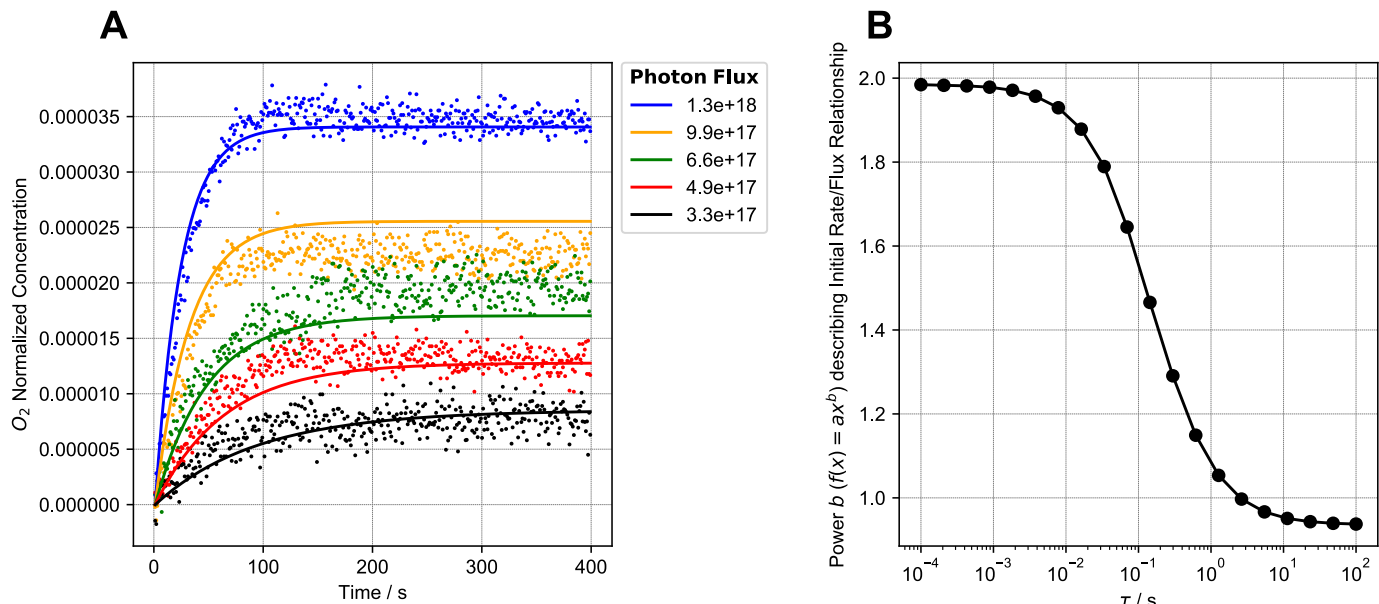
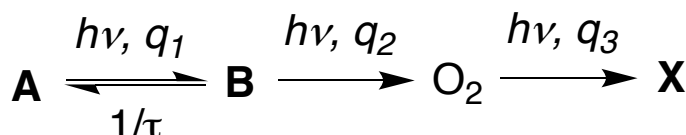


Figure 10.3-1 Photochemical kinetic model used to describe the two-photon water splitting reaction

A Fit of photochemical kinetic model to experimental data. Experimental data is for irradiation with different photon fluxes (intensity dataset) and for each flux value, all measurements with this flux were averaged and converted to normalized O_2 concentration, yielding the shown data. For the photon flux = $3.3e+17$ data, Gaussian noise with the same standard deviation as the experimental data was appended from 240 s, since the experimental data was only available up to this time. Fit of the kinetic model is shown as solid lines.

B Dependence of power b on the lifetime of the intermediate in the two-photon mechanism. Power b describes the relationship between initial rate and photon flux. A value of 2 for b indicates a square dependence of the initial rate on photon flux (as observed experimentally), while a value of 1 indicates a linear relationship. It can be seen that for increasing lifetimes, the relationship of initial rate and photon flux transitions from a square to a linear one. For this modeling, the optimized parameters from **A** were used, changing only τ . The flux level range of the intensity dataset was used to determine b .

Table 10.3-1 Optimized parameters for photochemical kinetic model^[a]



Lifetime τ / ns	Quantum Efficiency q_1	Quantum Efficiency q_2	Quantum Efficiency q_3
65	0.661	0.145	0.0028

[a] Note that there are multiple solutions giving identical fits and only one solution is shown here.

When interpreting the optimized parameters obtained via fitting of the kinetic model to experimental data it should be noted that there is no unique solution. For example, keeping q_1 and q_3 the same, $\tau = 6.5 \mu\text{s}$ and $q_2 = 0.00145$ would give the same result as the parameters shown in Table 10.3-1. This model therefore only provides a rough idea for the underlying lifetime and quantum efficiencies operative in the system. However, through examination of the initial rate/photon flux relationship (Figure 10.3-1), we can see that the lifetime of intermediate **B** must be below $\tau = 10^{-1} \text{ s}$ to explain the experimentally observed square relationship between initial rate and photon flux. In turn, this provides us with lower bound for q_2 , although the lifetime of **B** is probably significantly shorter than $\tau = 10^{-1} \text{ s}$ (given its high energy, see DFT results), with q_2 thus being significantly higher than its lower bound. The lower bound for τ is $\tau \approx 10 \text{ ns}$, which would correspond to $q_2 \approx 1$.

10.4 Comparison of Experimental Dual Irradiation Rates with Kinetic Model

To further assess the validity of the kinetic model, an approximate comparison between the excess initial rate observed in dual irradiation experiments and the prediction by the kinetic model was made.

For this comparison it is necessary to know the 455 – 630 nm photon flux used during dual irradiation experiments. Since chemical actinometry cannot be used in this wavelength region (see 6.3), the flux has to be approximated using power meter measurements.

For the Hg light source (320 – 400 nm), a power of 76 mW was measured in place of the liquid phase O₂ reactor (photon flux of 4.15E+17 s⁻¹ in this position). Based on the mean photon wavelength (360 nm) and the measured flux, the theoretical power is 229 mW. Therefore, measurements using this power meter have to be corrected by a factor of 3.01 to reflect the power received by the reactor.

Using the same power meter, powers of 471 mW and 359 mW were measured for the QTH light source using 455 nm and 630 nm longpass filters, respectively (in place of the liquid phase O₂ reactor). The power in the wavelength range 455 – 630 nm is therefore 112 mW. Using the correction factor of 3.01, one obtains a corrected power of 337 mW. Based on a mean photon wavelength of 542.5 nm, the 455 – 630 nm photon flux is therefore roughly 9.23E+17 s⁻¹.

In dual irradiation experiments, an excess initial rate of ca. 0.001 μmol l⁻¹ s⁻¹ was observed when the 455 nm longpass filter was used. Based on a reaction volume of ca. 550 μl, this corresponds to ca. 3.3E+11 O₂ forming reactions per second. Given a 455 – 630 nm photon flux of ca. 9.23E+17 s⁻¹, this means that the probability of inducing an O₂ forming reaction is ca. 3.59E-07 per 455 – 630 nm photon.

To calculate the theoretical reaction probability, we will assume the same absorbance for the second-photon absorbing intermediate as used in the kinetic model (3000 M⁻¹ cm⁻¹). Based on this absorbance, an intermediate lifetime of 65 ns (see Table 10.3-1) and a 455 – 630 nm photon flux of 9.23E+17 s⁻¹, we can calculate that there is a probability of 6.93E-07 for the intermediate to absorb a photon in its lifetime (obtained by multiplying lifetime, photon flux and absorption cross section). Multiplying this absorption probability by a quantum yield for the second absorption of 0.145 (see Table 10.3-1) gives us a predicted reaction probability of 1.01E-07 per 450 – 630 nm photon.

Table 10.4-1 Comparison of experimental and predicted reaction probabilities

Experimental reaction probability per 455 – 630 nm photon	Predicted reaction probability per 455 – 630 nm photon
3.59E-07	1.01E-07

Experimental and predicted reaction probabilities are in the same order of magnitude, which we consider to be a rather good agreement, given the simplicity of the kinetic model. Through this comparison it can also be seen that the rather low experimental reaction probability per 455 – 630 nm photon is likely due to a short life time of the absorbing intermediate, making second photon absorption less probable. Increasing the lifetime could therefore significantly increase both reaction rate and overall quantum yield.

10.5 Modelling of Other Photochemical Mechanisms

We also assessed the validity of other photochemical mechanisms using the kinetic modelling procedures described in 10.1 and 10.2 (although with different differential equation systems and parameters). For each alternative mechanism, the following pieces of information are presented: a kinetic scheme representing the mechanism, a fit of the kinetic model to the experimental data and a plot showing the relationship between maximum rate and photon flux. The maximum rate/photon flux relationship is calculated based on the optimized kinetic model, not the experimental data. Furthermore, a table with the optimized parameters is shown, although also in these cases they are not unique solutions.

10.5.1 Bimolecular reaction pathways

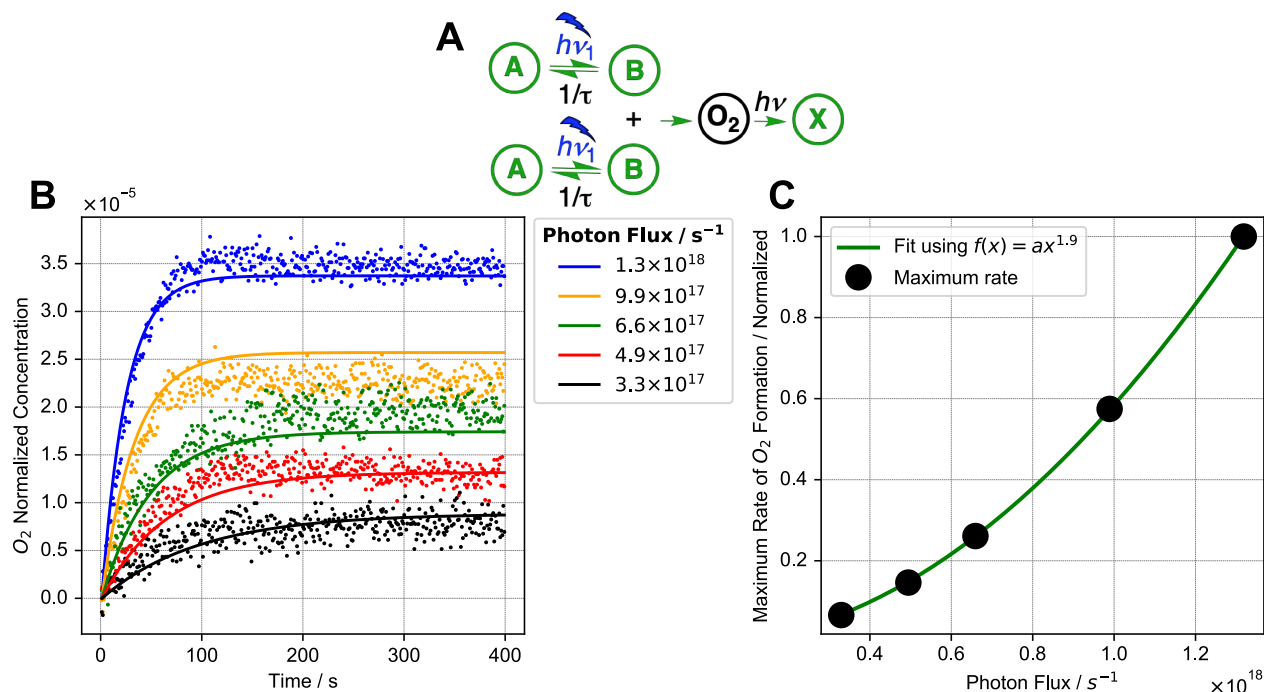


Figure 10.5-1 Photochemical kinetic model for bimolecular reaction pathway

A Kinetic scheme showing bimolecular reaction pathway.

B Fit of bimolecular model to experimental data.

C Maximum rate/photon flux relationship for bimolecular model.

Table 10.5-1 Optimized parameters for bimolecular reaction pathway

Lifetime τ ($\mathbf{B} \rightarrow \mathbf{A}$) / μs	$q_1 (\mathbf{A} \rightarrow \mathbf{B})$	$k_1 (2 \mathbf{B} \rightarrow \mathbf{O}_2)$	$q_2 (\mathbf{O}_2 \rightarrow \mathbf{X})$
2423	0.89	0.0014	0.0027

A bimolecular pathway was modelled by assuming that **A** reacts to **B** in a photochemical reaction. Subsequently, two equivalents of **B** react to \mathbf{O}_2 in a thermal reaction (followed by photochemical consumption of \mathbf{O}_2). As can be seen in Figure 10.5-1, this pathway yields a fit to the experimental data which is comparable in quality to the two-photon model. Furthermore, this model also gives an approximately square relationship between maximum rate and photon flux, which is in agreement with the experimental results. Two-photon or bimolecular mechanisms can therefore not be distinguished through kinetic modelling alone. Experimental results for the wavelength dependence of the reaction, however, provide evidence for the two-photon mechanism. This is because in the bimolecular reaction pathway, only **A** absorbs photons. Hence, the absorption behavior of **A** would completely determine the wavelength response of the reaction in case of a bimolecular pathway. In contrast, wavelength dependence experiments showed that light, which is not absorbed by the starting complex, enhances the reaction rate (see manuscript). This is only consistent with having more than one absorbing species in the reaction pathway, as is the case for the two-photon mechanism.

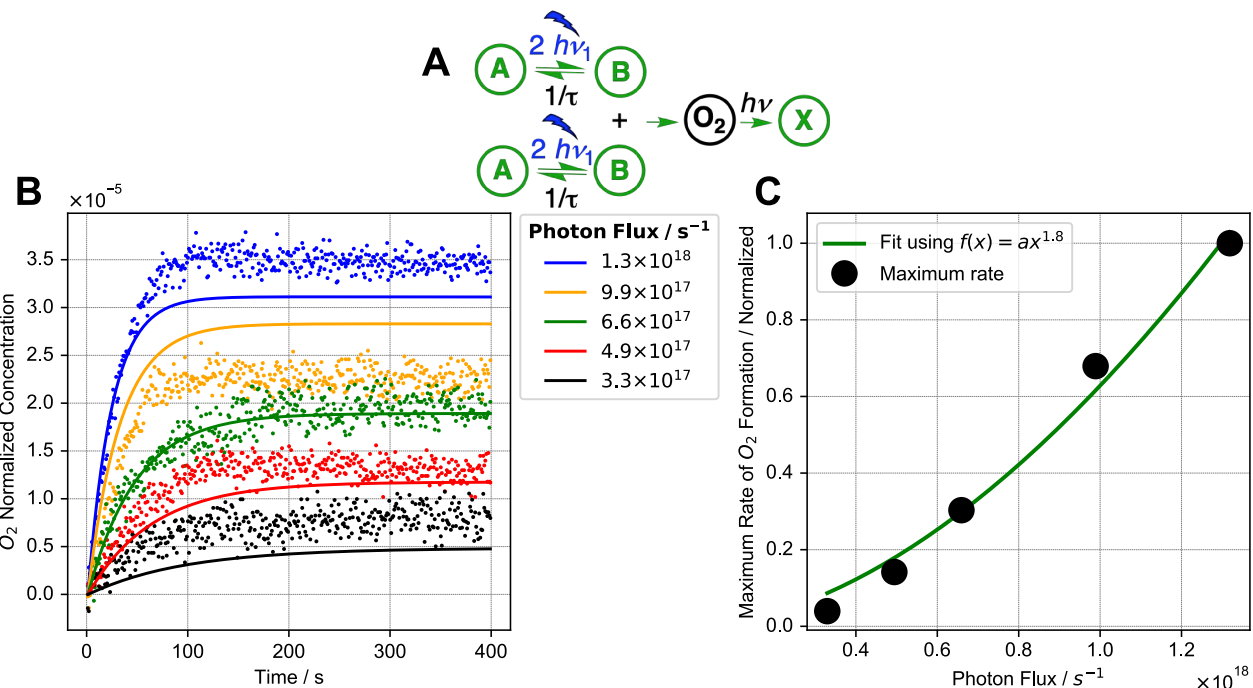


Figure 10.5-2 Photochemical kinetic model for bimolecular pathway with two-photon generation of intermediate

A Kinetic scheme showing bimolecular reaction pathway with two-photon generation of intermediate.

B Fit of bimolecular two-photon model to experimental data.

C Maximum rate/photon flux relationship for bimolecular two-photon model.

Table 10.5-2 Optimized parameters for bimolecular two-photon reaction pathway

Lifetime $\tau (\text{B} \rightarrow \text{A}) / \text{ms}$	$q_1 (\text{A} \rightarrow \text{B})$	$k_1 (2 \text{ B} \rightarrow \text{O}_2)$	$q_2 (\text{O}_2 \rightarrow \text{X})$
40.7	0.287	$2.45 \cdot 10^{-6}$	0.00275

An analogous bimolecular pathway was also modelled in which **B** is generated from **A** by a hypothetical two-photon absorption process (see Figure 10.5-2). It should be noted that in this case, two-photon absorption refers to simultaneous two-photon absorption typically only observed with high intensity light sources such as lasers. Hence, it does not refer to the sequential two-photon absorption discussed in other parts of this work.

As can be seen in Figure 10.5-2B, this model yields an inferior fit to the experimental data compared to the regular bimolecular pathway (see Figure 10.5-1B) or the sequential two-photon model (see Figure 10.3-1). Furthermore, also in this case all photons are absorbed by **A**, which is inconsistent with the wavelength dependency data for this reaction, as discussed above. Lastly, simultaneous photon absorption is typically only observed when using light sources with very high photon flux densities (such as ultrafast lasers). However, for the shown experimental data, an incoherent light source with a comparatively low flux density was used, rendering simultaneous two-photon absorption unlikely.

Based on these arguments, we conclude that the shown reaction pathway is likely not a valid description of the present reaction system.

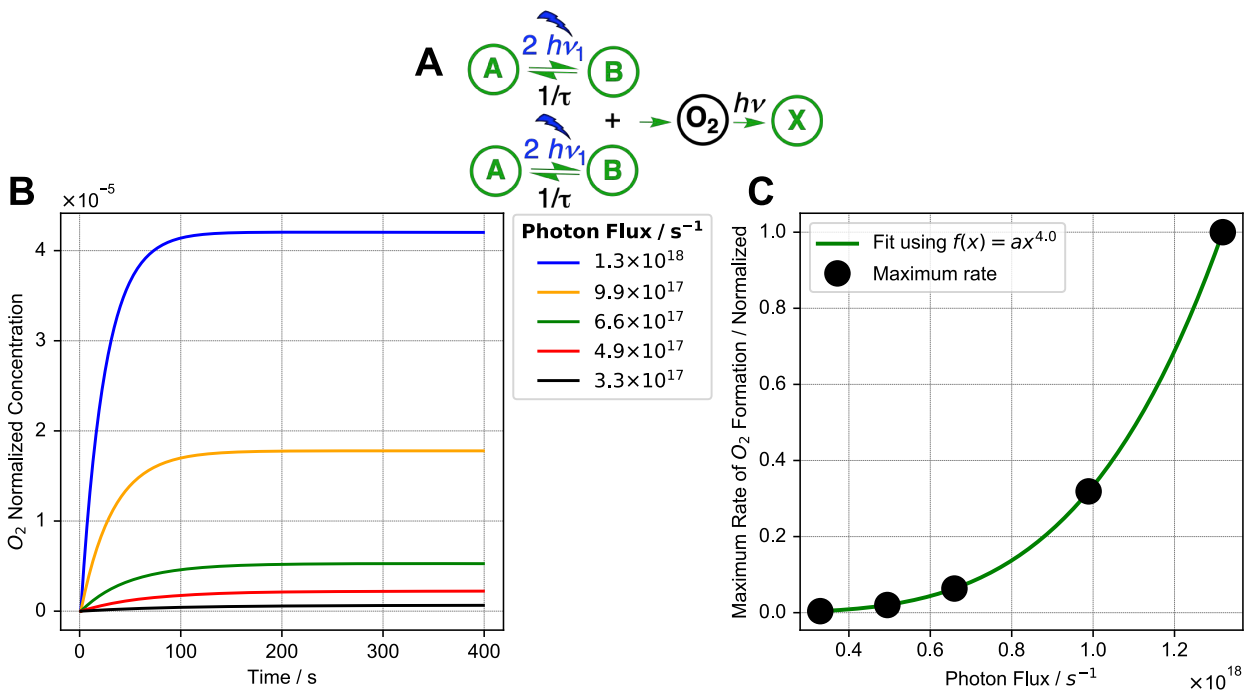


Figure 10.5-3 Photochemical kinetic model for bimolecular pathway with two-photon generation of short-lived intermediate

A Kinetic scheme showing bimolecular reaction pathway with two-photon generation of intermediate.

B Plot of bimolecular two-photon model with parameters shown in Table 10.5-3.

C Maximum rate/photon flux relationship for bimolecular two-photon model shown in **B**.

Table 10.5-3 Plotting parameters for bimolecular two-photon pathway with short-lived intermediate

Lifetime τ ($B \rightarrow A$) / μs	$q_1(A \rightarrow B)$	$k_1(2B \rightarrow O_2)$	$q_2(O_2 \rightarrow X)$
40.7	0.287	0.245	0.00275

Figure 10.5-3 shows the same bimolecular two-photon pathway as Figure 10.5-2, but the optimized model parameters were changed to instead model a relatively short-lived intermediate **B** with a lifetime of 40.7 μs . As can be seen in Figure 10.5-3C, when **B** is short-lived, a quartic relationship between maximum rate and photon flux results. This illustrates that there is only a relatively small window of lifetimes for **B** in which the maximum rate/photon flux relationship would be consistent with the experimentally observed quadratic relationship. In addition to the points detailed above, this is another reason to believe that the bimolecular two-photon pathway is not a suitable model to describe the present reaction.

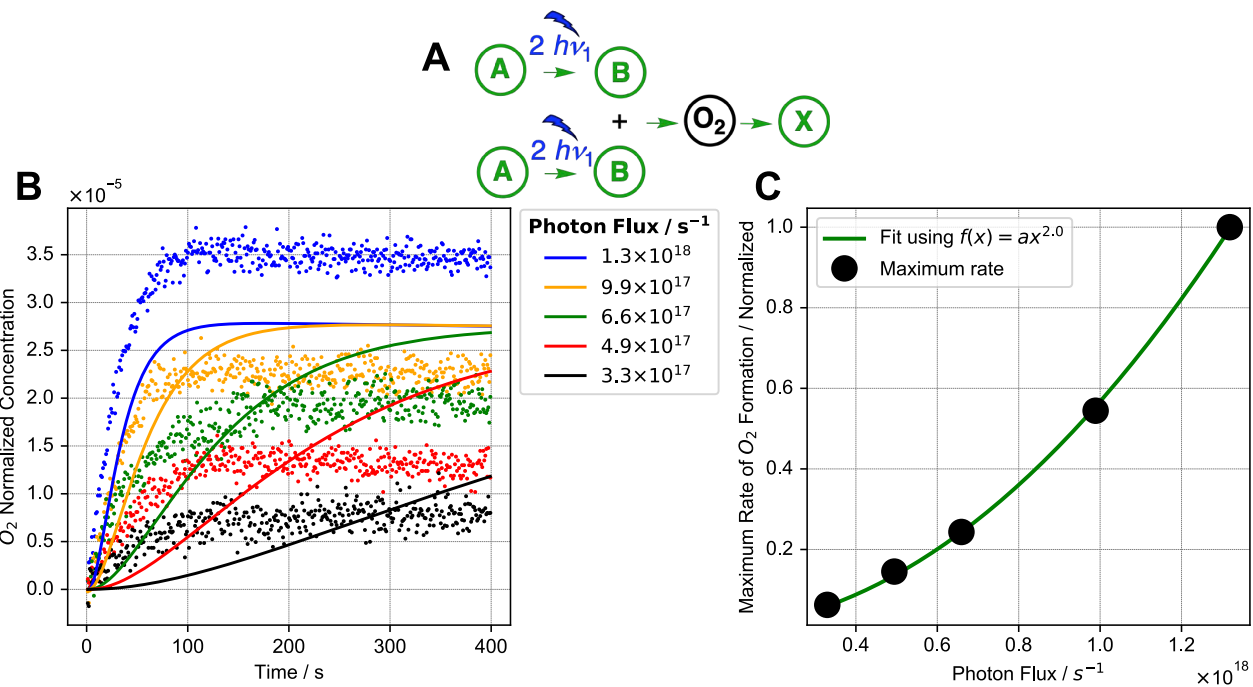


Figure 10.5-4 Photochemical kinetic model for bimolecular pathway with two-photon generation of stable intermediate

A Kinetic scheme showing bimolecular reaction pathway with two-photon generation of stable intermediate.

B Fit of bimolecular two-photon model to experimental data.

C Maximum rate/photon flux relationship for bimolecular two-photon model.

Table 10.5-4 Optimized parameters for bimolecular two-photon pathway with stable intermediate

$q_1(A \rightarrow B)$	$k_1(2B \rightarrow O_2)$	$k_2(O_2 \rightarrow X)$
$1.84 \cdot 10^{-4}$	$2.77 \cdot 10^{-5}$	0.986

Given that a short-lived intermediate **B** can give rise to an inconsistent description of the experimental data, we also modelled the bimolecular two-photon pathway with a stable intermediate **B** (see Figure 10.5-4). In this case, the O_2 consuming reaction had to be modelled as a thermal instead of photochemical reaction because for a photochemical consumption reaction, no reasonable solution could be found. However, even with this adjustment, this model does not yield an adequate description of the experimental data (see Figure 10.5-4B).

10.5.2 Three-photon pathway with one stable intermediate

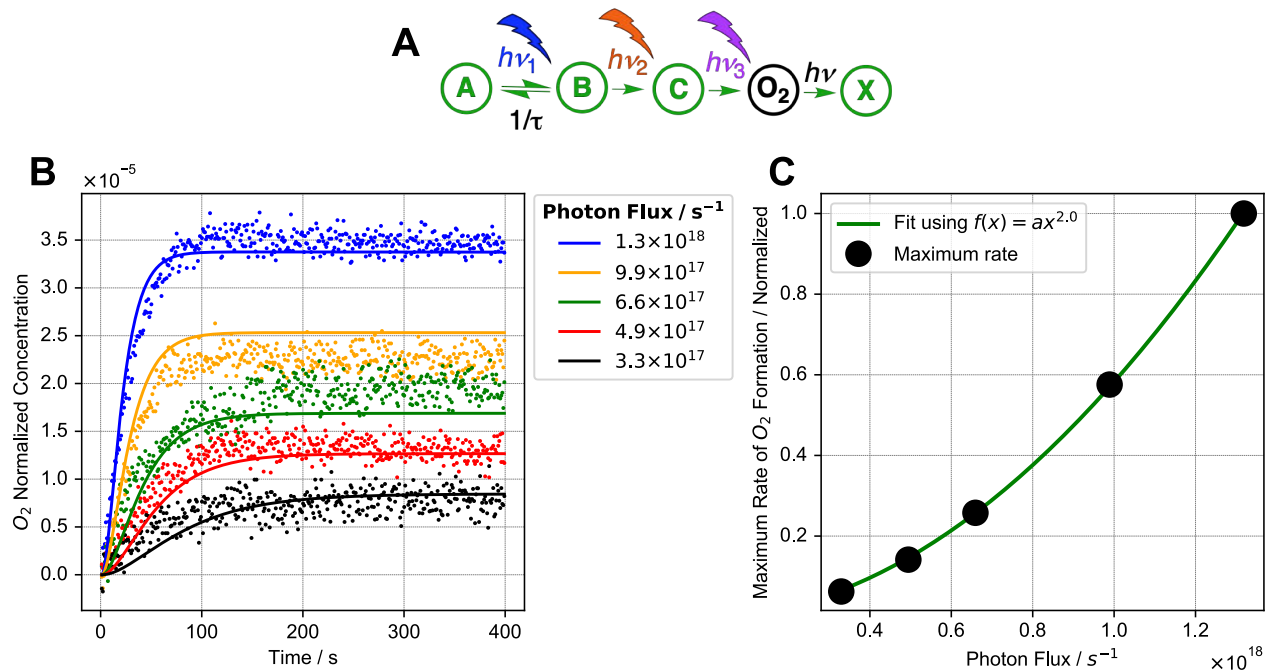


Figure 10.5-5 Photochemical kinetic model for three-photon pathway with one stable intermediate

A Kinetic scheme showing three-photon pathway with one stable intermediate.

B Fit of three-photon pathway to experimental data.

C Maximum rate/photon flux relationship for three-photon pathway.

Table 10.5-5 Optimized parameters for three-photon pathway (with one stable intermediate)

Lifetime τ ($\mathbf{B} \rightarrow \mathbf{A}$) / μs	$q_1 (\mathbf{A} \rightarrow \mathbf{B})$	$q_2 (\mathbf{B} \rightarrow \mathbf{C})$	$q_3 (\mathbf{C} \rightarrow \mathbf{O}_2)$	$q_3 (\mathbf{O}_2 \rightarrow \mathbf{X})$
16.5	0.528	0.0012	0.0079	0.0047

A three-photon pathway was modelled analogously to the two-photon model, but instead of **B** reacting directly to \mathbf{O}_2 in a photochemical reaction, it reacts first to **C**, which then reacts in a third photochemical step to \mathbf{O}_2 . **C** is a stable intermediate and does not revert back to a previous reaction intermediate or the starting complex. The fit of this kinetic model to experimental data can be seen in Figure 10.5-5B. While this optimized model also results in a square maximum rate/photon flux relationship (see Figure 10.5-5C), the fit to experimental data is inferior compared to the two-photon model. This is because the presence of a stable intermediate (**C**) leads to an induction period (especially apparent for the lowest photon flux level). This induction period is due to accumulation of **C** over time, which increases the \mathbf{O}_2 formation rate accordingly. No induction period has been observed experimentally, making it unlikely that such a mechanism is operative. These observations and conclusions also hold when **C** does revert back to a previous intermediate or the starting complex but with a lifetime which is comparatively long on the experimental timescale (400 s).

Using a global optimization algorithm (Differential Evolution) instead of the local Nelder-Mead algorithm, a better solution can be found (see Figure 10.5-6). For this solution, the induction period is only very short, yielding a better fit to the experimental data. However, there is only a small range of parameters for which a three-photon pathway with one stable intermediate yields a consistent description of the experimental data. We therefore consider it unlikely that this pathway is operative, instead of the two-photon pathway which is valid over a much wider range of parameters.

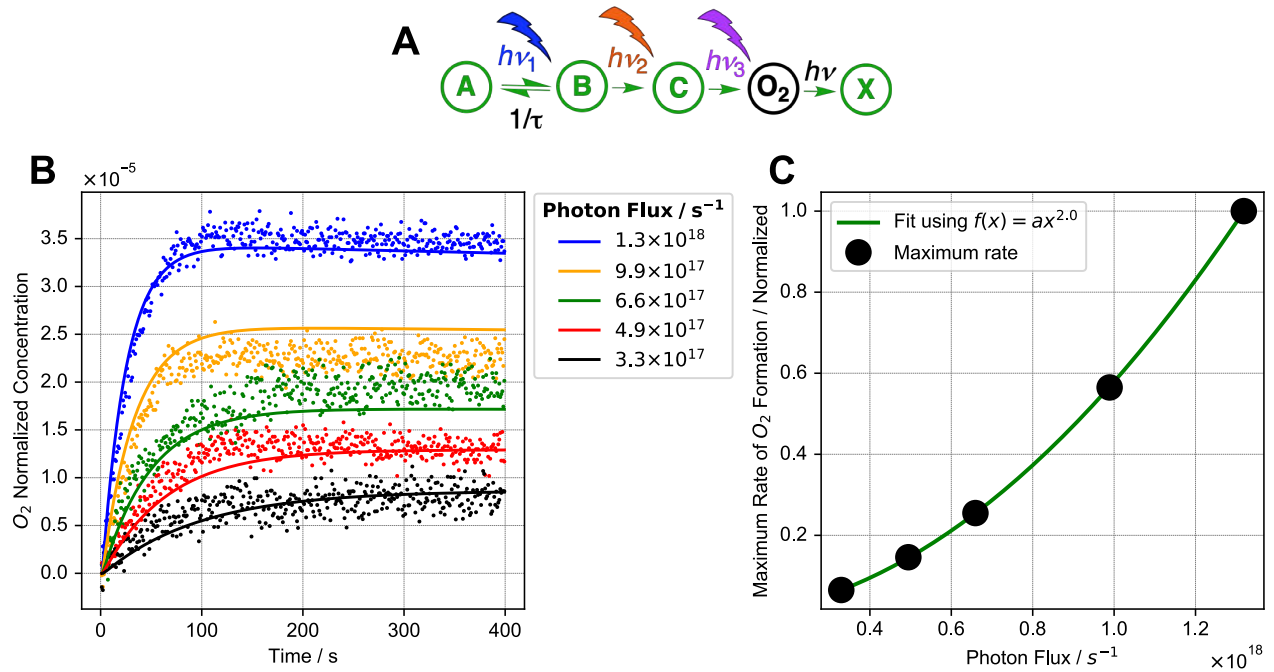


Figure 10.5-6 Photochemical kinetic model for three-photon pathway with one stable intermediate, optimized using Differential Evolution

A Kinetic scheme showing three-photon pathway with one stable intermediate.

B Fit of three-photon pathway to experimental data.

C Maximum rate/photon flux relationship for three-photon pathway.

Table 10.5-6 Optimized parameters for three-photon pathway (with one stable intermediate), optimized using differential evolution

Lifetime τ ($B \rightarrow A$) / μs	$q_1 (A \rightarrow B)$	$q_2 (B \rightarrow C)$	$q_3 (C \rightarrow O_2)$	$q_3 (O_2 \rightarrow X)$
1339.7	0.392	0.00062	0.00275	0.14

10.5.3 Three-photon pathway with two transient intermediates

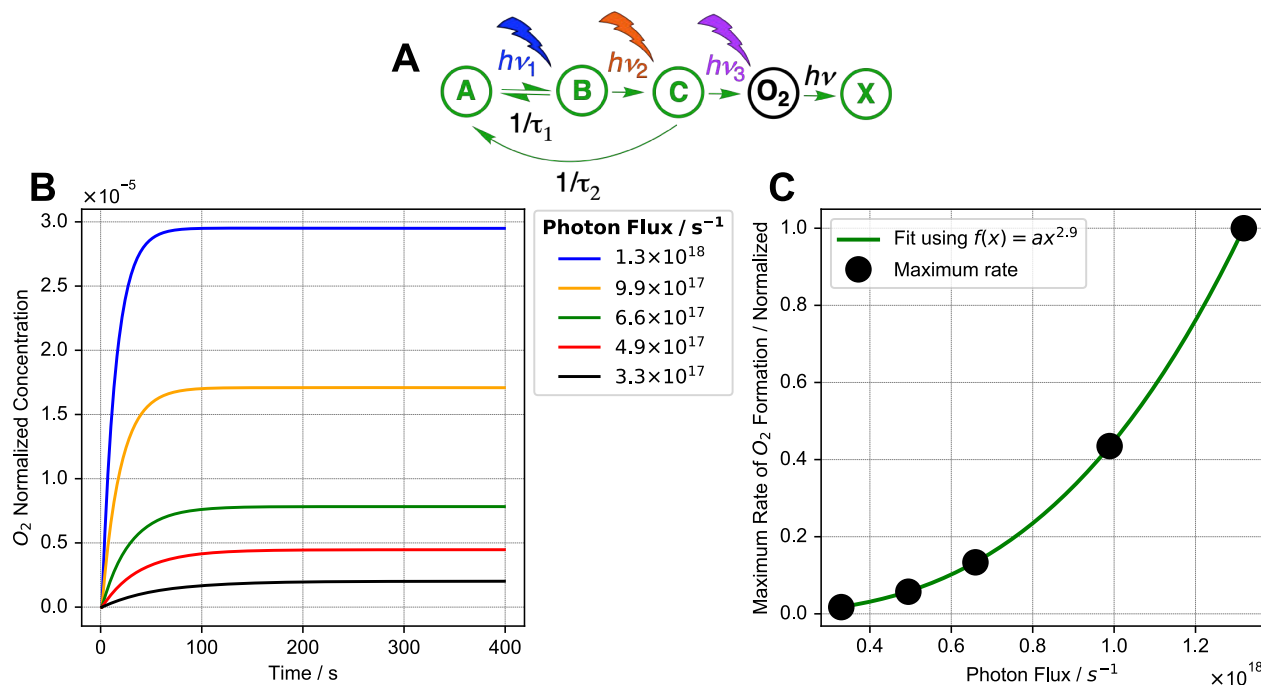


Figure 10.5-7 Photochemical kinetic model for three-photon pathway with two transient intermediates

A Kinetic scheme showing three-photon pathway with two transient intermediates.

B Plot of three-photon pathway with parameters shown in Table 10.5-7.

C Maximum rate/photon flux relationship for three-photon pathway shown in B

Table 10.5-7 Plotting parameters for three-photon pathway (with two transient intermediates)

Lifetime τ_1 (B → A) / ms	q_1 (A → B)	q_2 (B → C)	q_3 (C → O_2)	q_3 (O_2 → X)	Lifetime τ_2 (C → A) / ms
8.7	0.969	0.0013	0.0075	0.0048	8.7

A three-photon pathway with two transient intermediates was modelled as described in 10.5.2, but adding the back-reaction **C** → **A**. Figure 10.5-7B shows a plot of this kinetic model using the parameters in Table 4.1-1. These parameters were not optimized by fitting the model to experimental data. Instead, they serve to illustrate that when both **B** and **C** are transient intermediates with sufficiently short lifetimes ($\tau_{1/2} = 8.7$ ms), no noticeable induction period occurs but there is an approximately cubic relationship between maximum rate and photon flux (see Figure 10.5-7C). As the experimentally observed rate/flux relationship is square, this would be inconsistent with those results.

When this kinetic model is fitted to the experimental data (see Figure 10.5-8), a good fit can be obtained using Differential Evolution. Furthermore, for the optimized parameters, there is a square maximum rate/photon flux relationship (see Figure 10.5-8C). This is because one of the intermediates (**B** in this case) is modelled to be sufficiently long lived (τ_1 ca. 1 s) to lower the order of the rate/flux dependency (same logic as in Figure 10.3-1) but not so long lived that an induction period results. The other intermediate (**C** in this case) is short lived (τ_2 ca. 1 ms), giving rise to the square rate/flux dependency. In this range for the lifetimes of **B** and **C**, the three-photon pathway with two transient intermediates becomes kinetically identical to the two-photon pathway (in terms of experimental data fit quality and square rate/flux dependency). Since the three-photon pathway also includes multiple absorbing species, its wavelength dependence could be consistent with experimental results.

In our view, however, it is rather unlikely that a three-photon pathway instead of a two-photon pathway is operative in the reaction. This is because there is only a small range of lifetimes for **B** and **C** where the three-photon pathway would be consistent with experimental data, while this range is much larger for a two-photon pathway. Furthermore, based on our computational studies (see manuscript and section 11), there is no energetic necessity for a third photon absorption. Overall,

the two-photon pathway therefore offers a fully consistent description of the reaction with fewer variables and validity over a wider range compared to a potential three photon pathway.

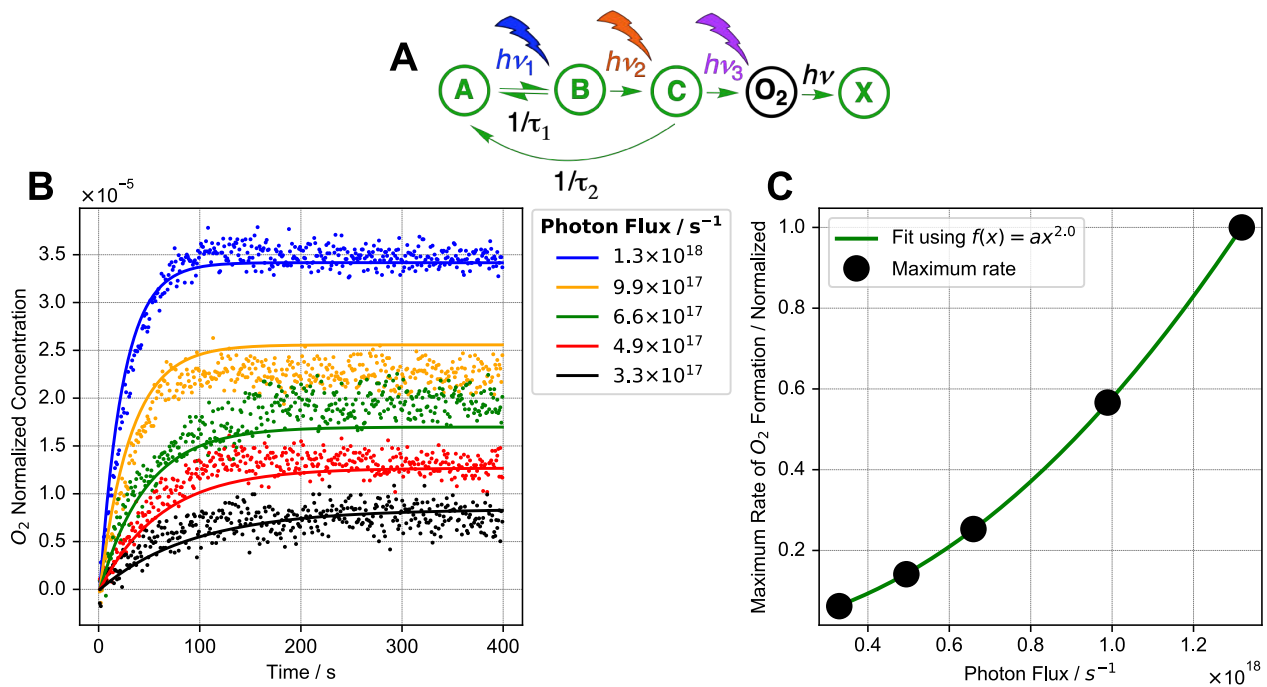


Figure 10.5-8 Photochemical kinetic model for three-photon pathway with two transient intermediates, fitted to experimental data

A Kinetic scheme showing three-photon pathway with two transient intermediates.

B Fit of three-photon pathway (with two transient intermediates) to experimental data.

C Maximum rate/photon flux relationship for three-photon pathway shown in **B**

Table 10.5-8 Optimized parameters for three-photon model (with two transient intermediates)

Lifetime $\tau_1 (B \rightarrow A) / ms$	$q_1 (A \rightarrow B)$	$q_2 (B \rightarrow C)$	$q_3 (C \rightarrow O_2)$	$q_3 (O_2 \rightarrow X)$	Lifetime $\tau_2 (C \rightarrow A) / ms$
983	0.99	0.00043	0.014	0.0029	1.1

11 Computational Section

11.1 Computational Methods

11.1.1 DFT Methods

All DFT calculations were performed using the PBE0 (PBE1PBE) hybrid functional, along with Grimme D3 dispersion with Becke-Johnson damping (GD3BJ). For all calculations, the SDD basis set and effective core potential was used for ruthenium, while all other atoms were described using the indicated basis set. Closed shell calculations (singlet) were performed as restricted (RHF), while open shell (doublet and triplet) calculations were performed as unrestricted (UHF) calculations. Calculations were performed using three different model chemistries:

1. Dimeric model of two ruthenium complexes interacting via non-covalent bonds. This model was used for [A], [B], [C], TS-[CD] and [D] [F] (dimer model).
2. Monomeric model, in which only the ruthenium complex on which O-O bond formation takes place (or [F]) is modeled. This model was used for [A-Mono], [B-Mono], [C-Mono], [D], [E] and [F].
3. In some cases, a simplified version of the monomeric model was used, in which the ligand *t*Bu and Et groups were replaced by methyl. Use of this model is indicated by "Me model".

Use of the “-Up” designation indicates opposite (relative to the normal models) PNN ligand conformation. Geometry optimizations and frequency calculations (298 K, 1 atm) were performed in the gas phase using the cc-pVDZ basis set. Structures were confirmed to be minima or first-order saddle points by having either zero (minima) or one (first-order saddle points) imaginary frequencies. Reported gas phase Gibbs free energies are based on Gibbs free energies obtained using frequency calculations.

Single point energy calculations were performed using the cc-pVTZ basis set and SMD solvation (the solvent being water). Reported solution phase Gibbs free energies are based on singlet point energy calculations, corrected by using the thermal correction to Gibbs free energy obtained using frequency calculations.

Electronic excitations and theoretical UV/Vis spectra were calculated using TD-DFT, using the cc-pVDZ basis set and SMD solvation (in water). Typically, the 25 lowest energy transitions were computed. Theoretical UV/Vis spectra were constructed using the calculated transition wavelengths and oscillator strengths. Furthermore, transitions were broadened using Gaussian curves with a half-width at half-height of 0.333 eV. To visualize excitations, natural transition orbitals were computed, and the resulting hole-particle pairs with the highest contribution (typically > 1.7) are shown.

Scans were performed as relaxed potential energy surface scans using the cc-pVDZ basis set in the gas phase. For Scan-[DE]T₀, single point energy calculations using cc-pVTZ and SMD solvation (water) were performed for all optimized geometries along the scan. Since frequency calculations are not meaningful for scan geometries, only relative energies instead of Gibbs free energies (either gas phase or solution phase) are reported.

NMR calculations were performed using the cc-pVTZ basis set and SMD solvation (water). Reported chemical shifts are relative to tetramethylsilane (¹H) or H₃PO₄ (³¹P).

All calculations were performed using Gaussian 16, Revision A.03.¹¹ Structures were prepared and visualized using Avogadro.¹² Furthermore, surfaces for closed shell molecules were also visualized using Avogadro. Surfaces for open shell molecules were visualized using Gabedit.¹³ Simplified structures were visualized using PyMOL.¹⁴ Visualizations were rendered using POV Ray.¹⁵ In all visualizations, ruthenium is shown in turquoise, phosphorous in orange, oxygen in red, nitrogen in blue, carbon in grey and hydrogen in white. For surfaces: orbitals are shown in yellow/magenta and spin densities are shown in green.

11.1.2 CASSCF Methods

All CASSCF calculations were performed as state averaged (SA)-CASSCF calculations, using the five lowest energy states weighed equally. An active space consisting of 13 electrons in 11 orbitals, CAS(13,11), was used (see Figure 11.3-2). The active space consists of two Ru-OH σ and σ^* , four pyridine π and π^* , two Ru-CO π and π^* (combining with oxygen lone pair orbitals), two OH and O lone pair and the singly occupied O lone pair orbitals.

The ANO-RCC-VDZ all-electron basis set was used for all atoms (which includes relativistic effects). To improve computational performance, the resolution of identity Cholesky decomposition (RICD) method was used.^{16,17} For computational tractability, the simplified monomeric model using methyl groups instead of *t*Bu and ethyl on the ligand (Me model) was used for all CASSCF calculations.

For **[B-Mono]** and **[C-Mono]**, geometries obtained using DFT geometry optimization were used. The geometries of conical intersections (**[BC]** D₂/D₁ MECI and **[BC]** D₁/D₀ MECI) were optimized using CASSCF with analytical gradients in the gas phase.¹⁸ Gas phase energies are reported relative to the energy of **[B-Mono]**D₀ root 1.

Solvation was taken into account by performing single point calculations for all intermediates with the PCM conductor version and water as the solvent. For **[B-Mono]**, equilibration solvation based on root 1 was used for root 1, while non-equilibrium solvation based on root 3 was used for all other roots (modeling vertical excitation from root 1 to root 3). For **[BC]** D₂/D₁ MECI, equilibrium solvation based on root 3 was used for all roots. For **[BC]** D₁/D₀ MECI, equilibrium solvation based on root 2 was used for all roots. For **[C-Mono]**, equilibrium solvation based on root 1 was used. Solution phase energies are reported relative to the energy of **[B-Mono]**D₀ root 1.

All calculations were performed using OpenMolcas version 19.11.^{19,20} Visualizations were performed using Pegamoid. In all visualizations, ruthenium is shown in turquoise, phosphorous in orange, oxygen in red, nitrogen in blue, carbon in grey and hydrogen in white. For surfaces: orbitals are shown in yellow/magenta, spin densities are shown in green and transition difference densities are shown in red/blue.

11.2 DFT Results

11.2.1 Relative Energies of [A] and [B] Isomers, Oxo Dimer, $[F]S_0 \rightarrow [A\text{-Mono}]S_0$

Table 11.2-1 Relative energies of $[A]S_0$ and $[A\text{-Mono}]S_0$

	$[A]S_0$	$[A\text{-Mono}]S_0$
$\Delta G^\circ(\text{SMD}) / \text{kJ/mol}$	33.7	0.00
$\Delta G^\circ(\text{Gas Phase}) / \text{kJ/mol}$	0.00	10.5

In Table 11.2-1 it can be seen that while dimeric $[A]S_0$ is predicted to be more stable in the gas phase compared to monomeric $[A\text{-Mono}]S_0$, it is predicted to be less stable in solution. However, the lower stability in solution might be attributed to the challenging description of hydrogen bonding energies using DFT.²¹

Table 11.2-2 Relative energies of [A] isomers

	$[A]S_0$	$[A\text{-RR}]S_0$	$[A\text{-RS-1}]S_0$	$[A\text{-RS-2}]S_0$	$[A]T_0$
$\Delta G^\circ(\text{SMD}) / \text{kJ/mol}$	0.00	2.0	4.4	7.9	91.7

Different isomers of $[A]S_0$ were computed, varying in their configuration ($[A\text{-Mono}]S_0$ is chiral, therefore either a homo- or heterochiral dimer can be formed) and conformation of the ligand. Among the computed isomers, $[A]S_0$ was found to be the most stable, although the energy differences are small. $[A]T_0$ was found to be relatively low in energy, being only ca. 92 kJ/mol less stable than $[A]S_0$.

Table 11.2-3 Relative energies of $[B]T_0$ isomers

	$[B]T_0$	$[B\text{-Trans}]T_0$
$\Delta G^\circ(\text{SMD}) / \text{kJ/mol}$	35.8	0.00

Table 11.2-4 Relative energies of [B-Mono]D₀ isomers

	[B-Mono]D ₀	[B-Mono-Up]D ₀	[B-Mono-Trans]D ₀	[B-Mono-Trans-Up]D ₀
ΔG°(SMD) / kJ/mol	28.8	36.3	6.4	0.00

When comparing [B] and [B-Trans] in both the dimeric and monomeric model, [B-Trans] was found to be slightly more stable.

Table 11.2-5 Relative energy of [B-Alt]T₀

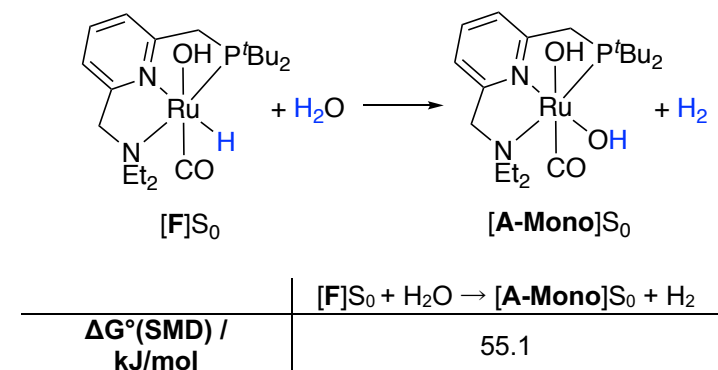
	[B-Alt]T ₀
ΔG°(SMD) / kJ/mol	33.3 ([B-Alt]T ₀ + H ₂ O + [F]S ₀ relative to [B]T ₀) 69.1 ([B-Alt]T ₀ + H ₂ O + [F]S ₀ relative to [B-Trans]T ₀)
ΔG°(Gas Phase) / kJ/mol	163.6 ([B-Alt]T ₀ + H ₂ O + [F]S ₀ relative to [B-Trans]T ₀)

[B-Alt]T₀ would be an alternative reaction intermediate, obtained via two consecutive proton-coupled electron transfers from [A] (forming one equivalent of [F]S₀ in the process). It is, however, less stable than either [B]T₀ or [B-Trans]T₀.

Table 11.2-6 Relative energy of Oxo Dimer

	[Oxo Dimer]S ₀
ΔG°(SMD) / kJ/mol	51.0 (relative to [A-Mono]S ₀) 17.4 (relative to [A]S ₀)

Table 11.2-7 Reaction Energy for [F]S₀ + H₂O → [A-Mono]S₀ + H₂



Considering the energy change for [F]S₀ + H₂O → [A-Mono]S₀ + H₂ (55.1 kJ/mol) and [A]S₀ → 2 [F]S₀ + O₂ (346.1 kJ/mol), as well as the relative stability of [A]S₀ vs. [A-Mono]S₀ (33.7 kJ/mol), one arrives at an energy change of 490.0 kJ/mol. This value is identical with the energy change of 2 H₂O → O₂ + 2 H₂ when using our DFT methodology, which is in good agreement with the thermodynamical value (4-electron 1.23 V, 474.7 kJ/mol).

11.2.2 TD-DFT Computed UV-Vis Spectra

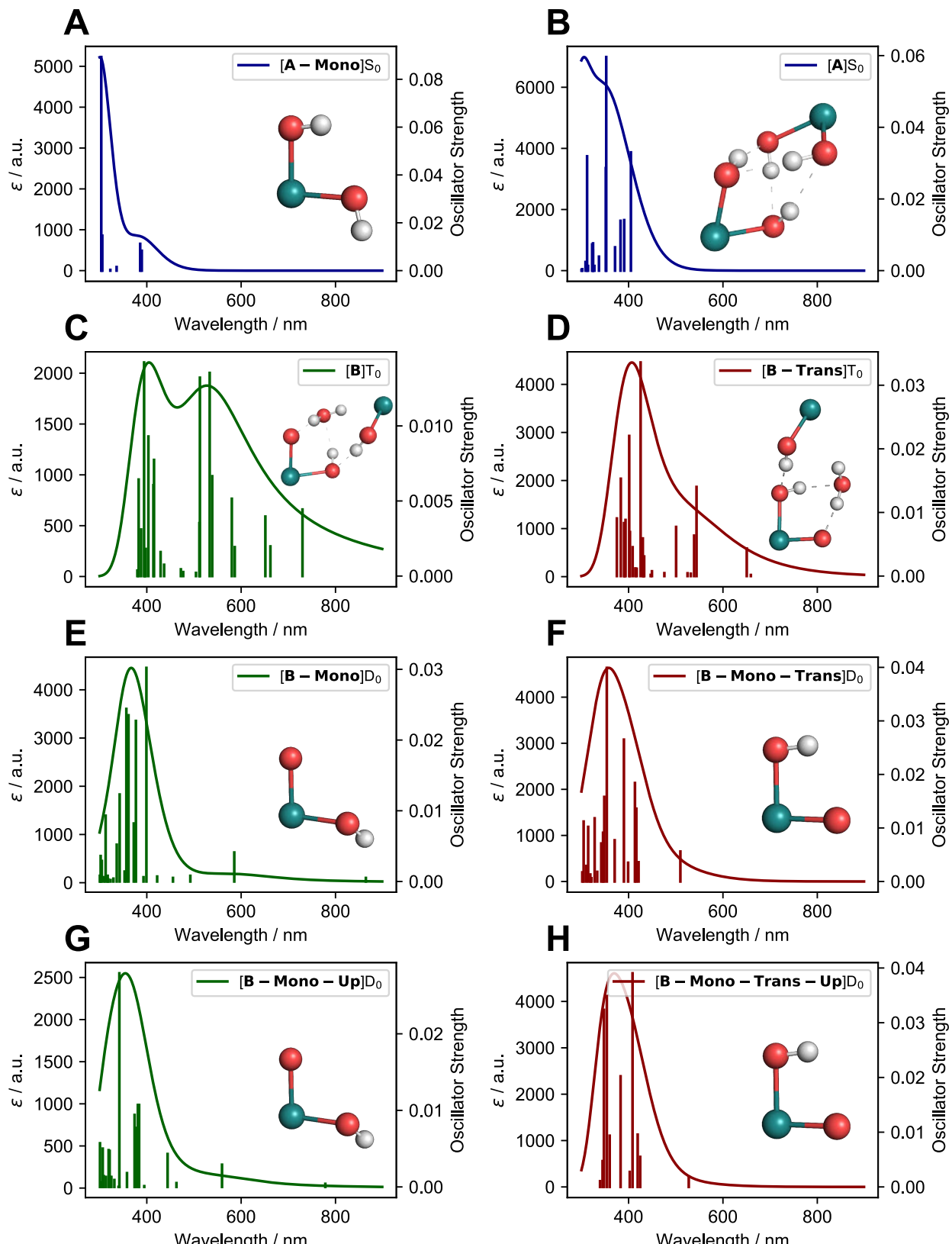


Figure 11.2-1 UV-Vis spectra computed for $[A]S_0$ and $[B]T_0$ along with isomers/monomers

Spectra for **[A]** are shown in blue, **[B]** in green and **[B-Trans]** in red. Vertical lines indicate individual transitions (oscillator strength for these transitions are shown on the right). Smooth curves show the UV-Vis spectrum, which was computed using the sum of Gaussian curves with a half-width half-maximum of 0.333 eV. Insets show the simplified, corresponding molecular structures. “-Up” indicates opposite PNN ligand conformation. Up to 25 transitions between 300 nm and 900 nm are shown.

11.2.3 Natural Transition Orbitals for [A]S₀

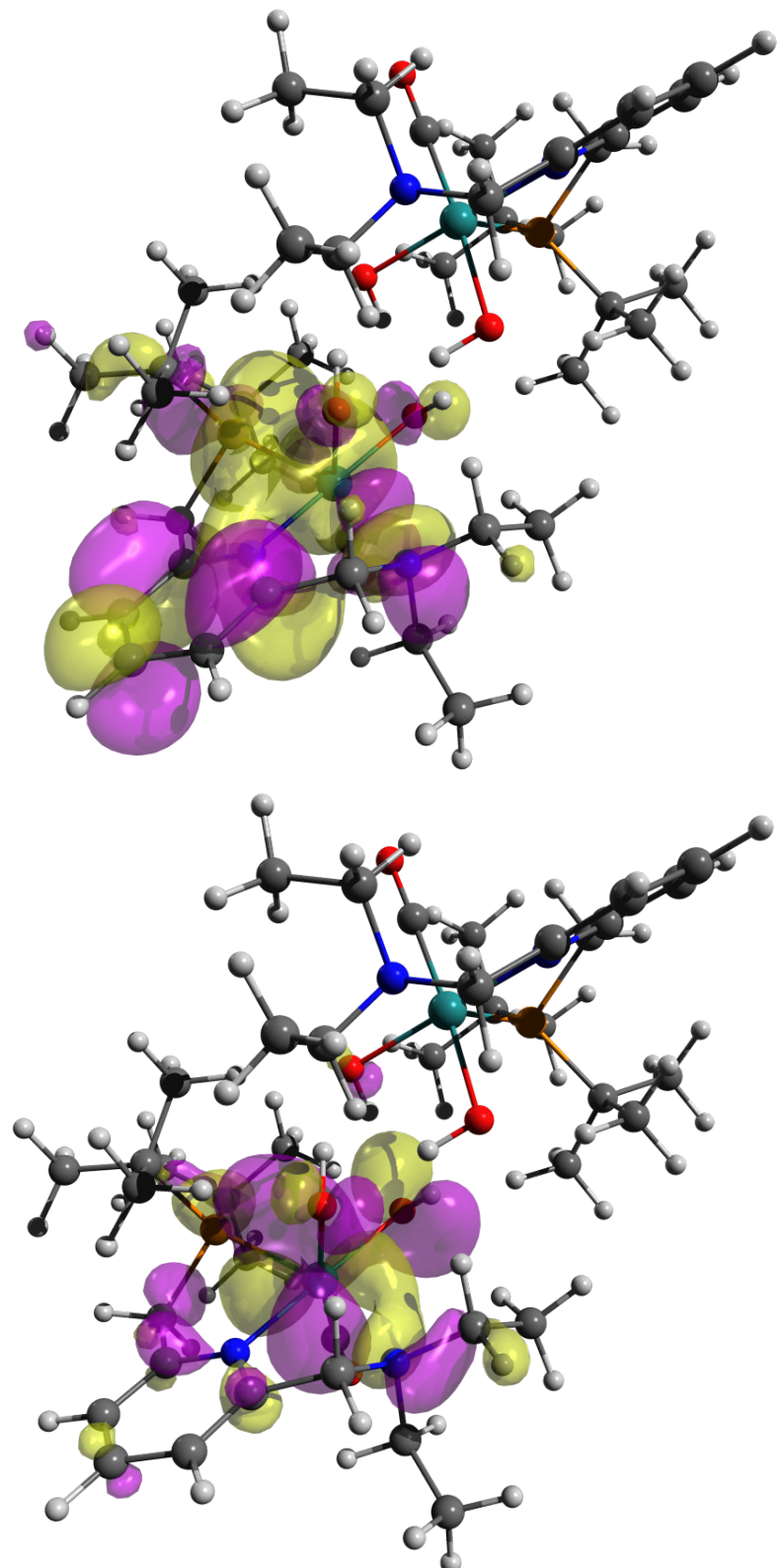


Figure 11.2-2 Transition 1 (405 nm, $f = 0.033$) for [A]S₀, particle (top) and hole (bottom), isovalue = 0.02

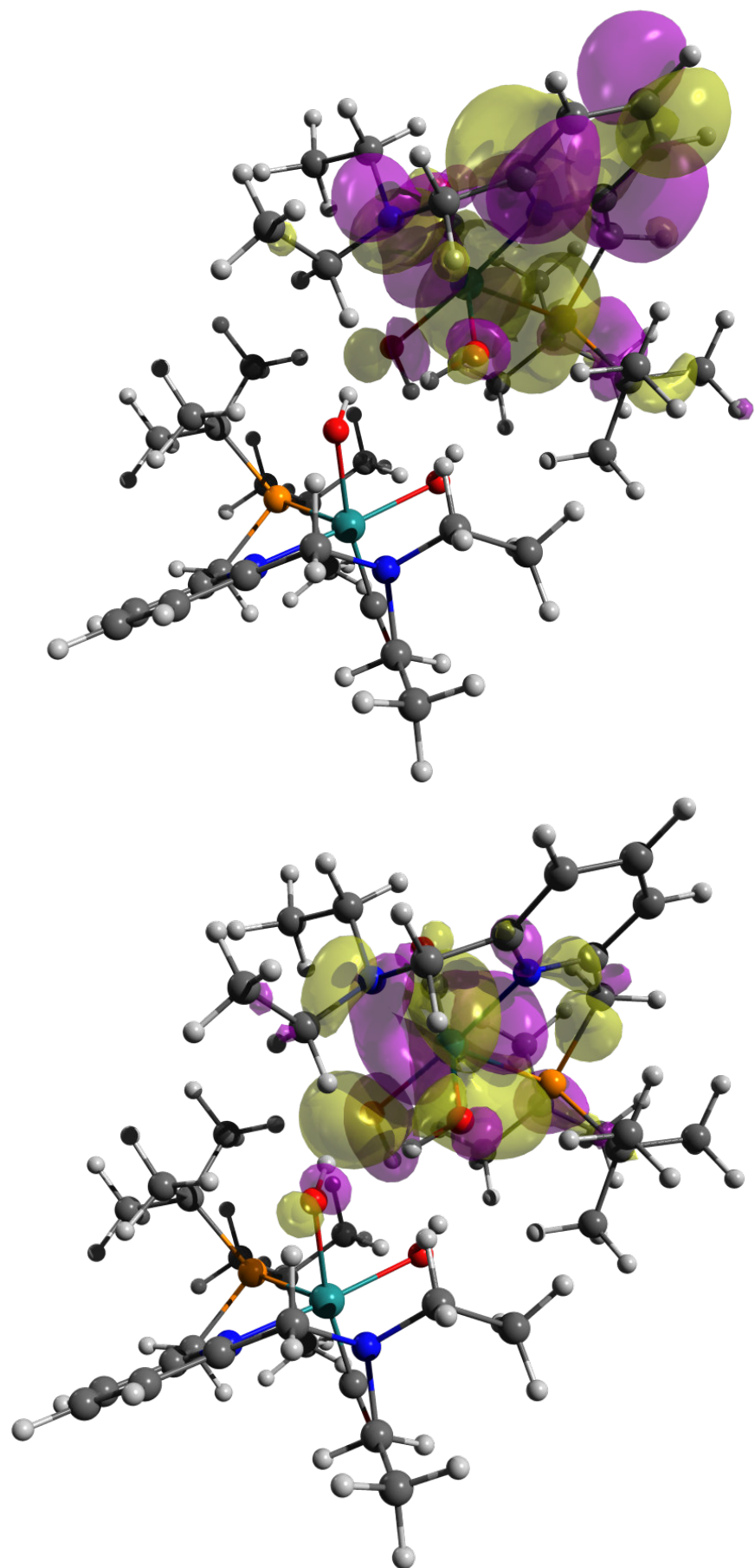


Figure 11.2-3 Transition 2 (391 nm, $f = 0.0141$) for $[A]S_0$, particle (top) and hole (bottom), isovalue = 0.02

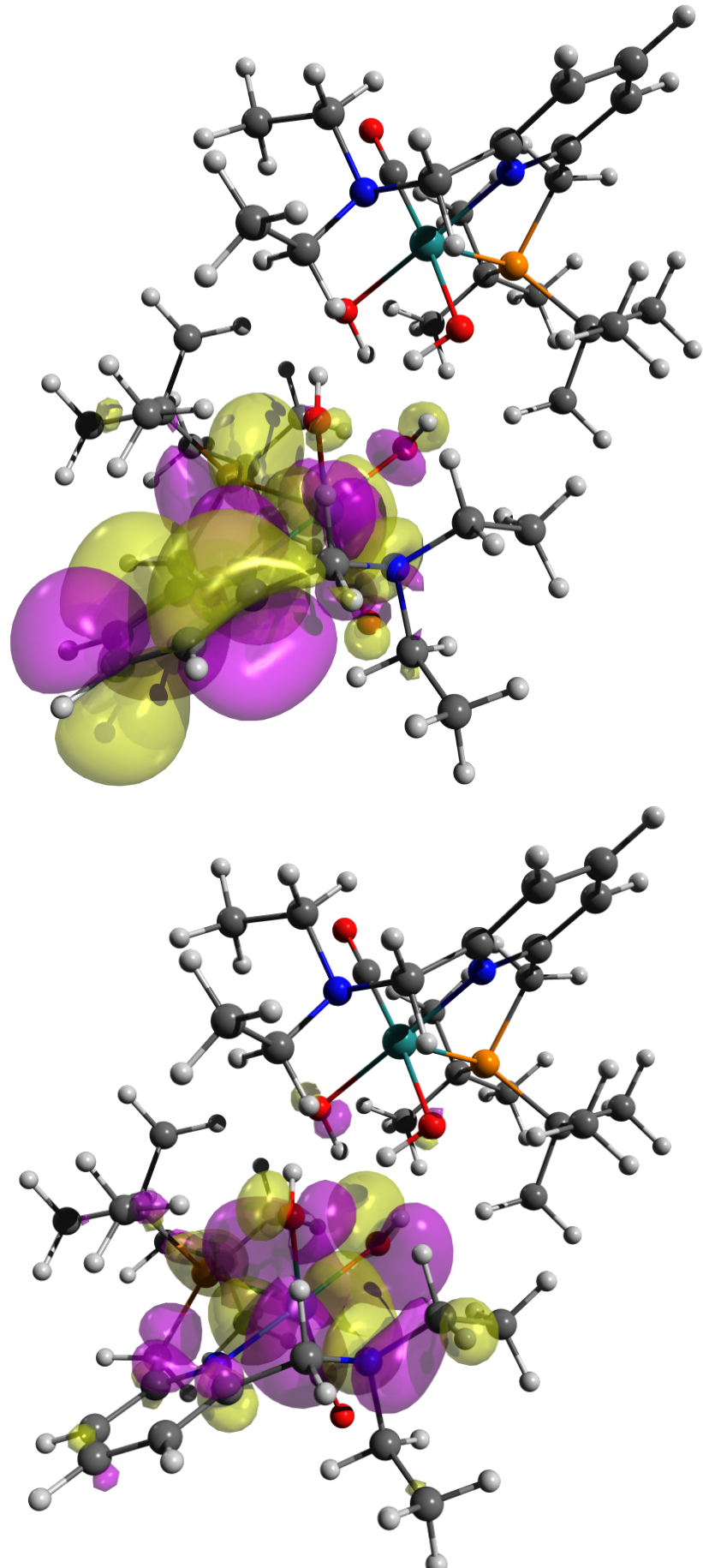


Figure 11.2-4 Transition 3 (383 nm, $f = 0.014$) for $[A]S_0$, particle (top) and hole (bottom), iso-value = 0.02

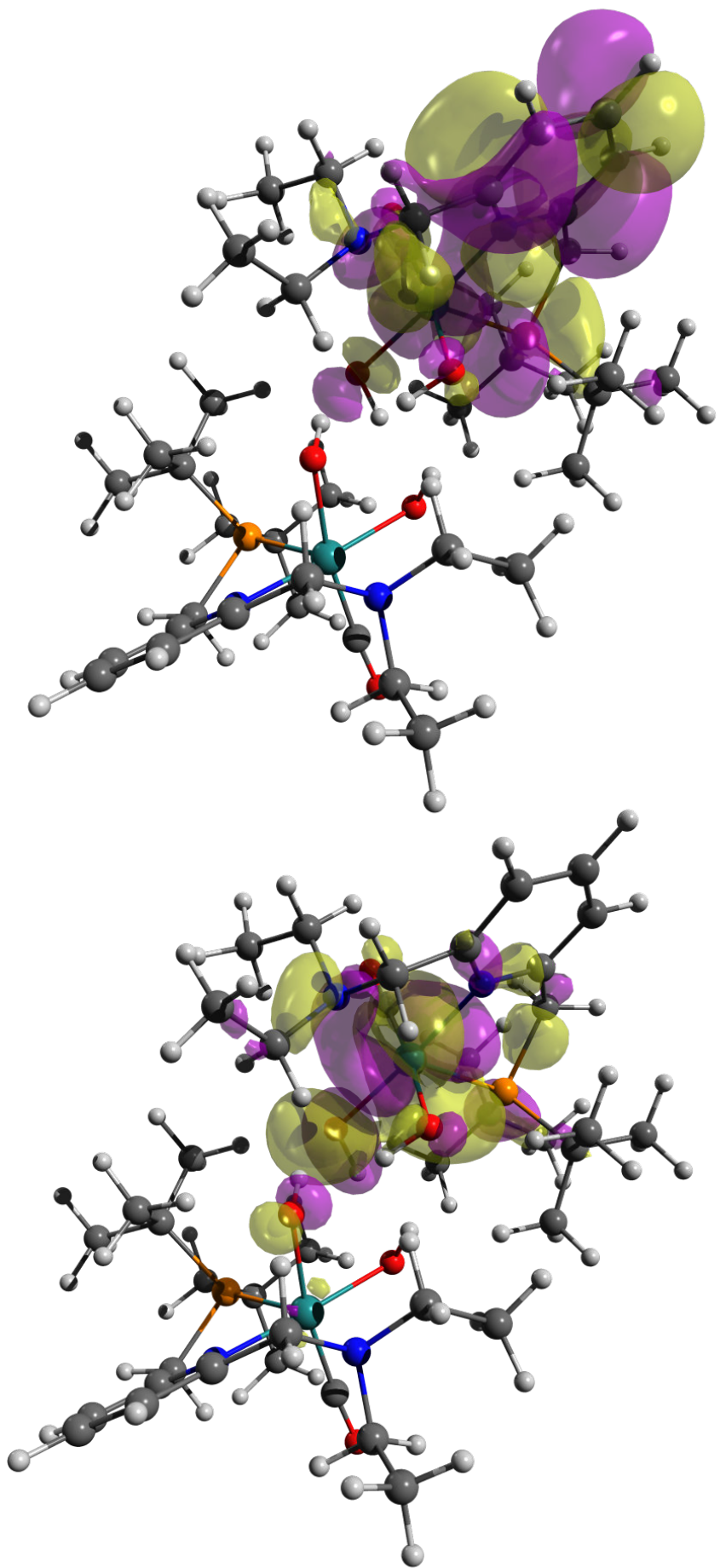


Figure 11.2-5 Transition 4 (371 nm, $f = 0.0065$) for $[A]S_0$, particle (top) and hole (bottom), isovalue = 0.02

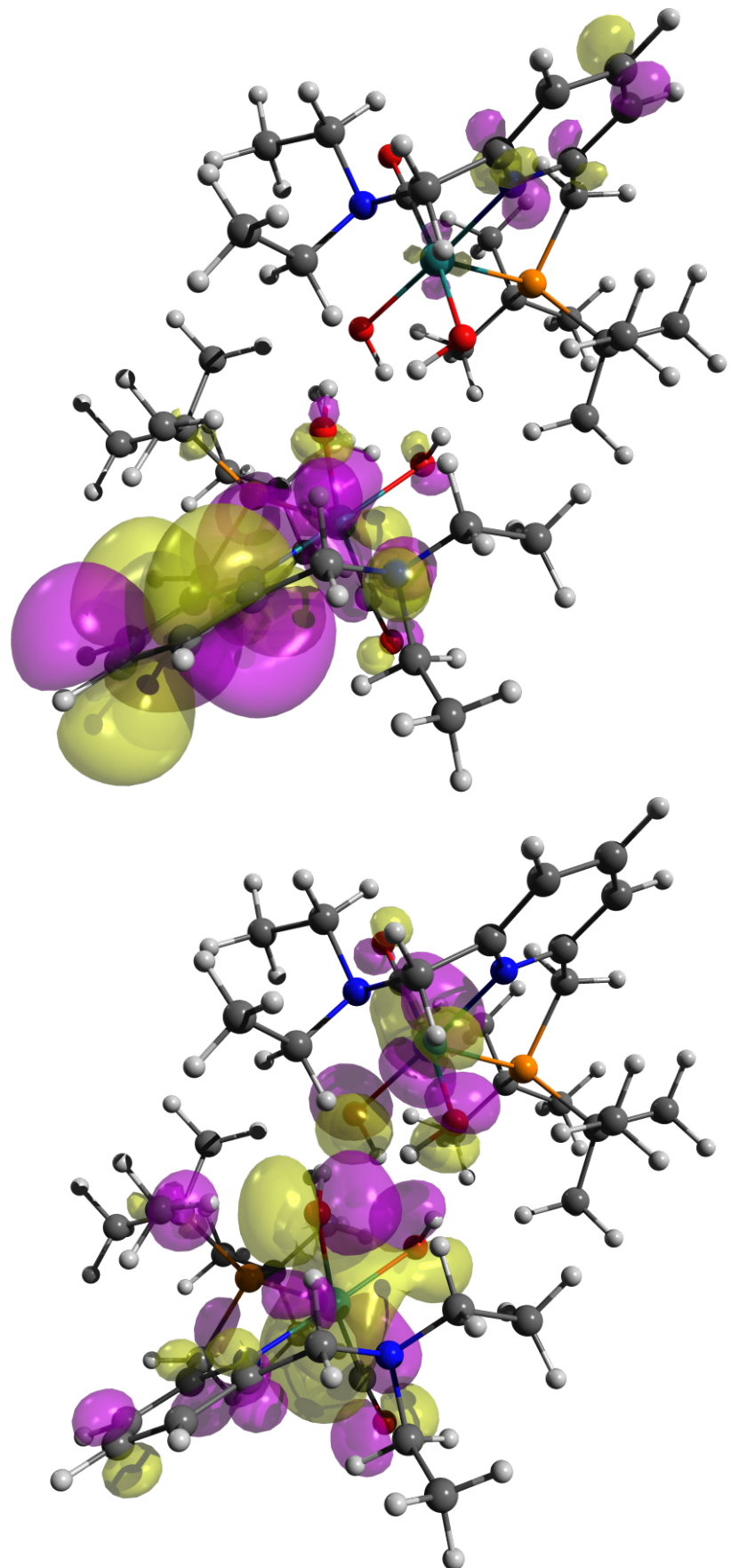


Figure 11.2-6 Transition 5 (353 nm, $f = 0.0596$) for $[A]S_0$, particle (top) and hole (bottom), isovalue = 0.02

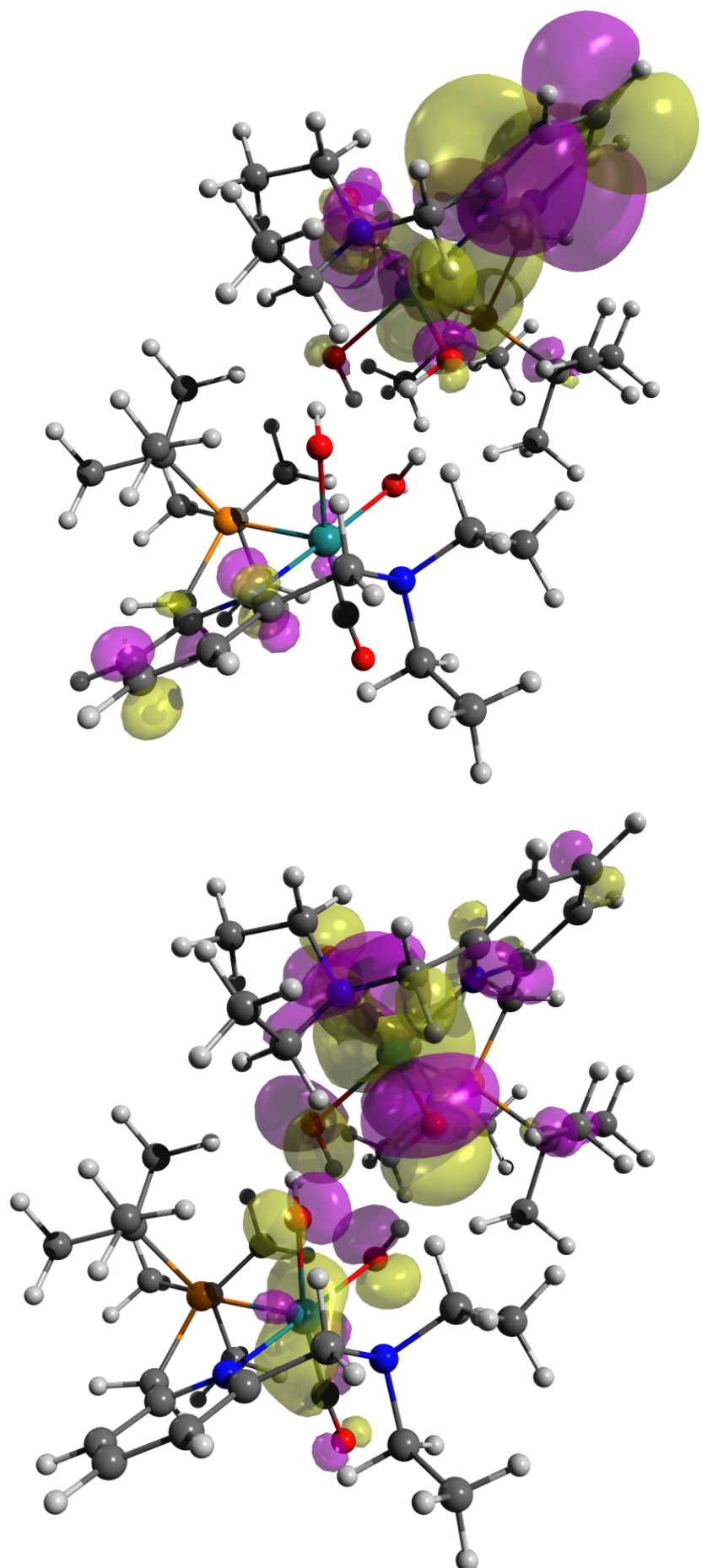


Figure 11.2-7 Transition 6 (352 nm, $f = 0.0287$) for $[A]S_0$, particle (top) and hole (bottom), isovalue = 0.02

11.2.4 Natural Transition Orbitals for $[B]T_0$

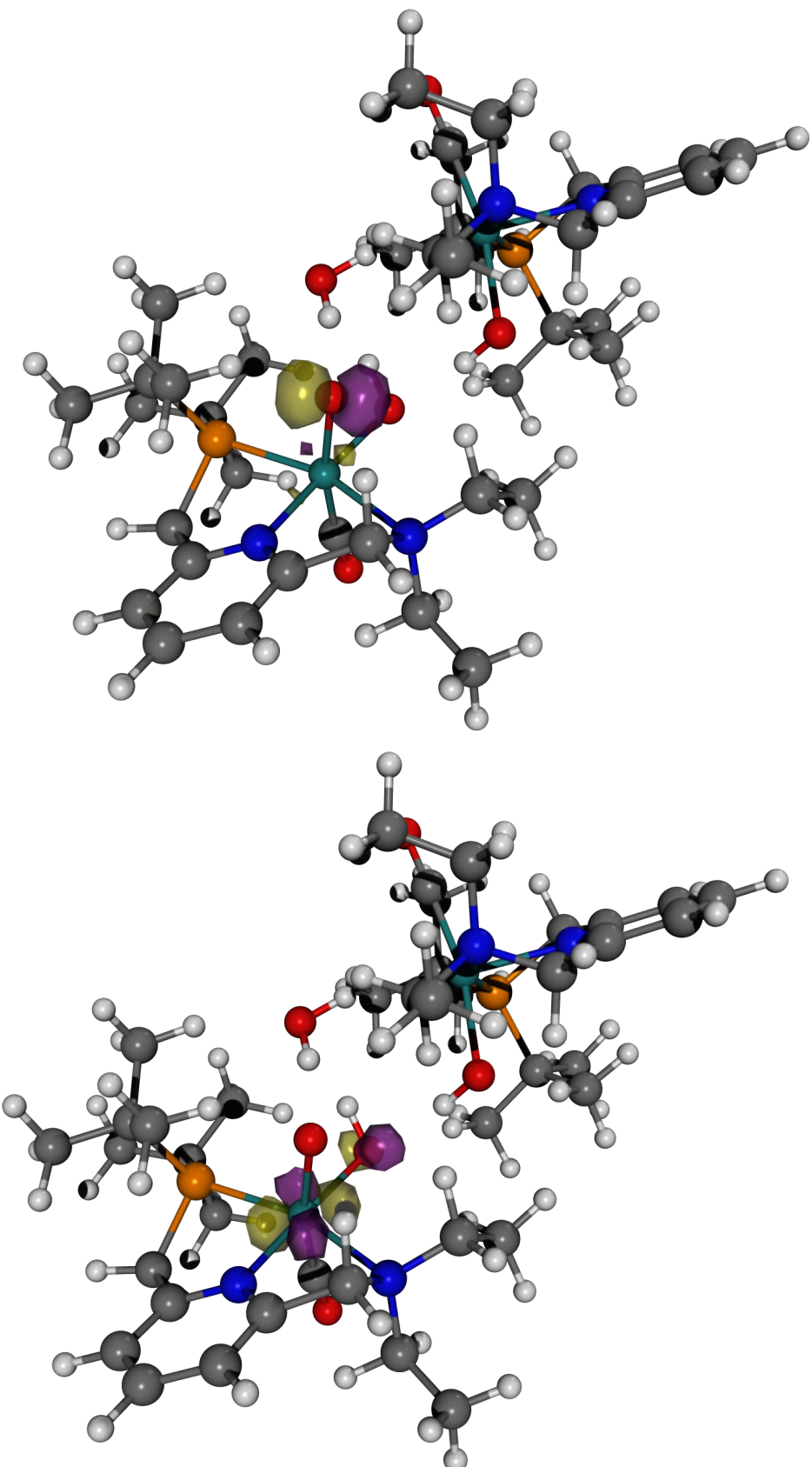


Figure 11.2-8 Transition 2 (933 nm, $f = 0.0029$) for $[B]T_0$, particle (top) and hole (bottom), isovalue = 0.1

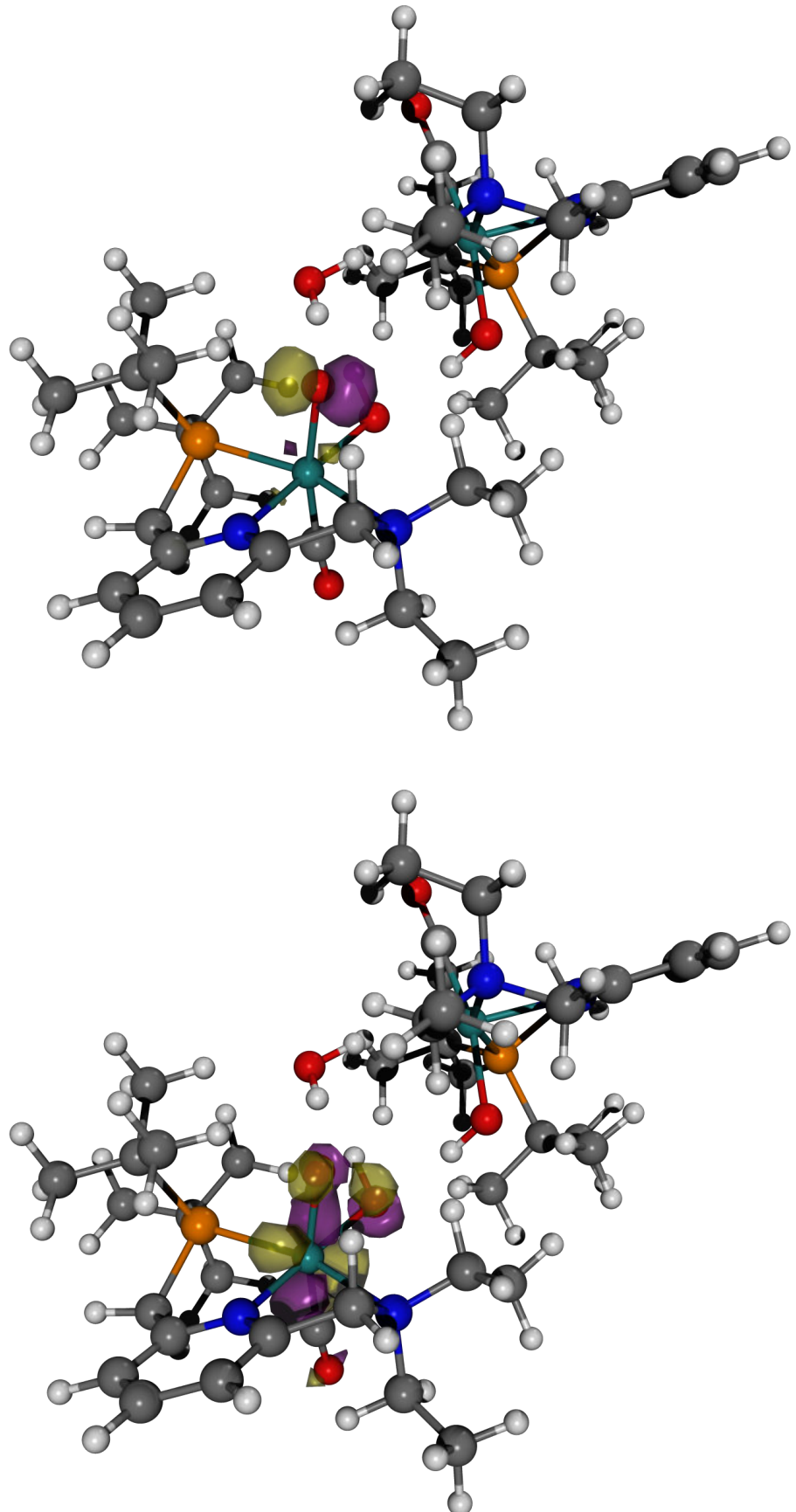


Figure 11.2-9 Transition 8 (539 nm, $f = 0.0066$) for $[B]T_0$, particle (top) and hole (bottom), isovalue = 0.1

11.2.5 Natural Transition Orbitals for [B-Mono]D₀ (Me Model)

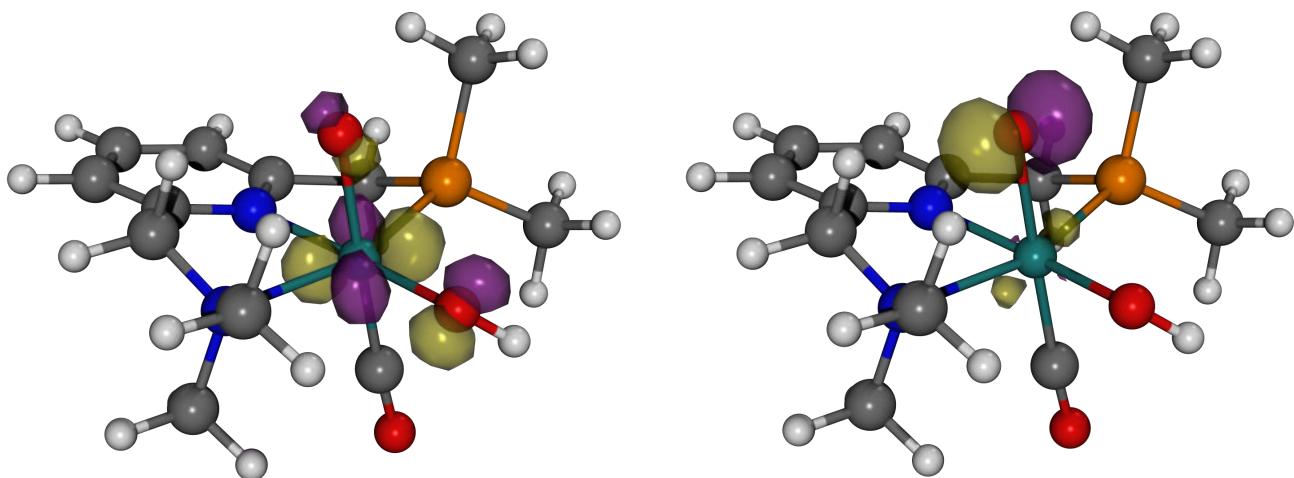


Figure 11.2-10 Transition 2 (804 nm, $f = 0.0004$) for [B-Mono]D₀ (Me model), hole (left) and particle (right), isovalue = 0.1

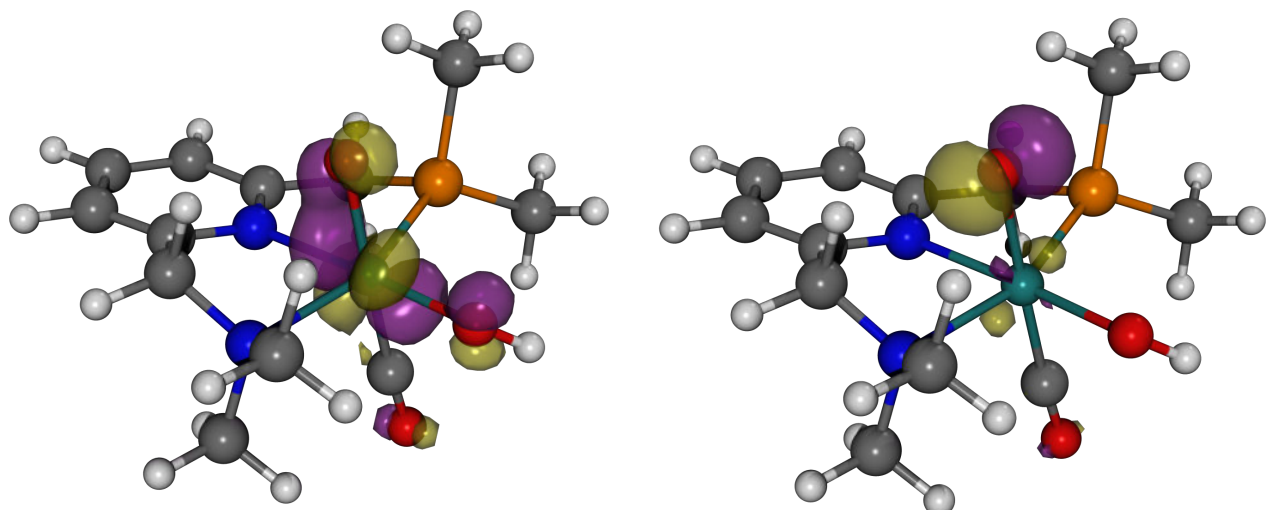


Figure 11.2-11 Transition 4 (495 nm, $f = 0.0027$) for [B-Mono]D₀ (Me model), hole (left) and particle (right), isovalue = 0.1

11.2.6 Spin Density Plots

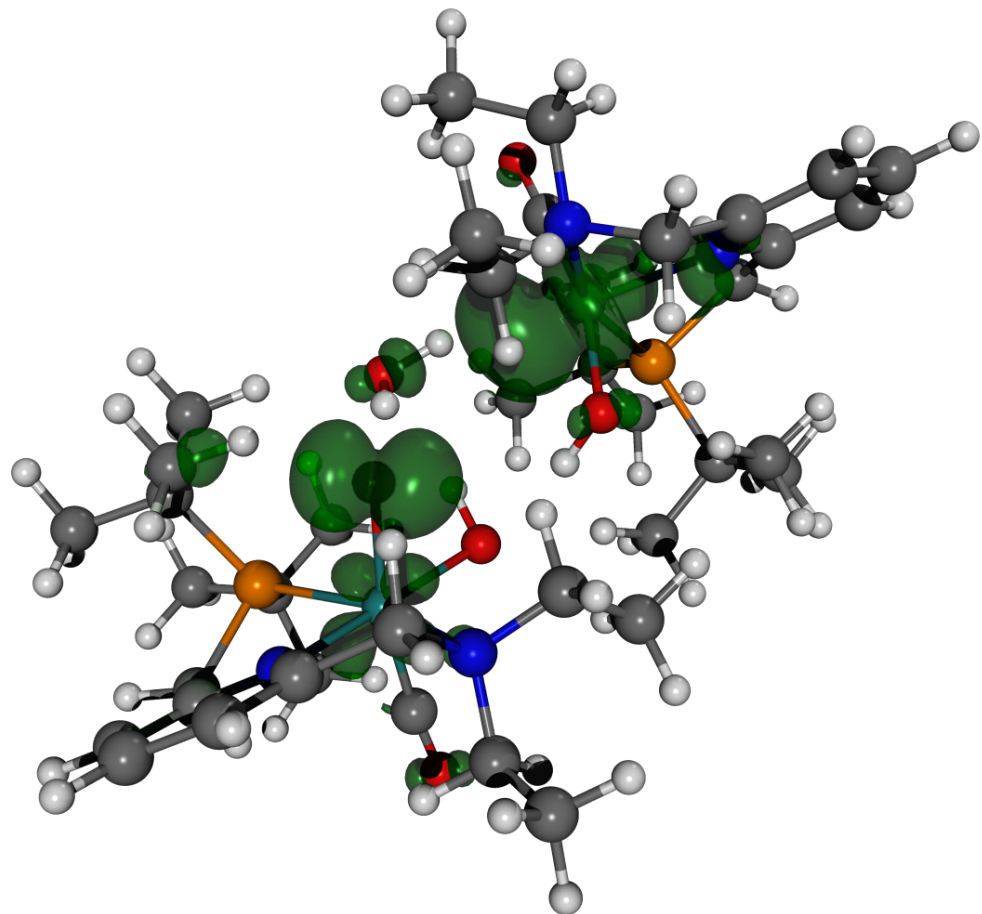


Figure 11.2-12 Spin density (isovalue = 0.004) for $[B]T_0$

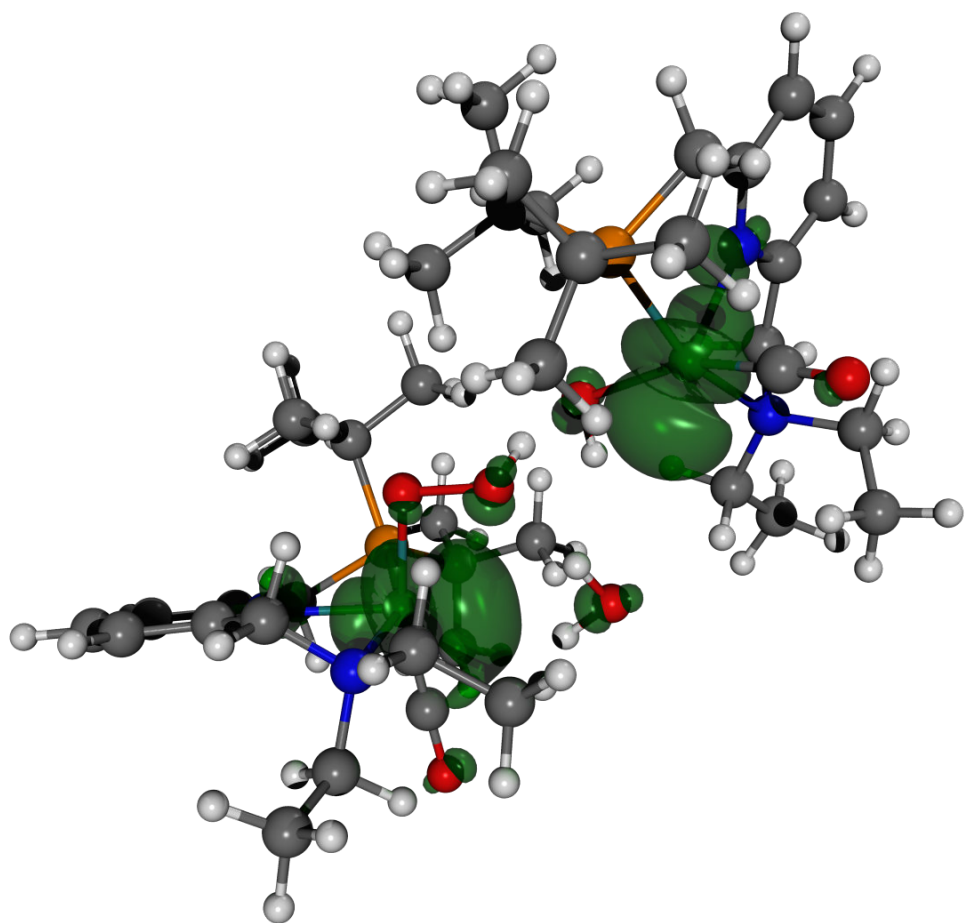


Figure 11.2-13 Spin density (isovalue = 0.004) for [C]T₀

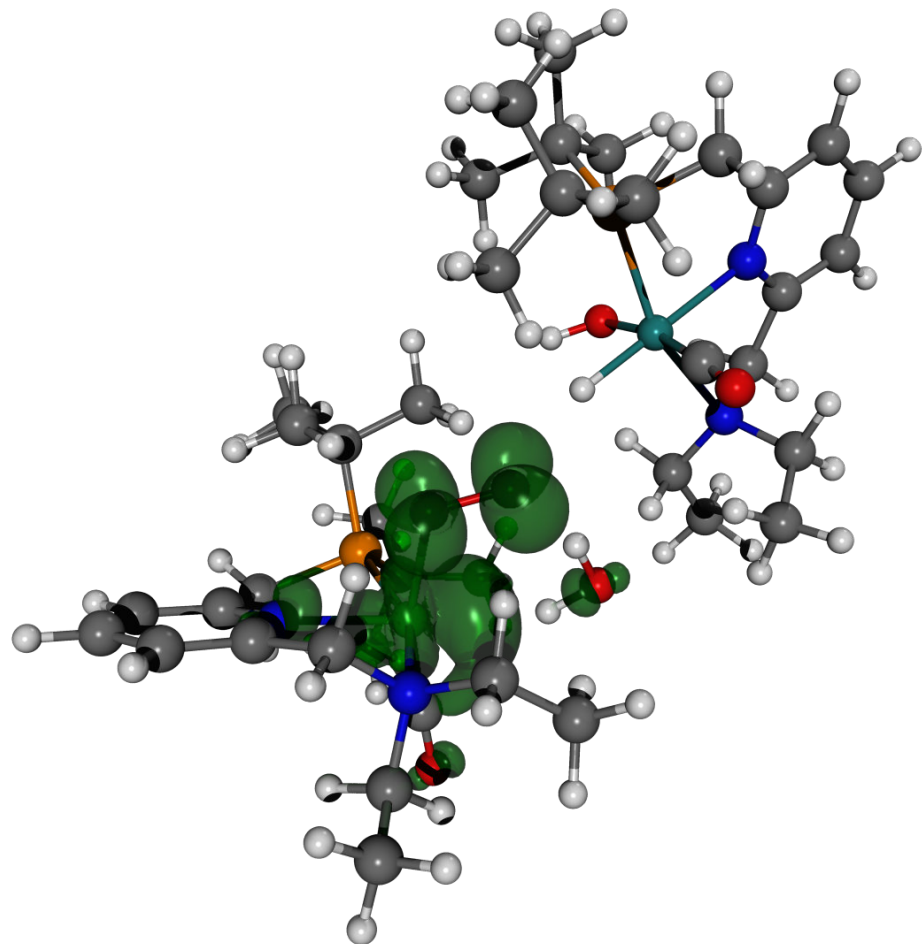


Figure 11.2-14 Spin density (isovalue = 0.004) for $[D]T_0 [F]S_0$ (Dimer Model)

11.2.7 Scan-[DE]T₀

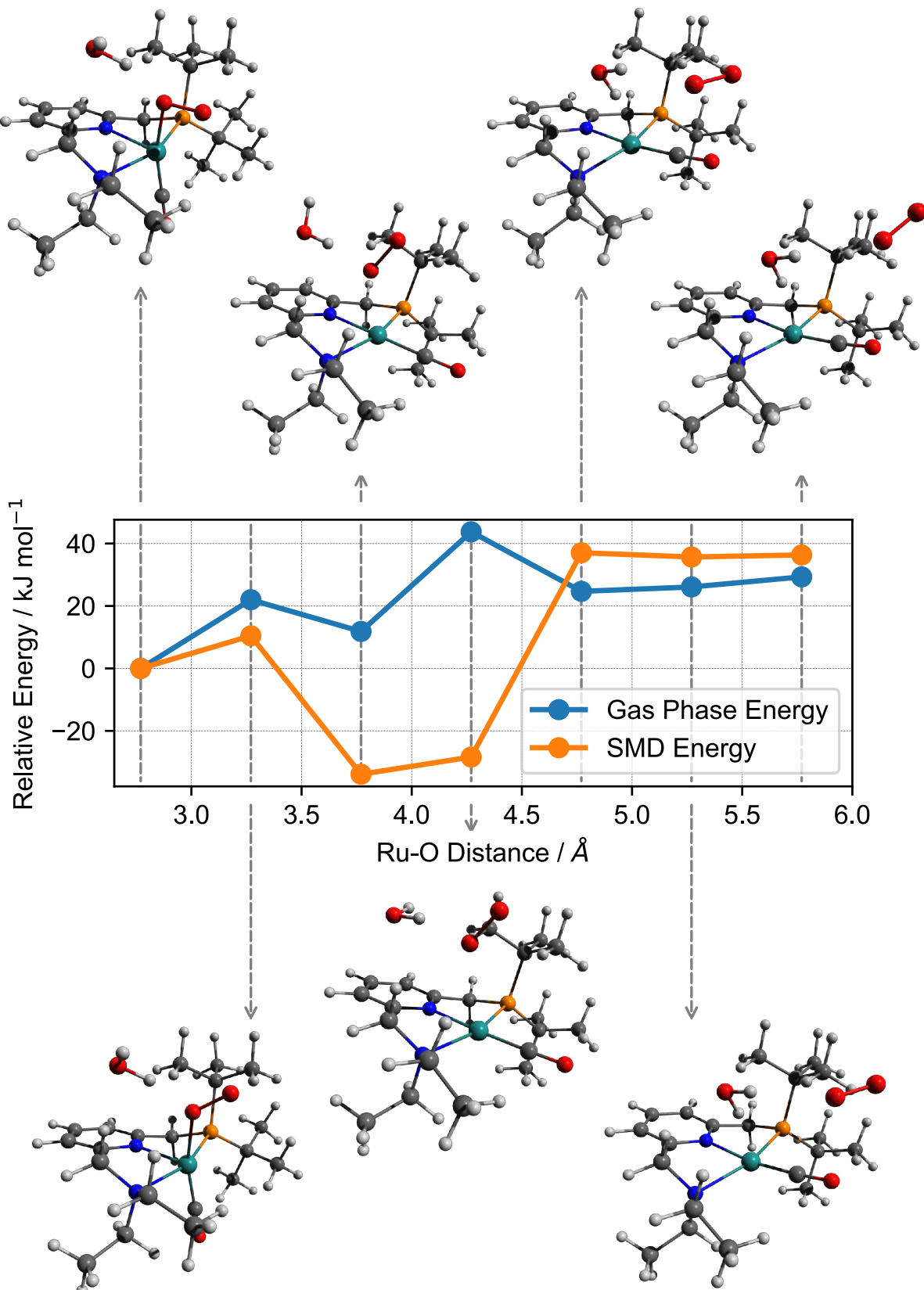


Figure 11.2-15 Energy profile for relaxed PES Scan-[DE]T₀ (gas phase and SMD energies)

Ru-O distance refers to the distance between the ruthenium center and the most distant oxygen atom of the superoxo ligand. Structures corresponding to the different points along the scan are shown outside of the plot. The decrease in energy for the third scan geometry can be attributed to movement of the CO ligand from an axial to an equatorial position.

11.2.8 O-O Bond Formation Scans

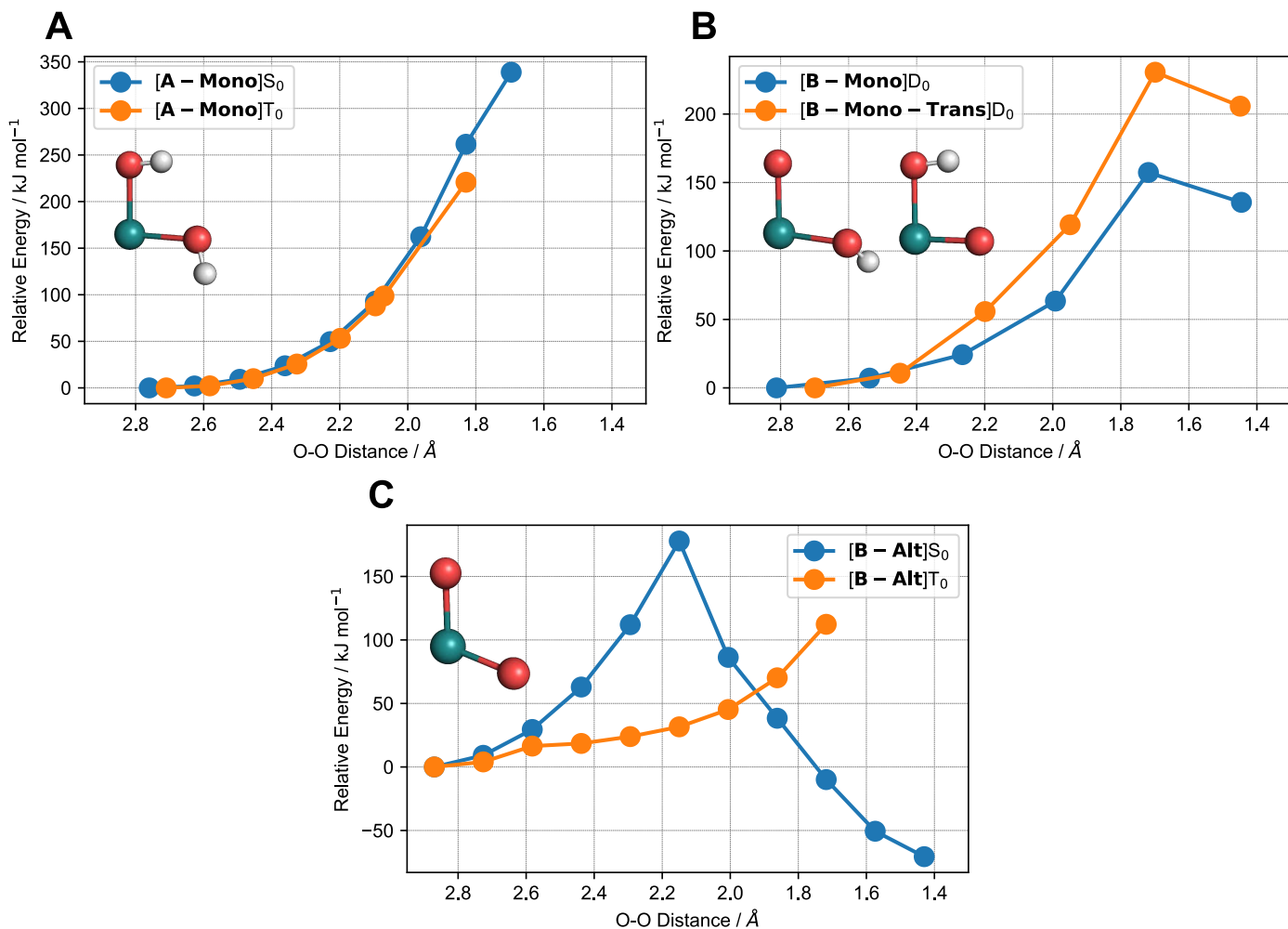


Figure 11.2-16 Energy profiles for relaxed PES scans of O-O bond formation

A Scan of O-O distance for **[A-Mono]** in singlet and triplet state. Inlet shows **[A-Mono] S_0**

B Scan of O-O distance for **[B-Mono] D_0** (Me model) as well as **[B-Mono-Trans] D_0** (Me model). Note that for these scans, the same methyl substituted models were used that were also used for CASSCF calculations. Insets show **[B-Mono] D_0** (left) and **[B-Mono-Trans] D_0** (right).

C Scan of O-O distance for **[B-Alt]** in singlet and triplet state (**[B-Alt]** would be the hypothetical result of a second PCET preceding O-O bond formation). Inlet shows **[B-Alt] T_0** .

Energy of starting point for each scan is set to 0 kJ/mol.

Relaxed potential energy surface scans were performed to investigate potential O-O bond formation for six different reaction intermediates. These intermediates span the various possibilities of intramolecular O-O bond formation (fully protonated, singly deprotonated and doubly deprotonated). For **[A]** and **[B-Alt]**, calculations were performed in the singlet or triplet ground state, while calculations for **[B-Mono]** and **[B-Mono-Trans]** were performed in the duplet ground state. These scans therefore provide an estimate for the lower bound of O-O bond formation for each intermediate.

For **[A-Mono]** in both the singlet and triplet state, no O-O bond formation could be observed (see Figure 11.2-16A). For **[A-Mono] T_0** , constrained geometry optimizations for O-O distances smaller than 1.83 Å were unsuccessful. These results are consistent with previous findings on the lack of O-O bond formation starting from **[A]**.^{22,23}

When comparing **[B-Mono] D_0** and **[B-Mono-Trans] D_0** , it can be seen that the barrier for O-O bond formation is significantly lower for **[B-Mono] D_0** (by more than 60 kJ/mol, see Figure 11.2-16B).

For **[B-Alt]**, potential O-O bond formation was studied in both the singlet and triplet state. For **[B-Alt] S_0** , O-O bond formation can be observed, although with a barrier of over 160 kJ/mol (in

comparison, the barrier for O-O bond formation in **[B-Mono]D₀** is 157.3 kJ/mol). Furthermore, it is questionable whether **[B-Alt]S₀** is even a feasible intermediate. This is based on the observation that **[B]S₀** was found to be unstable during geometry optimizations, reverting back to **[A]S₀**. Such instability can be attributed to the fact that in the S₀ state, there is no charge separation between the two ruthenium centers (as is the case in the T₀ state, see Figure 11.2-12). Therefore, proton transfer from one complex to another is less favorable, explaining why **[B]S₀** reverts back to **[A]S₀**. The same reasoning can be applied to **[B-Alt]S₀**, which would likely not be formed. Hence, **[B-Alt]T₀** was also investigated, but no O-O bond formation was found in this case (constrained geometry optimizations failed for short O-O bond lengths).

11.2.9 Theoretical NMR Data for **[F]S₀** Isomers

Table 11.2-8 Relative energies and theoretical NMR data for **[F]S₀ isomers**

	[F]S₀	[F-Up]S₀	[F-Cis]S₀	[F-Cis-Up]S₀	[F-Trans]S₀	[F-Trans-Up]S₀
ΔG°(SMD) / kJ/mol	19.3	13.3	55.5	58.3	10.3	0.0
δ(¹H, hydride) / ppm	-9.28	-7.98	0.13	0.08	-10.02	-10.22
δ(³¹P) / ppm	125.28	108.47	112.55	106.05	110.59	109.14
Experimental	/		$\delta(^1H) = -5.5 \text{ ppm}$ $\delta(^{31}P) = 104.3 \text{ ppm}$		$\delta(^1H) = -18.9 \text{ ppm}$ $\delta(^{31}P) = 104.2 \text{ ppm}$	

It can be seen that **[F-Trans-Up]S₀** is the most stable isomer of **[F]**, with the cis isomers being significantly less stable. While theoretical hydride chemical shifts are somewhat overestimated, the relative experimental difference between cis and trans isomers of 13.4 ppm is well reproduced (10.2 ppm). **[F]S₀** is only slightly less stable than the trans isomers.

11.2.10 Theoretical UV-Vis Spectrum for [F-Trans-Up]S₀

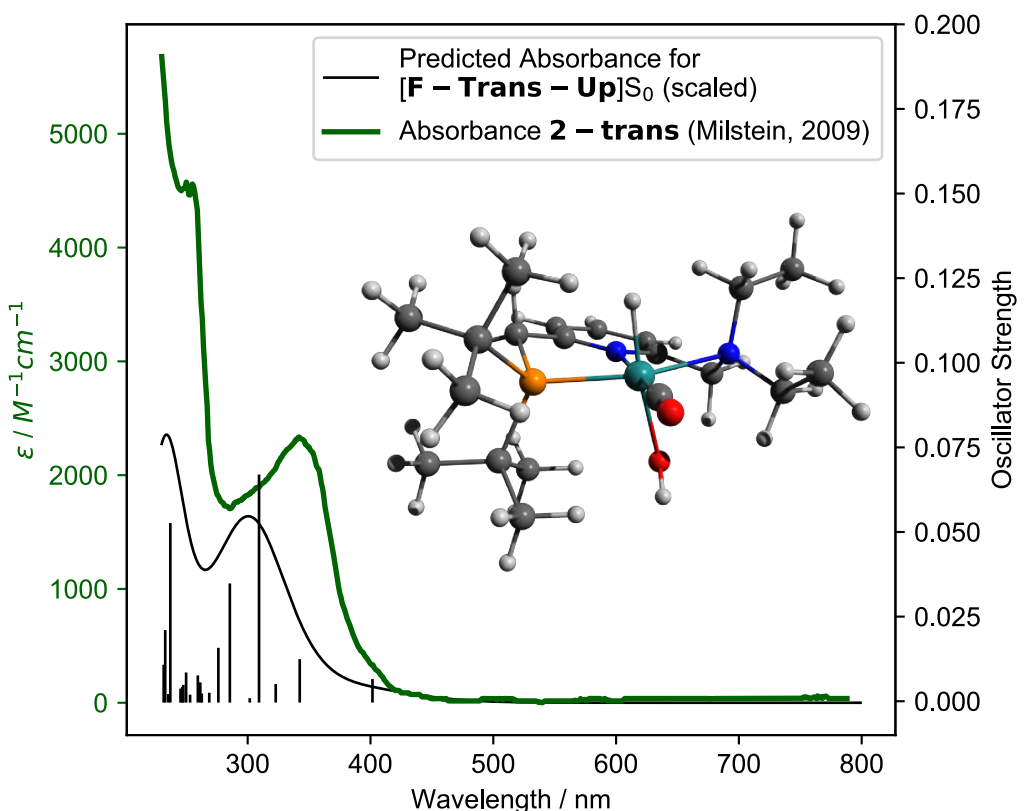


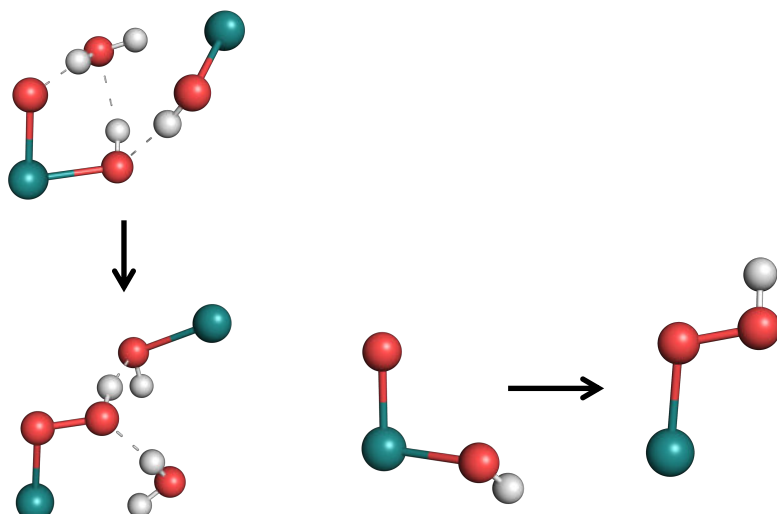
Figure 11.2-17 Comparison of computed UV-Vis spectrum for [F-Trans-Up]S₀ and experimental spectrum for 2-trans reported by Milstein and co-workers
UV-Vis spectrum of 2-trans was taken from ref. 2. Inlet shows computed structure of [F-Trans-Up]S₀.

Figure 11.2-17 shows the experimental UV-Vis spectrum for **2-trans** as reported by Milstein and co-workers² as well as the computed spectrum for **[F-Trans-Up]S₀** (which is analogous in structure to **2-trans** based on the crystal structure reported by Milstein and co-workers²). As can be seen, there is good agreement between experimental data and the computed spectrum for the used model.

11.3 CASSCF Results

11.3.1 Comparison of DFT and CASSCF Energies and Absorption Wavelengths

Table 11.3-1 Comparison of DFT and CASSCF reaction energies for $[B] \rightarrow [C]$ and absorption wavelengths for $[B\text{-Mono}]D_0$



Method	Parameter	$[B]T_0 \rightarrow [C]T_0$	$[B\text{-Mono}]D_0 \rightarrow [C\text{-Mono}]D_0$	$[B\text{-Mono}]D_0 \rightarrow [C\text{-Mono}]D_0$ (Me model)
DFT	$\Delta G^\circ / \text{kJ/mol}^{[a]}$	146.5 (150.2)	140.2	133.5
	Transition Wavelength / nm ^[b]	539 (Trans. 8)	/	495 (Trans. 4)
CASSCF	$\Delta E / \text{kJ/mol}^{[c]}$	/	/	124.7 (151.9)
	Transition Wavelength / nm ^[d]	/	/	482

[a] Gas phase ΔG° (SMD ΔG° in parentheses). [b] Transition corresponding to second lowest energy transition of CASSCF model of $[B\text{-Mono}]D_0$, calculated using SMD solvation. [c] Gas phase ΔE (PCM ΔE in parentheses). [d] Second lowest energy transition of $[B\text{-Mono}]D_0$, calculated in gas phase.

Table 11.3-1 assesses the agreement between different model chemistries as well as between DFT and CASSCF for O-O bond formation from $[B]$ to $[C]$ as well excitation of $[B]$.

For DFT, it can be seen that there is good agreement for reaction Gibbs free energies between the different model chemistries, with all of them being within 16.7 kJ/mol. This validates the use of either $[B\text{-Mono}]D_0$ or $[B\text{-Mono}]D_0$ (Me model) to describe O-O bond formation in $[B]T_0$. Also, relative energies of $[B\text{-Mono}]D_0$ to $[C\text{-Mono}]D_0$ (Me model) calculated using CASSCF reproduces the DFT results well.

Furthermore, excitation of $[B]$ was compared between the different model chemistries/methods. In all cases, the lowest energy transition (< 0.4 eV) is an excitation of an electron from the fully occupied to the singly occupied oxo ligand lone pair. Due to its low excitation energy, this transition is likely not photochemically active.

Given the selected active space, CASSCF predicts the second lowest transition to be an excitation from a Ru d_{xz}/OH lone pair orbital to the singly occupied oxygen lone pair (see Figure 11.3-4), with a transition wavelength of 482 nm.

Corresponding transitions can be found in the TD-DFT results for $[B]T_0$ (transition 8, see Figure 11.2-9) and $[B\text{-Mono}]D_0$ (Me model, transition 4, see Figure 11.2-11), with similar transition wavelengths (see Table 11.3-1). It should be noted that the corresponding transition wavelength for $[B]T_0$ is red-shifted by ca. 45 nm. TD-DFT also predicts other, lower energy transitions: in case of $[B\text{-Mono}]D_0$ (Me model), the second lowest energy transition involves a Ru- d_{xy}/OH lone pair orbital

(see Figure 11.2-10), while the third lowest energy transition involves an oxo p_z orbital. For $[\mathbf{B}]T_0$, in addition to these, transitions involving the second ruthenium complex can be found. The reason that these lower energy transitions predicted using TD-DFT for $[\mathbf{B}\text{-Mono}]D_0$ are not found using CASSCF is due to the selection of the active space, which does not include orbitals which would be necessary to describe them. This limitation has to be accepted, as inclusion of more electrons and orbitals in the active space would make calculations computationally infeasible. However, as can be seen below, it was found that the second lowest energy transition in CASSCF does indeed lead to O-O bond formation.

Overall, good agreement between DFT and CASSCF results for reaction energies and excitation of $[\mathbf{B}]$ was found, justifying the applied CASSCF methodology.

11.3.2 Energy Profile including PCM Solvation

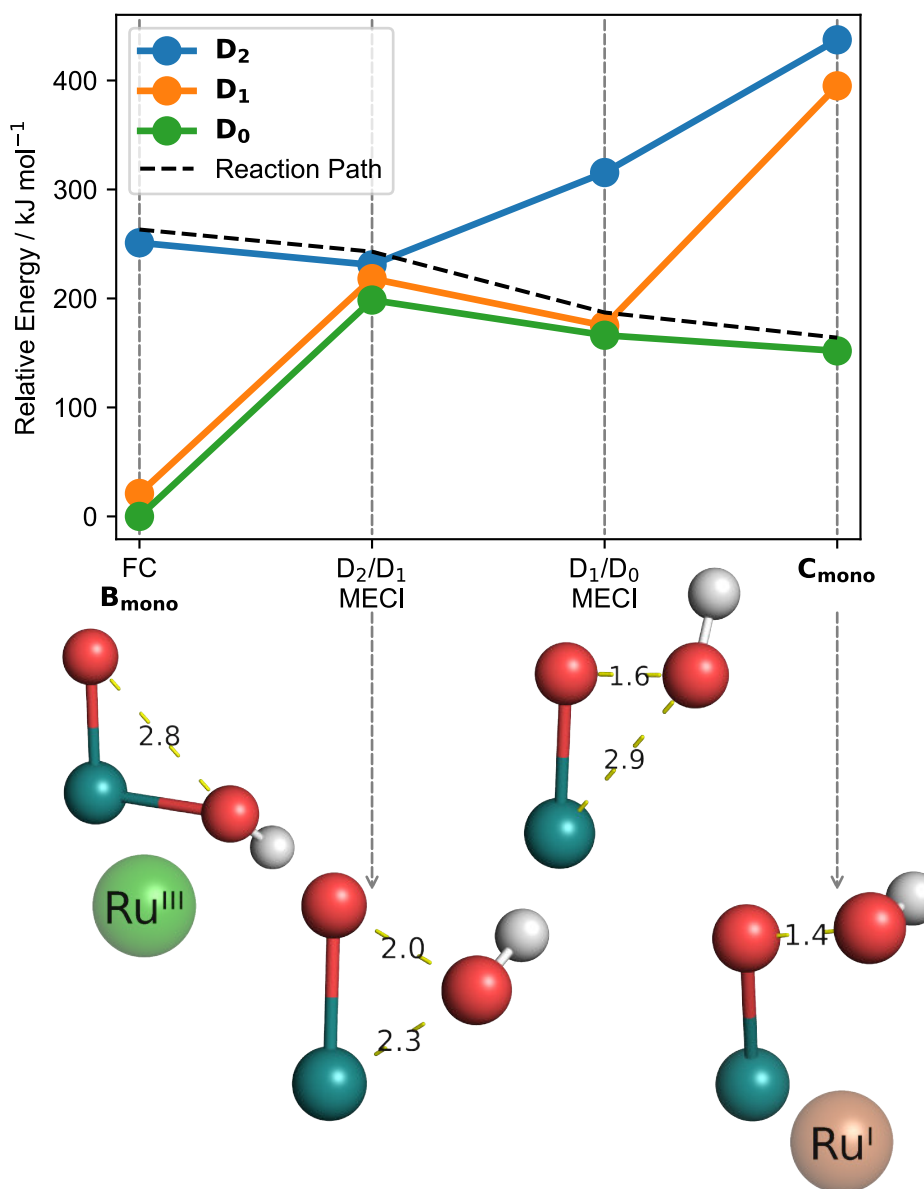
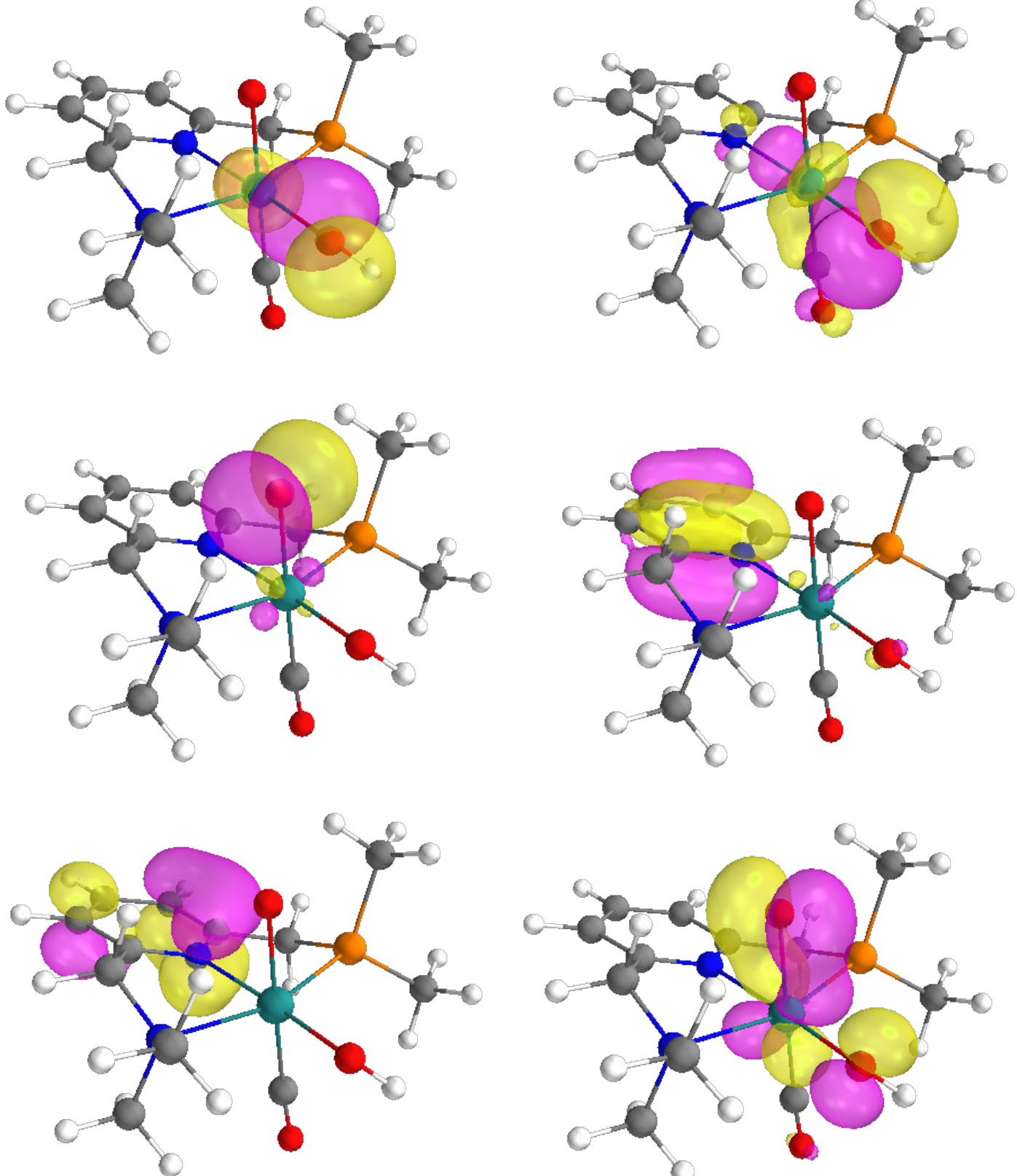


Figure 11.3-1 CASSCF energy profile including PCM solvation

Corresponding structures are shown below the plot, with bond lengths shown in Ångström. Note that degeneracy for conical intersections is slightly lost, since geometries were optimized in the gas phase. Spheres below structures indicate formal oxidation state of ruthenium center.

11.3.3 Active Space Orbitals



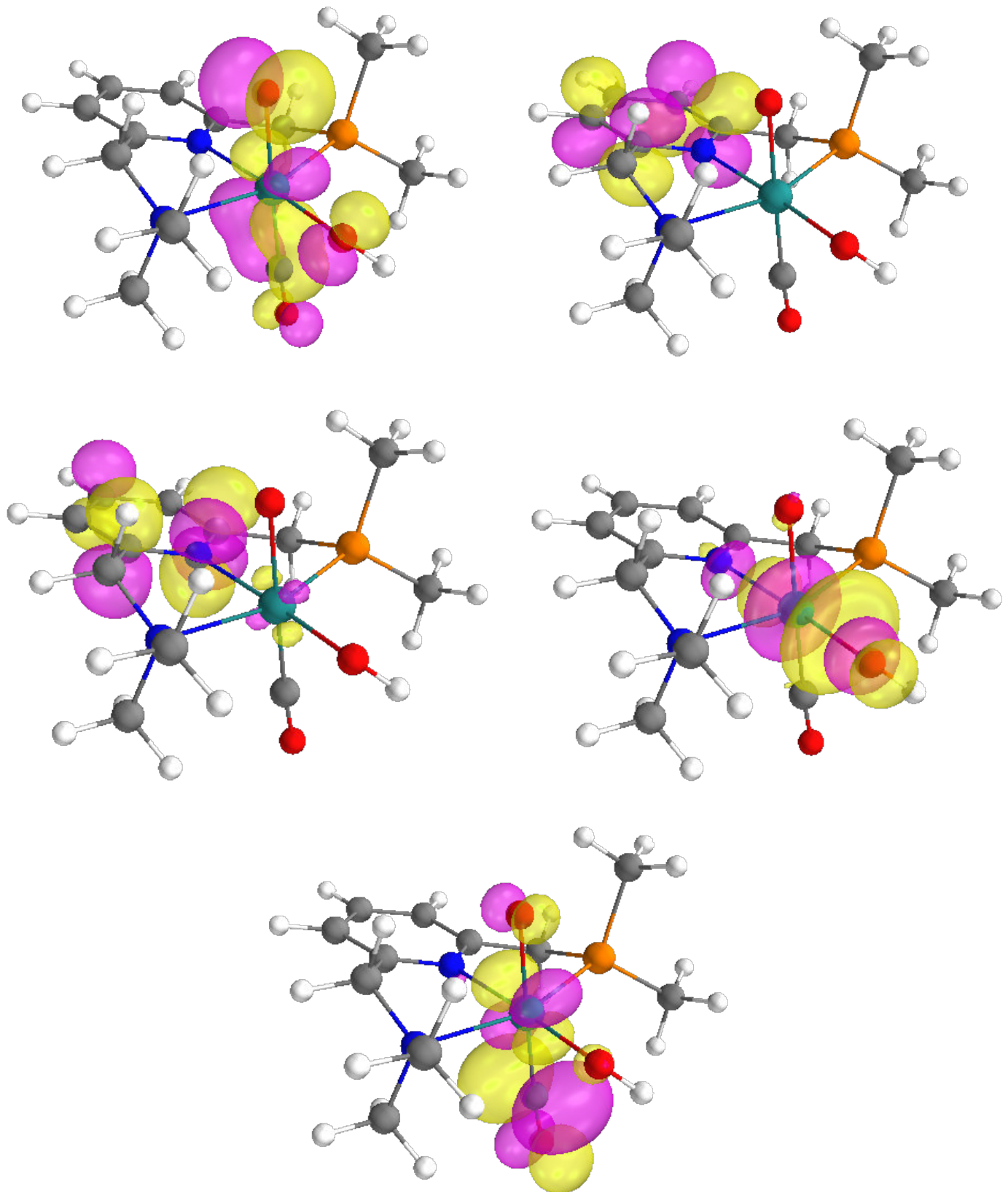


Figure 11.3-2 Active space orbitals of [B-Mono]D₀ used for CASSCF(13,11) calculations (isovalue = 0.05)
(average orbitals from SA-CASSCF(13,11) calculation for five lowest energy states are shown)

11.3.4 Surfaces for [B-Mono]D_n

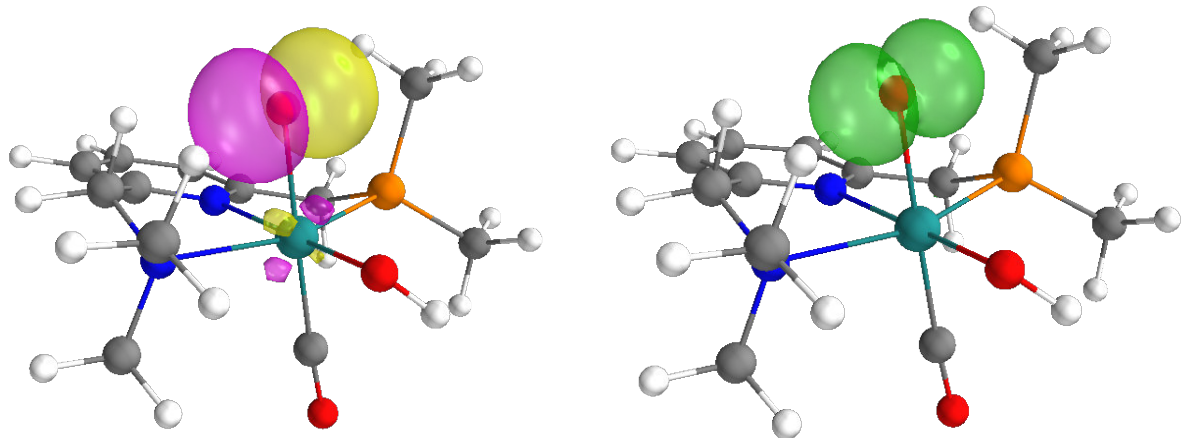


Figure 11.3-3 Singly occupied MO (left, isovalue = 0.05) and spin density (right, isovalue = 0.006) for [B-Mono]D₀

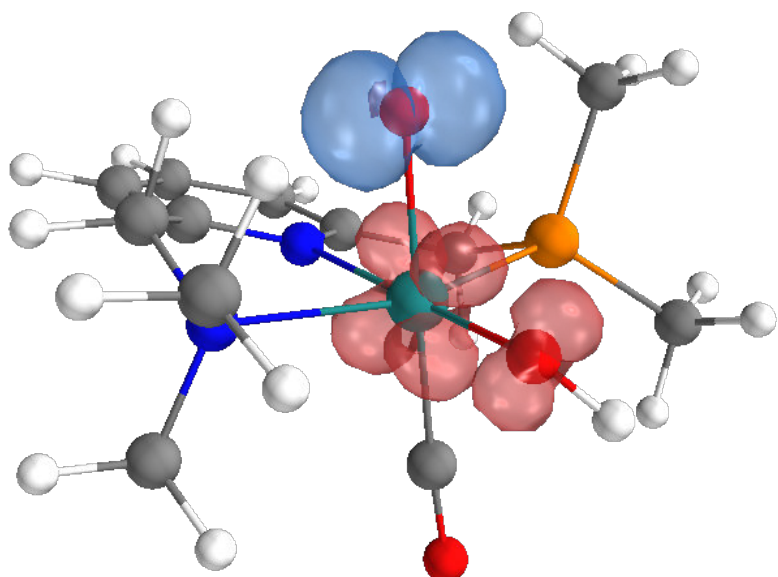


Figure 11.3-4 Unrelaxed transition difference density for [B-Mono]D₀ → [B-Mono]D₂ (detachment density in red, attachment density in blue, isovalue = 0.0005)

11.3.5 Difference Orbitals for Conical Intersections

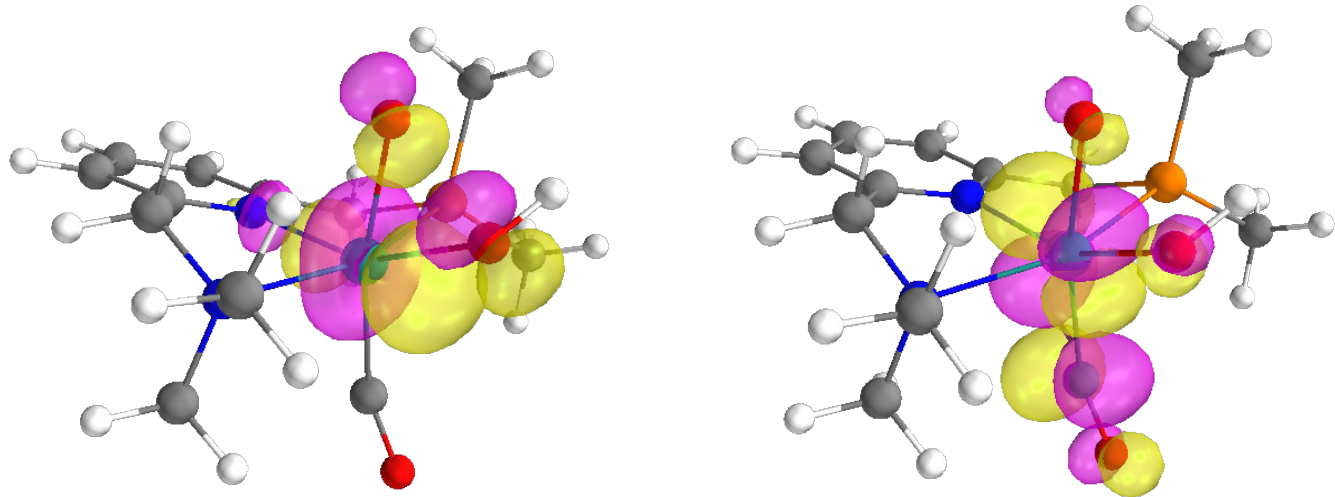


Figure 11.3-5 Difference orbitals for [BC] D₂/D₁ MECI with largest population changes (isovalue = 0.05)
(population change left: -0.8269, population change right: 0.9811)

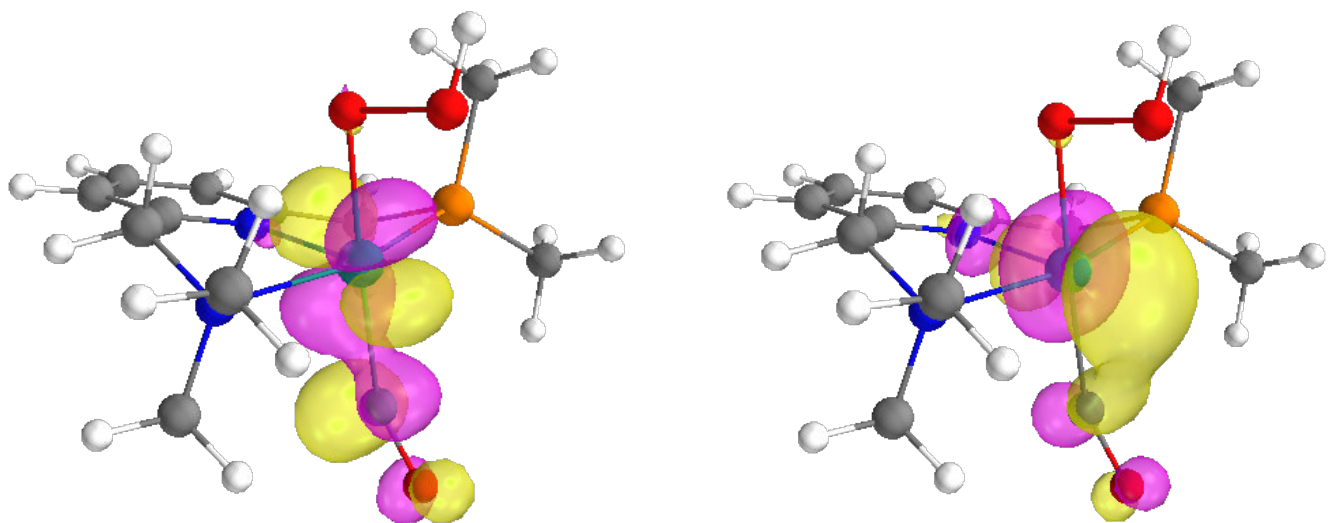


Figure 11.3-6 Difference orbitals for [BC] D₁/D₀ MECI with largest population changes (isovalue = 0.05)
(population change left: -0.8193, population change right: 0.7764)

11.3.6 Surfaces for [C-Mono]D₀

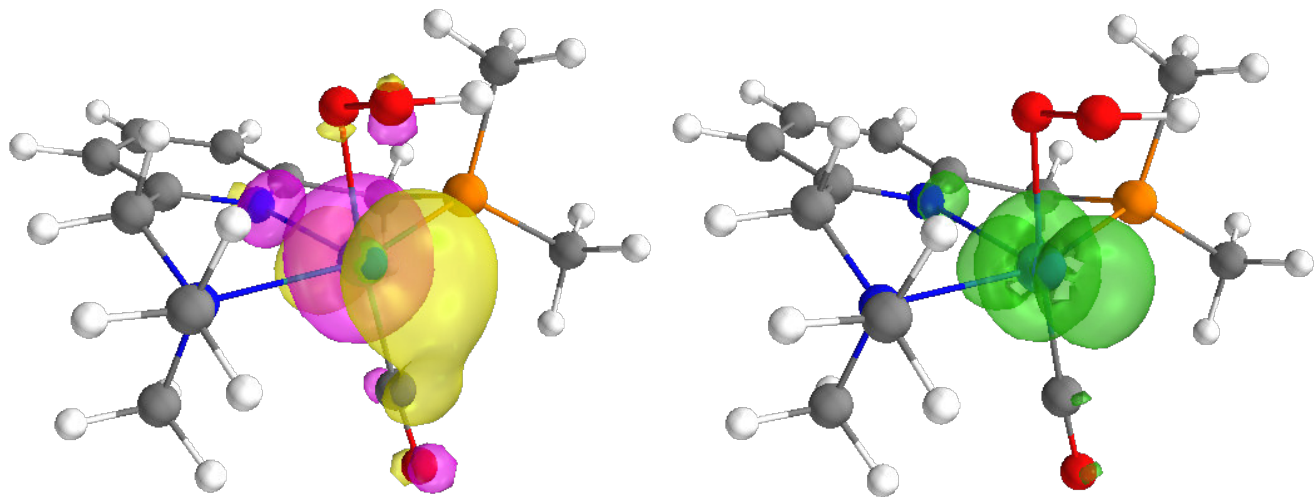


Figure 11.3-7 Singly occupied MO (left, isovalue = 0.05) and spin density (right, isovalue = 0.006) for [C-Mono]D₀

11.4 Integration of Computational and Experimental Results

11.4.1 Dual Irradiation Experiments

The liquid phase O₂ dual irradiation experiments can be seen as a way to probe the absorption characteristics of the second-photon absorbing intermediate. We developed a model convert to theoretical UV/Vis spectra into predicted dual irradiation behavior. This allows for the comparison of experimental dual irradiation data with predicted behavior of various computed intermediates.

Conversion of theoretical UV/Vis spectra to predicted dual irradiation behavior takes place in the following steps:

1. The QTH light source spectrum is described as an ideal blackbody (see Figure 6.1-2) using Planck's law with a blackbody temperature of 3400 K. The spectral power distribution is converted to a spectral photon distribution through division of the power distribution by respective photon energies.
2. For a given longpass filter wavelength (e.g. 630 nm) the corresponding intervals of the theoretical UV/Vis spectrum and spectral photon distribution are selected. Interval end is determined by the cut-off wavelength of the water filter (1000 nm for these calculations), resulting e.g. in [630 nm, 1000 nm] intervals.
3. To calculate the excess reaction rate corresponding to this longpass filter wavelength, the overlap of spectral photon distribution and theoretical UV/Vis spectrum is calculated by multiplying the corresponding intervals and then taking the sum of the resulting vector.
4. This procedure was repeated for each desired longpass filter wavelength. To obtain smooth curves, calculations were performed in 1 nm steps.
5. Resulting curves were scaled vertically through multiplication with a scaling factor to give the best possible fit to experimental data (since it is not trivial to perform this calculation to obtain accurate absolute reaction rates).

In the following, dual irradiation plots with experimental data (black dots) and thus calculated predicted behavior for different potential intermediate are shown.

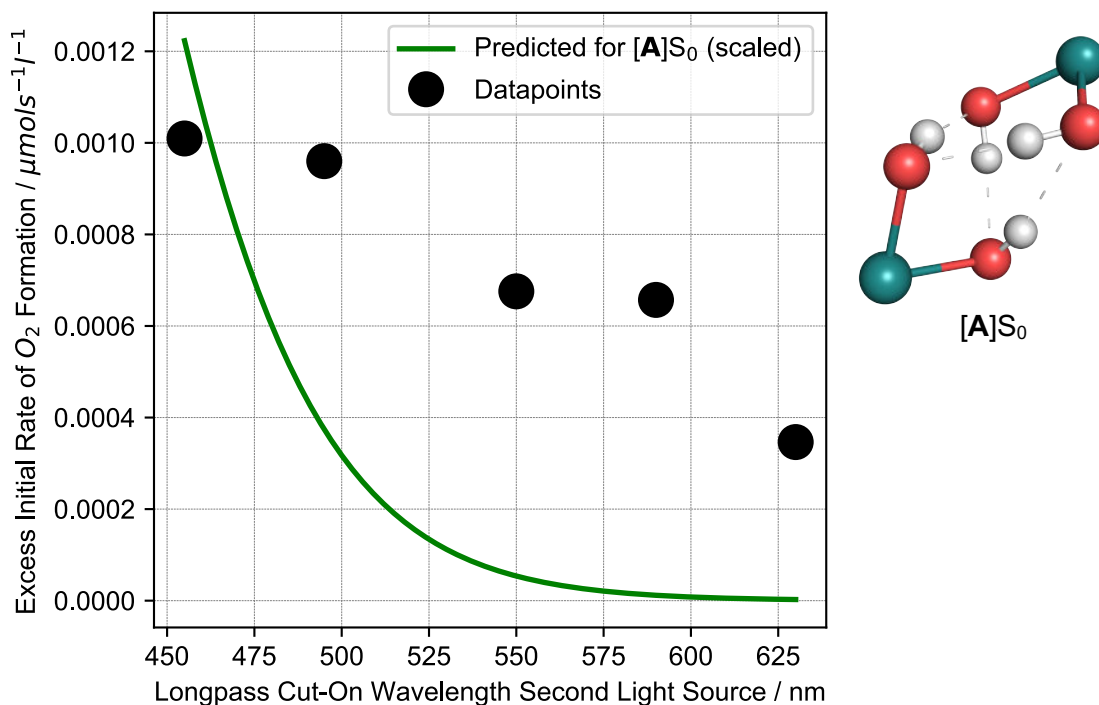


Figure 11.4-1 Dual irradiation data and predicted behavior of [A]S₀ (scaled)

As can be seen in Figure 11.4-1, predicted behavior for $[A]S_0$ is not consistent with experimental data. This is because $[A]S_0$ does not significantly absorb any wavelengths longer than 500 nm, although experimental data shows that these wavelengths already contribute to O_2 formation. Therefore, it can be ruled out that both photons involved in water splitting are absorbed by $[A]S_0$.

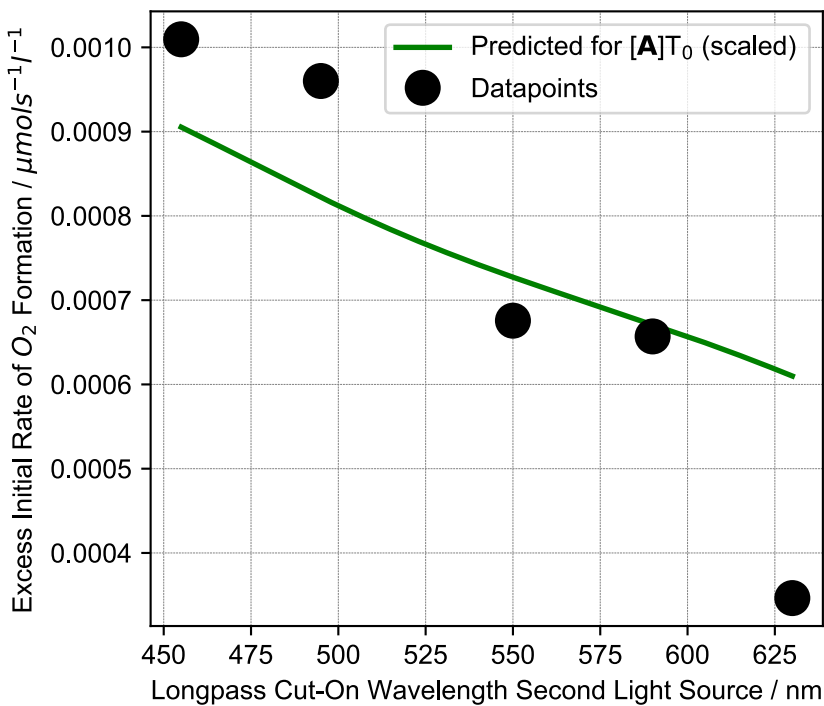


Figure 11.4-2 Dual irradiation data and predicted behavior of $[A]T_0$ (scaled)

The triplet state of $[A]$, $[A]T_0$, could be considered another candidate for the second-photon absorbing intermediate. However, in this case poor agreement is obtained as well. This is due to the fact that $[A]T_0$ absorbs longer wavelengths only very weakly, giving a slope for longpass filter wavelength/reaction rate which is smaller than the one observed experimentally. These results showing that $[A]T_0$ is likely not the second-photon absorbing intermediate are also consistent with DFT calculations showing that O-O bond formation at $[A]T_0$ is unlikely.

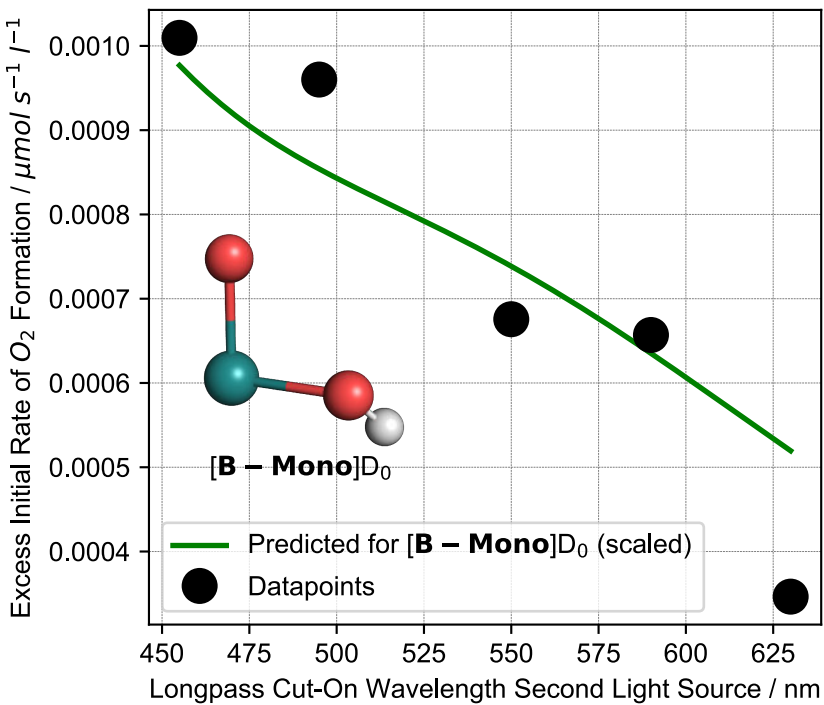


Figure 11.4-3 Dual irradiation data and predicted behavior of $[B\text{-Mono}]D_0$ (scaled)
Inset shows structure of $[B\text{-Mono}]D_0$ with other ligands omitted for clarity.

As can be seen in Figure 11.4-3, $[B\text{-Mono}]D_0$ gives an acceptable fit for the dual irradiation data, although it is slightly inferior compared to the fit of $[B\text{-Mono-Up}]D_0$. As the ligand conformation does not have a significant effect on the obtained energies (see 11.2.1), the choice of ligand conformation does not have a major impact on computations. Calculations studying O-O bond formation were performed using $[B\text{-Mono}]D_0$.

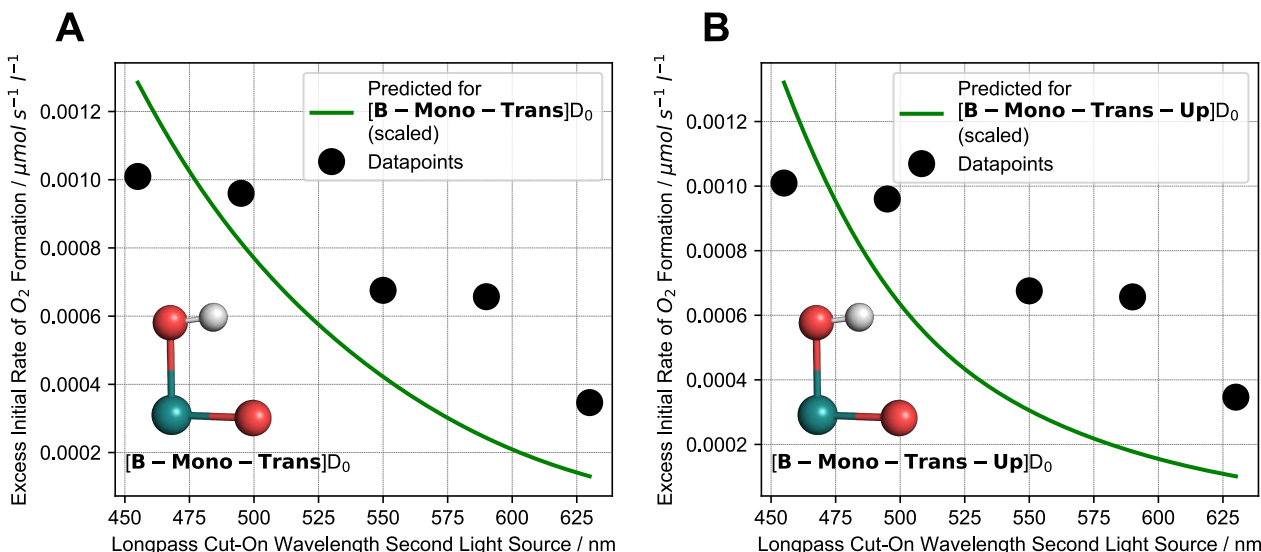


Figure 11.4-4 Dual irradiation data and predicted behavior of $[B\text{-Mono-Trans}]D_0$ (A, scaled) and $[B\text{-Mono-Trans-Up}]D_0$ (B, scaled)
Inlets show structures of $[B\text{-Mono-Trans}]D_0$ and $[B\text{-Mono-Trans-Up}]D_0$ with other ligands omitted for clarity.

As can be seen in Figure 11.4-4, neither $[B\text{-Mono-Trans}]D_0$ nor $[B\text{-Mono-Trans-Up}]D_0$ give an acceptable fit for the dual irradiation data, suggesting that neither is the intermediate responsible for absorption of the second photon. This is consistent with the conclusion of 9.2, which found that $[B\text{-Trans}]D_0$, as observed by ultrafast pump-probe spectroscopy, is too short-lived to be a viable candidate for the second photon absorbing intermediate.

11.4.2 Decay Associated Spectra

Theoretical decay associated spectra (DAS) were computed using theoretical UV/Vis spectra for a reference and an intermediate of interest. Theoretical UV/Vis spectra were used as reference (instead of experimental UV/Vis spectra) so as to allow for error cancellation between theoretical UV/Vis spectra.

DAS were computed using the following formula:

$$DAS = (p_{pop} Abs_{int} + (1 - p_{pop})Abs_{ref}) - Abs_{ref} \quad \text{Equation (8)}$$

Wherein Abs_{int} is the absorption spectrum of the intermediate of interest, Abs_{ref} is the absorption spectrum of the reference and p_{pop} is the population of the intermediate of interest after excitation. p_{pop} was assumed to be 0.1, although p_{pop} only effects the DAS magnitude and not its shape.

Thus calculated DAS were scaled vertically by multiplication with a scaling factor to yield the best fit to experimental data.

11.5 Modelling Solar-to-Hydrogen Efficiency

11.5.1 Model Description

Maximum theoretical solar-to-hydrogen (STH) efficiencies are modelled based on the approach laid out by Bolton *et al.*²⁴ and are also set into relation with more recent results by Seitz *et al.*²⁵ The following assumptions are made to model ideal systems, whereas “photoabsorber” refers to any material absorbing photons (for example a molecular complex/intermediate or semiconductor):

1. Solar irradiation is modelled using the reference air mass 1.5 solar spectrum (AM 1.5 G) with a total irradiance of 1000.3 W/m^2 and all calculations are normalized to an area of 1 m^2 .
2. Photoabsorbers ([A], [B], [C], ...) are characterized by their longest absorption wavelength. For each photoabsorber, all available photons with shorter wavelengths are absorbed while no photons with longer wavelengths are absorbed.
3. Photoabsorbers are ordered by their longest absorption wavelengths: [A] absorbs all photons from 0 nm to λ_1 , [B] absorbs all photons from λ_1 to λ_2 , [C] absorbs all photons from λ_2 to λ_3 etc. Such an arrangement describes a stacked absorber configuration (as used by Seitz *et al.*) or a solution containing different molecular species at different concentrations (e.g. if the concentration of [A] is higher than the concentration of [B], [A] will absorb most photons from 0 nm to λ_1 even if [B] could in principle also absorb photons in this wavelength region).
4. Quantum efficiencies are assumed to be 100%, meaning that each photon absorption contributes to the reaction.

The following loss mechanisms are considered in this model:

1. Photons with longer wavelengths than the longest absorption wavelength of the entire system are not absorbed, thus limiting the maximum solar-to-hydrogen efficiency.
2. Photons with higher energy than the longest absorption wavelength of the respective photoabsorber do not generate charge carriers with a higher energy than the longest absorption wavelength due to immediate relaxation to that energy level. Thus, no hot carrier effects are considered.
3. Free energy and kinetic losses: it is assumed that the chemical potential of generated charge carriers is lower than the longest absorption wavelength of the respective photoabsorber due to free energy losses within the photoabsorber (this refers to a drop in photovoltage in case of semiconductors). The lower bound for these free energy losses has been estimated to be between 0.3 and 0.5 eV.^{24,25} Furthermore, there are kinetic barriers (transition state energy/overpotential) which increase the required chemical potential to drive a reaction beyond the reaction’s thermodynamic minimum. For water splitting, Seitz *et al.* estimate a lower bound of ca. 0.4 – 0.5 eV for these kinetic barriers. In our model, we combine free energy and kinetic losses into the E_{loss} parameter, which is subtracted from the longest absorption wavelength of a photoabsorber to obtain the Gibbs free energy which can be converted by this absorber. Based on our computational results, $E_{\text{loss}} = 73.2 \text{ kJ/mol}$ (0.76 eV) is a reasonable lower bound, given that this is the free energy difference between [A] S_n and [B] T_0 as well as close to the difference between [B] T_8 and [C] T_0 within the DFT method (relative energy of [B] T_8 to [B] T_0 : 221.7 kJ/mol, 539 nm absorption wavelength, relative energy of [C] T_0 to [B] T_0 : 150.2 kJ/mol). It should be noted that [B] T_8 is the excited state corresponding to [B-Mono] D_2 (see Table 11.3-1). 0.76 eV is also close to the minimum combined free energy and kinetic losses from the literature described above. A more conservative value for E_{loss} (96.2 kJ/mol, 1 eV) was also used, which facilitates comparison with the results of Seitz *et al.*

Based on the described assumptions and considered loss mechanisms, the solar-to-hydrogen efficiency model was implemented in the following way:

1. The Gibbs free energy for the considered reaction ($\Delta G_{\text{reaction}}$) is defined. In case the entire water splitting reaction is considered, this value is equal to $4 \times 1.229 \text{ eV}$ (474.7 kJ/mol). A

- partial water splitting reaction can also be considered, such as the reaction $[A]S_0 \rightarrow 2 [F]S_0 + {}^3O_2$ (346.1 kJ/mol). Furthermore, the value for E_{loss} is defined.
2. The number of photoabsorbers and the mechanism type are defined, which are described using a letter-number combination (letter indicates number of photoabsorbers and numbers indicate how many photons each absorber absorbs to complete the considered reaction). A S4 mechanism refers to a single photoabsorber absorbing four photons to complete the reaction, which would be the case for a classical semiconductor water splitting catalyst. A D4 mechanism refers to two photoabsorbers each absorbing four photons, which would be the case in a Z-scheme system, where two photons are required for each of the four electron transfers.
 3. The longest absorption wavelength for each photoabsorber is defined.
 4. Based on the longest absorption wavelengths, E_{loss} , and number of photons absorbed by each absorber, the total Gibbs energy (ΔG_{total}) which can be converted by the system is calculated. If $\Delta G_{total} < \Delta G_{reaction}$, the probability of $\Delta G_{total} = \Delta G_{reaction}$ due to thermal effects based on a Boltzmann distribution is calculated. It should be noted, however, that in case of $\Delta G_{total} < \Delta G_{reaction}$, the reaction probability quickly drops to zero for increasing differences between ΔG_{total} and $\Delta G_{reaction}$.
 5. Based on the AM 1.5 G spectral photon flux, the number of photons absorbed (per second) by each photoabsorber are calculated. The obtained absorbed flux is then divided by the number of required photons to complete the reaction for the respective photoabsorber.
 6. To calculate how many reactions occur per second, the photoabsorber with the lowest photon-corrected absorbed flux is considered, since this absorber is the bottleneck for the reaction. The corresponding photon-corrected absorbed flux is multiplied by the Boltzmann probability value (which is 1 if $\Delta G_{total} > \Delta G_{reaction}$), obtaining the number of reactions per second (r_s).
 7. Based on the calculated number of reactions per second (r_s , in mol/s) and the reaction Gibbs free energy ($\Delta G_{reaction}$, in J/mol) the solar-to-hydrogen efficiency is calculated using Equation (9):

$$STH = \frac{r_s \Delta G_{reaction}}{P A} \quad \text{Equation (9)}$$

Where P is the total solar irradiance (1000.3 W/m²) and A is the area in m² (set to 1 m²).

The optimal longest absorption wavelengths for each photoabsorber for a given mechanism type are computed via global optimization using differential evolution as implemented in *SciPy*. Based on the optimal wavelengths, the maximum theoretical solar-to-hydrogen efficiencies for each mechanism type can be computed.

11.5.2 Results

11.5.2.1 Two-Photon Water Splitting and Thermal H₂ Release

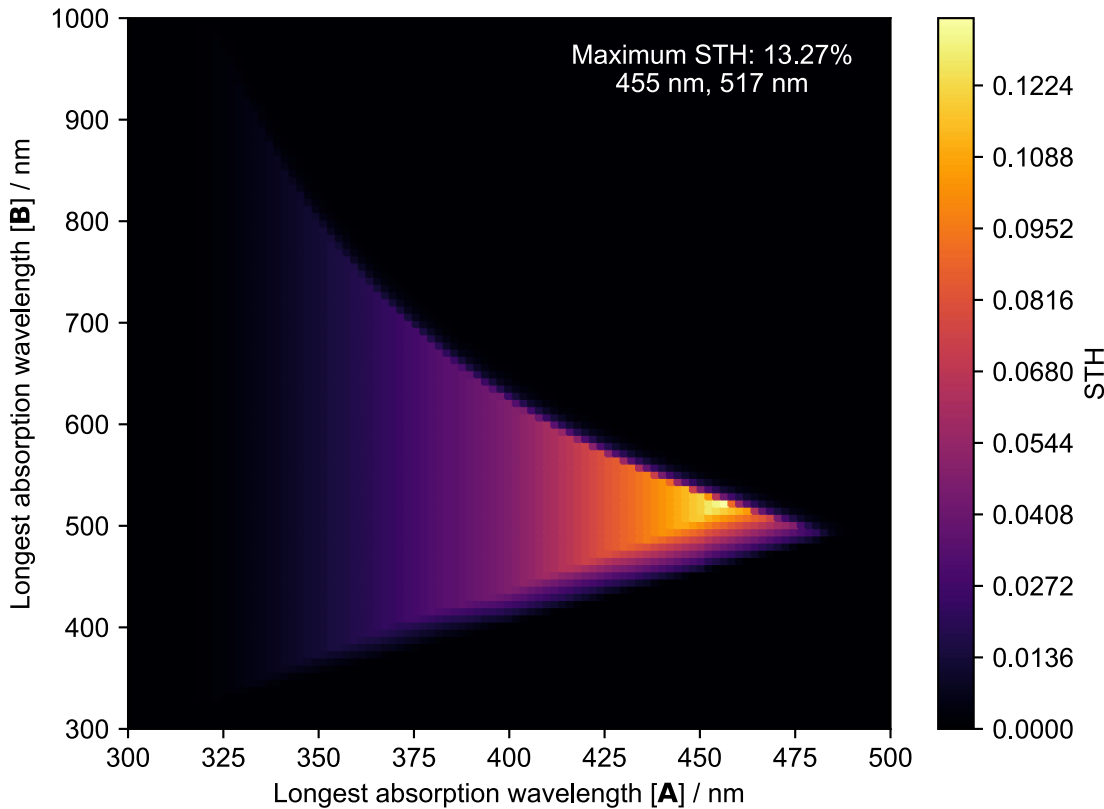


Figure 11.5-1 STH efficiency heat map for two-photon water splitting

Heat map showing dependence of STH efficiency on longest absorption wavelengths of intermediate [A] (bottom) and [B] (side). STH values are calculated based on the partial water splitting reaction $[A]S_0 \rightarrow 2 [F]S_0 + {}^3O_2$ ($\Delta G = 346.1 \text{ kJ/mol}$), thus the STH efficiency for thermal H₂ release has to be added to obtain the STH efficiency for full water splitting (see Table 11.5-2, entry "Two photon/thermal"). E_{loss} is set to 73.2 kJ/mol.

In Figure 11.5-1 the dependence of STH efficiency on longest absorption wavelength for each intermediate ([A] and [B]) in two-photon water splitting is shown. In this case, the partial water splitting reaction $[A]S_0 \rightarrow 2 [F]S_0 + {}^3O_2$ ($\Delta G = 346.1 \text{ kJ/mol}$) is considered, thus STH efficiency for thermal H₂ release to regenerate $[A]S_0$ has to be added to obtain the STH efficiency for full water splitting. E_{loss} is set to 73.2 kJ/mol. As expected, water splitting only occurs when λ_1 (longest absorption wavelength for [A]) is smaller than λ_2 (longest absorption wavelength for [B]), since [B] could otherwise not absorb any photons (lower bound of the triangle). ΔG_{total} has to exceed 346.1 kJ/mol, since otherwise no significant activity results (upper right bound of triangle). Optimal STH efficiency (13.27%) is achieved at $\lambda_1 = 455 \text{ nm}$ and $\lambda_2 = 517 \text{ nm}$. At this point, ΔG_{total} just barely exceeds 346.1 kJ/mol (by less than 2 kJ/mol) and the number of photons absorbed by [A] and [B] are almost equal, so that neither is a bottleneck for the reaction.

We can see that these optimal wavelengths are relatively close to the actual absorption wavelengths of $[A]S_0$ (ca. 400 nm) and $[B]T_0$ (ca. 630 nm). By connecting these insights with the photochemical kinetic model from section 10 we can develop an understanding for how a system with appreciable STH efficiency would have to look like:

For a reaction solution with a depth of 10 cm and a concentration of $[A] = 10^{-3} \text{ M}$, a molar attenuation coefficient of $\epsilon = 1000 \text{ M}^{-1}\text{cm}^{-1}$ up to 455 nm for [A] would be sufficient to absorb essentially all photons in this wavelength region.

Using the photochemical kinetic model and the AM 1.5 G solar spectrum we can compute the steady state concentration of [B]: since the 0 – 455 nm photon flux for the AM 1.5 G spectrum is

2.3E+16 cm $^{-2}\text{s}^{-1}$, a lifetime (τ) of ca. 50 ms for [B] would be sufficient to reach a steady state concentration of ca. 1% with respect to [A] ($[\text{B}] = 10^{-5}$ M). If [B] has a relatively high molar attenuation coefficient of $\epsilon = 10\,000$ M $^{-1}\text{cm}^{-1}$ up to 517 nm, this concentration would be sufficient to absorb ca. 90% of all 455 – 517 nm photons. We can therefore see that high photon absorption in the relevant wavelength regions can be achieved within reasonable bounds for concentration, molar attenuation coefficients and lifetime of [B]. The keys to achieve high STH are well matched absorption wavelengths of [A] and [B], relatively high molar attenuation coefficients, a sufficiently long lifetime of [B] and high quantum efficiencies for both photochemical steps.

To complete the water splitting reaction, two equivalents of H₂ have to be released from two equivalents of [F]S₀ in the reaction: $2 [\text{F}]S_0 + 2 \text{H}_2\text{O} \rightarrow [\text{A}]S_0 + 2 \text{H}_2$ ($\Delta G = 72$ kJ/mol per H₂, $\Delta G = 144$ kJ/mol total, see Table 11.2-7). Experimentally this reaction requires heating to 100 °C since it is associated with a relatively high activation barrier.²⁶ For an optimized system with a lower activation barrier, the reaction might proceed at 60 °C, which has been estimated to be the operating temperature for solar water splitting reactors without light concentration.²⁷ We can calculate the STH efficiency for this thermal reaction step by using the optimal reactions per second (r_s) value for two-photon water splitting ($\lambda_1 = 455$, $\lambda_2 = 517$ nm, $r_s = 383$ μmol/s) and the Gibbs free energy for H₂ release ($\Delta G = 144$ kJ/mol) along with Equation (9), giving an STH value of 5.52%. Adding this thermal contribution to the optimal STH efficiency of two-photon water splitting (13.27%) gives a total STH efficiency of 18.79%. If the higher E_{loss} value (96.2 kJ/mol, 1 eV) is used, the total STH efficiency drops to 10.83% (see Table 11.5-2, entry “Two-photon/thermal”).

11.5.2.2 Maximum Theoretical STH Efficiencies for Different Mechanism Types

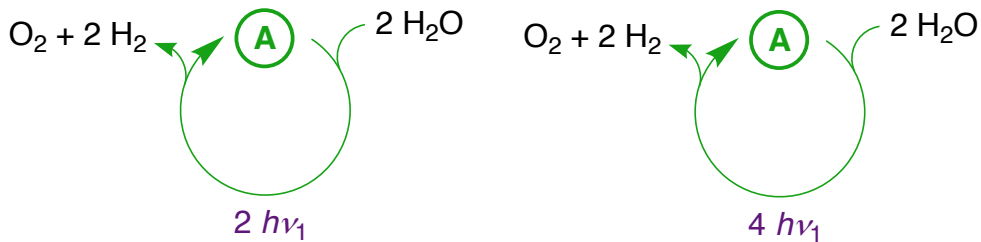
Table 11.5-1 to Table 11.5-4 show the maximum theoretical solar-to-hydrogen efficiencies for various mechanism types with either one, two, three or four photoabsorbers. In all cases, $\Delta G_{\text{reaction}} = 4 \times 1.229$ eV (474.7 kJ/mol) and $E_{\text{loss}} = 73.2$ or 96.2 kJ/mol. Seitz *et al.* investigated semiconductor S4 and D4 systems,²⁵ and their results agree well those presented herein for $E_{\text{loss}} = 96.2$ kJ/mol (see Table 11.5-1, entry S4 and Table 11.5-2 entry D4).

We would like to note that the minimum bound for E_{loss} is likely different for molecular photochemical reactions versus semiconductor systems: in case of semiconductors, electrons and holes generated by photon absorption have to diffuse to the active sites for hydrogen and oxygen evolution, which happens at comparatively slow timescales and allows for other free energy loss mechanisms such as charge carrier trapping.²⁸ For intramolecular photochemical reactions (such as [B-Mono]D₀ → [C-Mono]D₀) or those within supramolecular assemblies (such as [A]S₀ → [B]T₀), no diffusion is necessary and reactions can proceed on faster time scales, avoiding free energy loss mechanisms such as trapping. These considerations suggest that a lower bound for E_{loss} is appropriate for molecular systems as compared to semiconductor ones, although a quantitative assessment of this difference is beyond the scope of this work.

In Table 11.5-1 we can see that single absorber systems are limited to a maximum of STH efficiency of 18.11% and that there is a significant increase in STH efficiency when moving from a S2 (two photons in total) to a S4 system (four photons in total). The same increase in STH efficiency for moving from two to four photons can be seen for dual absorber systems (Table 11.5-2, D1 and D2), while the increase is only modest moving from D2 to D4. In contrast, two-photon water splitting combined with thermal H₂ release can actually achieve an STH efficiency of 18.79% despite utilizing only two photons in total.

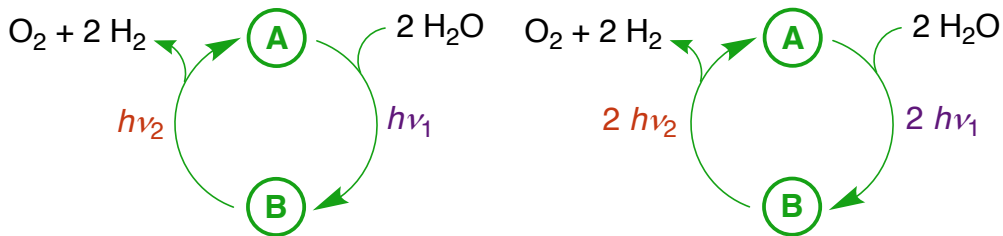
Triple absorber systems (Table 11.5-3) allow for a further increase in STH efficiency, with a maximum of 33.78% for T2 systems. Combining two-photon water splitting with photochemical H₂ release in a T-1-1-2 mechanism (one photon absorbed by [A] and [B] each, and two photons absorbed by two equivalents of [F]), allows for a maximum STH efficiency of 28.65%. This value is only slightly lower than the one for an ideal T2 system and it is a significant improvement over two-photon/thermal H₂ release.

Table 11.5-1 Maximum theoretical solar-to-hydrogen efficiencies for single absorber mechanisms

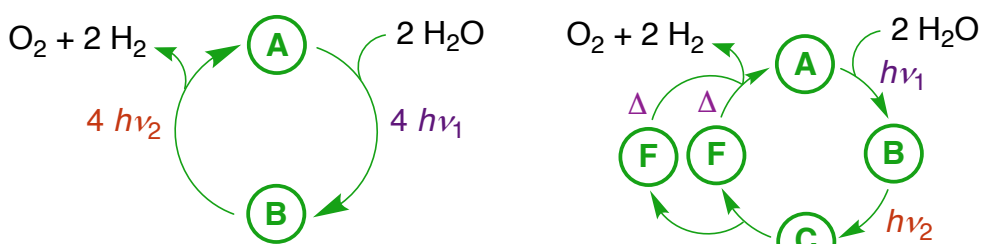


Mechanism type	S2	S4
STH, $E_{loss} = 73.2$ kJ/mol (0.76 eV), optimal λ	2.48% 385 nm	18.11% 623 nm
STH, $E_{loss} = 96.2$ kJ/mol (1 eV), optimal λ	1.22% 358 nm	12.33% 556 nm
STH Reference Seitz et al.	/	11.2%

Table 11.5-2 Maximum theoretical solar-to-hydrogen efficiencies for dual absorber mechanisms

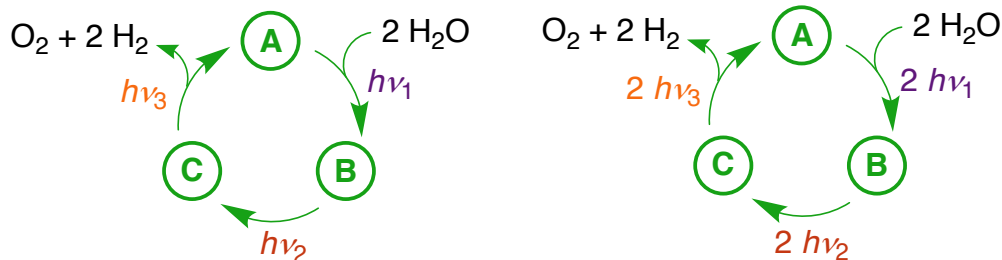


Mechanism type	D1	D2
STH, $E_{loss} = 73.2$ kJ/mol (0.76 eV), optimal λ	3.29% 370, 402 nm	25.16% 559, 703 nm
STH, $E_{loss} = 96.2$ kJ/mol (1 eV), optimal λ	1.66% 348, 369 nm	17.09% 509, 613 nm
STH Reference Seitz et al.	/	/

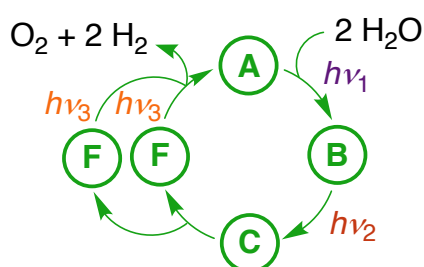


Mechanism type	D4	Two-photon/thermal
STH, $E_{loss} = 73.2$ kJ/mol (0.76 eV), optimal λ	27.72% 733, 1173 nm	18.79% 455, 517 nm
STH, $E_{loss} = 96.2$ kJ/mol (1 eV), optimal λ	21.28% 658, 919 nm	10.83% 421, 469 nm
STH Reference Seitz et al.	22.8%	/

Table 11.5-3 Maximum theoretical solar-to-hydrogen efficiencies for triple absorber mechanisms

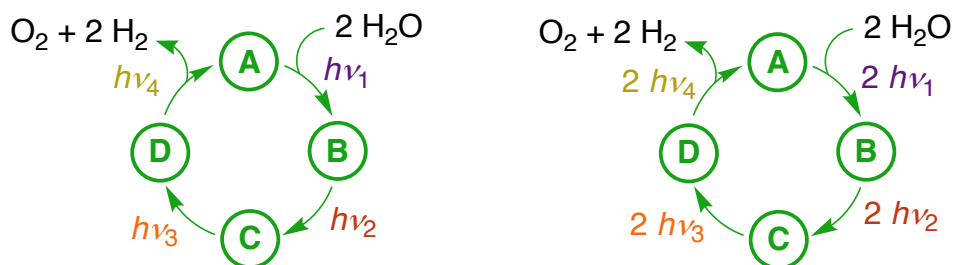


Mechanism type	T1	T2
STH, $E_{loss} = 73.2$ kJ/mol (0.76 eV), optimal λ	19.22% 459, 524, 584 nm	33.78% 610, 807, 1062 nm
STH, $E_{loss} = 96.2$ kJ/mol (1 eV), optimal λ	11.79% 428, 475, 515 nm	24.68% 557, 699, 850 nm



Mechanism type	T-1-1-2
STH, $E_{loss} = 73.2$ kJ/mol (0.76 eV), optimal λ	28.65% 491, 584, 748 nm
STH, $E_{loss} = 96.2$ kJ/mol (1 eV), optimal λ	19.58% 460, 526, 642 nm

Table 11.5-4 Maximum theoretical solar-to-hydrogen efficiencies for quadruple absorber mechanisms



Mechanism type	Q1	Q2
STH, $E_{loss} = 73.2$ kJ/mol (0.76 eV), optimal λ	31.16% 500, 597, 685, 781 nm	34.05% 611, 809, 1068, 1603 nm
STH, $E_{loss} = 96.2$ kJ/mol (1 eV), optimal λ	21.08% 466, 536, 600, 661 nm	26.37% 566, 716, 880, 1098 nm

Figure 11.5-2 visualizes the ideal absorption wavelengths for each photoabsorber in a T-1-1-2 system ($\lambda_1 = 491$ nm, $\lambda_2 = 584$ nm, $\lambda_3 = 748$ nm), for which ΔG_{total} is only slightly larger than $\Delta G_{\text{reaction}}$ and the absorbed photon fluxes are ideally matched (1:1:2). In this case, λ_1 (491 nm) describes the longest absorption wavelength of **A**, λ_2 (584 nm) the longest absorption wavelength of **B** and λ_3 (748 nm) the longest absorption wavelength of **F**.

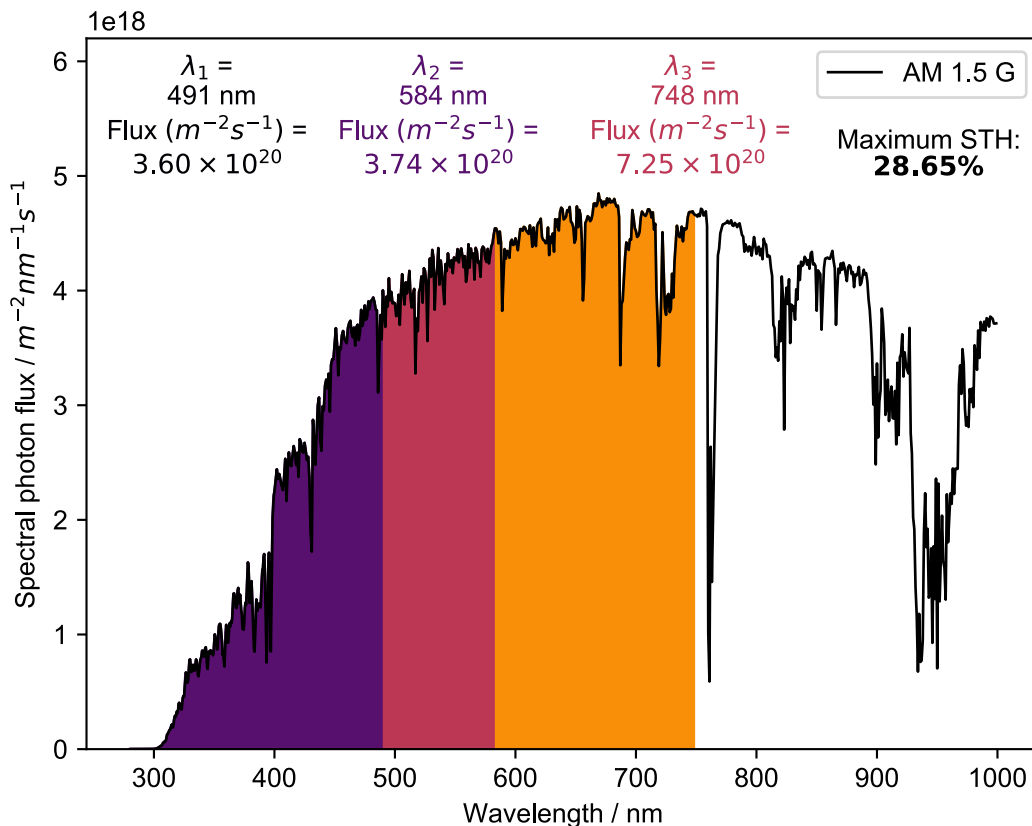


Figure 11.5-2 Solar AM 1.5 G spectrum with highlighted wavelength ranges for optimal T-1-1-2 water splitting

$$\Delta G_{\text{reaction}} = 474.7 \text{ kJ/mol} \text{ and } E_{\text{loss}} = 73.2 \text{ kJ/mol}$$

Table 11.5-4 shows that quadruple absorber systems further increase maximum STH efficiencies, although the increase is rather modest compared to triple absorber systems (34.05% for D2 versus 33.78% for T2).

Overall, two-photon water splitting combined with thermal H₂ release has the highest STH efficiency for any mechanism requiring only two photons while a T-1-1-2 mechanism has the second highest STH efficiency for any mechanism requiring four photons, only surpassed by Q1.

11.6 Structures and Coordinates for Computed Species

Figure 11.6-1 [A]S₀ Structure and Coordinates

128 Energy: -1951573.6088386

H	0.45669	-1.41554	-3.91019
C	-0.60849	-1.19121	-3.76131
H	-1.11536	-1.29884	-4.73276
H	-0.68914	-0.14799	-3.42124
H	-0.74297	0.90882	2.57857
O	-0.73313	0.99069	-1.30811
H	-0.86407	3.10316	1.53230
O	-1.30655	-1.17052	0.32709
H	-0.11798	0.23950	-1.31847
C	-1.15605	-2.12135	-2.70053
H	-1.34189	0.63234	4.24389
H	-1.19394	-3.16363	-3.07447
C	-1.54956	1.15446	3.29347
H	-1.17142	2.92058	-0.19928
H	-1.50205	2.23286	3.50526
H	-0.49457	-2.11224	-1.82445
C	-1.48683	3.46582	0.70359
H	-1.28687	4.54268	0.57069
H	-2.17348	-2.85488	-0.51445
Ru	-2.51776	0.09058	-0.76873
H	-2.32615	-1.22677	2.00794
N	-2.49410	-1.72633	-2.21407
C	-2.97419	-2.74821	-1.26400
C	-2.93493	0.72547	2.80365
H	-2.70322	-1.17497	3.77243
H	-2.82644	3.73565	3.11401
C	-2.99884	-0.80829	2.77427
C	-2.96136	3.26345	0.97102
P	-3.18200	1.37474	1.02207
H	-3.18200	-3.70108	-1.75468
C	-3.41191	4.01555	2.29952
H	-3.11689	0.67633	-3.90443
H	-2.77234	-3.04850	-4.74444
H	-3.24914	5.09319	2.05928
C	-3.46221	-1.53612	-3.31726
H	-3.76709	0.77330	4.77624
C	-3.39499	1.14602	-1.98472
C	-4.00916	1.20050	3.78848
H	-3.48450	3.39830	-1.16373
C	-3.76998	3.84199	-0.20428
H	-4.05874	2.28811	3.90782
H	-3.54789	4.92029	-0.26501
C	-4.20392	-2.27738	-0.54802
N	-4.18814	-0.97126	-0.21953
C	-3.69183	-2.73052	-4.23152
H	-4.02129	-1.17123	2.58909
H	-4.41501	-1.23043	-2.86054
H	-4.48087	3.87829	2.45436
H	-4.10485	-3.60071	-3.69946
C	-5.04785	1.04374	0.77758
H	-4.42084	-2.44844	-5.00597
H	-5.01097	0.83045	3.52344
C	-5.21189	-0.41068	0.46124
C	-5.27900	-3.08726	-0.20149
H	-4.85906	3.74404	-0.07432
H	-5.27592	-4.14092	-0.48292
H	-5.32999	1.63208	-0.11068
H	-5.69471	1.35408	1.60901
C	-6.31091	-1.17896	0.83734
C	-6.34379	-2.53021	0.50361
H	-7.12815	-0.71577	1.39103
H	-7.19795	-3.14636	0.78976
O	-3.88678	1.76908	-2.83721
C	0.53409	-3.71739	2.88972
H	1.03191	1.20848	-2.61109
O	0.65050	0.63916	1.17066
H	1.12549	3.11974	-1.16533
O	1.44261	-1.31103	-0.69485
H	0.26065	1.02485	0.36109
C	0.80054	-2.40419	2.17077
H	1.68202	1.04433	-4.26091
C	1.88201	1.46254	-3.26027
H	1.45188	2.85330	0.54886
H	1.90016	2.55632	-3.36662
C	1.77392	3.42698	-0.33278
H	1.60977	4.50161	-0.14530
H	2.21320	-3.13261	0.23384
Ru	2.48771	-0.14715	0.67409
H	2.42528	-1.08233	-2.29685
N	2.22014	-2.03548	1.98131
C	2.88466	-3.01698	1.10162
C	3.21523	0.90739	-2.75460
H	3.06582	-0.85253	-3.97218
H	3.14685	3.03696	-2.70611
C	3.21891	-0.61872	-2.90429
C	3.25842	3.18593	-0.62318
P	3.39813	1.30222	-0.89528
H	3.03776	-3.98536	1.60832
C	3.72389	4.05980	-1.78770
H	3.34789	-1.53905	3.86434
H	1.86000	-0.45924	3.86531
H	3.58700	5.11498	-1.49887
C	2.93991	-1.94811	3.26960
H	4.16382	1.16053	-4.65719
C	3.31771	0.77390	2.01601
C	4.36497	1.44823	-3.61143
H	3.80161	3.07198	1.51083
C	4.07551	3.61023	0.59852
H	4.47194	2.53769	-3.58867
H	3.87932	4.67993	0.78110
C	4.18485	-2.51032	0.55399
N	4.19730	-1.20307	0.23710
C	2.23139	-1.09489	4.30517
H	4.19048	-1.05275	-2.61958
H	3.09882	-2.96832	3.67033
H	4.79216	3.92068	-2.01152
H	1.37686	-1.62062	4.75467
C	5.18533	0.84532	-0.56671
H	2.93276	-0.83914	5.11222
H	5.33086	0.99479	-3.34259
C	5.28552	-0.62889	-0.31867
C	5.29319	-3.31376	0.30802
H	5.15955	3.50693	0.43450
H	5.26682	-4.37010	0.57750
H	5.44504	1.36569	0.36985
H	5.89468	1.17571	-1.33728
C	6.41479	-1.39237	-0.60461
C	6.41695	-2.74787	-0.28829
H	7.28349	-0.91982	-1.06390
H	7.29594	-3.35964	-0.49892
H	0.51938	-1.28667	-0.38188
O	3.84337	1.29469	2.91844
H	-0.55554	-3.85917	2.95147
H	0.92613	-3.74051	3.91838
H	0.94292	-4.58591	2.35026
H	0.33909	-2.42001	1.17789
H	0.32431	-1.56825	2.69632
H	-0.67343	-0.57507	0.79032

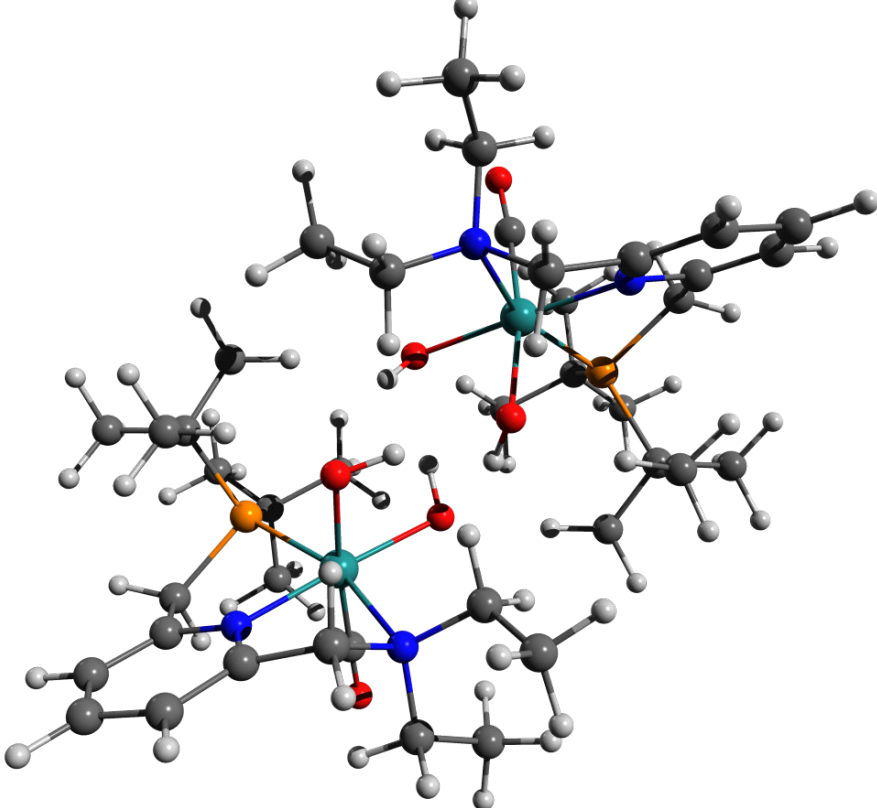


Figure 11.6-2 [A-RR]S₀ Structure and Coordinates

128

Energy: -1951572.9167082

C	-1.33476	1.62962	3.69683
H	-0.26977	-1.45456	-1.99998
O	-1.00000	-0.94847	1.55613
H	-0.69418	-3.51808	-0.61782
O	-1.16182	0.99921	-0.43577
C	-1.63792	2.42574	2.44563
H	-0.43706	-1.55601	-3.77219
C	-0.88137	-1.87525	-2.81475
H	-1.36512	-2.97340	0.92589
H	-0.80142	-2.97152	-2.77187
C	-1.50682	-3.69045	0.10226
H	-1.41068	-4.72148	0.48355
H	-2.11655	2.78328	-0.01923
Ru	-2.60257	-0.08485	0.60240
H	-1.90018	0.68204	-2.25402
N	-2.83716	1.95014	1.72806
C	-3.06271	2.80387	0.54647
C	-2.33492	-1.40393	-2.76955
H	-1.86051	0.28270	-4.00954
H	-2.24788	-4.41338	-2.45745
C	-2.38522	0.10267	-3.05592
C	-2.88702	-3.52920	-0.54760
P	-3.00905	-1.68496	-1.00600
H	-3.30495	3.84415	0.82365
C	-3.04458	-4.50892	-1.70925
H	-3.85094	1.17903	3.37948
H	-3.64271	3.64614	3.90445
H	-2.98825	-5.53336	-1.30402
C	-4.03307	1.92951	2.60067
H	-2.70959	-1.81161	-4.83771
C	-3.71958	-0.90744	1.79395
C	-3.14948	-2.09636	-3.86696
H	-3.90230	-3.25753	1.38718
C	-3.96162	-3.87414	0.48495
H	-3.13803	-3.18967	-3.81289
H	-3.81069	-4.92111	0.79619
C	-4.13209	2.22311	-0.32930
N	-4.09753	0.88119	-0.42939
C	-4.42734	3.25143	3.24266
C	-3.86625	0.45733	-3.30565
H	-4.86802	4.15718	-1.99693
H	-4.01792	-4.41009	-2.21348
H	-4.67408	4.02796	2.50298
C	-4.83154	-1.27709	1.21853
H	-5.32631	3.09131	3.85669
H	-4.19637	-1.75785	-3.88610
C	-4.98710	0.21414	-1.19742
C	-5.08534	2.96481	-1.01727
H	-4.97961	-3.80540	0.07074
H	-5.10111	4.05079	-0.91839
H	-5.32519	-1.69300	-0.32500
H	-5.30741	-1.72040	-2.10386
C	-5.95975	0.90972	-1.91117
C	-6.00672	2.29855	-1.82227
H	-6.66897	0.36131	-2.53192
H	-6.76286	2.85910	-2.37469
H	-0.42438	0.37664	-0.58526
O	-4.37127	-1.37026	2.64145
C	1.30359	-1.37352	3.78803
H	0.29481	1.58800	-1.99894
O	1.03826	1.02511	1.61441
H	0.88996	3.59972	-0.60082
O	1.09120	-0.88920	-0.40805
C	1.55019	-2.25202	2.58013
H	0.43562	1.60929	-3.77068
C	0.91906	1.93554	-2.83465
H	1.62411	3.10560	0.93434
H	0.91009	3.03531	-2.83283
C	1.74815	3.77187	0.06532
H	1.71600	4.82376	0.39669
H	1.98309	-2.72548	0.11055
Ru	2.60225	0.12276	0.61552
H	1.74851	-0.65907	-2.22066
N	2.75934	-1.86762	1.82092
C	2.92848	-2.78423	0.67748
C	2.33958	1.37024	-2.79326
H	1.76399	-0.31890	-3.98372
H	2.40859	4.37481	-2.55388
C	2.28703	-0.14409	-3.02839
C	3.08265	3.51160	-0.64424
P	3.06784	1.64973	-1.05231
H	3.11897	-3.82273	0.99687
C	3.23871	4.44917	-1.84065
H	3.84335	-1.07408	3.41866
H	3.51821	-3.49458	4.06914
H	3.25147	5.48578	-1.46371
C	3.97091	-1.86838	2.67360
H	2.69610	1.69491	-4.87946
C	3.76844	0.93623	1.76348
C	3.17664	1.97283	-3.92616
H	4.19024	3.22897	1.23990
C	4.22682	3.82382	0.32206
H	3.24462	3.06520	-3.90259
H	4.14280	4.88270	0.61809
C	4.00735	-2.29506	-0.23921
N	4.03247	-0.99918	-0.40353
C	4.30793	-3.17694	3.37295
C	3.29447	-0.57481	-3.15262
H	4.81461	-1.55973	2.03898
H	4.18438	4.42658	-2.37953
H	4.86654	-4.00159	2.06092
O	4.86699	1.12496	-1.29099
H	5.22779	-3.03581	3.96020
H	4.19586	1.55927	-3.95705
C	4.93388	0.37027	-1.21712
C	4.90832	-3.11179	-0.91452
H	5.21535	3.69907	-0.14678
H	4.87646	-4.19174	-0.76656
H	5.39407	1.54156	-0.42312
H	5.33725	1.51112	-2.20034
C	5.85550	-1.14217	-1.92095
C	5.83838	-2.52595	-1.76976
H	6.57610	-0.65667	-2.57971
H	6.55364	-3.14599	-2.31319
H	0.38008	-1.02765	0.25693
O	4.44257	1.39800	2.59466
H	-1.75243	3.50226	2.68089
H	-0.80012	2.33087	1.74631
H	-2.02715	1.84874	4.52480
H	-0.31432	1.86898	4.02428
H	-1.36384	0.55228	3.47461
H	1.62589	-3.31834	2.87075
H	0.69051	-2.14886	1.90309
H	2.03483	-1.52819	4.59704
H	0.30462	-1.60278	4.18461
H	1.30428	-0.31685	3.48018
H	-0.38513	-0.22179	1.78772
H	0.41886	1.21775	0.88892

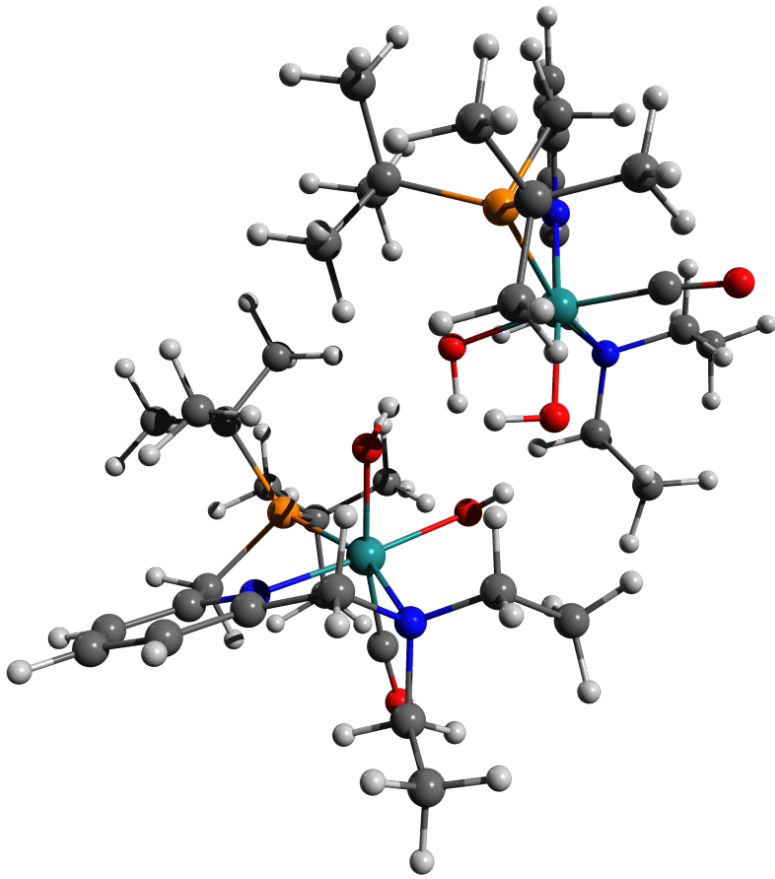


Figure 11.6-3 [A-RS-1]S₀ Structure and Coordinates

128

Energy: -1951573.3041640

C	0.44944	1.22488	-3.77639
H	0.85001	-1.78901	2.23509
O	0.88713	-1.26790	-1.44493
H	1.57788	-3.69098	0.87899
O	0.98095	0.88491	0.39954
C	0.79921	2.22961	-2.69815
H	1.26570	-1.62533	3.95664
H	0.64403	3.26790	-3.05872
C	1.65776	-1.92898	2.97132
H	1.93112	-3.16660	-0.77294
H	1.88358	-3.00310	3.03292
H	0.12105	2.06733	-1.84896
C	2.32505	-3.74865	0.07538
H	2.42815	-4.80718	-0.21773
H	1.57306	2.83785	-0.37216
Ru	2.44962	-0.09044	-0.75468
H	1.79048	0.71994	2.13147
N	2.16494	2.06545	-2.18577
C	2.41038	2.98380	-1.07523
C	2.90298	-1.09150	2.67002
H	2.20094	0.53729	3.87486
H	3.52988	-4.02953	2.56215
C	2.56397	0.39387	2.84285
C	3.69327	-3.21981	0.52014
P	3.42989	-1.36334	0.85447
H	2.44494	4.04258	-1.39333
C	4.21952	-4.02271	1.70965
H	3.05995	1.30047	-3.90411
H	2.34497	3.63209	-4.57434
H	4.34614	-5.06930	1.38574
C	3.20642	2.14589	-3.21895
H	3.61588	-1.23685	4.68387
C	3.53938	-0.75838	-2.05905
C	4.01472	-1.42166	3.67240
H	4.38662	-2.90712	-1.54788
C	4.69148	-3.40826	-0.62397
H	4.35525	-2.46207	3.74201
H	4.75181	-4.48669	-0.84501
C	3.66112	2.63839	-0.31581
N	3.72266	1.16366	-0.07070
C	3.27034	3.44640	-4.00884
H	3.45963	1.03171	2.72334
H	4.17171	1.96408	-2.72147
H	5.20328	-3.66674	2.05212
H	3.45657	4.32098	-3.36660
C	5.12282	-0.55440	0.79579
H	4.09598	3.39154	-4.73430
H	4.88799	-0.76266	3.55393
C	4.95773	0.92694	0.62682
C	4.54049	3.60455	0.16296
H	5.70742	-3.07897	-0.35564
H	4.34930	4.65660	-0.05122
H	5.59454	-0.95183	-0.11779
H	5.77818	-0.79507	1.64343
C	5.86173	1.85499	1.13857
C	5.64754	3.20948	0.90675
H	6.72471	1.50940	1.70833
H	6.34577	3.95253	1.29638
H	0.16102	0.80024	-0.13289
O	4.15621	-1.09821	-2.98708
C	-1.19301	-3.84473	-1.18152
H	-0.26419	2.42261	1.01026
O	-0.73798	-1.41373	0.85327
H	-0.39436	1.23053	3.13584
O	-1.36411	0.39954	-1.19688
H	-0.16417	-0.63117	0.95056
C	-1.71073	-2.77480	-2.11892
H	-0.62877	4.16044	0.81622
C	-0.94210	3.23229	1.32537
H	-1.01484	-0.42043	2.99262
H	-0.79963	3.39421	2.40359
C	-1.12835	0.52400	3.54629
H	-0.88319	0.35518	4.60876
H	-2.46759	-0.43411	-2.77867
Ru	-2.53285	-0.62460	0.18044
H	-2.00588	2.17779	-1.04332
N	-2.90366	-2.07190	-1.59740
C	-3.34620	-1.07479	-2.59111
C	-2.40466	2.95723	0.96836
H	-2.18292	3.96727	-0.91269
H	-2.01998	3.12487	3.94360
C	-2.56224	2.99352	-0.55736
C	-2.56286	1.05027	3.43758
P	-2.88694	1.20278	1.56571
H	-3.68593	-1.54294	-3.53017
C	-2.72345	2.33878	4.24338
H	-3.66771	-3.63450	-0.44206
H	-3.69938	-4.57063	-2.78946
H	-2.52085	2.10771	5.30280
C	-4.00430	-3.01267	-1.28002
H	-2.94425	5.02381	1.12511
C	-3.41776	-1.74699	1.32201
C	-3.29761	4.06429	1.53923
H	-3.44526	-0.96318	3.57207
C	-3.51212	0.01888	4.05009
H	-3.26800	4.14975	2.63062
H	-3.23066	-0.15157	5.10783
C	-4.40472	-0.19363	-0.201841
N	-4.21751	0.14522	-0.72650
C	-4.48118	-3.90161	-2.41608
H	-3.91973	2.92771	-0.07771
H	-4.84222	-2.41181	-0.89722
H	-3.74677	2.74021	4.18907
H	-4.88329	-3.32890	-3.26859
C	-4.75401	1.23729	1.35498
H	-5.30745	-4.53433	-2.04271
H	-4.34603	3.95500	1.22413
C	-5.07513	0.96578	-0.08390
C	-5.48543	0.32174	-2.73305
H	-4.56123	0.35307	4.03718
H	-5.62270	0.04053	-3.77768
H	-5.11703	0.37291	1.94924
C	-5.25224	2.13269	1.72618
C	-6.16943	1.50670	-0.75472
H	-6.37327	1.18280	-2.09319
H	-6.85123	2.17357	-0.22620
H	-7.22639	1.59603	-2.63427
H	-6.61046	-0.19239	-1.42034
O	-3.91652	-2.56087	1.99078
H	-6.62551	1.30058	-3.99399
H	0.64812	0.20448	-3.41292
H	0.99685	1.39251	-4.71719
H	-1.00677	-3.40740	-0.18877
H	-0.23452	-4.21439	-1.57202
H	-1.87164	-4.70722	-1.08997
H	-0.92118	-2.02245	-2.25956
H	-1.94765	-3.19941	-3.11412
H	0.39291	-1.52961	-0.63555

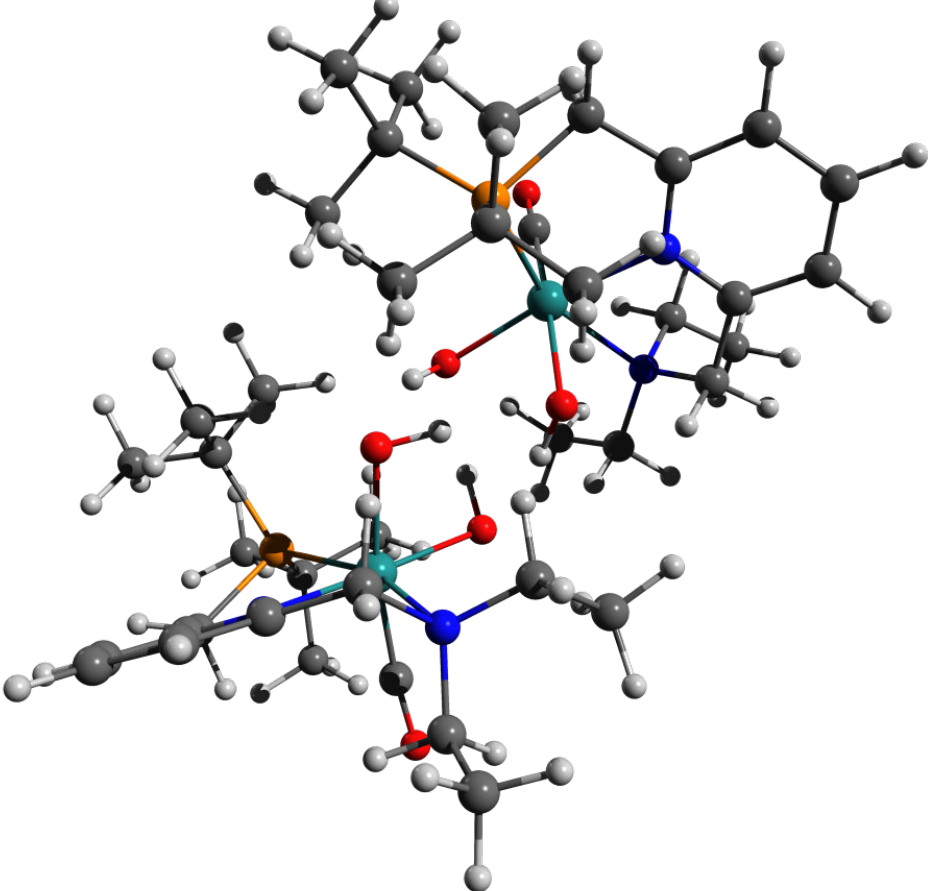


Figure 11.6-4 [A-RS-2]S₀ Structure and Coordinates

128 Energy: -1951572.5055138

C	-1.16194	-3.96254	0.55819
H	-0.26547	2.56698	-0.56039
O	-0.71633	-1.22947	-1.04323
H	-0.41574	1.72547	-2.90022
O	-1.37163	0.23431	1.25980
H	-0.14262	-0.44333	-0.99728
C	-1.67727	-3.05991	1.65360
H	-0.64876	4.24417	-0.11099
C	-0.95882	3.40685	0.76038
H	-1.04447	0.07567	-3.01956
H	-0.80424	3.73235	-1.79927
C	-1.15597	1.09668	-3.41404
H	-0.91646	1.09973	-4.49107
H	-2.46097	-0.86938	2.68486
Ru	-2.52248	-0.57308	-0.26885
H	-2.04005	1.99190	1.39806
N	-2.87838	-2.29591	1.25096
C	-3.33255	-1.47943	2.39246
C	-2.42515	3.08378	-0.46455
H	-2.22018	3.77888	1.55552
H	-2.02347	3.73102	-3.37496
C	-2.59537	2.87446	1.04586
C	-2.58569	1.60700	-3.21317
P	-2.89982	1.44899	-1.33940
H	-3.66860	-2.09820	3.24145
C	-2.73620	3.01159	-3.79611
H	-3.62358	-3.65750	-0.14564
H	-3.64930	-4.96047	2.02194
H	-2.53836	2.95472	-4.87985
C	-3.96814	-3.18351	0.78104
H	-2.97044	5.14641	-0.27862
C	-3.38552	-1.50789	-1.58371
C	-3.31123	4.27088	-0.85685
H	-3.49938	-0.34703	-3.66603
C	-3.54712	0.69940	-3.98296
H	-3.26008	4.54057	-1.91680
H	-3.26225	0.72878	-5.04784
C	-4.39988	-0.51775	1.97028
N	-4.21716	0.01904	0.74920
C	-4.44520	-4.24977	1.75605
H	-3.65521	2.76763	1.32441
H	-4.81111	-2.53646	0.49757
H	-3.75507	3.40879	-3.67224
H	-4.85141	-3.82674	2.68713
C	-4.76609	1.42433	-1.12500
H	-5.25455	-4.82416	1.28070
H	-4.36541	4.10888	-0.58674
C	-5.08332	0.92583	0.25017
C	-5.48466	-0.14662	2.75743
H	-4.59044	1.04577	-3.92042
H	-5.61757	-0.59610	3.74205
H	-5.12379	0.67768	-1.85267
H	-5.27147	2.37505	-1.34127
C	-6.18240	1.33887	0.99587
C	-6.38195	0.79836	2.26671
H	-6.87085	2.07685	0.56868
H	-7.23854	1.10900	2.86765
H	-0.60569	-0.38424	1.38092
O	-3.86464	-2.21004	-2.38127
H	-0.53829	0.49268	4.17835
C	0.52979	0.40722	3.92102
H	1.0249	0.42571	4.88139
H	0.07910	-0.54051	3.39085
H	0.79315	-1.31744	-2.52205
O	0.91432	-1.17223	1.94448
H	1.46974	-3.38523	-1.45868
O	1.03384	0.96896	-0.20626
O	0.84882	1.56908	3.00435
H	1.21054	-0.84276	-4.19128
H	0.72851	2.53846	3.52091
C	1.59831	-1.32480	-3.27797
H	1.90942	-3.21844	0.24600
H	1.80927	-2.37257	-3.53444
H	0.13824	1.55332	2.16730
C	2.24561	-3.62799	-0.71930
H	2.31753	-4.72653	-0.64710
H	1.58278	2.70824	0.86890
Ru	2.49862	-0.13997	0.78538
H	1.77452	1.12681	-1.96506
N	2.20456	1.49639	2.42021
C	2.42865	2.68434	1.57538
C	2.85422	-0.57162	-2.83232
H	2.16359	1.25552	-3.72049
H	3.38851	-3.48871	-3.25647
C	2.53404	0.92498	-2.73502
C	3.61447	-3.05813	-1.10613
P	3.37383	-1.16762	-1.09234
H	2.45643	3.61668	2.16440
C	4.09113	-3.65265	-2.43111
H	3.12402	0.42379	3.95740
H	2.37123	2.55660	5.08958
H	4.18984	-4.74341	-2.29982
C	3.25511	1.39149	3.45879
H	3.55876	-0.36720	-4.84451
C	3.57726	-1.09645	1.89839
C	3.95888	-0.73043	-3.88287
H	4.37145	-3.13218	0.96251
C	4.63697	-3.46765	-0.04444
H	4.28934	-1.76320	-4.03702
H	4.67512	-4.56940	-0.01908
C	3.66953	2.53433	0.74934
N	3.88766	1.28977	0.28531
C	3.29696	2.50194	4.49834
C	3.43367	1.52044	-2.51419
H	4.22093	1.33668	2.93511
H	5.08000	-3.27043	-2.72699
H	3.48085	3.49358	4.05824
C	5.08766	-0.41751	-0.91673
H	4.12250	2.29925	5.19710
H	4.83902	-0.11051	-3.65529
C	4.95052	1.01411	-0.50029
C	4.52900	3.57781	0.42300
H	5.65342	-3.11756	-0.28298
H	4.33800	4.57849	0.81212
H	5.55431	-0.97211	-0.08606
H	5.73358	-0.52553	-1.79812
C	5.83620	2.02474	-0.86699
C	5.62030	3.31907	-0.40233
H	6.68860	1.79111	-1.50887
H	6.03554	4.12275	-0.67778
H	0.21147	0.79237	0.29747
O	4.18237	-1.67371	2.04045
H	-1.04711	-3.63043	2.56906
H	-0.89587	-2.38029	1.91152
H	-1.82472	-4.80355	0.32849
H	-0.19204	-4.38523	0.89338
H	-0.96821	-3.36937	0.35049
H	0.46736	-1.56382	0.44287

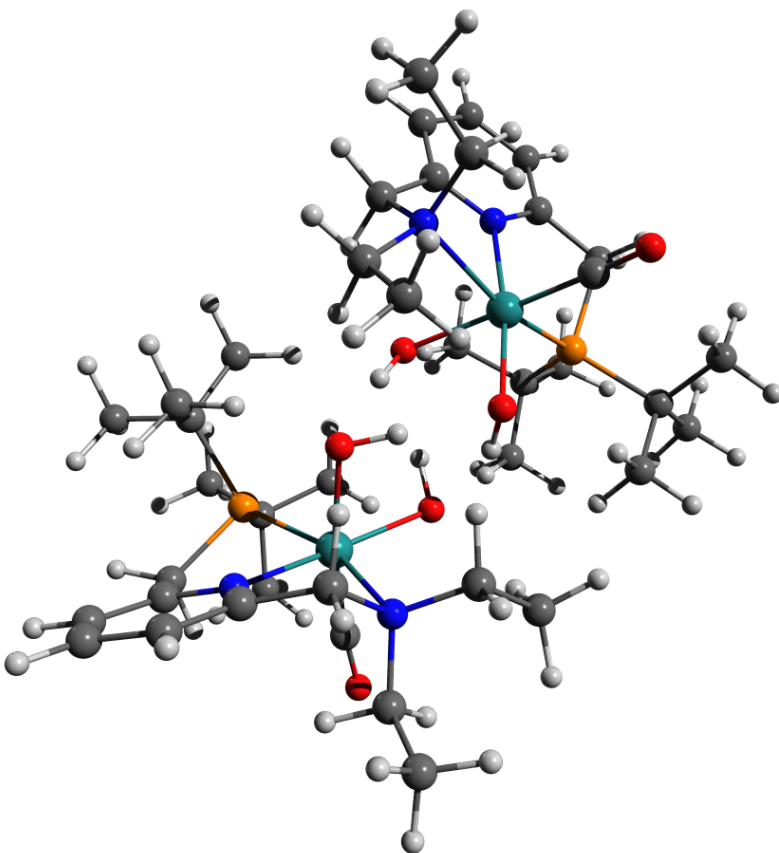


Figure 11.6-5 [A]T₀ Structure and Coordinates

128

Energy: -1951545.5657542

H	0.31863	-4.29565	-0.54368
C	-0.74782	-4.05620	-0.66007
H	-1.25666	-4.95812	-1.03476
H	-0.83424	-3.25902	-1.41383
H	-0.89863	2.85473	0.60480
O	-0.81090	-0.46520	-1.74247
H	-1.03805	3.35602	-1.86063
O	-1.24485	-0.42066	1.01348
H	-0.19731	-0.01036	-1.12069
C	-1.29305	-3.57816	0.66899
H	-1.52275	4.12018	1.69653
H	-1.26491	-4.40087	1.41479
C	-1.71674	3.57878	0.75441
H	-1.15604	1.73456	-2.60268
H	-1.68868	4.32026	-0.05772
H	-0.65852	-2.76439	1.04954
C	-1.58651	2.74850	-2.59407
H	-1.43788	3.20907	-3.58570
H	-2.24912	-1.89079	2.23744
Ru	-2.42361	-0.74411	-0.65979
H	-2.34600	1.11425	1.95336
N	-2.64389	-3.01925	0.56942
C	-3.08084	-2.50418	1.85122
C	-3.07295	2.87641	0.85781
H	-2.70549	2.56665	2.95908
H	-3.18995	4.76240	-1.58997
C	-3.03607	1.96444	2.09462
C	-3.08836	2.68472	-2.28609
P	-3.24831	1.72285	-0.65451
H	-3.31703	-3.29603	2.58922
C	-3.70208	4.08183	-2.28393
H	-3.31453	-4.05086	-1.10616
H	-2.95781	-5.89569	0.63487
H	-3.61235	4.51704	-3.29444
C	-3.62965	-3.89593	-0.06466
H	-4.02518	4.49554	1.97149
C	-3.36456	-1.34120	-2.25361
C	-4.19650	3.89629	1.03496
H	-3.37346	0.82330	-3.40463
C	-3.73514	1.85180	-3.30797
H	-4.22593	-5.12822	1.64853
C	-5.03521	1.18702	-0.58544
H	-4.63688	-5.80115	0.05987
H	-5.17972	3.41023	1.13140
C	-5.19506	0.18768	0.51919
C	-5.31278	-1.58449	2.60864
H	-4.84681	1.83379	-3.30016
H	-5.31214	-2.30225	3.42990
H	-5.22278	0.68777	-1.54863
H	-5.75961	2.00674	-0.47589
C	-6.28110	0.23361	1.39299
C	-6.34423	-0.66720	2.44904
H	-7.05853	0.98311	1.24109
H	-7.18533	-0.64836	3.14469
O	-3.95239	-1.78104	-3.03127
C	0.46634	0.92944	4.49928
H	1.05119	-1.86914	-1.77387
O	0.68245	1.25187	-0.04535
H	1.17504	0.58034	-3.03899
O	1.59054	-1.20381	0.91053
H	0.68848	1.87513	-0.77795
C	0.80149	0.86998	3.01811
H	1.58372	-3.34978	-2.61470
C	1.79147	-2.27601	-2.47557
H	1.80904	2.09388	-2.35449
H	1.63051	-1.78465	-3.44595
C	1.94625	1.35647	-3.15761
H	1.77585	1.87055	-4.11806
H	2.26759	-1.13380	2.93873
Ru	2.56684	0.54429	0.42633
H	2.69920	-2.51644	0.11657
N	2.23960	0.90872	2.67109
C	2.92162	-0.28578	3.20523
C	3.22067	-2.10962	-1.96357
H	3.14970	-3.95308	-0.87315
H	2.92299	-0.73598	-4.64067
C	3.38740	-2.89712	-0.65726
C	3.37353	0.79744	-3.12893
P	3.47221	-0.27104	-1.54417
H	3.06077	-0.22542	4.29811
C	3.64980	0.06049	-4.43884
H	3.92137	2.13685	2.74600
H	1.86747	3.41929	1.76505
H	3.57127	0.79015	-5.26218
C	2.90572	2.12915	3.17040
H	4.10409	-3.77616	-2.97141
C	3.37619	2.16288	0.15103
C	4.22365	-2.69001	-2.97180
H	4.28215	2.54675	-2.13157
C	4.36811	1.98833	-3.05241
H	4.06518	-2.33910	-3.99929
H	4.16442	2.71113	-3.89428
C	4.46212	-0.65244	2.26944
N	4.26066	-0.29347	1.20812
C	2.17837	3.41271	2.81830
H	4.42733	-2.87195	-0.29351
H	3.02487	2.05820	4.26026
H	4.66297	-0.36397	-4.47338
H	1.28096	3.55834	3.43643
C	5.26488	-0.21591	-0.98745
H	2.84597	4.27026	2.98512
H	5.26986	-2.47853	-2.69355
C	5.35194	-0.57317	0.46505
C	5.33575	-1.10622	3.16925
C	5.40872	1.61545	-3.16035
H	5.29714	-1.30072	4.24147
H	5.57622	0.83481	-1.10176
H	5.94760	-0.82993	-1.59141
C	6.47694	-1.14500	1.05423
C	6.46875	-1.41095	2.41990
H	7.34875	-1.37413	0.44085
H	7.34436	-1.85234	2.89915
H	0.63496	-1.05555	0.77572
O	3.87246	3.21300	0.03062
H	-0.62825	0.88816	4.60526
H	0.80880	1.85473	4.98886
H	0.87716	0.07545	5.06003
H	0.39995	-0.04647	2.56943
H	0.32600	1.69534	2.47519
H	-0.66325	0.32172	0.76362

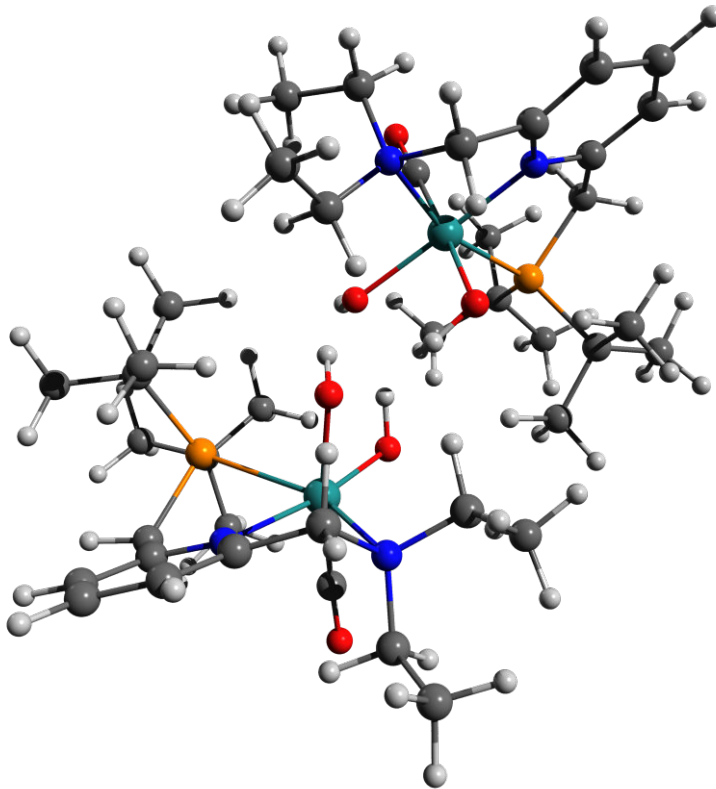


Figure 11.6-6 [A-Mono]S₀ Structure and Coordinates

64
 Energy: -975781.7288466
 N -0.71461 1.41145 -0.05552
 C -1.93725 1.87355 0.26183
 C 0.19459 2.20723 -0.65239
 C -2.28128 3.20265 0.05361
 C -1.33114 4.06030 -0.49717
 C -0.08773 3.55709 -0.86171
 C -2.85043 0.84429 0.85528
 H -3.27959 3.55437 0.31562
 H -1.56883 5.11248 -0.66341
 H 0.66192 4.19707 -1.32817
 C 1.45721 1.55183 -1.11784
 N -2.72411 -0.45534 0.16951
 H -3.89160 1.21043 0.86121
 H -2.55608 0.68653 1.90573
 H 1.24304 1.16737 -2.13027
 P 1.78985 -0.01998 -0.16505
 H 2.29722 2.25937 -1.16090
 Ru -0.39928 -0.61383 0.08172
 C -3.28283 -0.39340 -1.19918
 C 2.97324 -0.99546 -1.29362
 C -3.38475 -1.48595 1.00200
 C 2.72182 0.58988 1.38220
 C 2.11769 -1.74151 -2.32039
 C 3.72410 -2.04167 -0.46792
 C 3.96342 -0.09780 -2.03899
 C 1.86381 1.68472 2.02822
 C 4.09031 1.19356 1.06301
 C 2.89349 -0.54913 2.39174
 C -0.39429 -0.83617 1.89956
 O -0.45848 -1.02652 3.05049
 H -2.68999 0.34812 -1.75005
 C -4.77475 -0.11819 -1.30549
 H -3.03278 -1.34793 -1.67752
 H -2.89003 -1.49718 1.96295
 C -3.35227 -2.86901 0.38750
 H -4.42405 -1.16918 1.22192
 O -0.32253 -2.62404 -0.30069
 H 0.22403 -3.10148 0.30746
 O -0.53805 -0.04410 -1.96323
 H -0.32192 1.34094 -2.28979
 H -2.32157 -3.10175 -2.06512
 H -4.05521 -2.96053 -0.47067
 H -3.67404 -3.60285 1.14184
 H -5.05270 -0.10914 -2.37017
 H -5.06413 0.86089 -0.89282
 H -5.38839 -0.88876 -0.81452
 H 2.78956 -2.35108 -2.94866
 H 1.55854 -1.05021 -2.96420
 H 1.38471 -2.39095 -1.81685
 H 4.25560 -2.71733 -1.15807
 H 3.03302 -2.65720 0.12777
 H 4.47476 -1.60264 0.20341
 H 4.59861 -0.73497 -2.67721
 H 4.62793 0.47120 -1.37696
 H 3.44808 0.60833 -2.70613
 H 4.81061 0.44266 0.71220
 H 4.50493 1.63794 1.98338
 H 4.03158 1.99636 0.31245
 H 3.57490 -1.32971 2.03359
 H 1.93780 -1.01914 2.65161
 H 3.32255 -0.13633 3.32020
 H 2.33188 1.98025 2.98143
 H 0.84386 1.34147 2.24529
 H 1.79979 2.58622 1.40116

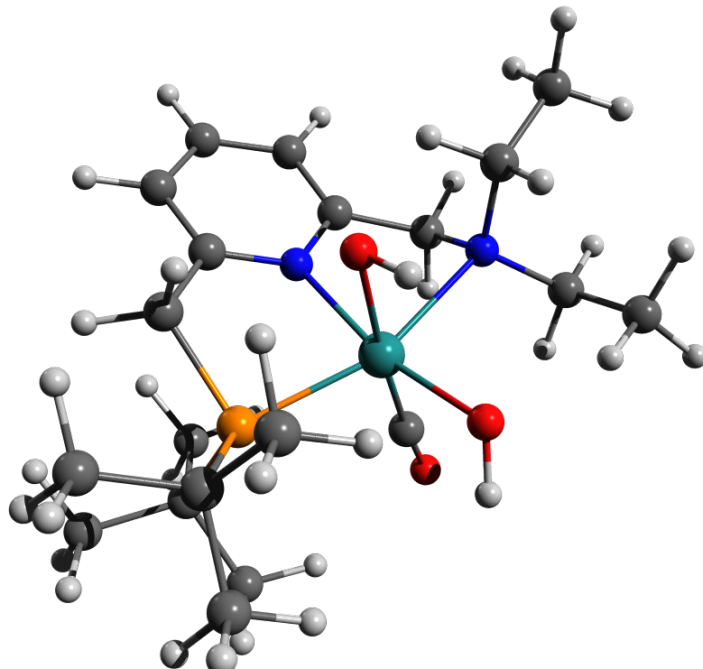


Figure 11.6-7 [B]To Structure and Coordinates

128

Energy: -1951514.6685434

H	0.84052	-2.25311	-2.78417
C	-0.23016	-2.03744	-2.88605
H	-0.57102	-2.40557	-3.86621
H	-0.34157	-0.94451	-2.83707
H	-1.64170	1.80046	2.89472
O	-0.72294	0.62491	-1.06975
H	-1.47959	3.47388	1.34965
O	-1.68143	-1.00834	0.89192
H	-0.59535	0.16002	1.52690
C	-0.95291	-2.67994	-1.72274
H	-2.72120	1.84010	4.31167
H	-0.92044	-3.78459	-1.80117
C	-2.64606	2.08586	3.23880
H	-1.25654	2.94128	-0.32533
H	-2.75935	3.17491	3.15115
H	-0.44556	-2.38791	-0.79259
C	-1.83479	3.61673	0.32271
H	-1.62574	4.65797	0.02470
H	-2.39869	-2.96096	0.34173
Ru	-2.59566	-0.16092	-0.64776
H	-2.65270	-0.58334	2.49333
N	-2.36315	-2.24342	-1.59784
C	-3.03659	-3.03916	-0.55326
C	-3.74898	1.31946	2.50435
H	-3.64812	-0.26873	3.94669
H	-3.94625	4.28929	2.05223
C	-3.60773	-0.16651	2.84936
C	-3.33511	3.34700	0.15613
P	-3.59593	1.52157	0.59701
H	-3.14219	-4.09816	-0.84126
C	-4.18056	4.31684	0.98119
H	-2.63361	-1.64826	-3.57898
H	-2.17894	-4.14639	-3.16682
H	-3.98035	5.34225	0.62908
C	-3.10242	-2.34818	-2.87765
H	-5.10774	1.73192	4.11432
C	-3.15199	0.56368	-2.27223
C	-5.11937	1.78407	3.01304
H	-3.02838	2.96955	-1.97683
C	-3.67118	3.55859	-1.19797
H	-5.08774	2.01755	2.70222
H	-3.50398	4.62220	-1.56798
C	-3.36789	-2.43769	0.21014
N	-4.39113	-1.09200	0.21354
C	-3.17526	-3.73298	-3.50339
H	-4.42527	-0.77276	2.43354
H	-4.11879	-1.96813	-2.69623
H	-5.26952	4.13449	0.85440
H	-3.72043	-4.45666	-2.87920
C	-5.34568	1.09320	0.04616
H	-3.71432	-3.66016	-4.45984
H	-5.93331	1.12663	2.67327
C	-5.49449	-0.39610	0.10003
C	-5.50907	-3.15651	0.12748
H	-4.72847	3.34280	-1.55912
H	-5.48528	-4.24674	0.12427
H	-5.39920	1.41082	-1.00804
H	-6.14654	1.60481	0.59464
C	-6.66267	-1.06745	0.45377
C	-6.66638	-2.45986	0.46973
H	-7.55649	-0.49909	0.71248
H	-7.57298	-3.00206	0.74405
O	-3.40404	0.96102	-3.33181
C	0.89904	-3.73171	2.71449
H	1.01359	1.04158	-2.29506
O	-0.12798	0.98651	1.82267
H	1.24131	3.20125	-0.85621
O	1.51852	-1.13690	-0.49408
H	0.82336	0.81278	1.65421
C	1.17691	-2.34510	2.15621
H	1.49211	1.02732	-4.01085
C	1.75687	1.42185	-3.01446
H	1.76771	3.00575	0.82090
H	1.64899	2.51591	-3.06415
C	1.97639	3.54475	-0.11382
H	1.81802	4.62383	0.05364
H	2.53022	-3.00441	0.15890
Ru	2.76648	-0.04139	0.73767
H	2.67561	-1.03155	-2.07911
N	2.60090	-1.98701	1.95836
C	3.23282	-2.92416	1.00403
C	3.19079	1.00164	-2.68368
H	2.99687	-0.79961	-3.83875
H	2.98925	4.01912	-2.61904
C	3.31565	-0.52190	-2.81920
C	3.41729	3.30850	-0.58173
P	3.54254	1.42138	-0.85356
H	3.38858	-3.91959	1.45665
C	3.70547	4.17978	-1.80325
H	4.35562	-1.54072	2.98214
H	2.38435	-0.23237	4.03344
H	3.62357	5.23765	-1.50059
C	3.37597	-1.98434	3.21683
H	3.94360	1.20083	-4.67999
C	3.49418	0.94625	2.09061
C	4.16731	1.62428	-3.68610
H	4.29331	3.15174	1.43832
C	4.38621	3.74278	0.52040
H	4.08475	2.12124	-3.77194
H	4.16181	4.79133	0.78363
C	4.51619	-2.40174	0.04993
N	4.51001	-1.09843	0.14339
C	2.72102	-1.22694	4.35416
H	4.35911	-0.85558	-2.70433
H	3.56560	-3.03025	3.52008
H	4.72349	4.02930	-2.19144
H	1.85839	-1.76843	4.76853
C	5.37414	0.99133	-0.69100
H	3.45166	-1.08927	5.16455
H	5.21502	1.36975	-3.46452
C	5.54851	-0.48094	-0.44195
C	5.65844	-3.17209	0.18390
H	5.43282	3.70979	0.17958
H	5.67600	-4.23157	0.44358
H	5.70147	1.52347	0.21738
H	6.00622	1.33539	-1.52244
C	6.69878	-1.20598	-0.75386
C	6.75075	-2.56054	-0.43242
H	7.54228	-0.71178	-1.23800
H	7.64639	-3.14154	-0.66061
H	0.78527	-0.56025	-0.78993
O	3.92481	1.54918	3.00268
H	-0.18949	-3.84641	2.83096
H	1.35456	-3.90128	3.70334
H	1.23928	-4.53427	2.04175
H	0.71188	-2.20240	1.17126
H	0.74400	-1.57738	2.80962
H	-0.43434	0.98733	-0.21631

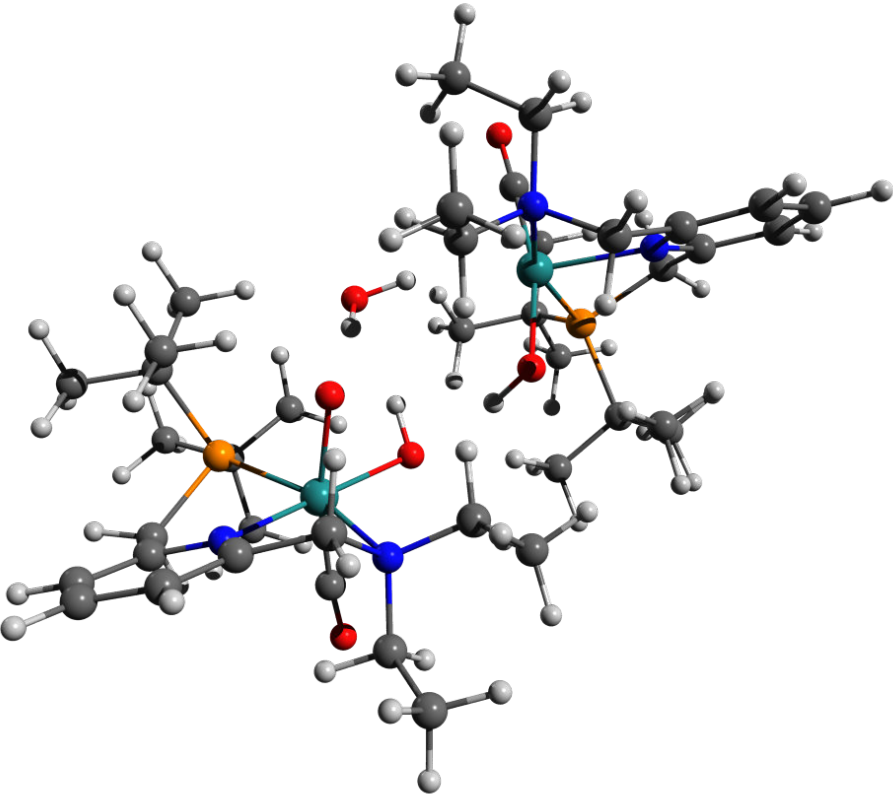


Figure 11.6-8 [B-Mono]D₀ (Me Model) Structure and Coordinates

39 Energy: -778002.1873236
 O -0.55505 -2.76423 -0.44723
 O 0.12508 -0.53954 -0.02669
 C 2.33494 -2.33026 -0.93340
 H 2.32532 0.00079 -1.74955
 N 2.03471 -1.17743 -0.07897
 C 2.56292 0.06058 -0.67376
 C -2.66050 0.70913 -1.96705
 C -3.68291 -0.22283 0.57254
 P -2.13697 0.26298 -0.27867
 H 3.65817 0.13929 -0.54726
 C 2.57390 -1.37539 1.26528
 C -0.47743 -1.05726 1.74030
 C 1.86506 1.29245 -0.16828
 N 0.54935 1.13551 0.08192
 C -1.69729 1.88636 0.55815
 C -0.24327 2.19517 0.34859
 C 2.46033 2.54481 -0.08112
 H 3.52962 2.65191 -0.26713
 H -1.87475 1.70669 1.63369
 H -2.33600 2.73055 0.25599
 C 0.29836 3.47682 0.41385
 C 1.66531 3.64977 0.21585
 H -0.35016 4.32785 0.62448
 H 2.10798 4.64516 0.28014
 O -0.72992 -1.22961 2.86076
 H -3.43464 1.49046 -1.96458
 H -3.04101 -0.20175 -2.45134
 H -1.76103 1.01476 -2.51817
 H -3.45978 -0.44094 1.62671
 H -4.05811 -1.14273 0.10074
 H -4.45366 0.55989 0.50619
 H 1.84660 -3.21136 -0.49936
 H 3.42719 -2.48162 -1.02251
 H 1.87627 -2.14584 -1.91327
 H 2.34750 -0.50001 1.89028
 H 3.67065 -1.52383 1.23530
 H 2.10148 -2.29869 1.71336
 Ru -0.17204 -0.78748 -0.08391
 H -1.30296 -3.07172 0.07743

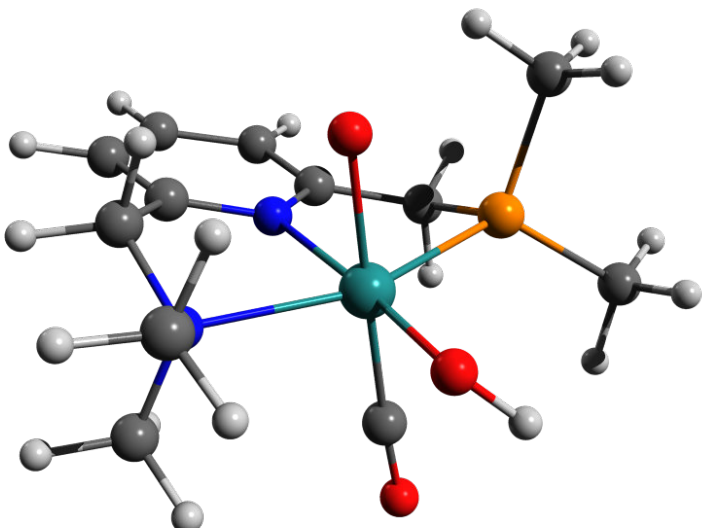


Figure 11.6-9 [B-Mono]D₀ Structure and Coordinates

63

Energy: -975165.8829902

H	-3.59713	-3.37011	1.85732
C	-3.30686	-2.75815	0.99015
H	-4.05420	-2.93520	0.20058
H	-2.30651	-3.08263	0.65924
H	1.49110	-0.73473	2.72708
O	-0.25026	-2.58975	0.68320
H	4.33842	-1.68060	0.66041
O	-0.48413	-0.19782	2.04727
C	-3.23487	-1.31048	1.42488
H	2.87147	0.05390	3.54960
H	-4.22373	-0.93932	1.76129
C	2.52841	-0.39286	2.60092
H	2.86422	-2.66213	0.46270
H	3.17429	-1.25419	2.38812
H	-2.52682	-1.20764	2.26099
C	3.65433	-2.11887	-0.07818
H	4.22969	-2.85168	-0.66789
H	-2.32081	0.92236	1.90782
Ru	-0.39555	-0.61368	0.13394
H	0.70178	1.55765	2.11987
N	-2.70573	-0.40463	0.37971
C	-2.75145	0.97496	0.89198
C	2.59529	0.67933	1.50764
H	2.14556	2.24447	2.90814
H	4.76596	0.33218	-0.95365
C	1.74084	1.87352	1.95171
C	3.06317	-1.07233	-1.02616
P	1.79654	-0.02448	-0.06751
H	-3.78161	1.36308	0.96435
C	4.17182	-0.23927	-1.67502
H	-3.20025	-1.51011	-1.31426
H	-5.43814	-1.02668	-0.23633
H	4.85933	-0.91938	-2.20537
C	-3.41984	-0.14442	-0.90804
H	4.35612	1.64830	2.25763
C	-0.57605	-1.06302	-1.67290
C	4.03188	1.16478	1.32064
H	1.56839	-2.50274	-1.74162
C	2.32624	-1.81575	-2.40468
H	4.07007	0.77007	1.11946
H	3.06007	-2.41085	-2.70890
C	-1.88057	1.90873	0.10674
N	-0.69360	1.38892	-0.26425
C	-4.92463	-0.29098	-0.87206
H	1.77858	2.70973	1.23656
H	-2.95208	0.20869	-1.59418
H	3.77213	0.46010	-2.42482
H	-5.19915	0.71495	-0.51997
C	1.54856	1.47139	-1.17724
H	-5.32498	-0.39766	-1.89143
H	4.12562	1.91569	0.52060
C	0.25002	2.15170	-0.85440
C	-2.18830	3.23851	-0.15518
H	1.83157	-1.13894	-2.85135
H	-3.15904	3.63838	0.13975
H	1.48976	1.05781	-2.19907
H	2.38389	2.18731	-1.16170
C	-0.00188	3.49525	-1.12311
C	-1.23569	4.04003	-0.77988
H	0.76850	4.10418	-1.59729
H	-1.45156	5.08839	-0.99284
O	-0.79262	-1.32801	-2.78212
H	0.34645	-3.05966	0.08963

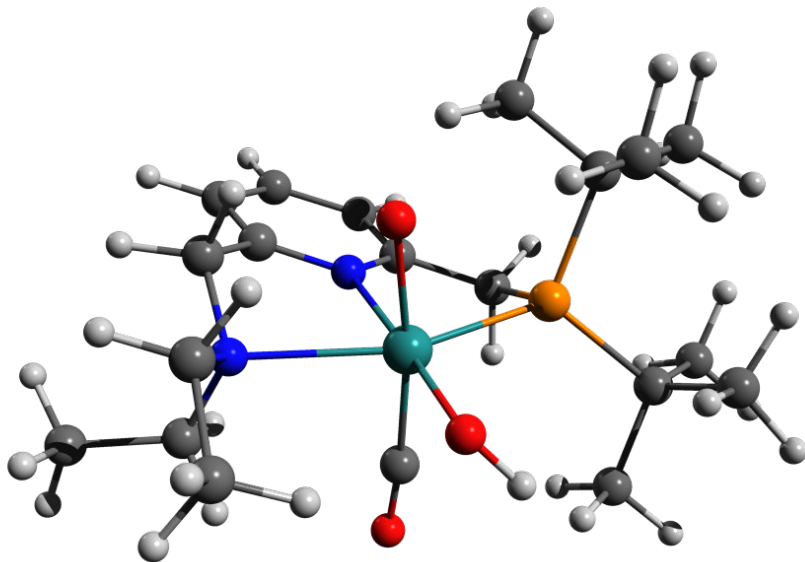


Figure 11.6-10 [B-Mono-Up]D₀ Structure and Coordinates

63
 Energy: -975164.6396053
 N -0.74074 1.42138 -0.09733
 C -1.96289 1.88374 0.22032
 C 0.17622 2.21737 -0.68254
 C -2.30204 3.21558 0.02029
 C -1.34598 4.07348 -0.52001
 C -0.10169 3.56952 -0.88257
 C -2.88430 0.85097 0.80217
 H -3.30015 3.56986 0.28000
 H -1.57919 5.12778 -0.67888
 H 0.65212 4.21228 -1.33854
 C 1.44448 1.56307 -1.13985
 N -2.70439 -0.46230 0.15473
 H -3.93071 1.19911 0.74917
 H -2.63964 0.72630 1.86984
 H 1.25253 1.19198 -2.16066
 P 1.78133 -0.01000 -0.18518
 H 2.28303 2.27367 -1.16965
 Ru -0.39601 -0.59869 0.12102
 C -3.20909 -0.43591 -1.23905
 C 2.85648 -1.04703 -1.35491
 C -3.36843 -1.49999 0.97491
 C 2.78394 0.59230 1.31399
 C 1.90070 -1.73018 -2.33764
 C 3.55725 -2.14341 -0.55043
 C 3.87599 -0.21711 -2.13684
 C 1.99413 1.73965 1.95477
 C 4.16940 1.11761 0.93685
 C 2.92947 -0.53336 2.34160
 C -0.40004 -0.68686 1.97617
 O -0.47562 -0.77910 3.13527
 H -2.68179 0.38306 -1.74960
 C -4.71270 -0.28445 -1.40559
 H -2.83982 -1.34707 -1.72405
 H -2.87188 -1.48262 1.96655
 C -3.26382 -2.88646 0.37557
 H -4.42473 -1.21202 1.4790
 O -0.18170 -2.28483 -0.04358
 H 0.14647 -3.01157 0.78796
 O -0.54564 -0.56134 -1.85533
 H -2.89126 -3.00398 0.07000
 H -3.89048 -3.00367 -0.51592
 H -3.60244 -3.62393 1.11892
 H -4.94265 -0.24441 -2.48080
 H -5.10743 0.64145 -0.95834
 H -5.27286 -1.13184 -0.98342
 H 2.49969 -2.36903 -3.00935
 H 1.34662 -1.00652 -2.95296
 H 1.16093 -2.34476 -1.80028
 H 4.02159 -2.85217 -1.25567
 H 2.83394 -2.70824 0.05660
 H 4.35550 -1.75779 0.09962
 H 4.42435 -0.89100 -2.81628
 H 4.61745 0.28340 -1.50127
 H 3.38880 0.54168 -2.76701
 H 4.83845 0.31922 0.58911
 H 4.63419 1.56882 1.82951
 H 4.12758 1.89776 0.16160
 H 3.52590 -1.37251 1.96409
 H 1.95694 -0.92246 2.66522
 H 3.44126 -0.13502 3.23371
 H 2.49440 2.03236 2.89242
 H 0.96381 1.44847 2.19949
 H 1.95863 2.63050 1.31020

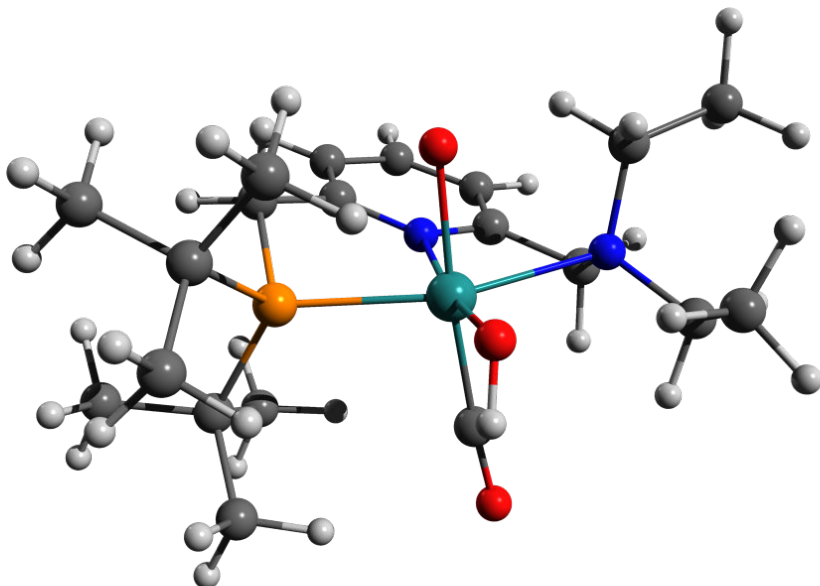


Figure 11.6-11 [B-Trans]T₀ Structure and Coordinates

128	Energy: -1951524.2043341		
H	-0.03271	1.60418	4.13717
C	0.93903	1.19234	3.83039
H	1.55757	1.10577	4.73755
H	1.40931	1.90577	3.44566
H	1.26657	1.50548	2.39319
O	1.96714	2.11966	1.02547
H	3.26370	3.56976	-1.40532
O	1.13721	-0.21512	-0.12088
H	0.67013	2.31304	-0.01713
C	0.70514	-0.13262	3.14136
H	1.65072	1.13562	-4.04736
H	0.23184	-0.85739	3.83074
C	2.20339	1.42983	-3.13929
H	3.78233	3.29263	0.25363
H	2.69252	2.39138	-3.35541
H	0.01209	-0.01986	2.29622
C	4.15143	3.47733	-0.76538
H	4.70769	4.42922	-0.78539
H	0.74442	-1.81454	1.29101
Ru	2.84345	0.41858	0.84464
H	1.84130	-0.99733	-1.75221
N	1.94541	-0.73808	2.59715
C	1.60894	-2.01774	1.94199
C	3.21917	0.33453	-2.80832
H	1.88886	-1.17928	-3.54147
H	4.74593	2.90046	-3.37196
C	2.49751	-1.00907	-2.63714
C	5.06992	2.35683	-1.26636
P	4.03937	0.75614	-1.14019
H	1.31415	-2.78482	2.67687
C	5.56579	2.70422	-2.66978
H	3.29420	0.02463	4.00180
H	1.72024	-1.32990	5.41648
H	6.15948	3.63055	-2.59746
C	2.96490	-0.96123	3.65394
H	3.65865	-0.29008	-4.80620
C	4.23993	0.99765	1.88691
C	4.20926	0.16512	-3.98646
H	6.07936	1.98017	0.66517
C	6.30687	2.25095	-0.37099
H	4.63229	1.10637	-4.32961
H	6.79448	3.23921	-0.34468
C	2.74500	-2.50792	1.09336
N	3.49427	-1.54532	0.52592
C	2.53635	-1.79930	4.84880
H	3.21037	-1.84541	-2.56623
H	3.83516	-1.42327	3.16440
H	6.22003	1.92761	-3.09094
H	2.22104	-2.81646	4.57277
C	5.23608	-0.66838	-0.89074
H	3.39534	-1.89987	5.52898
H	5.03647	-0.52011	-3.72437
C	4.50474	-1.84421	-0.31228
C	3.00870	-3.89068	0.84361
H	7.04318	1.53799	-0.77358
H	2.39588	-4.62062	1.31359
H	5.96418	-0.30988	-0.14538
H	5.79248	-0.94732	-1.79631
C	4.80936	-3.17184	-0.60228
C	4.05194	-4.18314	-0.1677
H	5.62669	-3.04935	-1.28555
H	4.27449	-5.22961	-0.23262
O	5.05375	1.38425	2.62202
C	-0.17527	-3.07144	-1.16567
H	-1.24457	1.94143	1.62104
O	0.05360	2.34163	-0.80701
H	-2.09722	3.655271	-0.87619
O	-1.42466	-0.63826	0.77242
H	-0.74198	1.85095	-0.54158
C	-0.72051	-2.49274	1.60285
H	-1.71046	2.83297	3.09142
C	-2.00864	2.60120	2.05539
H	-2.73850	2.72199	-2.23269
H	-2.00637	3.54772	1.49496
C	-2.98459	3.51026	-1.50902
H	-3.16278	4.44821	-2.06195
H	-1.89005	-2.72701	0.59986
Ru	-2.72275	-0.16773	-0.79566
H	-2.56150	-0.09991	2.23946
N	-2.17984	-2.34650	-1.40602
C	-2.59716	-3.05718	-0.18043
C	-3.37671	1.92043	2.06136
H	-2.87080	0.75163	3.79098
H	-3.78661	4.67535	0.82229
C	-3.25875	0.56585	2.77370
C	-4.24013	3.16238	-0.70340
P	-3.83908	1.54269	0.24875
H	-2.55567	-4.15280	-0.31104
C	-4.61001	4.36190	0.16717
H	-4.00259	-2.53275	-2.38774
H	-2.33659	-1.32908	-3.95335
H	-4.83577	5.21175	-0.49896
C	-2.96552	-2.86448	-2.54726
H	-4.14001	2.67516	3.91761
C	-3.52292	0.24424	-2.37986
C	-4.38657	2.76361	2.84614
H	-5.27115	2.04492	-2.30541
C	-5.40753	2.92610	-1.66678
H	-4.35929	3.82863	2.59535
H	-5.48364	3.80019	-2.33498
C	-3.96012	-2.64603	0.30186
N	-4.22295	-1.33845	0.18289
C	-2.48161	-2.41610	-3.91157
H	-4.24057	0.07946	2.89004
H	-2.97449	-3.97228	-2.50949
H	-5.50385	4.17952	0.78007
H	-1.54098	-2.90786	-4.19977
C	-5.50898	0.68212	0.44494
H	-3.23887	-2.67937	-4.66455
H	-5.42152	2.40630	2.72913
C	-5.34408	-0.79136	0.67597
C	-4.86654	-3.49958	0.92281
H	-6.36742	2.84197	-1.13418
H	-4.65076	-4.56583	1.00540
H	-6.00520	0.80826	-0.53016
H	-6.16164	1.13571	1.20551
C	-6.28211	-1.59085	1.33036
C	-6.03973	-2.95704	1.44578
H	-7.19058	-1.14560	1.73742
H	-6.76658	-3.60086	1.94491
H	-0.51848	-0.41630	0.47013
O	-3.98373	0.48462	-3.63933
H	0.61129	-3.83545	-1.90240
H	-0.61138	-4.65496	-2.57866
H	-0.32861	-4.49142	-0.82007
H	-0.24340	-1.96131	-0.75600
H	-0.46742	-1.89627	2.49584
H	0.80147	0.56698	-0.59067

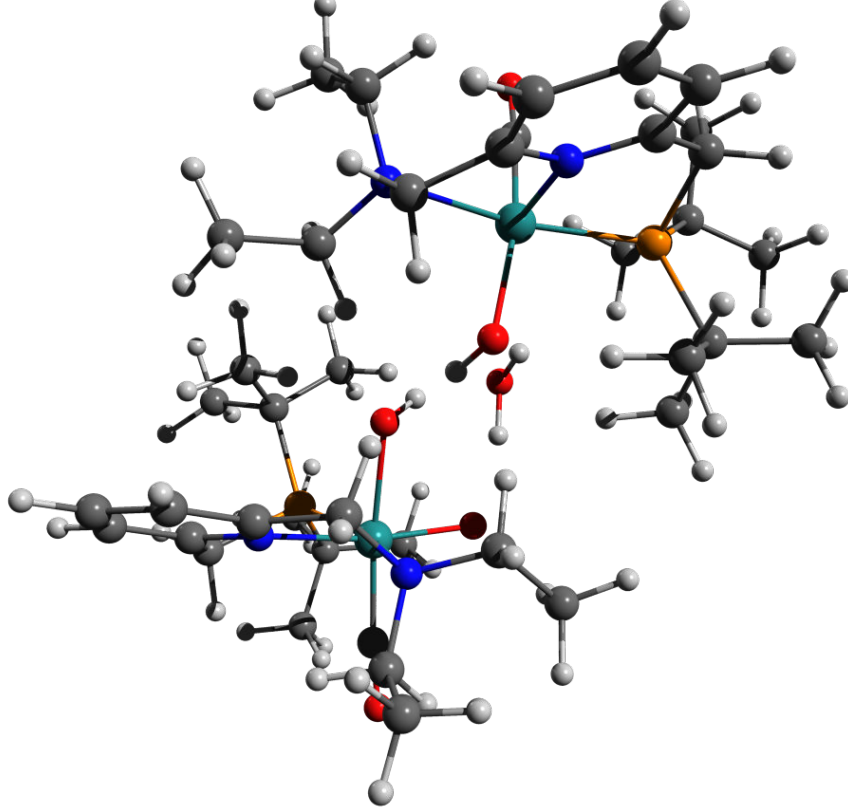


Figure 11.6-12 [B-Mono-Trans]D₀ Structure and Coordinates

63

Energy: -975172.0784791

H	-3.52147	-3.33180	1.91476
C	-3.21273	-2.73924	1.04103
H	-3.90569	-2.97992	0.22015
H	-2.91116	-3.04829	0.76397
H	1.03926	-0.60328	2.60179
O	-0.16459	-2.37754	0.90223
H	2.96531	-2.60730	0.75502
O	-0.51143	-0.09534	2.16923
C	-3.22818	-1.27357	1.41611
H	3.26996	0.29760	3.34665
H	-4.25213	-0.93762	1.66951
C	2.88237	-0.19169	2.43768
H	1.61419	-2.86521	-0.35016
H	3.61834	-0.94831	2.12774
H	-2.58714	-1.09775	2.29149
C	2.68130	-2.59912	-0.30746
H	3.27596	-3.37305	-0.82088
H	-2.30473	0.98017	1.86228
Ru	-0.40986	-0.62255	0.17304
H	0.70035	1.43941	2.15670
N	-2.67307	-0.38667	0.36774
C	-2.74464	1.00794	0.85003
C	2.64564	0.86733	1.36016
H	2.10188	2.34881	2.81099
H	4.81260	-0.98398	0.21233
C	1.66058	1.91369	1.89823
C	2.97237	-1.24134	-0.95698
P	1.80265	0.00325	-0.10829
H	-3.78248	1.37546	0.90262
C	4.46192	-0.92727	-0.82616
H	-3.12810	-1.53856	-1.31205
H	-5.39232	-1.04930	-0.30824
H	5.02152	-1.68584	-1.39840
C	-3.35946	-0.53418	-0.93590
H	4.21857	2.22703	1.87501
C	-0.54036	-1.26267	-1.54368
C	3.94788	1.59477	1.01331
H	1.59523	-1.50593	-2.66402
C	2.65159	-1.30784	-2.45228
H	4.79263	0.92558	0.82327
H	3.22919	-2.13934	-2.88826
C	-1.88127	1.92541	0.03882
N	-0.70686	1.38778	-0.33782
C	-4.86498	-0.31800	-0.93794
H	1.51175	2.74169	1.18775
H	-2.87726	0.17266	-1.62817
H	4.72653	0.05722	-1.23858
H	-5.15359	0.69064	-0.60641
C	1.50175	1.40498	-1.31722
H	-5.23715	-0.44030	-1.96609
H	3.83783	2.26939	0.14977
C	0.23022	2.12364	-0.96564
C	-2.18126	3.25278	-0.24505
H	2.95743	-0.39133	-2.98035
H	-3.14183	3.67075	0.05806
H	1.36682	0.92202	-2.29851
H	2.34420	2.10582	-1.40654
C	-0.00850	3.46423	-1.25873
C	-1.22962	4.03010	-0.90145
H	0.75780	4.05357	-1.76333
H	-1.43685	5.07689	-1.13027
O	-0.71029	-1.72257	-2.59914
H	-0.30740	-0.97807	2.52158

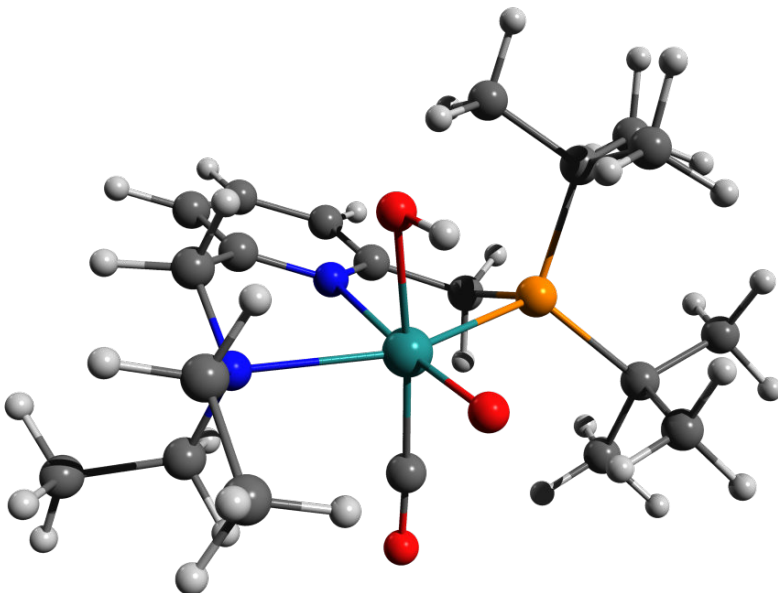


Figure 11.6-13 [B-Mono-Trans-Up]D₀ Structure and Coordinates

```

63          Energy: -975173.7263503
N   -0.73550   1.42125   -0.02208
C   -1.96750   1.86456   0.28053
C    0.17340   2.23170   -0.05298
C   -2.32652   3.19045   0.08017
C    1.18899   4.06578   -0.44217
C   -0.11894   3.59115   -0.79053
C   -2.86501   0.81117   0.85662
C   -3.33302   3.52853   0.32890
H   -1.62190   5.11719   -0.59960
H    0.63046   4.23614   -1.23640
C    1.44263   1.58998   -1.06790
N   -2.69846   -0.49240   0.16027
H   -3.91549   1.14707   0.85267
H   -2.57625   0.65027   1.90818
H    1.23589   1.24028   -2.09463
P    1.78869   -0.00874   -0.17117
H    2.28334   2.29787   -1.08076
Ru   -0.41448   -0.64096   0.07272
C   -3.25948   -0.42483   -1.21093
C    2.95262   -0.96472   -1.33095
C   -3.33235   -1.54129   0.98082
C    2.72034   0.54474   1.39552
C    2.10182   -1.66971   -2.38906
C    3.68224   -2.04466   -0.52984
C    3.95300   -0.04857   -2.03970
C    1.85805   1.61627   2.07491
C    4.08721   1.16239   1.09591
C    2.89745   -0.62801   2.36501
C   -0.39102   -0.90857   1.88917
O   -0.43996   -1.10599   3.03685
H   -2.69139   0.34337   -1.75061
C   -4.75996   -0.20438   -1.31443
H   -2.97355   -1.36336   -1.70059
H   -2.84433   -1.50672   1.96523
C   -3.19827   -2.93071   0.39736
H   -4.39647   -1.28329   1.14499
O   -0.22382   -2.50500   -0.32104
O   -0.53886   -0.35007   -1.97302
H   -2.14096   -3.15136   0.17157
H   -3.79382   -3.05995   -0.51852
H   -3.56282   -3.66199   1.13397
H   -5.03187   -0.17514   -2.38023
H   -5.08940   0.75050   -0.87617
H   -5.34650   -1.01228   -0.85134
H   2.78023   -2.24866   -3.03846
H   1.53741   -0.95722   -3.00423
H   1.37671   -2.35037   -1.91752
H   4.20178   -2.71174   -1.23693
H   2.97485   -2.65965   0.04710
H   4.44129   -1.63469   0.15033
H   4.59219   -0.66907   -2.68980
H   4.61277   0.49757   -1.35440
H   3.44634   0.67926   -2.69033
H   4.80829   0.42454   0.71985
H   4.50075   1.57465   2.03148
H   4.02741   1.99115   0.37408
H   3.61500   -1.37036   1.99704
H   1.95320   -1.14306   2.57572
H   3.28477   -0.23823   3.32116
H   2.32646   1.88437   3.03586
H   0.83963   1.26332   2.28304
H   1.76947   2.53610   1.47544
H   -0.52065   -1.27160   -2.26913

```

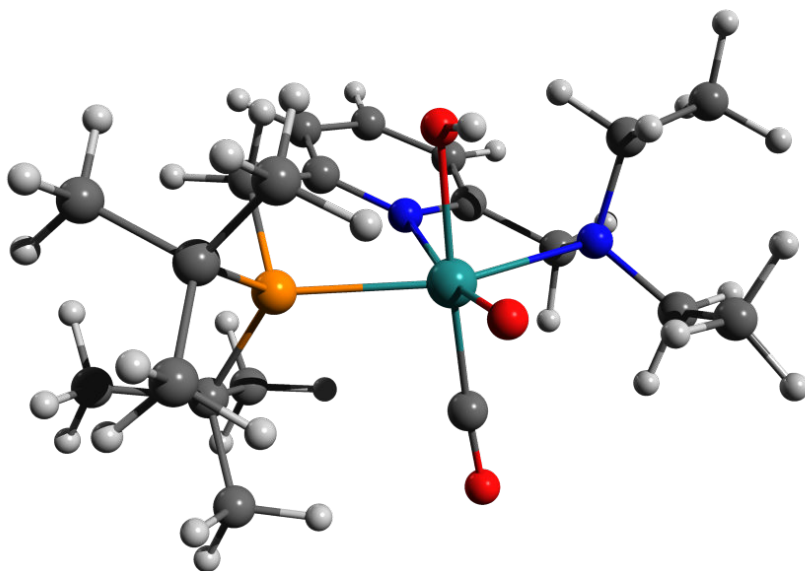


Figure 11.6-14 [B-Alt]T₀ Structure and Coordinates

62

Energy: -974727.8788646

H	-3.37170	-3.45409	1.93521
C	-3.14617	-2.83166	1.05673
H	-3.86927	-3.03852	0.28600
H	-2.86478	-3.11364	0.68908
H	1.43283	-0.73896	2.71410
O	0.00504	-2.50545	0.26301
H	4.24011	-1.78082	0.62515
O	-0.44643	-0.21944	1.93866
C	-3.15723	-1.37684	1.47382
H	2.86230	-0.05299	3.56056
H	-4.15576	-1.07734	1.84982
C	2.49277	-0.45756	2.60301
H	2.72915	-2.70038	0.34332
H	3.09225	-1.34501	2.36268
H	-2.41870	-1.21361	2.27597
C	3.55747	-2.16404	-0.14512
H	4.11907	-2.88986	-0.75579
H	-2.27115	0.85962	1.90665
Ru	-0.35462	-0.69712	0.13791
H	0.71569	1.51588	2.12337
N	-2.72905	-0.45400	0.40380
C	-2.76769	0.92147	0.91974
C	2.60744	0.64126	1.54098
H	2.14954	2.16794	2.97809
H	4.79589	0.24930	-0.92510
C	1.76287	1.83665	1.99980
C	3.02434	-1.06043	-1.06208
P	1.82004	0.00258	-0.05920
H	-3.79654	1.30265	1.03468
C	4.16657	-0.24589	-1.67315
H	-3.23597	-1.56796	-1.28232
H	-5.44523	-1.22885	-0.10792
H	4.81250	-0.92768	-2.25088
C	-3.48927	-0.59015	-0.84988
H	4.38508	1.54946	2.32069
C	-0.62707	-0.88215	-1.78209
C	4.05739	1.09118	1.37284
H	1.45359	-2.38214	-1.79420
C	2.24643	-1.73425	-2.19388
H	4.74174	0.25774	1.16261
H	2.95067	-2.35439	-2.77279
C	-1.92243	1.87476	0.12878
N	-0.71947	1.39723	-0.22866
C	-5.00080	-0.44809	-0.74224
H	1.83617	2.69550	1.31409
H	-3.09450	0.16548	-1.54675
H	3.79683	0.51719	-2.37522
H	-5.30680	0.53018	-0.34161
C	1.53853	1.52825	-1.10810
H	-5.44435	-0.54324	-1.74477
H	4.17855	1.85301	0.58630
C	0.21961	2.17956	-0.78374
C	-2.25559	3.20258	-0.12104
H	1.80126	-1.01008	-2.89205
H	-3.23994	3.57988	0.15842
H	1.51330	1.16638	-2.15038
H	2.36129	2.25550	-1.03714
C	-0.04789	3.52524	-1.03064
C	-1.30354	4.03277	-0.70786
H	0.71959	4.41713	-1.47237
H	-1.53725	5.00626	-0.90722
O	-0.88592	-0.86035	-2.90796

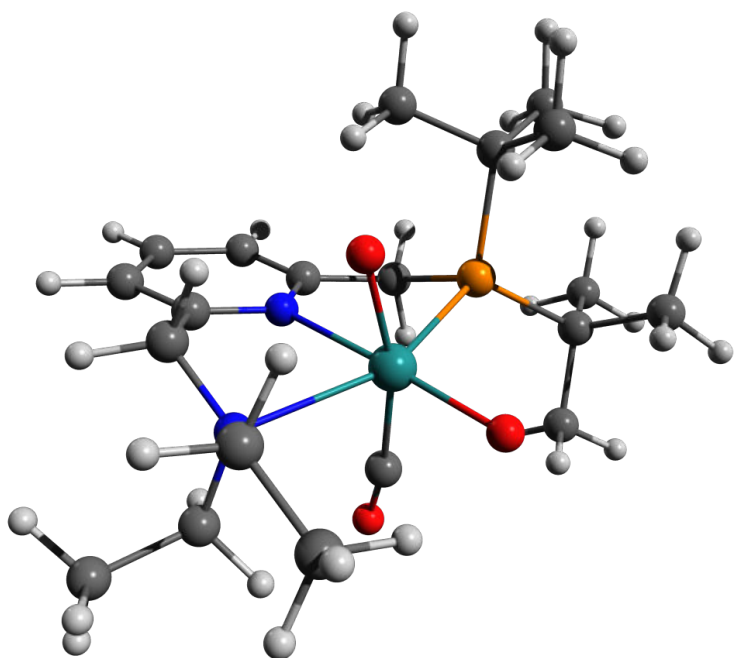


Figure 11.6-15 [BC] D₁/D₀ MECI Structure and Coordinates

```

39
-5669.6564319599938
O -0.34914799 -2.36258133 -2.38144151
O 0.11685657 -0.82199044 -2.03587137
C 2.45971115 -2.48770283 -0.59692125
H -0.47951778 -0.22805005 -1.63105341
N 2.10379531 -1.25231934 0.14256947
C 2.62880006 -0.06033524 -0.57056869
C 0.95592546 0.76139328 -1.79019937
C -3.85195267 -0.02730160 0.89974336
P -2.30795928 0.27308186 -0.10621931
H 3.69309868 0.06167002 -0.37783977
C 2.62840602 -1.30970376 1.52619968
C -0.41490170 -1.04519197 2.19364736
C 1.88732304 1.20543682 -0.20269598
N 0.57933910 1.07344928 0.06366621
C -1.66417890 1.89643400 0.62849087
C -0.20953457 2.14595474 0.30032474
C 2.47868580 2.46568668 -0.22235894
H 3.52977925 2.55859074 -0.42706967
H -1.75784807 1.78995768 1.70762753
H -2.26840551 2.74654963 0.32032961
C 0.34078846 3.42118238 0.26751214
C 1.70205995 3.57535527 0.01007743
H -0.28345471 4.27631644 0.45043994
H 2.13906704 4.55889235 -0.00585560
O -0.73061464 -1.74610669 3.13055667
H -3.67933575 1.55973355 -1.72787910
H -3.42495100 -0.11461877 -2.24627638
H -2.12184913 1.04499984 -2.41770806
H -3.57230091 -0.26896885 1.91967123
H -4.38840515 -0.87507903 0.48484844
H -4.50670963 0.83997556 0.89817174
H 2.07210958 -3.34198547 -0.05431959
H 3.54399273 -2.58737731 -0.68353774
H 2.00477094 -2.45857026 -1.57612531
H 2.34624449 -0.41525499 2.06620993
H 3.71628435 -1.40166085 1.51688219
H 2.20065294 -2.16034732 2.03867858
Ru -0.11705731 -0.88144683 0.05896810
H -0.69487285 -2.18311611 -3.27277416

```

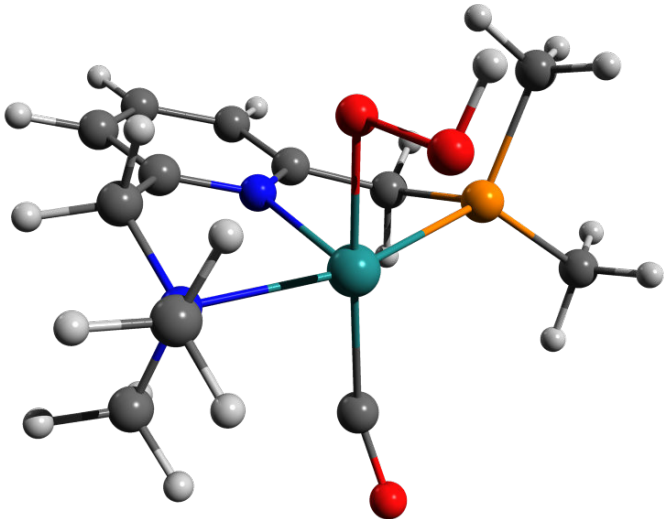


Figure 11.6-16 [BC] D₂/D₁ MECI Structure and Coordinates

```

39
-5669.6347902092621
O -0.43728033 -2.88986880 -1.22059513
O 0.01072006 -1.15926324 -2.16057615
C 2.54758921 -2.43747772 -0.70310219
H 2.44612775 -0.14246022 -1.70346216
N 2.12497170 -1.23114238 0.04303850
C 2.62047055 -0.00886238 -0.64061489
C 0.87559717 0.87962919 -1.85693339
C -3.87797477 -0.02746943 0.75622607
P -2.29420613 0.29809104 -0.17808649
H 3.68994019 0.11231407 -0.47556600
C 2.63446526 -1.29572540 1.43245880
C -0.42517600 -1.11796295 2.03526966
C 1.88531427 1.24155372 -0.20809201
N 0.57880933 1.09855615 0.05344743
C -1.66441087 1.88021247 0.65687480
C -0.21056753 2.15434403 0.34797870
C 2.47760799 2.50106027 -0.16125789
H 3.52818477 2.60713109 -0.36260372
H -1.76355295 1.70866859 1.72754258
H -2.27528270 2.73776658 0.39383644
C 0.33884029 3.42996022 0.38761050
C 1.70049336 3.59590110 0.13645007
H -0.28294042 4.27462591 0.62127536
H 2.13843195 4.57847672 0.17568621
O -0.76941542 -1.65784233 3.06345115
H -3.61280414 1.67336524 -1.77222999
H -3.30868937 0.04220119 -2.39389968
H -2.02276168 1.22893868 -2.42838256
H -3.63710698 -0.33324758 1.76890258
H -4.41890407 -0.83703111 0.27598941
H -4.51302617 0.85388025 0.78345248
H 2.17775313 -3.31465047 -0.19503086
H 3.63727585 -2.48753836 -0.76820659
H 2.11698942 -2.41043829 -1.69912923
H 2.31779191 -0.42179048 1.98604882
H 3.72491453 -1.35349895 1.43491293
H 2.22794279 -2.16974797 1.92250448
Ru -0.11712086 -0.90963409 -0.04038537
H -1.23425376 -2.88666281 -1.78515039

```

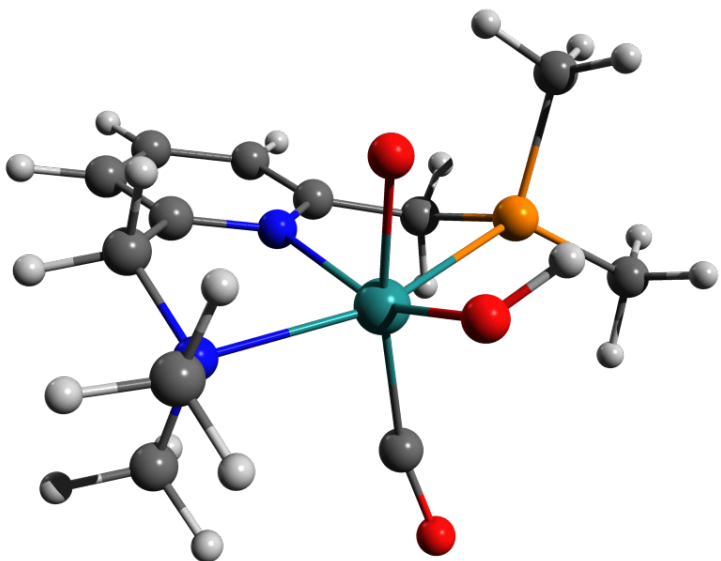


Figure 11.6-17 [C]T₀ Structure and Coordinates

128 Energy: -1951476.7711256

H	-0.89663	2.64296	3.71461
C	-1.82051	2.11644	3.49322
H	-2.52055	2.20530	4.27664
H	-1.56165	1.05757	3.90411
H	-0.87688	1.17047	1.92357
O	-1.54793	1.14940	-0.36805
H	-0.46505	-3.21252	-0.62748
O	-0.38495	1.09269	0.49880
H	-1.30571	-1.13414	2.37114
C	-2.35690	2.72304	2.15547
H	-0.42762	-1.22931	-3.69580
H	-2.65393	3.77688	2.32440
C	-0.84201	-1.63173	-2.75572
H	-1.18192	-2.88659	0.96029
H	-0.63509	-2.71240	-2.75244
H	-1.57419	2.71034	1.38621
C	-1.23079	-3.54977	0.08471
H	-0.97429	-4.57457	0.40376
H	-3.02154	2.81209	-0.24934
Ru	-2.93506	-0.05255	0.62261
H	-2.02696	0.77702	-2.20712
N	-3.49882	1.98143	1.57545
C	-3.93458	2.70522	0.36143
C	-2.34021	-1.32858	-2.71150
H	-2.10229	0.40068	-3.95847
H	-1.91428	-4.32214	-2.46486
C	-2.53641	0.17115	-2.96995
C	-2.63204	-3.54713	-0.53522
P	-3.01159	-1.72473	-0.96046
H	-4.32824	3.70825	0.59832
C	-2.68172	-4.52591	-1.70733
H	-4.26739	1.16253	3.33244
H	-4.46718	3.66488	3.69854
H	-2.49882	-5.54360	-1.32226
C	-4.62093	1.81899	2.52745
H	-2.60217	-1.77874	-4.79210
C	-3.82632	-1.03527	1.88254
C	-3.06771	-2.07353	-3.83578
H	-3.68005	-3.38462	1.39545
C	-3.62992	-4.03671	0.51621
H	-3.00493	-3.16488	-3.76707
H	-3.30884	-5.03384	0.86118
C	-4.92528	1.91027	-0.43937
N	-4.60825	0.61301	-0.54372
C	-5.20538	3.09470	3.11539
H	-3.60002	0.44820	-3.01407
H	-5.40405	1.25428	2.00043
H	-3.66651	-4.53633	-2.19830
H	-5.62643	3.76339	2.34944
C	-4.87492	-1.67125	-1.24538
H	-6.02607	2.82596	3.79731
H	-4.12726	-1.78721	-3.89992
C	-5.34574	-0.24586	-1.26668
C	-6.04579	2.42206	-1.08448
H	-4.64439	-4.15039	0.10438
H	-6.29988	3.47895	-0.99280
H	-5.30252	-2.14906	-0.34836
H	-5.22703	-2.22986	-2.12386
C	-6.47205	0.21034	-1.95158
C	-6.82062	1.55588	-1.89653
H	-7.06783	-0.48277	-2.54710
H	-7.71616	1.92430	-2.38145
O	-4.36685	-1.58430	2.76199
C	2.21617	-4.23949	2.27755
H	0.39812	1.03942	-1.04836
O	-0.36653	-0.90591	2.49840
H	0.73781	3.27401	0.09012
O	1.22609	-0.75221	-0.35429
H	-0.31008	-0.13011	1.88696
C	2.07281	-2.87484	1.75462
H	0.50681	1.61081	-3.53587
C	0.94319	1.88673	-2.56096
H	1.64615	2.93677	1.37694
H	0.75294	2.95902	-2.41240
C	1.58882	3.61533	0.51389
H	1.38245	4.63756	0.87464
H	3.15971	-2.92954	-0.49344
Ru	2.95689	0.02827	0.59441
H	2.12087	-0.58001	-2.18738
N	3.30918	-2.12648	1.41908
C	3.95399	-2.77327	0.25460
C	2.43551	1.55263	-2.57945
H	2.13359	-0.10386	-3.91191
H	2.01166	4.50714	-2.06629
C	2.60575	0.06800	-2.92953
C	2.90834	3.61726	-0.26354
P	3.17228	1.81398	-0.83471
H	4.37478	-3.75778	0.52349
C	2.85567	4.65771	-1.38144
H	5.09599	-1.45939	2.25320
H	3.06137	-0.67203	3.66314
H	2.72919	5.65276	-0.92212
C	4.25634	-2.10181	2.55628
H	2.66689	2.10290	-4.63927
C	3.93524	0.88083	1.86610
C	3.13950	2.35789	-3.67561
H	4.19371	3.31580	1.50469
C	4.03763	4.02757	0.68557
H	3.05890	3.44287	-3.55122
H	3.76725	4.99536	1.13992
C	5.01008	-1.92268	-0.38787
N	4.65226	-0.63829	-0.54253
C	3.63809	-1.59024	3.84198
H	3.66631	-0.21033	-3.02644
H	4.66912	-3.11774	2.71260
H	3.78625	4.68653	-1.96801
H	2.96626	-2.32853	4.30224
C	5.01901	1.67387	-1.14702
H	4.43318	-1.35802	4.56463
H	4.20379	2.09398	-3.76710
C	5.47119	0.24205	-1.14904
C	6.23062	-2.39505	-0.85291
H	4.99148	4.17700	0.15630
H	6.50582	-3.44076	-0.70779
H	5.48192	2.15371	-0.26885
H	5.37597	2.21375	-2.03570
C	6.69276	-0.17940	-1.67161
C	7.07707	-1.50981	-1.52099
H	7.34110	0.53679	-2.17889
H	8.03659	-1.85275	-1.91186
H	0.79995	-1.32491	0.29707
O	4.5414	1.39186	2.73121
H	1.19379	-4.72934	2.26773
H	2.78425	-4.6160	3.23914
H	2.77813	-4.94998	1.56809
H	1.49693	-2.91660	0.82732
H	1.48877	-2.26647	2.43624
H	0.21945	0.42705	0.02318

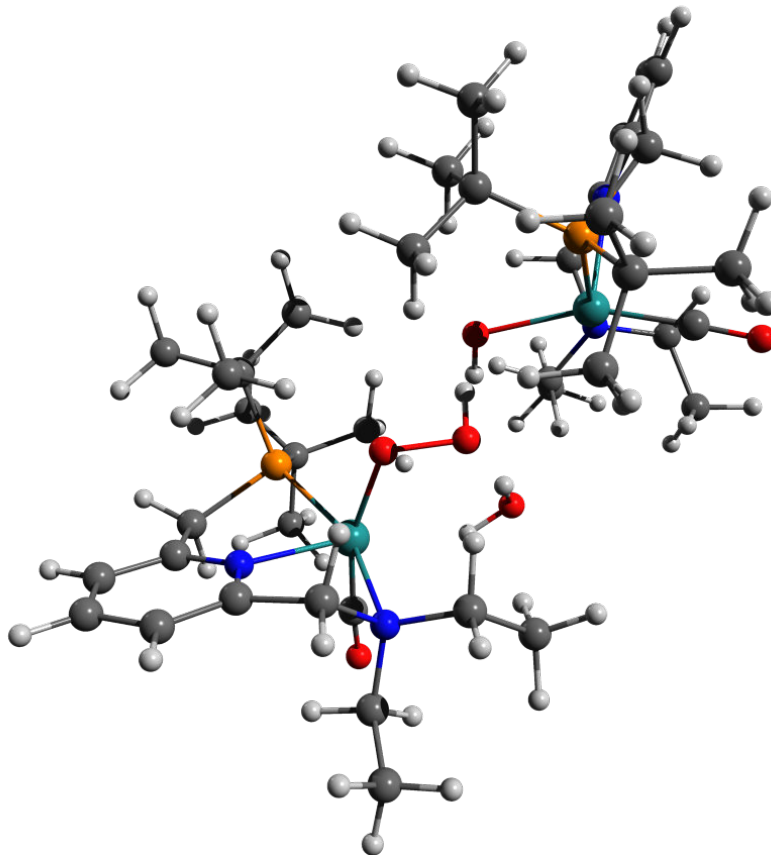


Figure 11.6-18 [C-Mono]D₀ Structure and Coordinates

63

	Energy: -975022.8334593		
H	-3.38754	-3.53397	1.53840
C	-3.08449	-2.85544	0.72800
H	-3.69964	-3.09181	-0.15375
H	-2.02893	-3.06009	0.48536
H	1.99577	-1.06227	2.50906
O	-0.60729	-0.32762	2.13706
H	2.91476	-2.67415	0.32376
O	-0.29406	-1.59179	2.77994
C	-3.23558	-1.42286	1.19263
H	3.29360	-0.11419	3.30022
H	-4.29666	-1.18668	1.40319
C	2.92046	-0.49241	2.33282
H	1.67766	-2.81774	-0.93524
H	3.68266	-1.17982	1.93491
H	-2.65945	-1.27479	2.11627
C	2.72113	-2.52891	-0.74944
H	3.38511	-3.20716	-1.31153
H	-2.40630	0.82036	1.83739
Ru	-0.40306	-0.64584	0.07794
H	0.71185	1.15314	2.25711
N	-2.68196	-0.44490	0.23274
C	-2.79962	0.91046	0.81070
C	2.66361	0.68570	1.39125
H	2.11002	1.99137	3.00737
H	4.82850	-0.98794	0.00830
C	1.67173	1.65167	2.05304
C	2.98786	-1.08366	-1.18558
P	1.78598	-0.00807	-0.15417
H	-3.84706	1.25313	0.89767
C	4.47434	-0.77937	-1.00993
H	-3.05069	-1.46953	-1.54924
H	-5.36112	-1.12644	-0.59265
H	5.04465	-1.43274	-1.69173
C	-3.32237	-0.50644	-1.09993
H	4.21925	1.99983	2.06831
C	-0.46669	-1.34241	-1.60788
C	3.95614	1.46644	1.13930
H	1.60134	-1.06715	2.90517
C	2.66553	-0.93812	-2.67536
H	4.21498	0.83160	0.87403
H	3.21498	-1.16007	-3.26945
C	-1.93606	1.91036	0.09217
N	-0.72433	1.44206	-0.24299
C	-4.83357	-0.32937	-1.13733
H	1.50488	2.55053	1.43893
H	-2.83484	0.26308	-1.71691
H	4.72459	0.26002	-1.26605
H	-5.16291	0.63819	-0.72947
C	1.49998	1.54859	-1.18068
H	-5.16880	-0.37078	-2.18449
H	3.83990	2.23298	0.35738
C	0.20761	2.22244	-0.81205
C	-2.28018	3.23402	-0.15629
H	3.00074	0.03562	-3.06956
H	-3.27064	3.60548	0.11039
H	1.39644	1.18659	-2.21609
H	2.33907	2.26030	-1.16633
C	-0.06943	3.56719	-1.06201
C	-1.32544	4.07116	-0.73425
H	0.68993	4.20635	-1.51470
H	-1.56279	5.11805	-0.93256
O	-0.59256	-1.84912	-2.65857
H	0.00586	-1.27580	3.64525

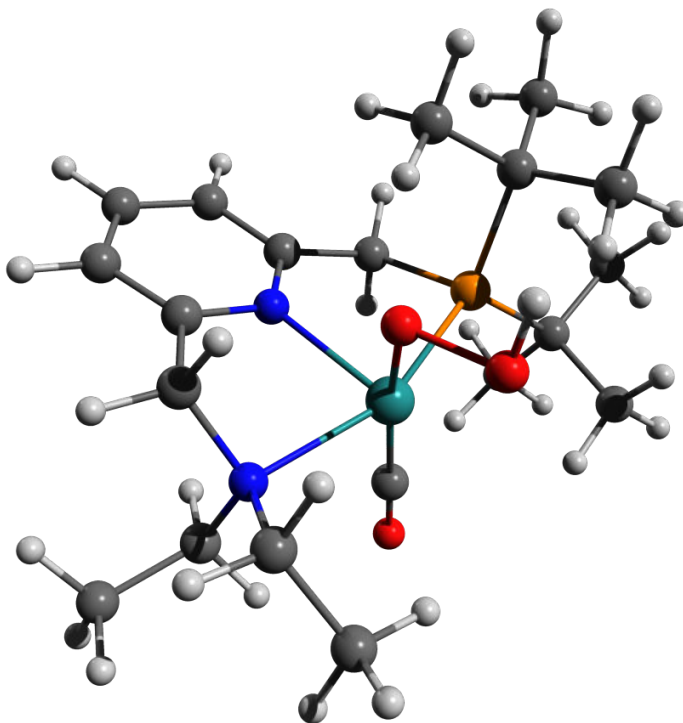


Figure 11.6-19 [C-Mono]D₀ (Me Model) Structure and Coordinates

39

O	-0.04819	-2.01605	-2.47646
O	0.05657	-0.67749	-1.94195
C	2.39625	-2.47917	-0.55239
H	2.24729	-0.24392	-1.65512
N	2.00393	-1.24720	0.14012
C	2.52464	-0.08266	-0.60105
C	-2.77035	0.64955	-1.70216
C	-3.70765	-0.11600	0.92180
P	-2.17257	0.20656	-0.02668
H	3.62423	-0.01324	-0.50776
C	2.53779	-1.24181	1.50431
C	-0.59321	-1.34333	1.86168
C	1.86066	1.20556	-0.19696
N	0.56759	1.08784	0.13363
C	-1.63830	1.86266	0.69978
C	-0.20747	2.16167	0.35840
C	2.46680	2.45591	-0.26299
H	3.52394	2.54286	-0.51795
H	-1.71414	1.71764	1.79252
H	-2.30447	2.69633	0.42805
C	0.33418	3.44392	0.27597
C	1.68706	3.58600	-0.02315
H	-0.29557	4.31699	0.45222
H	2.13311	4.58086	-0.07783
O	-0.87447	-1.61922	2.96363
H	-3.41804	1.53889	-1.69206
H	-3.33170	-0.20422	-2.11033
H	-1.88169	0.80270	-2.33215
H	-3.43984	-0.33107	1.96620
H	-4.19367	-1.00886	0.50298
H	-4.40554	0.73438	0.87989
H	2.04731	-3.33768	0.03619
H	3.49709	-2.54163	-0.66122
H	1.90799	-2.50833	-1.53414
H	2.24730	-0.31163	2.01051
H	3.64237	-1.32363	1.49550
H	2.11572	-2.08513	2.06483
Ru	-0.23290	-0.90538	0.11456
H	-1.00870	-2.14837	-2.48718

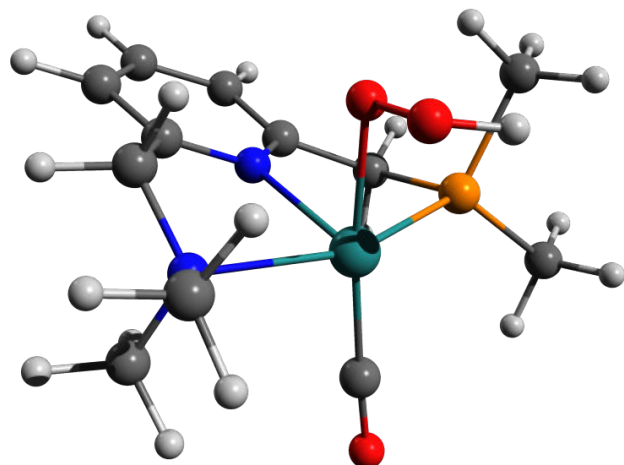


Figure 11.6-20 TS-[CD]T₀ Structure and Coordinates

128		Energy: -1951458.7937574
H	-1.35171	-0.17838
C	-2.22120	-0.15365
H	-3.12446	-0.09902
H	-2.38774	-0.76901
H	-0.31984	1.26165
O	-1.25225	-0.74231
O	-2.04379	3.71009
O	-0.24646	-0.24938
H	-1.89038	2.23946
C	-2.19157	-1.38740
H	0.17655	1.42283
H	-2.24584	-2.30644
C	-0.64075	1.60463
H	-3.45162	3.48734
H	-0.79077	2.69402
H	-1.24235	-1.41623
C	-3.13655	3.81978
H	-3.37821	4.89164
H	-2.03679	-2.65041
Ru	-3.10641	0.23167
H	-1.38113	-0.99773
N	-3.26666	1.65748
C	-3.09411	-2.63830
C	-1.88698	0.85737
H	-0.74066	-0.85900
H	-2.51385	3.83000
C	-1.61501	-0.65250
C	-3.86404	3.04233
P	-3.27352	1.22443
H	-3.29959	-3.55335
C	-3.58768	3.72103
H	-4.75083	-0.40596
H	-4.29652	-2.41845
H	-4.01674	4.73650
C	-4.62145	-1.39247
H	-1.44604	0.71039
C	-4.52409	1.17803
C	-2.20036	1.20480
H	-5.69123	2.59253
C	-5.37387	3.11646
H	-2.15025	2.27605
H	-5.65277	4.17603
C	-3.91805	-2.60747
N	-4.00636	-1.40192
C	-4.93924	-2.47766
H	-2.45667	-1.23429
H	-5.33710	-1.43361
H	-4.05587	3.19517
H	-4.85941	-3.49433
C	-4.69944	0.19101
H	-5.97838	-2.34659
H	-3.18328	0.83000
C	-4.63802	-1.22213
C	-4.49428	-3.72568
H	-5.94680	2.72917
H	-4.42361	-4.70178
H	-5.60672	0.65085
H	-4.79707	0.22148
C	-5.21629	-2.30917
C	-5.14552	-3.56846
H	-5.72485	-2.16529
H	-5.04045	-4.42954
O	-5.39774	1.77985
C	1.18454	4.45145
H	1.76986	-0.90476
O	-1.00918	2.26885
H	0.60556	-2.82294
O	2.64867	1.23333
H	-0.64410	1.39575
C	1.82668	3.27969
H	2.44368	-1.76675
C	2.29765	-1.81390
H	0.76110	-2.18235
H	1.65697	-2.68264
C	0.98977	-3.05220
H	0.44042	-3.93302
H	3.88465	2.90479
Ru	2.74747	0.27612
H	4.03241	0.24109
N	2.97292	2.46949
C	4.19078	2.85260
C	3.65643	-1.90891
H	4.59850	-0.68745
H	2.27417	-4.56489
C	4.51053	-0.69577
C	2.49685	-3.37191
P	3.34382	-1.78138
H	4.57184	3.83524
C	2.71632	-4.63490
H	3.99257	1.91376
H	1.46622	1.56247
H	2.21942	-5.47525
C	3.22476	2.65136
H	4.74656	-2.97798
C	2.63576	-0.38275
C	4.40805	-3.15803
H	2.87974	-2.81597
C	2.95820	-3.67481
H	3.79705	-4.06582
H	2.31666	-4.47217
C	5.28411	1.82581
N	4.86005	0.55630
C	1.99978	2.49775
H	5.53286	-0.77220
H	3.67222	3.65176
H	3.78033	-4.89358
H	1.28254	3.31870
C	5.09793	-1.84569
H	2.31440	2.48267
H	5.31141	-3.35708
C	5.71662	-0.47646
C	6.64396	2.12100
H	3.99235	-4.05282
H	6.98026	3.15737
H	4.98049	-2.16770
H	5.75382	-2.57682
C	7.09210	-0.24426
C	7.55456	1.06756
H	7.78759	-1.08325
H	8.62731	1.26910
H	1.77264	1.05510
O	2.05241	-0.76839
H	1.00924	5.04550
H	2.08318	5.00301
H	2.79123	5.21755
H	1.73166	3.00783
H	0.92661	2.92047
H	1.08400	0.09696

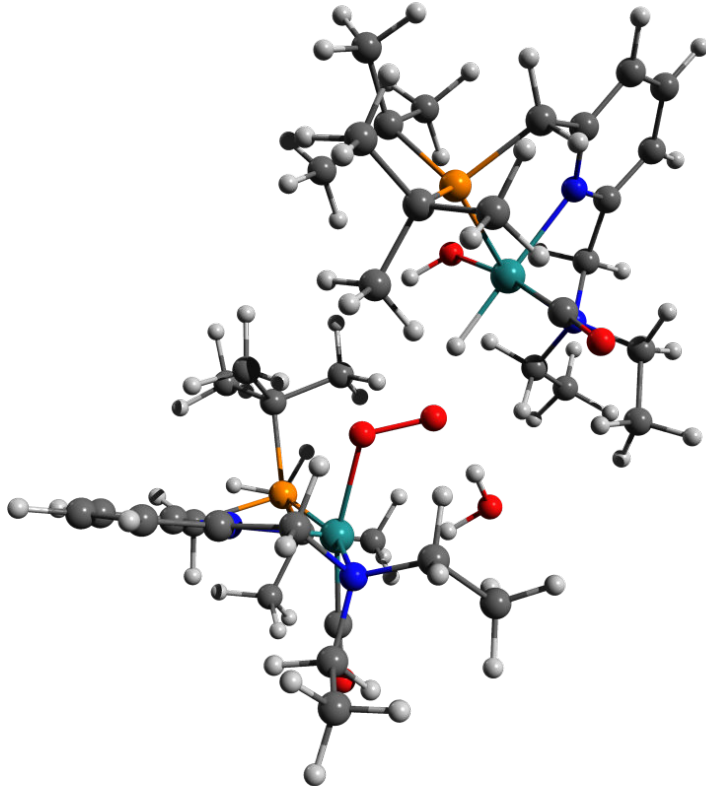


Figure 11.6-21 [D]T₀ [F]S₀ (Dimer Model) Structure and Coordinates

128

```

Energy: -1951474.5643316
H 2.21039 -2.23355 -4.32302
C 2.94020 -2.10065 -3.51092
H 3.78217 -2.79102 -3.70812
H 2.44399 -2.38608 -3.57405
H 0.28729 0.60700 0.03450
O 0.200197 0.80968 -1.11563
H 0.78753 -1.87017 2.19783
O 0.91009 0.32922 1.54921
H 1.65613 -2.28902 0.30684
C 3.35522 -0.64652 -3.46822
H -0.28740 1.93394 2.06713
H 3.81547 -0.34125 -4.42738
C 0.39308 1.07378 1.96078
H 2.17595 -2.85811 1.70881
H 0.04202 0.28934 2.64875
C 2.46663 -0.01909 -3.31819
C 1.70714 -2.35054 2.56204
H 1.42251 -3.11909 3.30019
H 3.62475 1.64598 -2.49829
Ru 3.37129 -0.49295 -0.27560
H 2.20172 2.33336 0.26632
N 4.28549 -0.32083 -2.36027
C 4.59308 1.12622 -2.42419
C 1.82021 1.51701 2.27687
H 1.50189 3.46666 1.44084
H 1.06378 -0.50582 4.44736
C 2.22635 2.64419 1.31726
C 2.67215 -1.35764 3.21999
P 2.96471 0.03118 1.93490
H 5.18433 1.37831 -3.32006
C 2.07975 -0.90767 4.55421
H 5.27240 -2.15699 -2.21825
H 5.77660 -1.42642 -4.57931
H 2.01230 -1.78895 5.21372
C 5.53971 -1.11357 -2.42389
H 1.38104 3.07219 3.68524
C 4.29326 -2.00741 0.16757
C 1.90014 2.09943 3.69185
H 4.54301 -2.36849 2.62207
C 3.99571 -2.06566 3.52316
H 1.41175 1.48031 4.44974
H 3.77400 -2.98486 4.09033
C 5.27474 1.61909 -1.17756
N 4.80159 1.08031 -0.04426
C 6.33553 -1.03327 -3.71762
H 3.22071 3.05100 1.55899
H 6.15890 -0.78525 -1.57600
H 2.70644 -0.16287 5.06443
H 6.66552 -0.01184 -3.95952
C 4.66614 0.73279 2.33966
H 7.24174 -1.64741 -3.60772
H 2.93471 2.29472 4.01482
C 5.24957 1.46071 1.16314
C 6.26361 2.59505 -1.14450
H 4.65486 -1.44802 4.15262
H 6.64712 3.02308 -2.07160
H 5.29860 -0.14991 2.52652
H 4.69246 1.35254 3.24800
C 6.22637 2.49204 1.26262
C 6.73820 3.01873 0.05971
H 6.58475 2.78847 2.24304
H 7.50665 3.78970 0.19685
O 4.86915 -3.0676 0.36731
C -1.97725 -4.45660 1.0002
H -2.24578 2.18935 2.19599
O 0.83058 -2.38124 -0.81491
H -1.09111 3.08609 -0.24809
O -3.05347 -0.36368 1.91451
H 0.67780 -1.44550 -1.07669
C -1.93640 -3.02562 1.01222
H -3.38713 3.54642 2.92734
C -3.08033 3.08788 1.97190
H -0.98099 1.82862 -1.48757
H -2.42915 3.80557 1.45027
C -1.33265 2.85094 -1.29582
H -0.75920 3.54442 -1.93434
H -4.12042 -2.21994 1.93269
Ru -2.98649 -0.33811 -0.18846
H -4.60200 0.80015 2.14753
N -3.08682 -2.59868 0.17864
C -4.34181 -2.68580 0.95879
C -4.32227 2.72502 1.15835
H -5.40323 2.20156 2.93768
H -2.90294 4.90516 -0.44755
C -5.16594 1.73059 1.96779
C -2.82692 3.02834 -1.58679
P -3.73776 1.81492 -0.42011
H -4.65609 -3.73378 1.10358
C -3.19232 4.50319 -1.42759
H -3.99955 -2.90770 -1.66592
H -1.44430 -2.68958 -2.03879
H -2.63751 5.07712 -2.18907
C -3.24244 -3.41453 -1.04746
H -5.65686 4.23734 1.88606
C -2.67460 -0.47959 -1.97443
C -5.18718 3.96793 0.92513
H -2.91367 1.59427 -3.26355
C -3.10729 2.65000 -3.04385
H -4.62460 4.84203 0.58295
H -2.43663 3.24323 -3.68784
C -5.45941 -1.89036 0.34516
N -5.07880 -0.71700 -0.17809
C -1.97227 -3.62881 -1.84239
H -6.12566 1.51303 1.47416
H -3.67063 -4.39812 -0.76872
H -4.26295 4.69503 -1.58765
H -1.26561 -4.29481 -1.32963
C -5.38276 1.41933 -1.25573
H -2.23230 -4.08566 -2.80909
H -6.00725 3.78417 0.21399
C -5.96411 0.15525 -0.68740
C -6.80155 -2.25763 0.36299
H -4.13958 2.89557 -3.33875
H -7.10272 -3.21866 0.78172
H -5.12461 1.22841 -2.30996
H -6.11529 2.23989 -1.23913
C -7.32551 -0.14837 -0.68226
C -7.74163 -1.36824 -0.15465
H -8.04567 0.56188 -1.10909
H -8.80221 -1.62728 -0.14874
H -2.21835 0.04458 2.20918
O -2.00941 -0.60536 -3.00882
H -1.00514 -4.64168 2.10887
H -2.00387 -5.20251 0.71828
H -2.83017 -4.64733 2.19805
H -1.92254 -2.30085 1.84537
H -1.02934 -2.85403 0.41887
H -1.41111 -0.09993 -0.07392

```

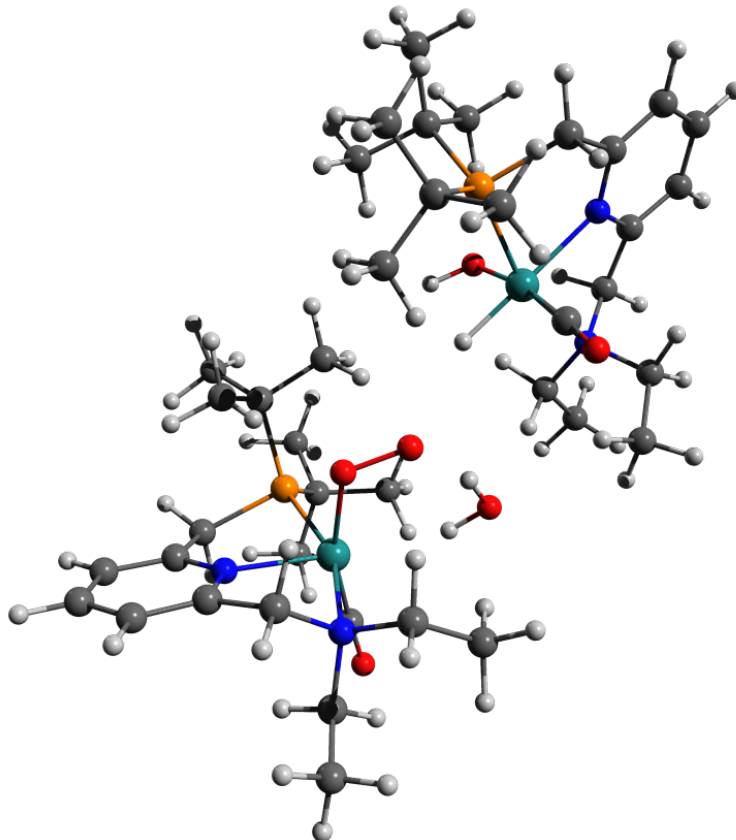


Figure 11.6-22 [D]T₀ Structure and Coordinates

65

```

Energy: -1022871.1899855
H   -3.38494   -3.31180   1.82737
C   -2.95512   -2.79277   0.95830
H   -3.30208   -3.24552   0.05218
H   -1.86643   -2.95916   0.96163
H   1.09881   -0.67840   2.70890
O   -0.53456   -0.35358   2.07755
H   3.01942   -2.52358   0.85085
O   -0.35394   -1.52334   2.63574
C   -3.25043   -1.31281   1.06133
H   3.09522   -0.44848   3.41532
H   -4.34039   -1.12453   1.05618
C   2.80965   -0.08705   2.49421
H   1.90559   -2.89679   -0.47328
H   3.63051   -0.77775   2.24948
H   -2.86486   -0.91811   2.00937
C   2.92191   -2.54757   -0.24458
H   3.64858   -3.27877   -0.63668
H   -2.66408   1.08616   1.35598
Ru  -0.31837   -0.68828   -0.00504
H   0.53186   1.44950   2.04182
N   -2.60517   -0.51691   -0.00635
C   -2.83355   0.92076   0.27621
C   2.56533   0.92876   1.37589
H   1.84035   2.41943   2.74501
H   4.91382   -0.82138   0.45058
C   1.49019   1.92961   1.82129
C   3.19596   -1.17605   -0.87243
P   1.87279   -0.00911   -0.13540
H   -3.88007   1.20620   0.07627
C   4.65112   -0.78951   -0.61501
H   -2.77125   -1.86864   -1.59665
H   -5.17070   -1.52766   -0.94783
H   5.29862   -1.51901   -1.13009
C   -3.12403   -0.85838   -1.35592
H   4.01544   2.38917   1.98578
C   -0.23183   -1.57996   -1.59320
C   3.83591   1.74231   1.11081
H   1.97571   -1.47843   -2.68860
C   3.00900   -1.26566   -2.38964
H   4.73044   1.12740   0.97445
H   3.63245   -2.09289   -2.76752
C   -1.89906   1.81367   -0.48819
N   -0.64961   1.34073   -0.61557
C   -4.63079   -0.78598   -1.55459
H   1.33192   2.72272   1.07485
H   -2.61559   -0.18268   -2.05967
H   4.89859   0.20539   -1.01207
H   -5.05049   0.20694   -1.33435
C   1.64357   1.37017   -1.39287
H   -4.85289   -1.00424   -2.60984
H   3.73636   2.40888   0.24034
C   0.31283   2.05126   -1.22985
C   -2.24178   3.06770   -0.98206
H   3.34686   -0.34867   -2.89655
H   -3.26161   3.43938   -0.87459
H   1.62986   0.85888   -2.36903
H   2.46623   2.10001   -1.42016
C   0.03643   3.32619   -1.72152
C   -1.25326   3.83625   -1.59409
H   0.82291   3.90564   -2.20703
H   -1.49541   4.82932   -1.90022
O   -0.24541   -2.20583   -2.93553
O   -2.15763   1.34600   3.37545
H   -1.45833   0.73127   3.05377
H   -2.60547   0.82846   4.05496

```

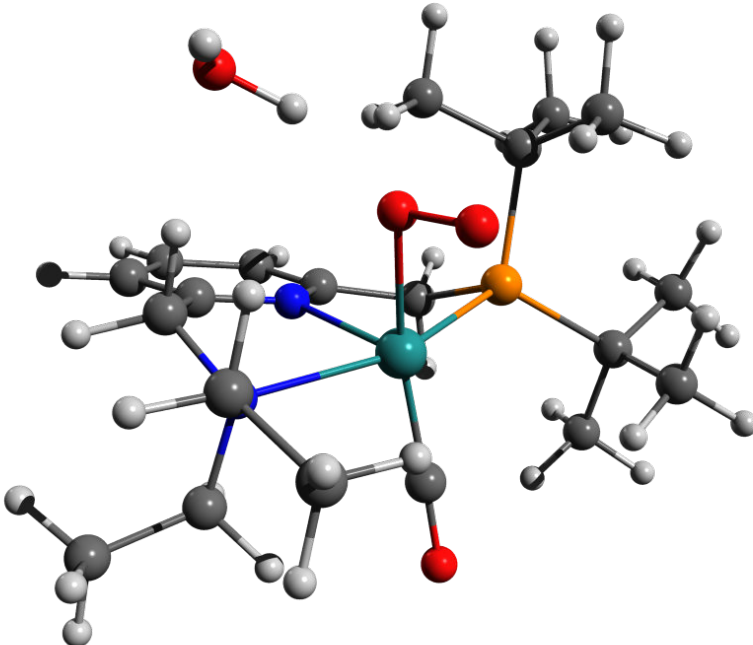


Figure 11.6-23 Scan-[DE]T₀ Geometry 5 Structure and Coordinates

65

```

Energy: -1022862.3266652
H   -3.52909    3.63066    0.69690
C   -3.14014    2.67577    1.07009
H   -3.70774    2.43237    1.98093
H   -2.06658    2.82341    1.92421
H   1.68759    1.64389    1.72549
O   -0.13249    4.15116   -1.87917
H   4.21495    1.15428    0.97408
O   1.02322    4.36975   -1.65856
C   -3.28448    1.62227   -0.00542
H   3.21108    1.41790   -2.58285
H   -4.35763    1.46172   -0.23123
C   2.68412    1.24653   -1.62884
H   2.71787    1.87703   -1.62409
H   3.19133    1.83450   -0.85194
H   -2.80464    1.95432   -0.93683
C   3.45799    1.07669    1.76795
H   3.96970    1.26101    2.72781
H   -2.73602   -0.06024   -1.72577
Ru  -0.40746    0.28477    0.36618
H   0.82599   -0.57996   -2.46733
N   -2.65529    0.31948    0.31333
C   -2.97713   -0.60257   -0.79572
C   2.66375   -0.25294   -1.32393
H   2.33072   -0.71345   -3.40479
H   4.61259   -1.38065    1.15940
C   1.86314   -0.94464   -2.43282
C   2.80169   -0.30485    1.80611
P   1.67304   -0.50435    0.28526
H   -4.05055   -0.86240   -0.81937
C   3.87043   -1.38738    1.96654
H   -2.68589    0.42603    2.39482
H   -5.14655    0.53499    1.74855
H   4.41231   -1.21646    2.91251
C   -3.09606   -0.23282    1.61775
H   4.51800   -0.71960   -2.31985
C   0.12668    1.97410    0.77974
C   4.08269   -0.81368   -1.31025
H   1.06471    0.39181    2.93114
C   1.86034   -0.36233    3.01447
H   4.74237   -0.26860   -0.62064
H   2.44092   -0.18706    3.93633
C   -2.13124   -1.83752   -0.76503
N   -0.88543   -1.64945   -0.28699
C   -4.59579   -0.41517    1.81058
H   1.85621   -2.04051   -2.32728
H   -2.57927   -1.19605    1.74069
H   3.43684   -2.39724    2.02516
H   -5.03675   -1.11348    1.08360
C   1.35159   -2.35785    0.29786
H   -4.77557   -0.83435    2.81187
H   4.10942   -1.88199   -1.04381
C   0.00997   -2.66200   -0.29230
C   -2.53968   -3.06661   -1.26824
H   1.37180   -1.34516    3.11201
H   -3.55523   -3.19103   -1.64581
H   1.33080   -2.64239    1.36285
H   2.14391   -2.98574   -0.17788
C   -0.33534   -3.90828   -0.80978
C   -1.62275   -4.14441   -1.29836
H   0.40247   -4.71134   -0.81812
H   -1.91004   -5.08739   -1.69392
O   0.53654    3.04860    1.91779
O   -1.02013    1.17283   -2.57593
H   -0.84821    2.12314   -2.60775
H   -0.64192    0.93092   -1.67189

```

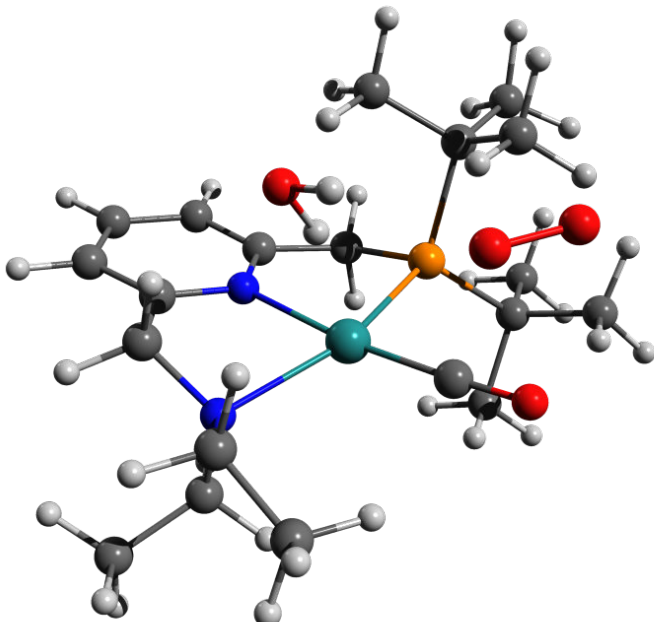


Figure 11.6-24 [E]S₀ Structure and Coordinates

```

63                                         Energy: -928588.5901943
N   -0.79133   1.42415   0.01683
C   -2.02380   1.84124   0.37017
C    0.13107   2.22628   -0.42940
O   -2.46585   3.17164   0.52270
C   -1.46998   4.09574   -0.20893
C   -0.18941   3.66159   -0.54037
C   -2.87907   0.77597   0.98864
H   -3.41494   3.47721   0.53136
H   -1.73711   5.14924   -0.30717
H   0.56365   -4.36371   -0.89999
C   1.46351   1.74417   -0.81210
N   -2.65212   -0.55453   0.39254
H   -3.94471   1.06478   0.96488
H   -2.59052   0.70030   2.04990
H   1.44545   1.53749   -1.89569
P   1.70832   0.05142   -0.03024
H   2.27274   2.46679   -0.62445
Ru  -0.40599   -0.62089   0.15361
C   -3.27363   -0.64358   -0.95219
C   2.97845   -0.74783   -1.20012
C   -3.18949   -1.56064   1.33979
C   2.53410   0.45347   1.64701
C   2.19457   -1.27404   -2.40610
C   3.63932   -1.93931   -0.50368
C   4.04527   0.22764   -1.70266
C   1.63138   1.49050   2.32374
C   3.95281   1.01018   1.57578
C   2.49280   -0.81727   2.50075
H   -2.80880   0.13549   -1.57050
C   -4.79102   -0.53396   -1.01525
H   -2.93530   -1.59110   -1.39047
H   -2.55934   -1.48842   2.23915
C   -3.18632   -2.98500   0.83054
H   -4.21908   -1.27293   1.63398
C   0.03994   -2.38933   0.14073
H   -2.18198   -3.29149   0.51148
H   -3.88327   -3.13688   -0.00645
H   -3.50338   -3.65153   1.64617
H   -5.10318   -0.62787   -0.06600
H   -5.16787   0.43500   -0.65414
H   -5.29928   -1.32900   -0.44968
H   2.90715   -1.71394   -3.12478
H   1.62743   -0.48790   -2.92492
H   1.47710   -2.04963   -2.10743
H   4.23655   -2.49727   -1.24443
H   2.89196   -2.63300   -0.09153
H   4.32107   -1.63378   0.30265
H   4.74182   -0.31648   -2.36279
H   4.63926   0.67500   -0.89613
H   3.60801   1.04018   -2.30181
H   4.67507   0.27479   1.19572
H   4.28265   1.29668   2.58941
H   4.01533   1.91267   0.94747
H   3.13835   -1.61377   2.10810
H   1.46338   -1.20515   2.54493
H   2.83194   -0.58265   3.52443
H   1.98486   1.65715   3.35522
H   0.59120   1.13131   2.36546
H   1.64500   2.46423   1.80977
O   0.39658   -3.50621   0.09718
O   -0.69010   0.21173   -2.97203
H   -0.95813   1.08513   -2.66151
H   -0.52984   -0.26674   -2.11021

```

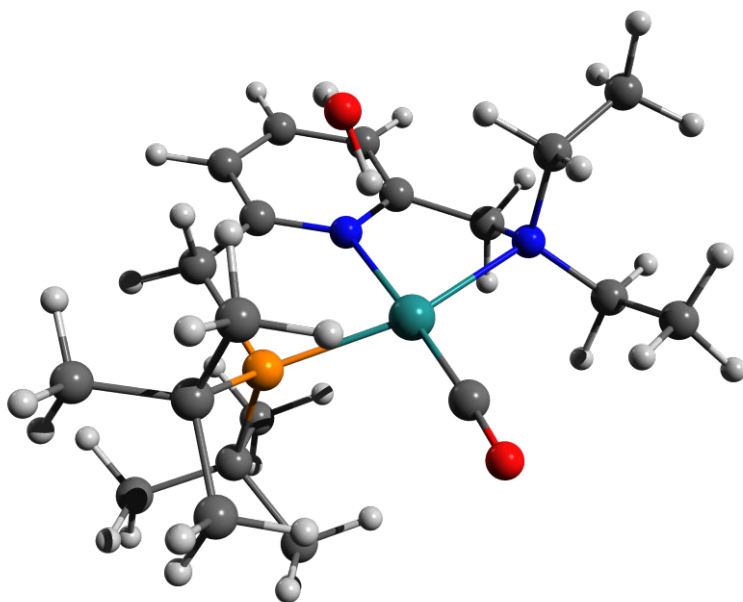


Figure 11.6-25 ³O₂ Coordinates

```

2                                         Energy: -94269.2503844
O   0.00000   0.00000   0.59806
O   0.00000   0.00000   -0.59806

```

Figure 11.6-26 [F]S₀ Structure and Coordinates

```

63          Energy: -928594.2422451
N   -0.74635   1.30730  -0.32033
C   -1.93878   1.84167  -0.01643
C    0.18858   2.01274  -0.97776
C   -2.25389   3.14457  -0.39308
C   -1.20925   3.89510  -1.07340
C   -0.06176   3.32937  -1.36675
C   -2.84306   0.97446  -0.81471
C   -3.23108   3.56209  -0.14724
H   -1.51749   4.92094  -1.37588
H    0.70480   3.89705  -1.89553
C   1.49478   1.30907  -1.27073
N   -2.84341   -0.42575  0.38117
H   -3.85953   1.40663  0.85274
H   -2.41290   0.96630  1.83054
H   1.39796   0.81902  -2.25631
P    1.79947  -0.10207  -0.06444
H   2.31636   2.02663  -1.33554
Ru  -0.32175   -0.78130  0.27359
C   -3.46183   -0.59919  -0.94190
C   3.10916   -1.14527  -0.97707
C   -3.42210   -1.26670  1.43622
C   2.61156   0.77486  1.42559
C   2.39457   -2.02743  -2.00009
C   3.80009   -2.06975  0.02702
C   4.14004   -0.29775  -1.72864
C   1.69299   1.93832  1.81948
C   4.00605   1.33256  1.14447
C   2.66301   -0.19905  2.60550
H   0.01026   -2.25575  0.83530
H   -2.91836   0.06098  -1.63552
C   -4.95759   -0.32754  -1.02895
H   -3.24790   -1.62263  -1.27730
H   -2.81556   -1.05375  2.32917
C   -3.36080   -2.74585  1.11743
H   -4.46441   -0.95652  1.65455
C   -0.50126   -1.51406  -1.38531
O   -0.57986   -0.11284  2.25077
H   -0.37245   -0.84709  2.84019
H   -2.32717   -3.02846  0.88111
H   -4.02163   -3.03305  0.28531
H   -3.67211   -3.32484  1.99945
H   -5.29191   -0.47074  -2.06746
H   -5.21847   0.70230  -0.74089
H   -5.54132   -1.01426  -0.39748
H   3.15437   -2.60299  -2.55465
H   1.81938   -1.44712  -2.73550
H   1.71136   -2.73530  -1.51456
H   4.41226   -2.80230  -0.52475
H   3.06264   -2.62841  0.62341
H   4.46906   -1.53042  0.71081
H   4.86572   -0.97439  -2.21023
H   4.70470   0.38269  -1.08198
H   3.67478   0.29404  -2.53093
H   4.75838   0.54920  0.98004
H   4.32884   1.91247  2.02544
H   4.02144   2.01981  0.28437
H   3.31205   -1.06440  2.42213
H   1.64926   -0.54891  2.83581
H   3.05547   0.33493  3.48741
H   2.10633   2.40374  2.73046
H   0.68234   1.56615  2.04803
H   1.65235   2.72159  1.04725
O   -0.74696   -2.01597  -2.41088

```

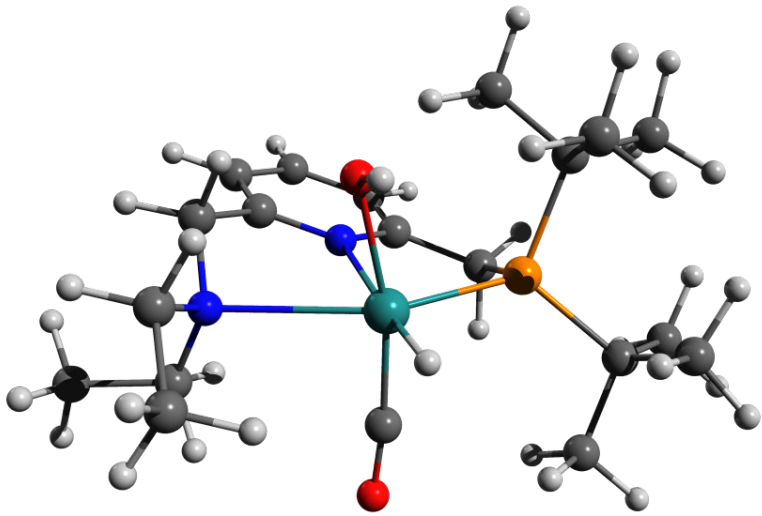


Figure 11.6-27 [F-Up]S₀

63 Energy: -928594.7107585
 N -0.76012 1.35702 0.06074
 C -1.99808 1.76019 0.41130
 C 0.14591 2.21168 -0.43933
 C -2.33911 3.09652 0.05530
 C -1.41501 4.01493 -0.19217
 C -0.15550 3.57248 -0.52449
 C -2.86432 0.65143 0.91583
 H -3.36391 3.41035 0.61035
 H -1.66922 5.07414 -0.20352
 H 0.58703 4.27030 -0.91343
 C 1.42575 1.61295 -0.94035
 N -2.71088 -0.57889 0.10904
 H -3.91695 0.97807 0.97223
 H -2.54157 0.40295 1.94000
 H 1.24037 1.35471 -1.99701
 P 1.76437 -0.06514 -0.17220
 H 2.26264 2.32326 -0.88030
 Ru -0.40278 -0.73311 0.00089
 C -3.28097 -0.39488 -1.24605
 C 2.98529 -0.86039 -1.40368
 C -3.35596 -1.69012 0.84091
 C 2.68585 0.37918 1.43916
 C 2.16082 -1.50296 -2.52121
 C 3.76716 -1.97521 -0.70760
 C 3.94668 0.14893 -2.03561
 C 1.78330 1.34786 2.21325
 C 4.02979 1.07014 1.20419
 C 2.90333 -0.86685 2.30296
 H -0.17741 -2.28874 -0.35044
 H -2.67991 0.38194 -1.73612
 C -4.77086 -0.09912 -1.32183
 H -3.04599 -1.30790 -1.80675
 H -2.86129 -1.74689 1.82075
 C -3.24236 -3.02668 0.14065
 H -4.41803 -1.44218 1.03317
 C -0.36341 -1.29063 1.73384
 O -0.55241 -0.24421 -0.29243
 H -0.51954 -1.07146 -2.52109
 H -2.19154 -3.21571 -0.12667
 H -3.85742 -3.08026 -0.76983
 H -3.58479 -3.82187 0.81910
 H -5.05260 -0.00593 -2.38153
 H -5.04794 0.84874 -0.83522
 H -5.39256 -0.89811 -0.88922
 H 2.85351 -1.96637 -3.24406
 H 1.53388 -0.76769 -3.04204
 H 1.49724 -2.27858 -2.11355
 H 4.30778 -2.55843 -1.47151
 H 3.09398 -2.66558 -0.17658
 H 4.51440 -1.59451 0.00201
 H 4.62443 -0.38964 -2.71936
 H 4.57013 0.67690 -1.30360
 H 3.41141 0.89676 -2.63846
 H 4.77741 0.39768 0.76244
 H 4.42961 1.40719 2.17539
 H 3.94093 1.96074 0.56358
 H 3.62536 -1.56423 1.86222
 H 1.96971 -1.41019 2.48923
 H 3.30471 -0.55087 3.28072
 H 2.24443 1.559018 3.19394
 H 0.78337 0.92780 2.38544
 H 1.66994 2.31323 1.69793
 O -0.39707 -1.72073 2.82230

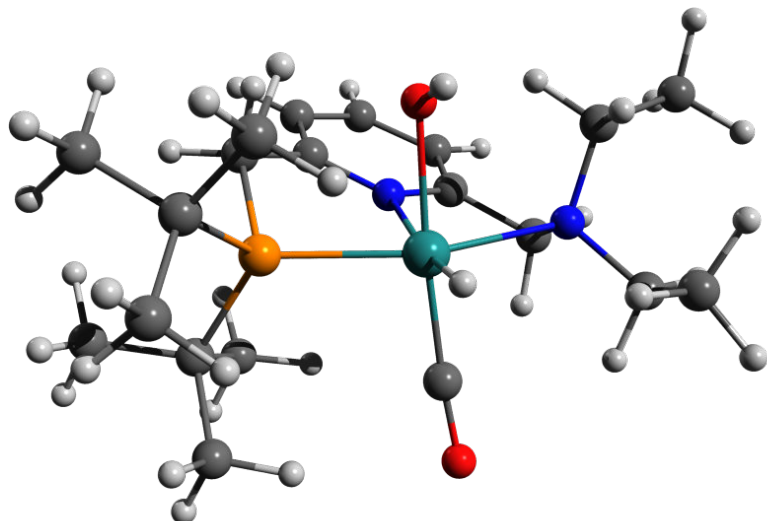


Figure 11.6-28 [F-Trans]S₀ Structure and Coordinates

```

63          Energy: -928595.0842646
N   -0.80008   1.42201  -0.04137
C   -2.01529   1.84205  -0.33314
C    0.08510   2.23307  -0.61339
C   -2.40612   3.16389  -0.15747
C   -1.49281   4.05289  -0.40859
C   -0.23606   3.59815  -0.79275
C   -2.83614   3.77931  -0.98500
H   -3.40192   3.48884  -0.46079
H   -1.76456   5.10007  -0.55239
H   0.49999   4.27366  -1.24616
C   1.38015   1.63724  -1.04565
C   -2.67460  -0.52971  0.33005
N   -3.89593   1.07920  1.06179
H   -2.45228   0.65674  2.02086
H   1.20532   1.24514  -2.06318
P   1.72843   0.07619  -0.07604
H   2.20011   2.36921  -1.06618
Ru  -0.40440  -0.63417  0.12216
C   -3.31677  -0.52889  -1.00610
C   2.98840  -0.83483  -1.17047
C   -3.23884  -1.55482  1.23772
C   2.56798   0.66948  1.52673
C   2.19557  -1.57220  -2.25448
C   3.75077  -1.87787  -0.35107
C   3.96721   0.12336  -1.85464
C   1.66301   1.74844  2.13123
C   3.95882   1.26826  1.32423
C   2.62271  -0.50133  2.51198
H   -0.38438  -0.55794  1.74376
H   -2.72303   0.14852  -1.63637
C   -4.80382  -0.21466  -1.04423
H   -3.12800  -1.52055  -1.43586
H   -2.59533  -1.54706  2.12912
C   -3.29428  -2.95019  0.65467
H   -4.25429  -1.24594  1.55620
C   0.02966  -2.39316  0.33554
O   -0.62223  -0.36430  -0.21252
H   -0.67378  -1.23608  -2.41991
H   -2.32106  -3.24701  0.24091
H   -4.05502  -3.04876  -0.13346
H   -3.55292  -3.66121  1.45301
H   -5.15707  -0.32368  -2.08074
H   -5.03248   0.81782  -0.73872
H   -5.40541  -0.89516  -0.42114
H   2.90435  -1.96849  -3.00088
H   1.45853  -0.92112  -2.74563
H   1.64034  -2.41699  -1.82452
H   4.33693  -2.50636  -1.04223
H   3.06523  -2.54178  0.19634
H   4.45549  -1.43199  0.36428
H   4.69269  -0.46925  -2.43693
H   4.53709   0.74184  -1.15000
H   3.45345   0.78874  -2.56369
H   4.69663   0.52824  0.98659
H   4.31802   1.67091  2.28640
H   3.95127   2.10330  0.60632
H   3.31040  -1.29420  2.19136
H   1.62198  -0.93940  2.63946
H   2.97139  -0.13229  3.49119
H   2.06319   2.03045  3.11924
H   0.63872   1.37235  2.26559
H   1.63082   2.66104  1.51667
O   0.36196  -3.49890  0.50636

```

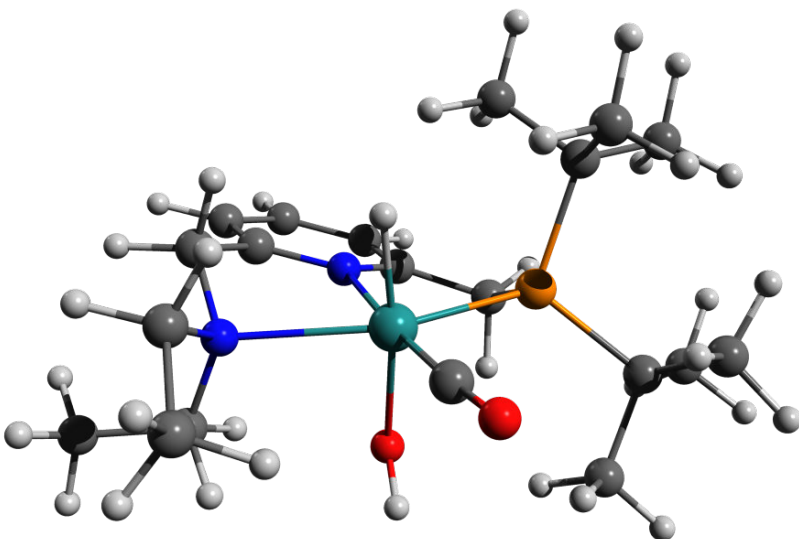


Figure 11.6-29 [F-Trans-Up]S₀ Structure and Coordinates

63

	Energy: -928597.8425380		
N	-0.80456	1.44495	-0.18829
C	-2.03468	1.86436	0.14891
C	0.12233	2.90384	-0.64514
C	-2.26507	3.20059	0.02647
C	-1.44432	4.11153	-0.42708
C	-0.17108	3.66150	-0.76372
C	-2.90916	0.80031	0.72946
H	-3.40264	3.52229	0.29686
H	-1.69505	5.16966	-0.52185
H	0.59223	4.35144	-1.12469
C	1.43744	1.70691	-1.03843
N	-2.68203	-0.50943	0.08359
H	-3.97137	1.09596	0.70925
H	-2.57049	0.66141	1.77189
H	1.38751	1.45664	-2.11168
P	1.72097	0.06691	-0.17905
H	2.26188	2.42278	-0.90504
Ru	-0.41200	-0.61319	0.08095
C	-3.20203	-0.52723	-1.30271
C	2.89886	-0.81317	-1.38767
C	-3.30408	-1.53096	0.95651
C	2.63956	0.54327	1.41642
C	2.06909	-1.36145	-2.55174
C	3.56812	-1.99337	-0.67902
C	3.96741	0.12012	-1.96582
C	1.76616	1.61361	2.08406
C	4.05425	1.08518	1.22993
C	2.65974	-0.68229	2.33407
H	-0.43417	-0.78203	-1.52042
H	-2.66778	0.26567	-1.84531
C	-4.70588	-0.35856	-1.46514
H	-2.86686	-1.46983	-1.75382
H	-2.72796	-1.47327	1.89224
C	-3.29003	-2.93590	0.39539
H	-4.34571	-1.23050	1.18415
C	0.02049	-2.37940	0.20529
O	-0.76410	-0.17688	2.17309
H	-0.41080	-0.88374	2.72358
H	-2.27615	-3.24304	0.10712
H	-3.94853	-3.05374	-0.47837
H	-3.64559	-3.63190	1.16954
H	-4.95447	-0.40248	-2.53621
H	-5.06907	0.60960	-1.08879
H	-5.27648	-1.15404	-0.96304
H	2.75551	-1.82586	-3.27975
H	1.50507	-0.57340	-3.07289
H	1.34279	-2.11174	-2.21769
H	4.12018	-2.59036	-1.42402
H	2.83098	-2.65636	-0.20339
H	4.29185	-1.66865	0.08138
H	4.61776	-0.46331	-2.63891
H	4.60846	0.57207	-1.20033
H	3.52795	0.92880	-2.56855
H	4.75887	0.32382	0.86597
H	4.42910	1.43550	2.20622
H	4.08739	1.94673	0.54444
H	3.28052	-1.50000	1.94507
H	1.63860	-1.05734	2.48408
H	3.06654	-0.38893	3.31631
H	2.20182	1.84961	3.07021
H	0.73467	1.22947	2.23546
H	1.74397	2.55309	1.50940
O	0.35357	-3.49676	0.25197

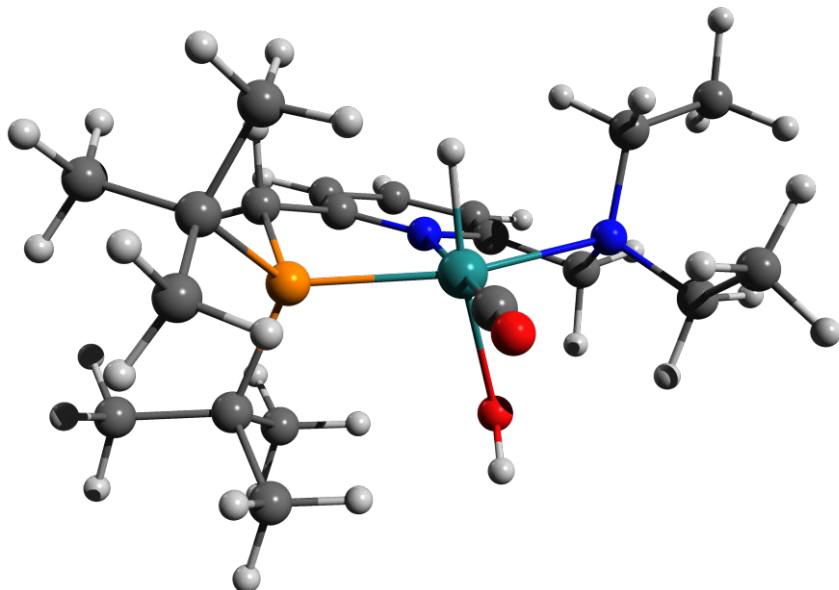


Figure 11.6-30 [F-Cis]S₀ Structure and Coordinates

63

	Energy: -928584.1363893		
N	0.71566	1.37102	0.24967
C	1.88001	1.90688	-0.14944
C	-0.22203	2.13284	0.85849
C	2.26985	3.23563	0.01033
C	1.26995	4.02958	0.76442
C	0.03258	3.47557	1.12784
C	2.73322	0.98067	-0.96914
H	3.15802	3.64155	-0.20754
H	1.47320	5.07710	0.98044
H	-0.73060	4.07916	1.62065
C	-1.51831	1.44743	1.18218
N	2.66800	-0.41382	-0.49369
H	3.77113	1.35162	-1.03319
H	2.30857	0.97872	-1.98663
H	-1.44297	0.99243	2.18545
P	-1.75656	-0.02385	0.03128
H	-2.35119	2.16642	1.20696
Ru	0.41346	-0.61138	-0.14255
C	3.42690	-0.55444	0.77262
C	-3.03865	-1.11267	0.91840
C	3.17947	-1.30585	-1.55970
C	-2.54199	0.74825	-1.53001
C	-2.28511	-1.92416	1.97289
C	-3.61065	-2.11050	-0.09137
C	-4.15196	-0.32493	1.61073
C	-1.68563	1.95376	-1.93209
C	-3.97745	1.23127	-1.32770
C	-2.47899	-0.26757	-2.67357
H	0.32800	-0.24845	-1.77202
H	2.99417	0.17132	1.47773
C	4.93463	-0.36535	0.69258
H	3.19723	-1.54836	1.17591
H	2.49649	-1.16511	-2.41000
C	3.19508	-2.76566	-1.16012
H	4.18443	-0.96125	-1.87714
C	0.60946	-1.12466	1.67406
O	0.15196	-2.61505	-0.66095
H	-0.04077	-2.60617	-1.60553
H	2.18267	-3.05345	-0.82169
H	3.93873	-2.98216	-0.37773
H	3.46261	-3.37173	-2.03913
H	5.35640	-0.47464	1.70297
H	5.22566	0.63128	0.32769
H	5.41672	-1.11829	0.05220
H	-3.00470	-2.58654	2.48267
H	-1.82336	-1.29010	2.74351
H	-1.50496	-2.54116	1.50536
H	-4.20342	-2.86484	0.45241
H	-2.79842	-2.63566	-0.61747
H	-4.27589	-1.63992	-0.82798
H	-4.82587	-1.03594	2.11799
H	-4.76170	0.26958	0.92036
H	-3.75465	0.34758	2.38635
H	-4.68328	0.40641	-1.16265
H	-4.30489	1.76218	-2.23745
H	-4.06683	1.93952	-0.48927
H	-3.11348	-1.14547	-2.49985
H	-1.44317	-0.60744	-2.81777
H	-2.82285	0.21757	-3.60270
H	-2.05123	2.33470	-2.90001
H	-0.63235	1.66355	-2.05282
H	-1.75400	2.77998	-1.20884
O	0.81361	-1.39650	2.78236

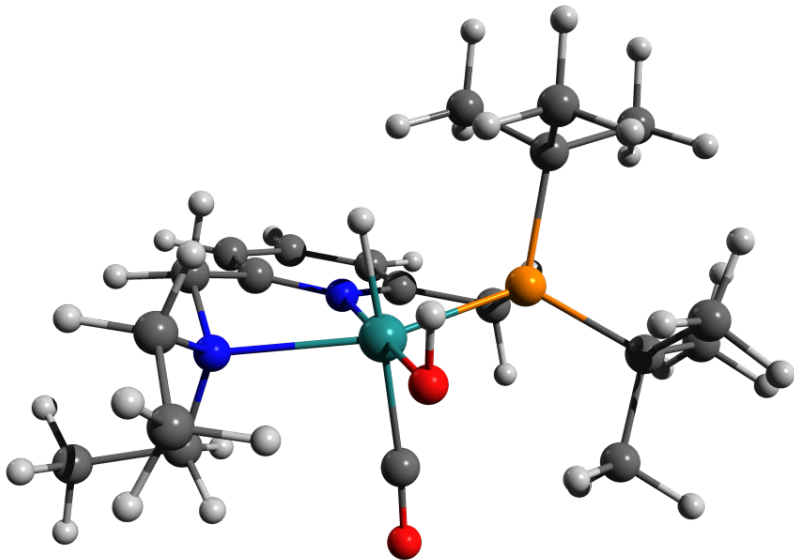


Figure 11.6-31 [F-Cis-Up]S₀

63 Energy -928583.3465243

N	-0.76649	1.41843	-0.07154
C	-2.01036	1.85279	0.21670
C	0.14794	2.20576	-0.59987
C	-2.37124	3.18384	0.09722
C	-1.41590	4.08495	-0.41404
C	-0.15168	3.61575	-0.75320
C	-2.92299	0.78241	0.73207
H	-3.38574	3.50509	0.29284
H	-1.66577	5.14026	-0.52683
H	0.60447	4.28902	-1.15994
C	1.43193	1.64925	-1.06883
N	-2.68842	-0.50404	0.04480
H	-3.97678	1.10586	0.66433
H	-2.69735	0.61853	1.79906
H	1.29444	1.38772	-2.13247
P	1.73612	-0.00383	-0.23635
H	2.26951	2.35979	-1.00852
Ru	-0.40632	-0.58507	0.12753
C	-3.13183	-0.43630	-1.37016
C	2.76388	-0.97221	-1.51000
C	-3.38459	-1.57380	0.79678
C	2.81626	0.48715	1.25846
C	1.79173	-1.54530	-2.54607
C	3.42342	-2.15521	-0.79768
C	3.81352	-0.12407	-2.23086
C	2.06226	1.60901	1.98221
C	4.20708	1.00144	0.88987
C	2.94913	-0.70018	2.21525
H	-0.38263	-0.54300	-1.52205
H	-2.58034	0.39612	-1.82922
C	-4.62669	-0.27589	-1.60563
H	-2.75557	-1.34493	-1.85563
H	-2.93436	-1.58370	1.80041
C	-3.24221	-2.94035	0.16087
H	-4.45015	-1.29713	0.92821
C	-0.42880	-0.79162	2.01232
O	-0.17639	-2.63743	-0.18445
H	0.11822	-3.04741	0.63704
H	-2.17636	-3.12248	-0.07293
H	-3.84319	-3.03847	-0.75619
H	-3.59094	-3.70383	0.86859
H	-4.80781	-0.21749	-2.68943
H	-5.03495	0.64510	-1.16155
H	-5.20838	-1.12709	-1.22230
H	2.37599	-2.14707	-3.26386
H	1.27463	-0.75585	-3.11162
H	1.03384	-2.17538	-2.05570
H	3.86573	-2.82409	-1.55452
H	2.67531	-2.73449	-0.23591
H	4.23239	-1.84668	-0.12066
H	4.32954	-0.75890	-2.97077
H	4.57883	0.28829	-1.56235
H	3.35837	0.70854	-2.78858
H	4.85268	0.20776	0.48993
H	4.69648	1.39303	1.79777
H	4.17387	1.82343	0.15832
H	3.52252	-1.52815	1.78067
H	1.96980	-1.08747	2.52084
H	3.47731	-0.36929	3.12537
H	2.57082	1.82424	2.93635
H	1.02509	1.32521	2.08860
H	2.04757	2.54327	1.40092
O	-0.46674	-0.98768	3.15824

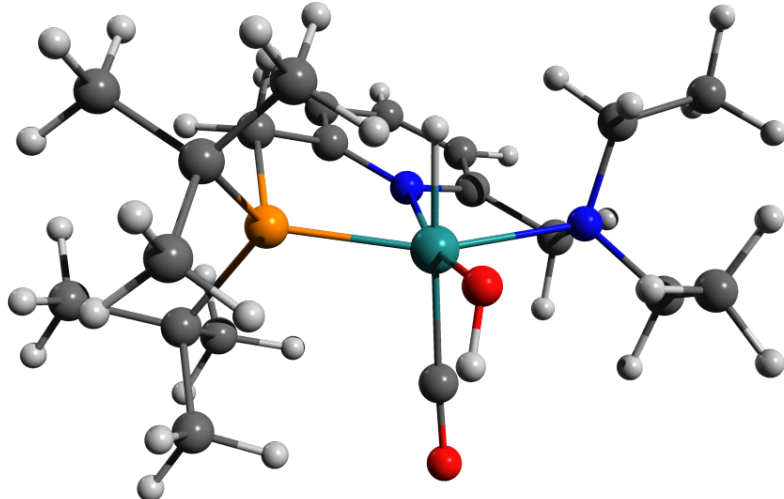
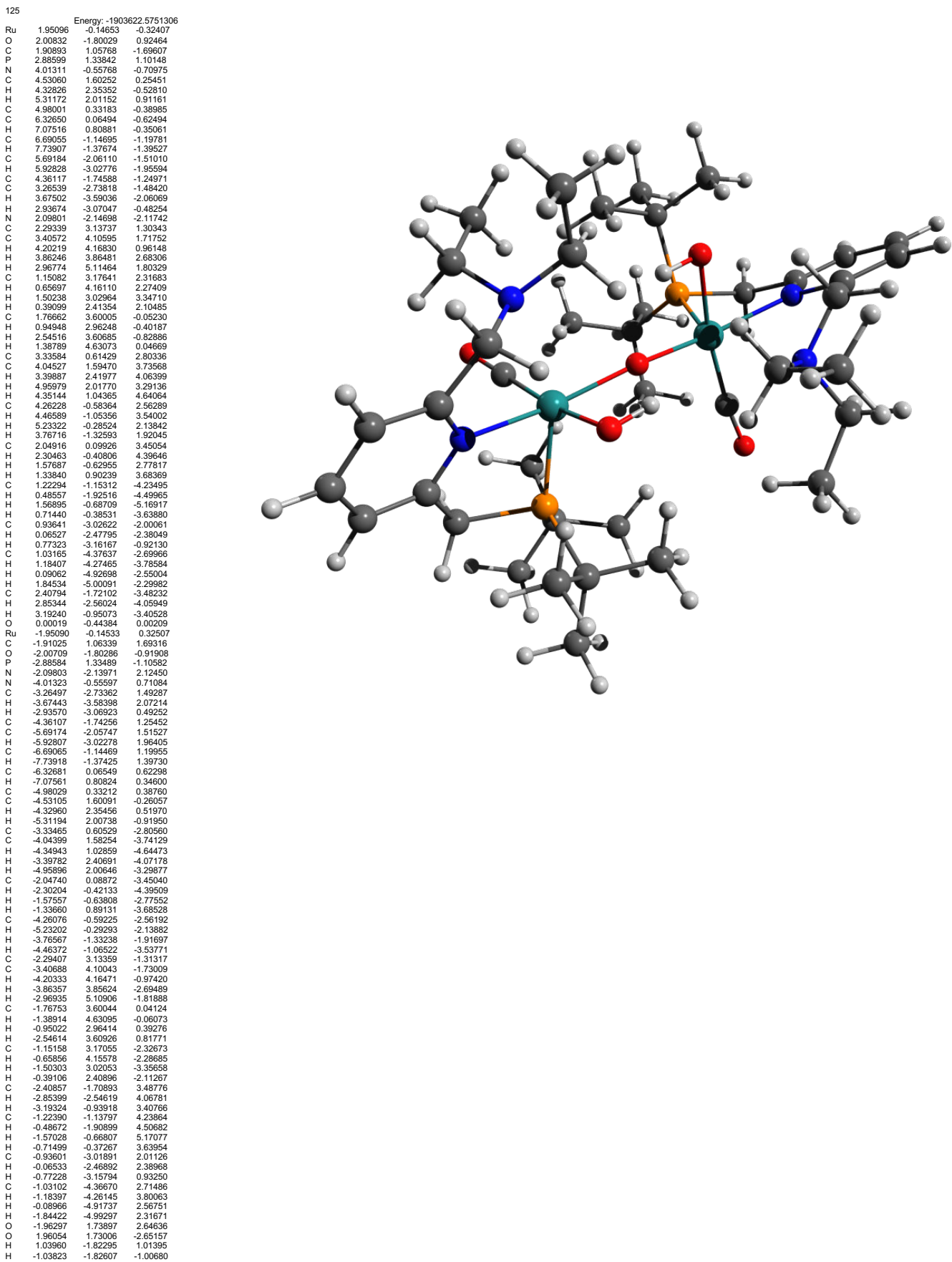


Figure 11.6-32 [Oxo Dimer]S₀ Structure and Coordinates



12 References

- 1 J. Zhang, G. Leitus, Y. Ben-David and D. Milstein, *J. Am. Chem. Soc.*, 2005, **127**, 10840–10841.
- 2 S. W. Kohl, L. Weiner, L. Schwartsburd, L. Konstantinovski, L. J. W. Shimon, Y. Ben-David, M. A. Iron and D. Milstein, *Science*, 2009, **324**, 74–77.
- 3 R. Dorta, H. Rozenberg, L. J. W. Shimon and D. Milstein, *Chem. – Eur. J.*, 2003, **9**, 5237–5249.
- 4 H. Weissman, 2004.
- 5 J. Zhang, M. Gandelman, L. J. W. Shimon and D. Milstein, *Dalton Trans.*, 2006, **0**, 107–113.
- 6 R. Barrios-Francisco, E. Balaraman, Y. Diskin-Posner, G. Leitus, L. J. W. Shimon and D. Milstein, *Organometallics*, 2013, **32**, 2973–2982.
- 7 C. K. Ng, J. Wu, T. S. A. Hor and H.-K. Luo, *Chem. Commun.*, 2016, **52**, 11842–11845.
- 8 M. Hippler, *J. Chem. Educ.*, 2003, **80**, 1074.
- 9 S. L. Murov, *Handbook of Photochemistry*, Section 13, pp. 299-313, Marcel Dekker, New York, 2nd edn., 1993.
- 10C. H. Camp, *J. Res. Natl. Inst. Stand. Technol.*, 2019, **124**, 124018.
- 11M. J. Frisch, G. W. Trucks, H. B. Schlegel, G. E. Scuseria, M. A. Robb, J. R. Cheeseman, G. Scalmani, V. Barone, G. A. Petersson and H. Nakatsuji, *Gaussian 16*, Gaussian, Inc. Wallingford, CT, 2016.
- 12M. D. Hanwell, D. E. Curtis, D. C. Lonie, T. Vandermeersch, E. Zurek and G. R. Hutchison, *J. Cheminformatics*, 2012, **4**, 17.
- 13A.-R. Allouche, *J. Comput. Chem.*, 2011, **32**, 174–182.
- 14W. L. DeLano, *CCP4 News! Protein Crystallogr.*, 2002, **40**, 82–92.
- 15T. Plachetka, in *Proc. of Spring Conf. on Computer Graphics, Budmerice, Slovakia*, 1998, vol. 123.
- 16M. G. Delcey, T. B. Pedersen, F. Aquilante and R. Lindh, *J. Chem. Phys.*, 2015, **143**, 044110.
- 17M. G. Delcey, L. Freitag, T. B. Pedersen, F. Aquilante, R. Lindh and L. González, *J. Chem. Phys.*, 2014, **140**, 174103.
- 18I. Fdez. Galván, M. G. Delcey, T. B. Pedersen, F. Aquilante and R. Lindh, *J. Chem. Theory Comput.*, 2016, **12**, 3636–3653.
- 19F. Aquilante, J. Autschbach, A. Baiardi, S. Battaglia, V. A. Borin, L. F. Chibotaru, I. Conti, L. De Vico, M. Delcey, I. Fdez. Galván, N. Ferré, L. Freitag, M. Garavelli, X. Gong, S. Knecht, E. D. Larsson, R. Lindh, M. Lundberg, P. Å. Malmqvist, A. Nenov, J. Norell, M. Odelius, M. Olivucci, T. B. Pedersen, L. Pedraza-González, Q. M. Phung, K. Pierloot, M. Reiher, I. Schapiro, J. Segarra-Martí, F. Segatta, L. Seijo, S. Sen, D.-C. Sergentu, C. J. Stein, L. Ungur, M. Vacher, A. Valentini and V. Veryazov, *J. Chem. Phys.*, 2020, **152**, 214117.
- 20I. Fdez. Galván, M. Vacher, A. Alavi, C. Angeli, F. Aquilante, J. Autschbach, J. J. Bao, S. I. Bokarev, N. A. Bogdanov, R. K. Carlson, L. F. Chibotaru, J. Creutzberg, N. Dattani, M. G. Delcey, S. S. Dong, A. Dreuw, L. Freitag, L. M. Frutos, L. Gagliardi, F. Gendron, A. Giussani, L. González, G. Grell, M. Guo, C. E. Hoyer, M. Johansson, S. Keller, S. Knecht, G. Kovačević, E. Källman, G. Li Manni, M. Lundberg, Y. Ma, S. Mai, J. P. Malhado, P. Å. Malmqvist, P. Marquetand, S. A. Mewes, J. Norell, M. Olivucci, M. Oppel, Q. M. Phung, K. Pierloot, F. Plasser, M. Reiher, A. M. Sand, I. Schapiro, P. Sharma, C. J. Stein, L. K. Sørensen, D. G. Truhlar, M. Ugandi, L. Ungur, A. Valentini, S. Vancoillie, V. Veryazov, O. Weser, T. A. Wesołowski, P.-O. Widmark, S. Wouters, A. Zech, J. P. Zobel and R. Lindh, *J. Chem. Theory Comput.*, 2019, **15**, 5925–5964.
- 21A. D. Boese, *ChemPhysChem*, 2015, **16**, 978–985.
- 22X. Yang and M. B. Hall, *J. Am. Chem. Soc.*, 2010, **132**, 120–130.
- 23Y. Chen and W.-H. Fang, *J. Phys. Chem. A*, 2010, **114**, 10334–10338.
- 24J. R. Bolton, S. J. Strickler and J. S. Connolly, *Nature*, 1985, **316**, 495–500.
- 25L. C. Seitz, Z. Chen, A. J. Forman, B. A. Pinaud, J. D. Benck and T. F. Jaramillo, *ChemSusChem*, 2014, **7**, 1372–1385.
- 26H. Li and M. B. Hall, *ACS Catal.*, 2015, **5**, 1895–1913.
- 27B. A. Pinaud, J. D. Benck, L. C. Seitz, A. J. Forman, Z. Chen, T. G. Deutsch, B. D. James, K. N. Baum, G. N. Baum, S. Ardo, H. Wang, E. Miller and T. F. Jaramillo, *Energy Environ. Sci.*, 2013, **6**, 1983–2002.
- 28Q. Wang and K. Domen, *Chem. Rev.*, 2020, **120**, 919–985.